Universiteit
Leiden
The Netherlands

Cellular models for fundamental and applied biomedical research

Liu, J.

Citation
Liu, J. (2018, November 28). *Cellular models for fundamental and applied biomedical research*. Retrieved from https://hdl.handle.net/1887/67296

Version:	Not Applicable (or Unknown)
License:	Licence agreement concerning inclusion of doctoral thesis in the Institutional Repository of the University of Leiden
Downloaded from:	https://hdl.handle.net/1887/67296

Note: To cite this publication please use the final published version (if applicable).

Cover Page

Universiteit Leiden

The handle http://hdl.handle.net/1887/67296 holds various files of this Leiden University dissertation.

Author: Liu, J.
Title: Cellular models for fundamental and applied biomedical research
Issue Date: 2018-11-28

Cellular models for fundamental and applied biomedical research

Jia Liu

Colophon

The research described in this thesis was performed at the department of Cardiology of the Leiden University Medical Centre, Leiden, the Netherlands.

Printed by: Ridderprint.nl
ISBN: 978-94-6375-161-2

©Copyright, 2018, Jia Liu.
All right reserved. No part of this book may be reproduced in any form or by any means without permission of the author.

Cellular models for fundamental and applied biomedical research

Proefschrift

ter verkrijging van
de graad van de doctor aan de Universiteit Leiden,
op gezag van Rector Magnificus prof. mr. C.J.J.M. Stolker,
volgens besluit van het College voor Promoties
te verdedigen op woensdag 28 november 2018
klokke 16.15 uur

door

Jia Liu

geboren te Shandong, China

in 1987

Promotor:
Prof. dr. M.J. Schalij

Co-promotors:
Dr. A.A.F. de Vries
Dr. D.A. Pijnappels

Leden promotiecommissie:
Prof. dr. D.E. Atsma
Prof. dr. IJzerman
Prof. dr. G. Zhou (Shenzhen University)
Prof. dr. B.J.J.M. Brundel (VU University Medical Center)
Dr. A.A. Ramkisoensing

Financial support by the Dutch Heart Foundation for the publication of this thesis is gratefully acknowledged.

Contents

Chapter 1	General introduction and outline of thesis.	**7**
Chapter 2	HP1α Mediates Defective Heterochromatin Repair and Accelerates Senescence in *Zmpste24*-deficient Cells. *Cell Cycle. 2014;13:1237-1247.*	**29**
Chapter 3	Development of a Lentivirus Vector-based Assay for Non-destructive Monitoring of Cell Fusion Activity. *PLoS One. 2014;9:e102433.*	**53**
Chapter 4	Generation and Characterization of Conditionally Immortalized Atrial Myocytes with Preserved Cardiomyogenic Differentiation Capacity: Genesis of the iAM-1 Cell Line. *Cardiovasc Res. 2018. doi: 10.1093/cvr/cvy134.*	**81**
Chapter 5	Generation and Characterization of Conditionally Immortalized Mice Brown Preadipocyte with Brown Adipocyte Differentiation Capacity. *Ready to submit.*	**131**
Chapter 6	Allosteric Modulation of Kv11.1 (hERG) Channels Protects Against Drug-Induced Ventricular Arrhythmias. *Circ Arrhythm Electrophysiol. 2016;9:e003439.*	**153**
Chapter 7	Summary and Future perspectives.	**193**
List of publications		**205**
Acknowledgements		**207**
Curriculum Vitae		**209**

Chapter 1

General introduction and outline of thesis

Background

Cell culture models play an important role in biomedical research and will continue to do so given the growing opposition to vivisection and the limited predictive value of animal models for human disease. Moreover, cell culture models can be easily established to mimic physiological or pathological processes, which is difficult to accomplish using *in silico* models. While non-cellular *in vitro* models are highly suitable for studying simple biochemical processes, cell culture models recapitulate many of the complex regulatory circuits governing protein activity *in vivo* and hence allow investigation of diverse physiological processes. Also, cell culture models offer the possibility to address fundamental research questions in a much more simplified, specific and controllable manner than can be achieved using *in vivo* models.

Aging is a complex and multifactorial process driven by genetic and environmental factors and govern by various interacting molecular pathways that lead to the physiological decline of biological systems. A variety of experimentally tractable cellular models were employed in recent years to study the basic mechanisms of aging, knowledge of which is essential to the development of effective therapeutic interventions against age-related diseases[1]. Due to the complexity of striated muscle structure and function, standardized cell culture models are a real asset for studying skeletal and cardiac muscle biology and disease. Cultures of skeletal myoblasts or cardiomyocytes (CMCs) can mimic physiological or pathological conditions, making them well-suited for proof-of-concept studies and for developing novel therapeutic interventions for specific diseases[2,3]. Especially, cultured cardiac cell monolayers have become a popular model system for electrophysiological studies[4] into the mechanisms of cardiac arrhythmias[5-7] as well as drug-induced ventricular pro-arrhythmic effects[8]. Brown adipose tissue (BAT) represents a potential therapeutic target to treat obesity and associated metabolic disorders because of its capacity to ingest and combust glucose and fatty acids for thermoregulation[9]. The properties of BAT has been investigated using cultures of primary brown preadipocytes (BPAs). Although these studies have yielded new insights into adipocyte biology[10-12], the full potential of BAT culture models has not been utilized due to the scarcity of starting material and the limited proliferation capability of primary BPAs. A potential solution to this problem would be to establish lines of BPAs by cellular immortalization. Although cell immortalization offers the possibility to produce virtually unlimited cell sources by inducing cell cycle reentry and by bypassing cell senescence, generation of robust cell lines that can recapitulate (most of) the properties of the primary cells from which they were derived requires a thorough understanding of the mechanisms of cell quiescence, proliferation, differentiation, senescence and apoptosis.

Cell cycle

To divide, a cell must grow, copy its genetic material (DNA), and physically split into two daughter cells. Cells perform these tasks in an orderly and tightly regulated series of events known as the cell cycle, which is divided into two major phases, the interphase and the mitotic phase. During the interphase, the cell grows and duplicates its nuclear DNA. The interphase is divided in three subphases. During gap phase 1 (G1 phase), the cell grows physically larger, copies organelles except for the nucleus

and synthesizes the molecular building blocks needed for the next subphase. In the synthesis (S) phase, the cell copies its chromosomal DNA and duplicates a microtubule-organizing structure called the centrosome, which helps to separate the DNA during the mitotic phase. During gap phase 2 (G2 phase), the cell grows more, makes additional macromolecules and organelles, and begins to reorganize its contents in preparation for mitosis. In the mitotic phase, the cell's chromosomal DNA is equally separated into two new daughter nuclei and the cell's cytoplasm and organelles are split after the formation of a cleavage furrow producing two new daughter cells. The segregation of duplicated chromosomes into daughter nuclei is called karyokinesis; the separation of cytoplasm and organelles is called cytokinesis.

The cell cycle is controlled by the activity of cyclin-CDK (cyclin-dependent kinase) complexes. CDKs are always present but need to be activated by phase-specific cyclins. Mitogens induce the synthesis of cyclin D early in the G1 phase. Cyclin D associates with CDK4 and CDK6 resulting in the hyperphosphorylation of the retinoblastoma protein pRB and the disruption of complexes between this pocket protein and several members of the E2F family of transcription factors. This allows these EF2 family members to form a complex with the in transcription factor DP (dimerization partner) and to induce the expression of various genes involved in cell cycle progression including the gene encoding cyclin E which is necessary for G1/S transition. CDKs are further activated during cell cycle by cyclin A and B to drive transition from S phase to G2 phase and from G2 phase to M phase, respectively. The activities of cyclin-CDK complexes are regulated by CKD inhibitors including the INK4 family (p15, p16, p18 and p19) and CIP/KIP family (p21, p27 and p57) which bind to CDKs and inactive the complexes (**Figure 1**).

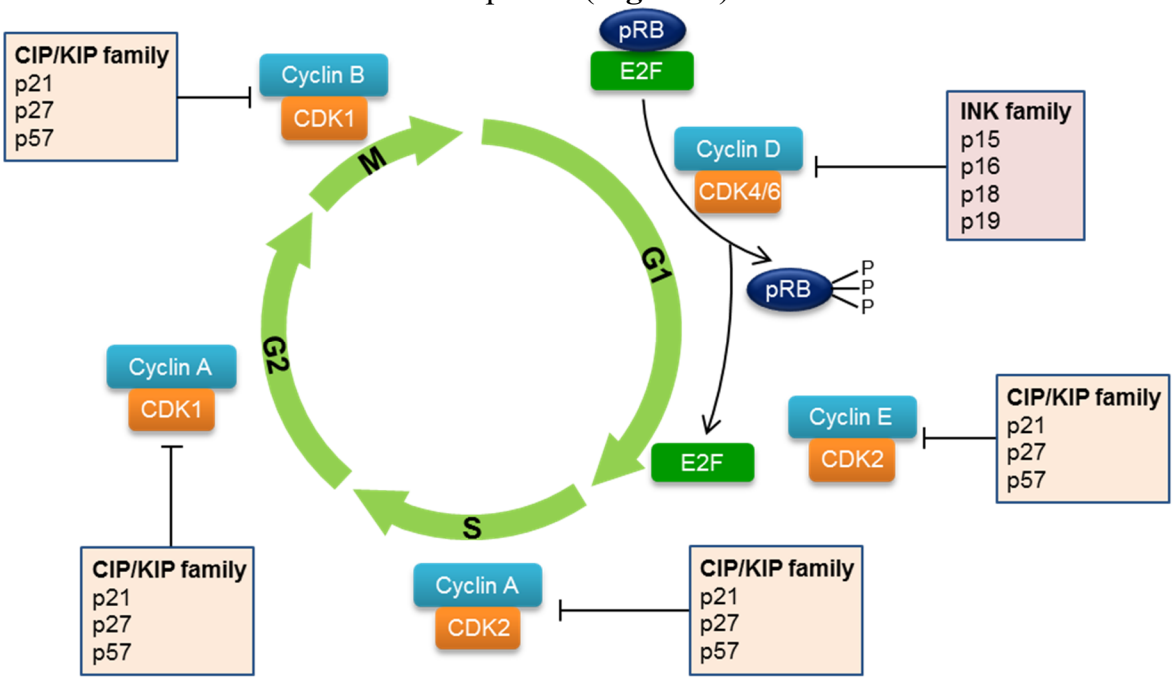

Figure 1. Cell cycle regulation.
The CDK-cyclin complexes promote cell cycle progression, while the CDK inhibitors stop it. CDK4/6-cyclin D is activated in phase G1, CDK2-cyclin E in phase G1/S, CDK2/1-cyclin A in phase S/G2 and CDK1-cyclin B in phase M. The CIP/KIP family (p21, p27 and p57) inhibit a wide range of cyclin-CDK complexes, yet the INK4 family (p15, p16, p18 and p19) specifically diminish CDK4/6 activity.

Cell fates

The fate of a cell is determined by the changes in its gene expression pattern and associated activities, which will lead to cell proliferation, quiescence, differentiation, senescence or death (**Figure 2**). Mitotic cells such as cells in the skin and gut repetitively progress through phases G1, S, G2 and M of the cell cycle. Mitotic cells can also enter the G0 phase of the cell cycle. This state of cell cycle arrest is observed in quiescent, (terminally) differentiated and senescent cells. Quiescent cells such as adult stem cells, fibroblasts and lymphocytes are temporarily arrested in G0 phase and readily reenter the cell cycle when exposed to mitogens. Dormant cells are quiescent cells showing very low metabolic activity, which is frequently interpreted as being in a deeply quiescent state. Cells like adipocytes, cardiomyocytes and neurons are believed to lose the capacity to enter the cell cycle and to permanently reside in the G0 phase of the cell cycle once they are fully differentiated. However, recent studies have shown that both self-renewal of cardiac tissue and regeneration upon damage mainly results from the cell cycle reentry and proliferation of existing cardiomyocytes[13-18]. In general mitotic cells will stop dividing and become senescent after a limited number of divisions. Senescent cells cannot replicate anymore because of telomeres shorting, irreparable DNA damage, nutritional deficiency, harmful chemicals, oxidative stress or physiologic stress. Except for the stem, progenitor and precursor cells that escape from death by being converted in more differentiated cell types, all other cells finally die because of natural turnover or due to injury, including the death of the organism. Cell deaths can occur by various different mechanisms. Two of the major types of cell death are apoptosis and necrosis[19]. Apoptosis, also known as programmed cell death, is a normal physiological, non-inflammatory process to remove unwanted cells. In this process, apoptotic bodies are formed to confine cell organelles and other parts, which will be phagocytosed by macrophages. Necrosis, also known as unprogrammed cell death, is a less orderly process than apoptosis, in which cells and organelles swells resulting in membrane rupture. As a consequence, the cellular content is released in the extracellular space triggering an inflammatory response and possible causing further damage to adjacent cells[20]. A major difference between normal somatic cells and transformed cells is their proliferation potential. Normal somatic cells in culture have a limited ability to multiply themselves known as the Hayflick limit (see below), while transformed cells have evaded normal cellular senescence due to mutations resulting in acquisition of unlimited proliferation ability, evasion of apoptosis, growth factor independency, non-responsiveness to growth inhibitors, promotion of angiogenesis and invasive capacity. Immortalized cells have not necessarily undergone neoplastic transformation, but have accumulated sufficient mutations to proliferate unlimitedly. Upon transplantation immunocompromised mice, transformed cells will form tumors in contrast to immortalized cells. More details about cellular senescence, quiescence and immortalization are described below.

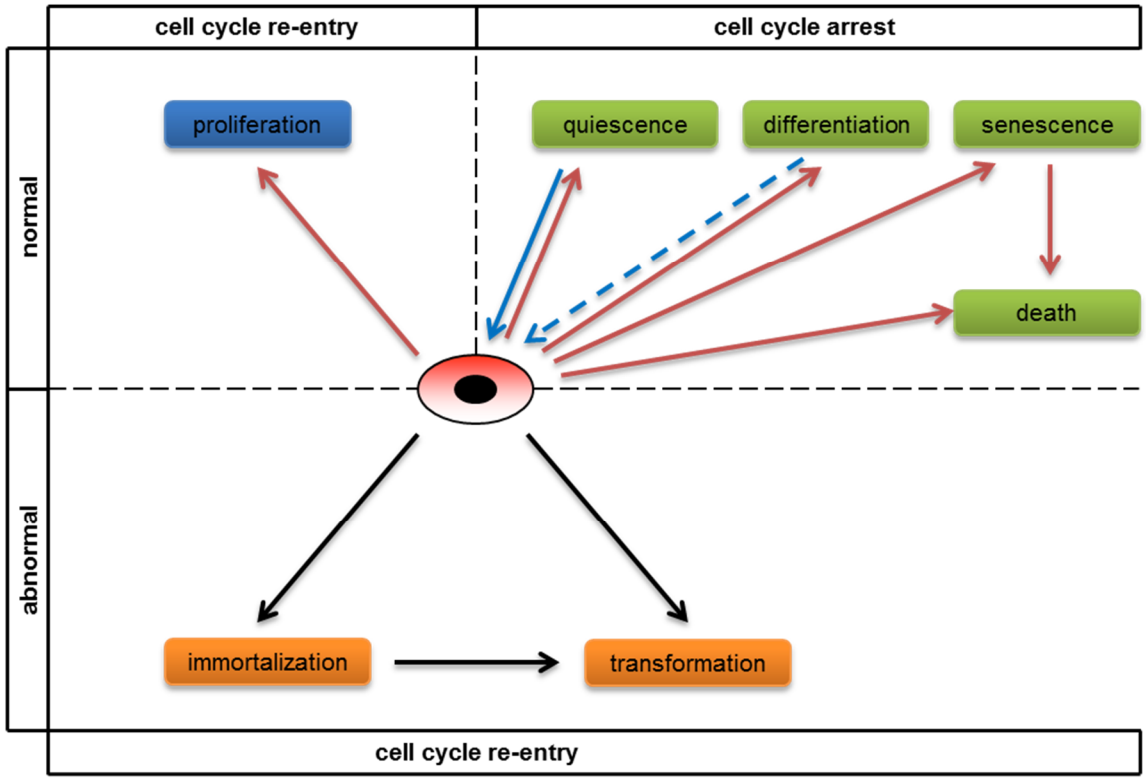

Figure 2. Possible cell fates.
Under normal conditions, cells adopt one of five distinct cell fates: they can remain in the cell cycle and continue to proliferate or leave the cell cycle and become quiescent, differentiated or senescent or undergo apoptotic or necrotic cell death. Under pathological conditions, cells can escape from senescence or apoptosis and become immortalized or transformed following the activation of endogenous oncogenes and/or the inactivation of endogenous tumor suppressor genes. Cell immortalization can also be brought about by oncogenic viruses or via genetic engineering.

Cellular senescence

Senescence as a common stress response

Normal mammalian somatic cells such as fibroblasts, myoblasts and preadipocytes, grown in culture fail to proliferate after a finite number of divisions and ultimately encounter senescence. This phenomenon was first found in human fibroblast cultures by Hayflick[21] and later referred to as replicative senescence[22-24]. Replicative senescence is thought to be the result of progressive telomere shortening as a cell-intrinsic mechanism[25,26]. Cellular senescence can also be stimulated by various types of cell stress like lack of nutrients, harmful chemicals (e.g. cytostatic drugs), oxidative stress or physiologic stress (e.g. caused by aberrant expression of tumor suppressor or oncogenes and excessive growth factor stimulation), which block the proliferation of cells[27-29]. This type of senescence is referred to as premature or induced senescence[30]. These findings have led to a distinction between "replicative senescence" which is induced by a cell-intrinsic mechanism, and "stress-induced premature senescence" which is triggered by extrinsic factors[31]. In many cases, replicative and premature senescence are interconnected. Telomere shortening is, for instance, accelerated by oxidative stress. Actually, cells may suffer cumulative damage from multiple stresses during culture. Senescence will be triggered when cellular damage has reached a

certain threshold, whatever has caused the damage. Senescent cells undergo dramatic changes in morphology and function. They generally become enlarged and flattened, have an increased lysosomal content, suffer from mitochondrial dysfunction and secrete increased amounts of inflammatory, growth-promoting, and remodeling factors. They may also form senescence-associated heterochromatin foci, often display a chronic DNA damage response, are incapable of synthesizing DNA for mitosis, show high resistance to apoptosis and are unresponsive to mitogenic stimuli. However, senescent cells are still metabolically active for months or even years[27,32-35].

p53 and pRB as key regulators of senescence

Molecular pathways of senescence are complex involving multiple layers of regulation with cooperative changes. The p53 tumour suppressor protein and the pocket proteins (*i.e.* pRB, p107 and p130) have been shown to play critical roles in the induction of senescence. The p53 protein is an important cell cycle regulator of both the G1/S and G2/M checkpoints by activating CDKN1A transcription. CDKN1A codes for p21 protein, which is a member of the CIP/KIP family of tumor suppressor proteins. These proteins inhibit various cyclin-CDK complexes required for promotion of the cell cycle (**Figure 3**). Hypophosphorylated pRB controls the G1/S checkpoint by directly binding to and inhibiting various E2F family members thereby repress gene transcription required for transition from the G1 to S phase of the cell cycle. In actively dividing cells, the suppressive effect of pRB on E2Fs is lost due to hyperphosphorylation of pRB by cyclin D-CDK4 and cyclin D-CDK6 complexes. In senescent cells the activity of these complexes is inhibited by members of the INK4 family of tumor suppressor proteins[36]. (**Figure 3**).

Numerous studies have explored the roles of p53 and pocket proteins in the induction and maintenance of senescence in mouse embryo fibroblasts (MEFs). Suppression of p53 expression allows cells to escape from senescence and leads to their indefinite expansion[37]. Inactivation of pRB alone is not enough to ease senescence of MEFs, while accompanying ablation of other pocket proteins including p107 and p130 strongly increased their proliferation capacity[38,39]. This demonstrates that the inactivation of either p53 or all three pocket proteins is sufficient to block the initiation of senescence. Suppression of either p53 or pRB in senescent MEFs is not enough to maintain senescence but leads to reactivation of the cell cycle[37,40]. Collectively, these findings suggest that p53 and the pocket proteins control cellular senescence in a hierarchical manner, in which the activation of pocket proteins is downstream of that of p53. Indeed, as mentioned before, p53 actives p21, which in turn inhibit cyclin-CDK complexes involved in the phosphorylation and inactivation of the pocket proteins. However, MEFs lacking p21 still undergo senescence and have a lifespan similar to wild-type cells[41], which shows that p21 is not the only link between p53 and pocket protein activity in the regulation of senescence (**Figure 3**).

Cellular quiescence

As indicated above, cells can enter into either of three different G0 states. While senescent and (terminally) differentiated cells have permanently excited the cell cycle (irreversible G0 arrest), quiescent cells only temporarily reside in the G0 phase

(reversible G0 arrest) and reenter the cell cycle in response to normal physiological stimuli[42]. The notion that terminally differentiated cells are irreversibly arrested in G0 has been challenged by the finding that mature hepatocytes dedifferentiate and reenter the cell cycle after injury of the liver and contribute to its regeneration[43-46]. Similar observation have recently been made for terminally differentiated cardiomyocytes[13-18]. Hence, not only quiescent cells but also terminally differentiated cells can exit the G0 phase and resume cell division.

In quiescent cells, p53 has been considered as main molecular regulator of cell cycle arrest[47]. Similar to senescence, the mechanism by which p53 mediates quiescence is dependent on the activation of p21, a CDK inhibitor and critical component of the pRB-E2F pathway[48]. In addition to p53, quiescent cells typically feature lower levels of pRB-E2F pathway activators, such as cyclin D[49-51] and high levels of pathway repressors, such as p21[48]. The disruption of all three pocket proteins and the acute loss of pocket protein function in quiescent cells lead to cell proliferation[38-40,52]. pRB deficiency in quiescent skeletal stem cells leads to an increase of proliferation and a loss of terminal differentiation capacity[38,53]. All of the above suggest that the RB-E2F pathway plays a pivotal role in quiescence. Among the E2F family of transcription factors, E2F1, -2 and -3 are considered "E2F transcriptional activators" and E2F4 and -5 are deemed "E2F transcriptional repressors"[54]. In cell cycle-arrested cells, hypophosphorylated pRB prevents cell cycle reentry by binding and repressing E2F1, -2 and -3, which activate genes required for the transition from G1 into S phase. In addition, hypophosphorylated p130 and p107 form complexes with E2F4 and -5. The complexes bind to the promotors of E2F target genes and recruit chromatin remodeling factors that block transcription[55,56]. In quiescent cells that are stimulated with mitogens, cyclin-CDK complexes phosphorylate pRB thereby releasing E2F1, -2 and -3. Similarly, phosphorylation of p130 and p107 abolishes their interaction with E2F4 and -5 repressors[57,58]. Especially E2F4-p130 complexes are very prominent in resting (*i.e.* G0-arrested) cells suggesting that they play a pivotal role in the maintenance of cell quiescence[59-61] (**Figure 3**).

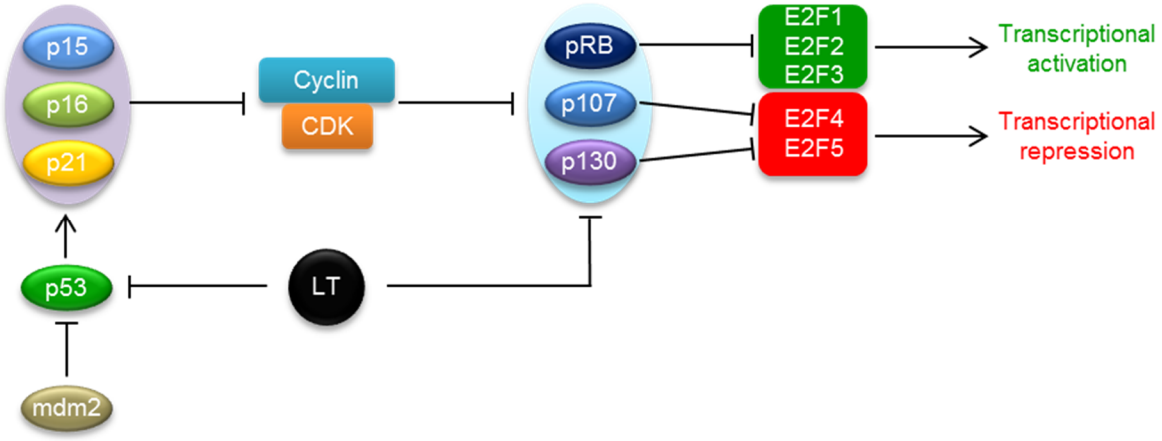

Figure 3. Participation of cell cycle regulators in cell cycle arrest.
p53 activates CDK inhibitors (e.g. p15, p16 and p21), which in turn disrupts cyclin-CKD complexes involved in the inactivation of the pocket proteins (pRB, p107 and p130). This allows the pocket proteins to arrest cell in a non-proliferative state by blocking the transcription of E2F target genes. LT, large tumor antigen. mdm2, mouse double minute 2.

Simian virus 40 LT antigens & cell immortalization

Simian virus 40 (SV40) is a small double-stranded non-enveloped DNA virus with a circular genome and an icosahedral capsid in the family of Polyomaviridae. The SV40 genome is composed of three main regions: (i) an early region encoding large tumor antigen (LT), 17kT and small tumor antigen (ST), (ii) a late region encoding the viral coat proteins (VP1, VP2, VP3 and VP4) and the agnoprotein (Agno) and (iii) the regulatory region containing the early and late promotor and the origin (Ori) of replication (**Figure 4A**). LT, 17kT and ST are produced from alternative splice products of the early viral pre-mRNA and are co-expressed in infected cells. The amino-terminus of LT contains a J domain which contributes to viral DNA replication[62]. Downstream of the the J domain, there is a LXCXE motif that can directly bind to the pocket proteins (*i.e.* pRB, p107 and p130)[63,64]. The J domain cooperates with the LXCXE motif to disrupt the interaction between E2F family members and the pocket proteins[63]. The DNA-binding domain (DBD) of LT recognizes Ori sequences and this interaction is essential for the initiation of viral DNA replication. The helicase domain works as DNA helicase to unwind the dsDNA template for viral replication and it also interacts with p53[65]. ST contains a J domain followed by a cellular protein phosphatase 2A (PP2A) binding region which contains two zinc fingers. ST binds the A and C subunits of PP2A and displaces the B subunit, thereby inhibiting the pro-apoptotic activity of PP2A[66,67.] 17kT shares several regulatory domains with LT that mediate some of its most important functions including stimulation of cell proliferation by binding to pocket proteins[68] (**Figure 4B**).

LT plays an essential role in multiple steps of the viral life cycle. After infection, LT induces host cells to enter the S phase thereby creating optimal conditions for the replication of viral DNA. Meanwhile, LT works as the DNA helicase and then utilizes the host's replication machinery to replicate the viral DNA. Besides, LT is also involved in transcription and virion assembly. Given the capability of LT to incite cell proliferation, LT has been successfully used to immortalize multiple primary cell types with no/limited proliferative capacity *in vitro*[69-71]. Our current understanding indicates LT's ability to drive cell proliferation is mainly due to its interaction with the pocket proteins and p53[72,73]. Quiescent cells including differentiated cells are trapped in G0 by the pocket proteins[42]. Hypophosphorylated pocket proteins bind to E2Fs and thereby block gene expression required for nucleotide synthesis, DNA replication, cell cycle progression and apoptosis. When cells are mitogenically stimulated, pocket proteins become phosphorylated allowing E2F-mediated S phase gene transcription. Instead of disrupting E2F-pocket protein complexes by pocket protein hyperphosphorylation, LT binds to hypophosphorylated pocket proteins setting free the pocket protein-bound E2Fs resulting in E2F-dependent gene expression and cell cycle reentry[74]. The p53 level in normal cells remains very low because it binds to Mdm2 which induces ubiquitination and subsequent degradation of p53[72,75]. Besides Mdm2, many other proteins affect the biological activity and stability of p53 through various types of post-translational modifications. Different cellular stress conditions lead to stabilization of p53 allowing it to act as a transcriptional activator of genes mediating apoptosis or cell cycle arrest[76,77]. LT inactivates p53 by covering its DNA-binding domain and thus block the expression of

p53-dependent genes, which leads to cell cycle reentry and avoids cell cycle arrest as well as apoptosis[78] (**Figure 3**).

Exposure of SV40 particles to chemical mutagens has resulted in the recovery of several temperature-sensitive LT mutants (ts-LTs) that can cause cell immortalization/transformation at permissive temperatures (≤ 34°C) but fail to do so at nonpermissive temperatures (≥ 37°C)[79,80]. These ts-LTs have been used to control the activity of LT allowing conditional immortalization of primary mammalian cells.

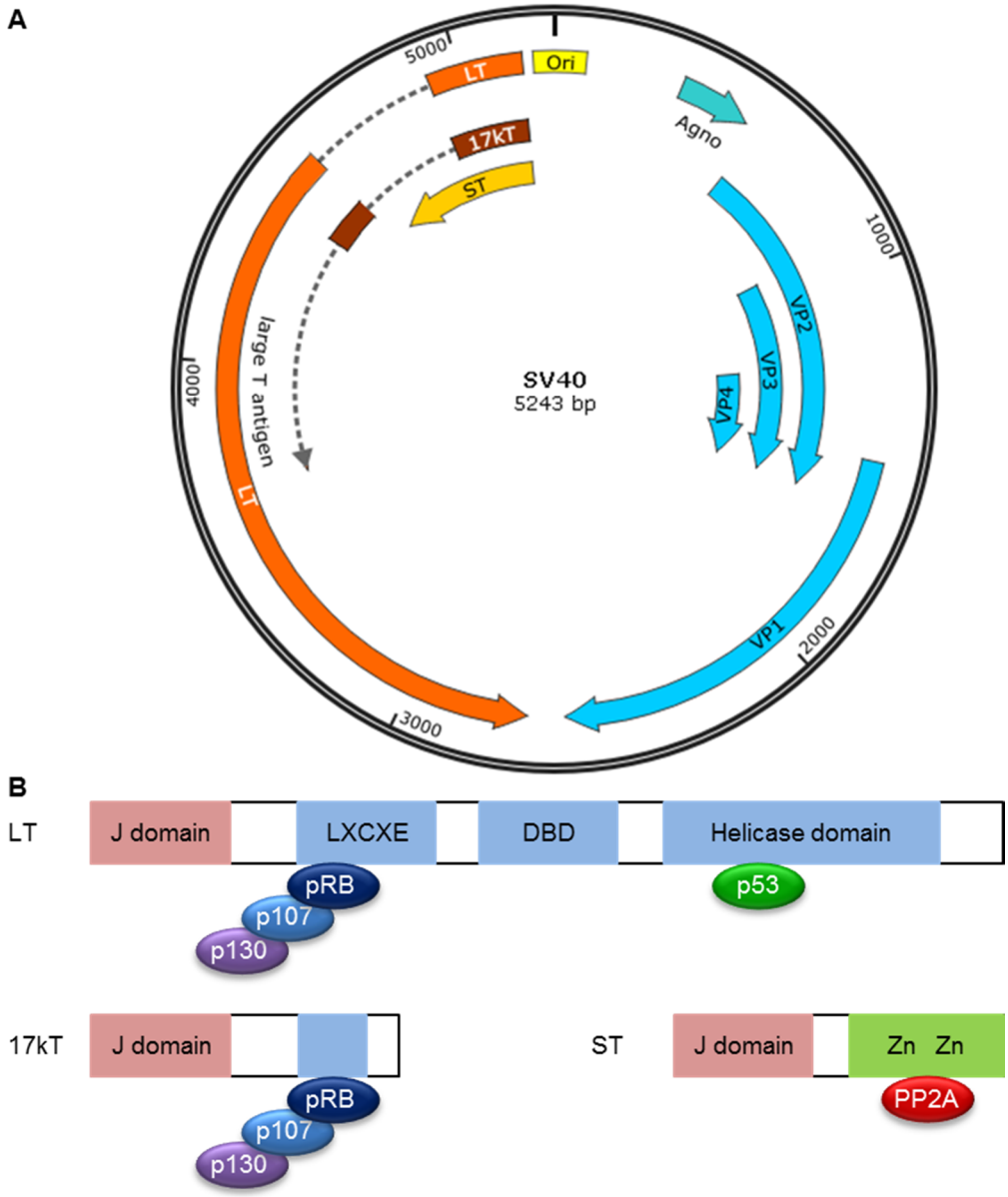

Figure 4. Structure of SV40
(A) Genomic structure of SV40. The circular double-stranded DNA genome contains three main regions: the regulatory region, an early region encoding LT, 17kT and ST, and a late region encoding the viral coat proteins VP1, VP2, VP3 and VP4 as well as the agnoprotein. (B) The functional domains of SV40 T antigens. The J domain is shared by all three antigens. LT also contains a pocket protein-binding LXCXE motif, a DNA-binding domain (DBD), a p53-binding helicase domain. 17kT shares several regulatory domains with LT including a pocket protein binding domain. ST contains a J domain followed by a PP2A-binding region with two zinc-fingers.

For instance, ts-LT tsA58, which carries an alanine to valine substitution at amino acid position 438 that abolishes its binding to and inhibition of p53 at nonpermissive temperatures[81] was expressed in transgenic mice to generate conditional immortalized cell lines from different tissues[82,83].

Cell cycle regulation in cardiomyocytes

In the embryonic and fetal hearts of vertebrates, including mammals, cardiomyocytes have high cell cycle activity and are capable of DNA synthesis, karyokinesis and cytokinesis resulting in cardiomyocyte division and an increase of cardiomyocyte number. However, the proliferative capacity of postnatal hearts differs from various species. Zebrafish have cardiomyocyte proliferative capacity throughout life. A complete regeneration of heart tissue lost from the resection of the ventricular apex can be managed in adult zebrafish through the proliferation of pre-existing cardiomyocytes[15,84]. In contrast, mammalian cardiomyocytes lose their proliferative capacity shortly after birth and the expansion of postnatal mammal heart driven by non-mitotic growth produces multinucleated or polyploid cells and hypertrophic cells[85-88]. In mice, during the first week of postnatal period, the majority of cardiomyocytes undergo karyokinesis in the absence of cytokinesis, which generates a population of binucleated cardiomyocytes[85]. In this event, cardiomyocytes enter the M phase of the cell cycle and perform nuclear division, but they do not undergo cytokinesis[86,88]. In contrast, the timeline of human cardiomyocyte proliferative capacity is not clear, however, more than half of all adult human cardiomyocytes are polyploid as a result of DNA duplication without nuclear division[87]. The polyploidazation results from shuttling between G1, S and G2 phase without entering into the M phase. Although damage-induced cardiomyocyte proliferation in adult mammals has been observed[13,89,90], the growth of stressed and injured mammalian hearts is largely caused by hypertrophy. Under physiological and pathological hypertrophy-stimulating conditions, cardiomyocytes enter the G1 phase of cell cycle where the grow in size by synthesis of extra RNAs and proteins, but they fail to undergo S phase[91-93] (**Figure 5**).

This different behavior of antenatal and postnatal cardiomyocytes is due to the developmental changes in cell cycle activity[86,94]. The cell cycle of cardiomyocyte is tightly controlled by transcription factors and regulators thereof like the pocket proteins, which play an essential role in cell cycle exit and differentiation of cardiomyocytse[95]. For example, p107 and p130 interact with E2F family members to inhibit DNA synthesis in the fetal and neonatal cardiomyocytes, respectively[96]. Moreover, pRB silences multiple proliferation-promoting genes in adult cardiomyocyte to maintain their post-mitotic state by interaction with heterochromatin protein 1γ[97,98]. Apart from the pocket proteins, transcription factors such as Meis1, MEF2D, FoxO1, and FoxO3, inhibit cell cycle progression by increasing the expression of p21, p27, p15, and p16[99-102]. In contrast, transcription factors, such as E2F1, E2F2, E2F4, CASZ1, GATA4, Tbx20, and FoxM1, stimulate cell cycling by increasing the expression of cyclins[99,101,103-106]. Besides, PI3K-AKT, Wnt/β-catenin and YAP signaling pathways play important roles in cardiomyocyte proliferation[107-111]. Manipulation of the cell cycle in post-mitotic cardiomyocytes may be an attractive strategy to obtain large numbers of cardiomyocytes for *in vitro* studies, cardiac cell

therapy and the regeneration of injured hearts from inside by re-awaking cell cycling in cardiomyocytes surrounding the site(s) of myocardial damage.

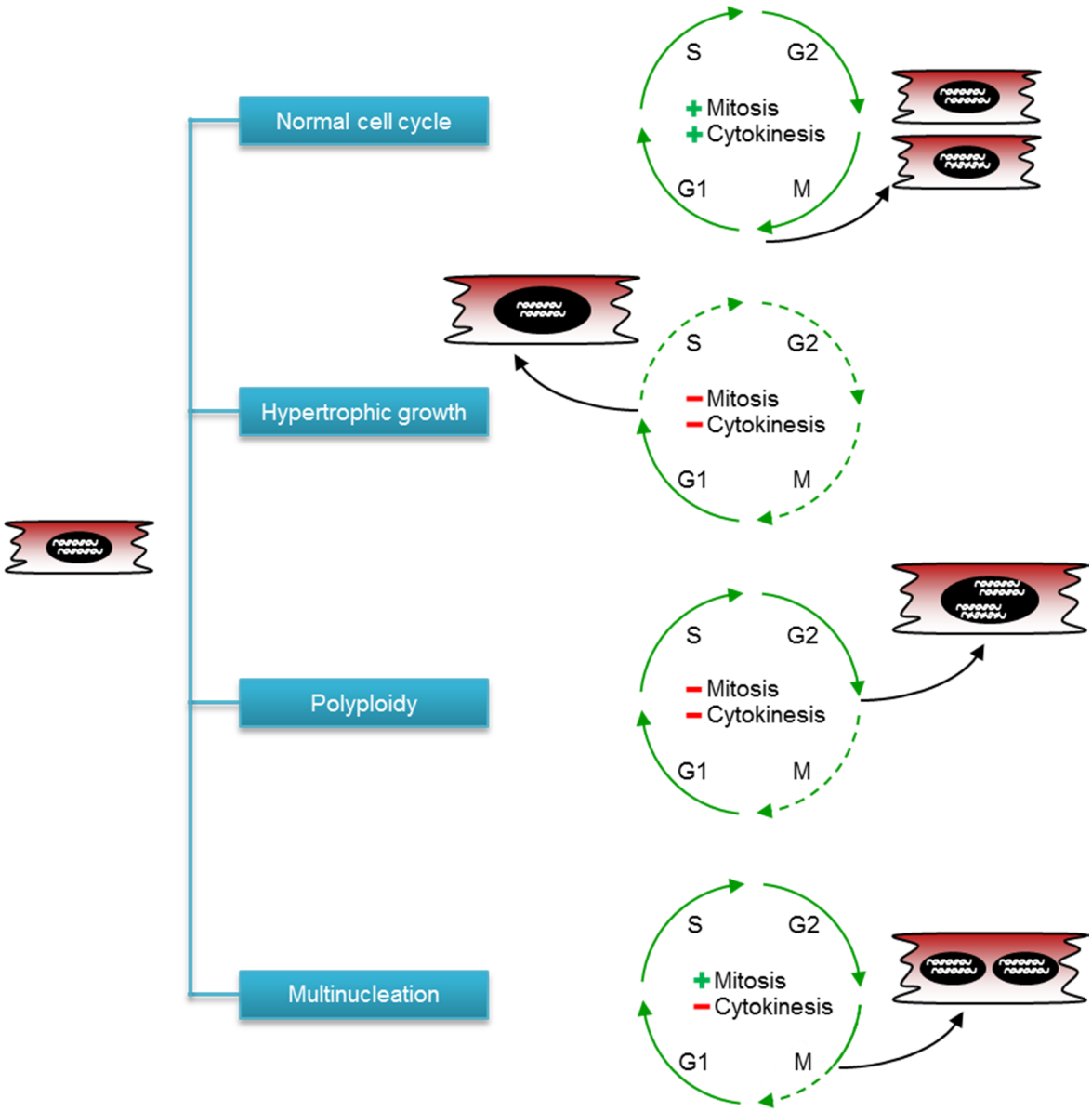

Figure 5. Cell cycle activities in cardiomyocytes.
In a typical cell cycle, cell successively enters the G1 phase (for synthesis of RNAs and proteins), S phase (for DNA synthesis), G2 phase (for additional growth) and M phase (for karyokinesis and cytokinesis) resulting in two individual cells. In the presence of hypertrophic stimuli, cardiomyocytes enter the G1 phase and grow in size by synthesis of RNAs and proteins, but they fail to enter the S phase. Polyploidazation results from shuttling between G1, S and G2 phase without entering into the M phase. Multinucleation occurs when cardiomyocytes enter the M phase and perform karyokinesis, but are withdraw from the cell cycle before cytokinesis.

Aim and outline of thesis

The aim of this thesis is to develop and use cell culture models for fundamental and applied biomedical research. Cell immortalization is a promising approach to produce large number of cells from same amounts/scarce primary staring material by inducing cell cycle reentry or bypassing cell senescence. Accordingly, a major part of this thesis was dedicated to the generation of robust cellular model systems by cell immortalization for addressing fundamental and applied research questions in a reproducible, flexible and standardized way.

Bypassing cellular senescence is a prerequisite for cell immortalization. It is therefore important to have a better understanding of the mechanism of senescence before immortalizing cells. A variety of proteins and pathways were found to be involved in senescence. However, the role of heterochromatin proteins and their contribution to abnormal chromatin organization in cell senescence is largely unknown. **Chapter II** of this thesis uses premature MEFs as a senescence model system which is derived from progeria disorder mice and studies the role of heterochromatin proteins and the associated chromatin organization in DNA damage response (DDR)-induced senescence.

In order to get familiar with the properties of immortalized cells including their culture conditions, proliferation and differentiation, an existing line of immortalized human myoblast is cultured and its differentiation is investigated in **Chapter III**. With the aid of this cell line, a novel non-destructive quantitative assay to monitor cell fusion is developed.

Cardiac cell therapy, tissue engineering and *in vitro* studies into cardiac arrhythmias or for testing the potential cardiotoxicity of drugs require large numbers of functional and homogeneous cardiomyocytes. Progress in these areas of research is impeded by the limited availability of heart tissue and the very low mitotic activity of cardiomyocytes highlight the urge to develop new/rich source of cadiomyocytes for both basic and translational research. **Chapter IV** describes the generation and characterization of a immortalized atrial myocyte cell line with preserved cardiomyogenic differentiation capacity. Through controlled expansion and differentiation of this cell line, large numbers of functional cardiomyocytes are generated, hence providing an attractive cell model for cardiac research.

BAT is regarded as a potential target to treat obesity and associated metabolic disorders because of its capacity to take up and combust glucose and fatty acids for thermoregulation. However, its cellular and molecular investigation has been hampered due to high cellular heterogeneity and a limited availability of cell material. In **Chapter V,** monoclonal lines of immortalized BPAs are generated by using mouse BAT as starting material. The long-term proliferation and high adipogenic capacity of the cell lines provide an attractive model system for fundamental and applied research into BAT.

Besides immortalized cell lines, primary cardiomyocytes were also used to solve research questions. In **Chapter VI**, neonatal rat ventricular myocyte cultures are established as an *in vitro* model for investigating the action potential-prolonging and associated proarrhythmic effects of Kv11.1 blockers. In this study, a newly designed

and synthesized compound LUF7244 is shown to prevent drug-induced proarrhythmic effects as by an allosteric mechanism.

Finally, **Chapter VII** provides the summary and conclusions drawn from each study of this thesis, as well as future perspectives related to the application of immortalized cells.

References

1. Ludovico P, Osiewacz HD, Costa V, Burhans WC. Cellular models of aging. *Oxid Med Cell Longev* 2012;**2012**.
2. Goetsch K, Myburgh K, Niesler CU. In vitro myoblast motility models: investigating migration dynamics for the study of skeletal muscle repair. *J Muscle Res Cell Motil* 2013;**34**:333-347.
3. Parameswaran S, Kumar S, Verma RS, Sharma RK. Cardiomyocyte culture—an update on the in vitro cardiovascular model and future challenges. *Can J Physiol Pharmacol* 2013;**91**:985-998.
4. Herron TJ, Lee P, Jalife J. Optical imaging of voltage and calcium in cardiac cells & tissues. *Circ Res* 2012;**110**:609-623.
5. Iravanian S, Nabutovsky Y, Kong C-R, Saha S, Bursac N, Tung L. Functional reentry in cultured monolayers of neonatal rat cardiac cells. *American Journal of Physiology-Heart and Circulatory Physiology* 2003;**285**:H449-H456.
6. Bub G, Glass L, Publicover NG, Shrier A. Bursting calcium rotors in cultured cardiac myocyte monolayers. *Proceedings of the National Academy of Sciences* 1998;**95**:10283-10287.
7. Bursac N, Tung L. Acceleration of functional reentry by rapid pacing in anisotropic cardiac monolayers: formation of multi-wave functional reentries. *Cardiovasc Res* 2006;**69**:381-390.
8. Yu Z, Liu J, van Veldhoven JP, IJzerman AP, Schalij MJ, Pijnappels DA, Heitman LH, de Vries AA. Allosteric modulation of Kv11. 1 (hERG) channels protects against drug-induced ventricular arrhythmias. *Circulation: Arrhythmia and Electrophysiology* 2016;**9**:e003439.
9. Townsend K, Tseng Y-H. Brown adipose tissue: recent insights into development, metabolic function and therapeutic potential. *Adipocyte* 2012;**1**:13-24.
10. Cohen P, Levy JD, Zhang Y, Frontini A, Kolodin DP, Svensson KJ, Lo JC, Zeng X, Ye L, Khandekar MJ, Wu J, Gunawardana SC, Banks AS, Camporez JP, Jurczak MJ, Kajimura S, Piston DW, Mathis D, Cinti S, Shulman GI, Seale P, Spiegelman BM. Ablation of PRDM16 and beige adipose causes metabolic dysfunction and a subcutaneous to visceral fat switch. *Cell* 2014;**156**:304-316.
11. Tseng YH, Cypess AM, Kahn CR. Cellular bioenergetics as a target for obesity therapy. *Nat Rev Drug Discov* 2010;**9**:465-482.
12. Stanford KI, Goodyear LJ. The therapeutic potential of brown adipose tissue. *Hepatobiliary Surg Nutr* 2013;**2**:286-287.
13. Beltrami AP, Urbanek K, Kajstura J, Yan SM, Finato N, Bussani R, Nadal-Ginard B, Silvestri F, Leri A, Beltrami CA, Anversa P. Evidence that human cardiac myocytes divide after myocardial infarction. *N Engl J Med* 2001;**344**:1750-1757.
14. Bergmann O, Bhardwaj RD, Bernard S, Zdunek S, Barnabe-Heider F, Walsh S, Zupicich J, Alkass K, Buchholz BA, Druid H, Jovinge S, Frisen J. Evidence for cardiomyocyte renewal in humans. *Science* 2009;**324**:98-102.
15. Jopling C, Sleep E, Raya M, Marti M, Raya A, Izpisua Belmonte JC. Zebrafish heart regeneration occurs by cardiomyocyte dedifferentiation and proliferation.

Nature 2010;**464**:606-609.
16. Kikuchi K, Holdway JE, Werdich AA, Anderson RM, Fang Y, Egnaczyk GF, Evans T, Macrae CA, Stainier DY, Poss KD. Primary contribution to zebrafish heart regeneration by gata4(+) cardiomyocytes. *Nature* 2010;**464**:601-605.
17. Mollova M, Bersell K, Walsh S, Savla J, Das LT, Park SY, Silberstein LE, Dos Remedios CG, Graham D, Colan S, Kuhn B. Cardiomyocyte proliferation contributes to heart growth in young humans. *Proc Natl Acad Sci U S A* 2013;**110**:1446-1451.
18. Senyo SE, Steinhauser ML, Pizzimenti CL, Yang VK, Cai L, Wang M, Wu TD, Guerquin-Kern JL, Lechene CP, Lee RT. Mammalian heart renewal by pre-existing cardiomyocytes. *Nature* 2013;**493**:433-436.
19. Nikoletopoulou V, Markaki M, Palikaras K, Tavernarakis N. Crosstalk between apoptosis, necrosis and autophagy. *Biochimica et Biophysica Acta (BBA)-Molecular Cell Research* 2013;**1833**:3448-3459.
20. Lauber K, Ernst A, Orth M, Herrmann M, Belka C. Dying cell clearance and its impact on the outcome of tumor radiotherapy. *Front Oncol* 2012;**2**:116.
21. Hayflick L, Moorhead PS. The serial cultivation of human diploid cell strains. *Exp Cell Res* 1961;**25**:585-621.
22. Dimri GP, Lee X, Basile G, Acosta M, Scott G, Roskelley C, Medrano EE, Linskens M, Rubelj I, Pereira-Smith O. A biomarker that identifies senescent human cells in culture and in aging skin in vivo. *Proceedings of the National Academy of Sciences* 1995;**92**:9363-9367.
23. Coates PJ. Markers of senescence? *The Journal of pathology* 2002;**196**:371-373.
24. Cong Y-S, Wright WE, Shay JW. Human telomerase and its regulation. *Microbiol Mol Biol Rev* 2002;**66**:407-425.
25. Bodnar AG, Ouellette M, Frolkis M, Holt SE, Chiu C-P, Morin GB, Harley CB, Shay JW, Lichtsteiner S, Wright WE. Extension of life-span by introduction of telomerase into normal human cells. *science* 1998;**279**:349-352.
26. Harley CB, Futcher AB, Greider CW. Telomeres shorten during ageing of human fibroblasts. *Nature* 1990;**345**:458-460.
27. Serrano M, Blasco MaA. Putting the stress on senescence. *Curr Opin Cell Biol* 2001;**13**:748-753.
28. Lloyd AC. Limits to lifespan. *Nat Cell Biol* 2002;**4**:E25-E27.
29. Serrano M, Lin AW, McCurrach ME, Beach D, Lowe SW. Oncogenic ras provokes premature cell senescence associated with accumulation of p53 and p16 INK4a. *Cell* 1997;**88**:593-602.
30. Drayton S, Peters G. Immortalisation and transformation revisited. *Curr Opin Genet Dev* 2002;**12**:98-104.
31. Ben-Porath I, Weinberg RA. The signals and pathways activating cellular senescence. *The international journal of biochemistry & cell biology* 2005;**37**:961-976.
32. Shelton DN, Chang E, Whittier PS, Choi D, Funk WD. Microarray analysis of replicative senescence. *Curr Biol* 1999;**9**:939-945.
33. Narita M, Nuñez S, Heard E, Narita M, Lin AW, Hearn SA, Spector DL, Hannon GJ, Lowe SW. Rb-mediated heterochromatin formation and silencing

of E2F target genes during cellular senescence. *Cell* 2003;**113**:703-716.
34. Bérubé NG, Smith JR, Pereira-Smith OM. The genetics of cellular senescence. *The American Journal of Human Genetics* 1998;**62**:1015-1019.
35. Gorbunova V, Seluanov A, Mao Z, Hine C. Changes in DNA repair during aging. *Nucleic Acids Res* 2007;**35**:7466-7474.
36. Lanigan F, Geraghty J, Bracken A. Transcriptional regulation of cellular senescence. *Oncogene* 2011;**30**:2901.
37. Dirac AM, Bernards R. Reversal of senescence in mouse fibroblasts through lentiviral suppression of p53. *Journal of biological chemistry* 2003;**278**:11731-11734.
38. Dannenberg J-H, van Rossum A, Schuijff L, te Riele H. Ablation of the retinoblastoma gene family deregulates G1 control causing immortalization and increased cell turnover under growth-restricting conditions. *Genes & development* 2000;**14**:3051-3064.
39. Sage J, Mulligan GJ, Attardi LD, Miller A, Chen S, Williams B, Theodorou E, Jacks T. Targeted disruption of the three Rb-related genes leads to loss of G1 control and immortalization. *Genes & development* 2000;**14**:3037-3050.
40. Sage J, Miller AL, Pérez-Mancera PA, Wysocki JM, Jacks T. Acute mutation of retinoblastoma gene function is sufficient for cell cycle re-entry. *Nature* 2003;**424**:223-228.
41. Pantoja C, Serrano M. Murine fibroblasts lacking p21 undergo senescence and are resistant to transformation by oncogenic Ras. *Oncogene* 1999;**18**.
42. Yao G. Modelling mammalian cellular quiescence. *Interface Focus* 2014;**4**:20130074.
43. Fausto N. Liver regeneration and repair: hepatocytes, progenitor cells, and stem cells. *Hepatology* 2004;**39**:1477-1487.
44. Fausto N. Liver regeneration. *J Hepatol* 2000;**32**:19-31.
45. Michalopoulos GK, DeFrances MC. Liver regeneration. *Science* 1997;**276**:60-66.
46. Bucher NL, Farmer SR. Liver regeneration following partial hepatectomy: genes and metabolism. Liver growth and repair: Springer, 1998:3-27.
47. Liu Y, Elf SE, Miyata Y, Sashida G, Liu Y, Huang G, Di Giandomenico S, Lee JM, Deblasio A, Menendez S. p53 regulates hematopoietic stem cell quiescence. *Cell stem cell* 2009;**4**:37-48.
48. Cheng T, Rodrigues N, Shen H, Yang Y-g, Dombkowski D, Sykes M, Scadden DT. Hematopoietic stem cell quiescence maintained by p21cip1/waf1. *Science* 2000;**287**:1804-1808.
49. Ladha MH, Lee KY, Upton TM, Reed MF, Ewen ME. Regulation of exit from quiescence by p27 and cyclin D1-CDK4. *Molecular and cellular biology* 1998;**18**:6605-6615.
50. Boonstra J. Progression through the G1-phase of the on-going cell cycle. *J Cell Biochem* 2003;**90**:244-252.
51. Pajalunga D, Mazzola A, Salzano AM, Biferi MG, De Luca G, Crescenzi M. Critical requirement for cell cycle inhibitors in sustaining nonproliferative states. *The Journal of cell biology* 2007;**176**:807-818.
52. Viatour P, Somervaille TC, Venkatasubrahmanyam S, Kogan S, McLaughlin

ME, Weissman IL, Butte AJ, Passegué E, Sage J. Hematopoietic stem cell quiescence is maintained by compound contributions of the retinoblastoma gene family. *Cell stem cell* 2008;**3**:416-428.
53. Hosoyama T, Nishijo K, Prajapati SI, Li G, Keller C. Rb1 gene inactivation expands satellite cell and postnatal myoblast pools. *Journal of Biological Chemistry* 2011;**286**:19556-19564.
54. Attwooll C, Denchi EL, Helin K. The E2F family: specific functions and overlapping interests. *The EMBO journal* 2004;**23**:4709-4716.
55. Vandel L, Nicolas E, Vaute O, Ferreira R, Ait-Si-Ali S, Trouche D. Transcriptional repression by the retinoblastoma protein through the recruitment of a histone methyltransferase. *Molecular and Cellular Biology* 2001;**21**:6484-6494.
56. Nielsen SJ, Schneider R, Bauer U-M, Bannister AJ, Morrison A, O'carroll D, Firestein R, Cleary M, Jenuwein T, Herrera RE. Rb targets histone H3 methylation and HP1 to promoters. *Nature* 2001;**412**:561.
57. Lavoie JN, L'Allemain G, Brunet A, Müller R, Pouysségur J. Cyclin D1 expression is regulated positively by the p42/p44MAPK and negatively by the p38/HOGMAPK pathway. *Journal of Biological Chemistry* 1996;**271**:20608-20616.
58. Cheng M, Sexl V, Sherr CJ, Roussel MF. Assembly of cyclin D-dependent kinase and titration of p27Kip1 regulated by mitogen-activated protein kinase kinase (MEK1). *Proceedings of the National Academy of Sciences* 1998;**95**:1091-1096.
59. Ikeda M-A, Jakoi L, Nevins JR. A unique role for the Rb protein in controlling E2F accumulation during cell growth and differentiation. *Proceedings of the National Academy of Sciences* 1996;**93**:3215-3220.
60. Shin EK, Shin A, Paulding C, Schaffhausen B, Yee AS. Multiple change in E2F function and regulation occur upon muscle differentiation. *Molecular and Cellular Biology* 1995;**15**:2252-2262.
61. Vairo G, Livingston DM, Ginsberg D. Functional interaction between E2F-4 and p130: evidence for distinct mechanisms underlying growth suppression by different retinoblastoma protein family members. *Genes & Development* 1995;**9**:869-881.
62. Campbell KS, Mullane KP, Aksoy IA, Stubdal H, Zalvide J, Pipas JM, Silver PA, Roberts TM, Schaffhausen BS, DeCaprio JA. DnaJ/hsp40 chaperone domain of SV40 large T antigen promotes efficient viral DNA replication. *Genes & development* 1997;**11**:1098-1110.
63. Stubdal H, Zalvide J, Campbell KS, Schweitzer C, Roberts TM, DeCaprio JA. Inactivation of pRB-related proteins p130 and p107 mediated by the J domain of simian virus 40 large T antigen. *Molecular and cellular biology* 1997;**17**:4979-4990.
64. DeCaprio JA, Ludlow JW, Figge J, Shew J-Y, Huang C-M, Lee W-H, Marsilio E, Paucha E, Livingston DM. SV40 large tumor antigen forms a specific complex with the product of the retinoblastoma susceptibility gene. *Cell* 1988;**54**:275-283.
65. Lilyestrom W, Klein MG, Zhang R, Joachimiak A, Chen XS. Crystal structure

of SV40 large T-antigen bound to p53: interplay between a viral oncoprotein and a cellular tumor suppressor. *Genes & development* 2006;**20**:2373-2382.
66. Pallas DC, Shahrik LK, Martin BL, Jaspers S, Miller TB, Brautigan DL, Roberts TM. Polyoma small and middle T antigens and SV40 small t antigen form stable complexes with protein phosphatase 2A. *Cell* 1990;**60**:167-176.
67. Pallas DC, Weller W, Jaspers S, Miller T, Lane W, Roberts T. The third subunit of protein phosphatase 2A (PP2A), a 55-kilodalton protein which is apparently substituted for by T antigens in complexes with the 36-and 63-kilodalton PP2A subunits, bears little resemblance to T antigens. *J Virol* 1992;**66**:886-893.
68. Comerford S, Schultz N, Hinnant E, Klapproth S, Hammer R. Comparative analysis of SV40 17kT and LT function in vivo demonstrates that LT's C-terminus re-programs hepatic gene expression and is necessary for tumorigenesis in the liver. *Oncogenesis* 2012;**1**:e28.
69. Ageberg M, Gullberg U, Lindmark A. The involvement of cellular proliferation status in the expression of the human proto-oncogene DEK. *Haematologica* 2006;**91**:268-269.
70. Lamplot JD, Liu B, Yin L, Zhang W, Wang Z, Luther G, Wagner E, Li R, Nan G, Shui W. Reversibly Immortalized Mouse Articular Chondrocytes Acquire Long-Term Proliferative Capability while Retaining Chondrogenic Phenotype. *Cell transplantation* 2014.
71. Richter C, Thieme S, Bandoła J, Laugsch M, Anastassiadis K, Brenner S. Generation of inducible immortalized dendritic cells with proper immune function in vitro and in vivo. *PloS one* 2013;**8**:e62621.
72. Bond GL, Hu W, Levine AJ. MDM2 is a central node in the p53 pathway: 12 years and counting. *Curr Cancer Drug Targets* 2005;**5**:3-8.
73. Linzer DI, Levine AJ. Characterization of a 54K dalton cellular SV40 tumor antigen present in SV40-transformed cells and uninfected embryonal carcinoma cells. *Cell* 1979;**17**:43-52.
74. Srinivasan A, McClellan AJ, Vartikar J, Marks I, Cantalupo P, Li Y, Whyte P, Rundell K, Brodsky JL, Pipas JM. The amino-terminal transforming region of simian virus 40 large T and small t antigens functions as a J domain. *Molecular and cellular biology* 1997;**17**:4761-4773.
75. Coutts AS, La Thangue NB. The p53 response: emerging levels of co-factor complexity. *Biochem Biophys Res Commun* 2005;**331**:778-785.
76. Brady CA, Jiang D, Mello SS, Johnson TM, Jarvis LA, Kozak MM, Broz DK, Basak S, Park EJ, McLaughlin ME. Distinct p53 transcriptional programs dictate acute DNA-damage responses and tumor suppression. *Cell* 2011;**145**:571-583.
77. Beckerman R, Prives C. Transcriptional regulation by p53. *Cold Spring Harb Perspect Biol* 2010;**2**:a000935.
78. Bargonetti J, Reynisdottir I, Friedman PN, Prives C. Site-specific binding of wild-type p53 to cellular DNA is inhibited by SV40 T antigen and mutant p53. *Genes & development* 1992;**6**:1886-1898.
79. Kimura G, Dulbecco R. Isolation and characterization of temperature-sensitive mutants of simian virus 40. *Virology* 1972;**49**:394-403.
80. Yamaguchi N, Kuchino T. Temperature-sensitive mutants of simian virus 40

selected by transforming ability. *J Virol* 1975;**15**:1297-1301.
81. Ray S, Anderson ME, Tegtmeyer P. Differential interaction of temperature-sensitive simian virus 40 T antigens with tumor suppressors pRb and p53. *J Virol* 1996;**70**:7224-7227.
82. Jat PS, Noble MD, Ataliotis P, Tanaka Y, Yannoutsos N, Larsen L, Kioussis D. Direct derivation of conditionally immortal cell lines from an H-2Kb-tsA58 transgenic mouse. *Proceedings of the National Academy of Sciences* 1991;**88**:5096-5100.
83. Yanai N, Suzuki M, Obinata M. Hepatocyte cell lines established from transgenic mice harboring temperature-sensitive simian virus 40 large T-antigen gene. *Exp Cell Res* 1991;**197**:50-56.
84. Mercola M, Ruiz-Lozano P, Schneider MD. Cardiac muscle regeneration: lessons from development. *Genes & development* 2011;**25**:299-309.
85. Soonpaa MH, Kim KK, Pajak L, Franklin M, Field LJ. Cardiomyocyte DNA synthesis and binucleation during murine development. *American Journal of Physiology-Heart and Circulatory Physiology* 1996;**271**:H2183-H2189.
86. Ikenishi A, Okayama H, Iwamoto N, Yoshitome S, Tane S, Nakamura K, Obayashi T, Hayashi T, Takeuchi T. Cell cycle regulation in mouse heart during embryonic and postnatal stages. *Development, growth & differentiation* 2012;**54**:731-738.
87. Bergmann O, Zdunek S, Felker A, Salehpour M, Alkass K, Bernard S, Sjostrom SL, Szewczykowska M, Jackowska T, Dos Remedios C. Dynamics of cell generation and turnover in the human heart. *Cell* 2015;**161**:1566-1575.
88. Chattergoon NN, Louey S, Stork P, Giraud GD, Thornburg KL. Unexpected maturation of PI3K and MAPK-ERK signaling in fetal ovine cardiomyocytes. *American Journal of Physiology-Heart and Circulatory Physiology* 2014;**307**:H1216-H1225.
89. Kajstura J, Zhang X, Reiss K, Szoke E, Li P, Lagrasta C, Cheng W, Darzynkiewicz Z, Olivetti G, Anversa P. Myocyte cellular hyperplasia and myocyte cellular hypertrophy contribute to chronic ventricular remodeling in coronary artery narrowing-induced cardiomyopathy in rats. *Circ Res* 1994;**74**:383-400.
90. Quaini F, Cigola E, Lagrasta C, Saccani G, Quaini E, Rossi C, Olivetti G, Anversa P. End-stage cardiac failure in humans is coupled with the induction of proliferating cell nuclear antigen and nuclear mitotic division in ventricular myocytes. *Circ Res* 1994;**75**:1050-1063.
91. Huang S, Zou X, Zhu JN, Fu YH, Lin QX, Liang YY, Deng CY, Kuang SJ, Zhang MZ, Liao YL. Attenuation of microRNA-16 derepresses the cyclins D1, D2 and E1 to provoke cardiomyocyte hypertrophy. *J Cell Mol Med* 2015;**19**:608-619.
92. Hinrichsen R, Hansen A, Haunsø S, Busk P. Phosphorylation of pRb by cyclin D kinase is necessary for development of cardiac hypertrophy. *Cell Prolif* 2008;**41**:813-829.
93. Busk PK, Bartkova J, Strøm CC, Wulf-Andersen L, Hinrichsen R, Christoffersen TE, Latella L, Bartek J, Haunsø S, Sheikh SP. Involvement of cyclin D activity in left ventricle hypertrophy in vivo and in vitro. *Cardiovasc*

Res 2002;**56**:64-75.
94. Tane S, Okayama H, Ikenishi A, Amemiya Y, Nakayama KI, Takeuchi T. Two inhibitory systems and CKIs regulate cell cycle exit of mammalian cardiomyocytes after birth. *Biochem Biophys Res Commun* 2015;**466**:147-154.
95. MacLellan W, Garcia A, Oh H, Frenkel P, Jordan M, Roos K, Schneider M. Overlapping roles of pocket proteins in the myocardium are unmasked by germ line deletion of p130 plus heart-specific deletion of Rb. *Molecular and Cellular Biology* 2005;**25**:2486-2497.
96. Flink IL, Oana S, Maitra N, Bahl JJ, Morkin E. Changes in E2F complexes containing retinoblastoma protein family members and increased cyclin-dependent kinase inhibitor activities during terminal differentiation of cardiomyocytes. *J Mol Cell Cardiol* 1998;**30**:563-578.
97. Sdek P, Zhao P, Wang Y, Huang C-j, Ko CY, Butler PC, Weiss JN, MacLellan WR. Rb and p130 control cell cycle gene silencing to maintain the postmitotic phenotype in cardiac myocytes. *The Journal of cell biology* 2011;**194**:407-423.
98. Tamamori-Adachi M, Goto I, Yamada K, Kitajima S. Differential regulation of cyclin D1 and D2 in protecting against cardiomyocyte proliferation. *Cell Cycle* 2008;**7**:3768-3774.
99. Sengupta A, Kalinichenko VV, Yutzey KE. FoxO1 and FoxM1 Transcription Factors Have Antagonistic Functions in Neonatal Cardiomyocyte Cell-Cycle Withdrawal and IGF1 Gene RegulationNovelty and Significance. *Circ Res* 2013;**112**:267-277.
100. Estrella NL, Clark AL, Desjardins CA, Nocco SE, Naya FJ. MEF2D deficiency in neonatal cardiomyocytes triggers cell cycle re-entry and programmed cell death in vitro. *Journal of Biological Chemistry* 2015;**290**:24367-24380.
101. Xiang F-l, Guo M, Yutzey KE. Overexpression of Tbx20 in adult cardiomyocytes promotes proliferation and improves cardiac function after myocardial infarction. *Circulation* 2016:CIRCULATIONAHA. 115.019357.
102. Mahmoud AI, Kocabas F, Muralidhar SA, Kimura W, Koura AS, Thet S, Porrello ER, Sadek HA. Meis1 regulates postnatal cardiomyocyte cell cycle arrest. *Nature* 2013;**497**:249-253.
103. Ebelt H, Hufnagel N, Neuhaus P, Neuhaus H, Gajawada P, Simm A, Müller-Werdan U, Werdan K, Braun T. Divergent Siblings. *Circ Res* 2005;**96**:509-517.
104. Dingar D, Konecny F, Zou J, Sun X, von Harsdorf R. Anti-apoptotic function of the E2F transcription factor 4 (E2F4)/p130, a member of retinoblastoma gene family in cardiac myocytes. *J Mol Cell Cardiol* 2012;**53**:820-828.
105. Dorr KM, Amin NM, Kuchenbrod LM, Labiner H, Charpentier MS, Pevny LH, Wessels A, Conlon FL. Casz1 is required for cardiomyocyte G1-to-S phase progression during mammalian cardiac development. *Development* 2015;**142**:2037-2047.
106. Rojas A, Kong SW, Agarwal P, Gilliss B, Pu WT, Black BL. GATA4 is a direct transcriptional activator of cyclin D2 and Cdk4 and is required for cardiomyocyte proliferation in anterior heart field-derived myocardium. *Molecular and cellular biology* 2008;**28**:5420-5431.
107. Bersell K, Arab S, Haring B, Kühn B. Neuregulin1/ErbB4 signaling induces cardiomyocyte proliferation and repair of heart injury. *Cell* 2009;**138**:257-270.

108. Novoyatleva T, Diehl F, van Amerongen MJ, Patra C, Ferrazzi F, Bellazzi R, Engel FB. TWEAK is a positive regulator of cardiomyocyte proliferation. *Cardiovasc Res* 2009;**85**:681-690.
109. Novoyatleva T, Sajjad A, Pogoryelov D, Patra C, Schermuly RT, Engel FB. FGF1-mediated cardiomyocyte cell cycle reentry depends on the interaction of FGFR-1 and Fn14. *The FASEB Journal* 2014;**28**:2492-2503.
110. Buikema JW, Mady AS, Mittal NV, Atmanli A, Caron L, Doevendans PA, Sluijter JP, Domian IJ. Wnt/β-catenin signaling directs the regional expansion of first and second heart field-derived ventricular cardiomyocytes. *Development* 2013;**140**:4165-4176.
111. Lin Z, Zhou P, von Gise A, Gu F, Ma Q, Chen J, Guo H, van Gorp PR, Wang D-Z, Pu WT. Pi3kcb Links Hippo-YAP and PI3K-AKT Signaling Pathways to Promote Cardiomyocyte Proliferation and SurvivalNovelty and Significance. *Circ Res* 2015;**116**:35-45.

Chapter 2

HP1α mediates defective heterochromatin repair and accelerates senescence in *Zmpste24*-deficient cells

Jia Liu[†], Xianhui Yin[†], Baohua Liu, Huiling Zheng, Guangqian Zhou, Liyun Gong, Meng Li, Xueqin Li, Youya Wang, Jingyi Hu, Vaidehi Krishnan, Zhongjun Zhou, and Zimei Wang

[†]Equal contribution

Adapted from: Cell Cycle. 2014; 13: 1237–1247.

Abstract

Heterochromatin protein 1 (HP1) interacts with various proteins, including lamins, to play versatile functions within nuclei, such as chromatin remodeling and DNA repair. Accumulation of prelamin A leads to misshapen nuclei, heterochromatin disorganization, genomic instability, and premature aging in *Zmpste24*-null mice. Here, we investigated the effects of prelamin A on HP1α homeostasis, subcellular distribution, phosphorylation, and their contribution to accelerated senescence in mouse embryonic fibroblasts (MEFs) derived from *Zmpste24*$^{-/-}$ mice. The results showed that the level of HP1α was significantly increased in *Zmpste24*$^{-/-}$ cells. Although prelamin A interacted with HP1α in a manner similar to lamin A, HP1α associated with the nuclease-resistant nuclear matrix fraction was remarkably increased in *Zmpste24*$^{-/-}$ MEFs compared with that in wild-type littermate controls. In wild-type cells, HP1α was phosphorylated at Thr50, and the phosphorylation was maximized around 30 min, gradually dispersed 2 h after DNA damage induced by camptothecin. However, the peak of HP1α phosphorylation was significantly compromised and appeared until 2 h, which is correlated with the delayed maximal formation of γ-H2AX foci in *Zmpste24*$^{-/-}$ MEFs. Furthermore, knocking down HP1α by siRNA alleviated the delayed DNA damage response and accelerated senescence in *Zmpste24*$^{-/-}$ MEFs, evidenced by the rescue of the delayed γ-H2AX foci formation, downregulation of p16, and reduction of senescence-associated β-galactosidase activity. Taken together, these findings establish a functional link between prelamin A, HP1α, chromatin remodeling, DNA repair, and early senescence in *Zmpste24*-deficient mice, suggesting a potential therapeutic strategy for laminopathy-based premature aging via the intervention of HP1α.

Introduction

Hutchinson–Gilford progeria syndrome (HGPS), an autosomal dominant human disorder with disastrous premature aging features, is predominantly caused by a de novo G608G point mutation in LMNA gene. LMNA gene encodes for A-type lamin proteins, which are components of the nuclear lamina, a scaffolding network lying beneath the inner nuclear membrane and further extending into the nucleoplasm. The G608G mutation activates a cryptic splice donor in exon 11 of LMNA gene, resulting in a 50-aa internal deletion (Δ50) in prelamin A that contains a proteolytic cleavage site required for lamin A maturation. The Δ50 prelamin A left behind is permanently modified by a farnesyl group, also called progerin.[1,2] A more severe progeria disorder, restrictive dermopathy (RD), has homozygous deficiency in *Zmpste24*, a zinc metalloproteinase responsible for the final cleavage step of prelamin A, resulting in a partially processed farnesyl full-length prelamin A instead of mature lamin A.[3] Recapitulating HGPS, *Zmpste24*-deficient mice exhibit severe growth retardation, hair loss, osteoporosis, dilated cardiomyopathy, muscular dystrophy, lipodystrophy, and their lifespan is shortened to 4–6 mo.[4] Thus one common characteristic of HGPS and RD is incomplete processing of prelamin A into mature lamin A. Lamin A as a type-V intermediate filament protein has head, tail, and connected rod domain structure and usually forms a head–tail dimer, which plays essential roles in nuclear membrane strength and shape, positioning of the nuclear pore complexes, lamina assembly, anchoring chromatin, and dynamic chromatin organization.[5] Progerin interferes with the integrity of the nuclear envelope, thus leading to misshapen nuclei with lobulation, thickening, and blebbing. Such irregular nuclei are also observed in cells derived from old healthy individuals.[6-8] Reducing farnesyl prelamin A accumulation on the nuclear lamina by farnesyltransferase inhibitor (FTI) or accelerating autophagic degradation of progerin through rapamycin ameliorates cellular senescence in HGPS cells and premature aging in *Zmpste24*-deficient mice.[9-13] Further studies revealed interphase aneuploidy chromatin, loss or aggregation of peripheral heterochromatin, abnormally clustered centromeres, and mislocalized telomeres in fibroblasts isolated from HGPS patients and *Zmpste24*-deficient mice.[14] These abnormalities in chromatin organization are related to epigenetic changes, including the trimethylation of histone H3 at Lys9 (H3K9me3) and Lys27 (H3K27me3), histone H4 at Lys20 (H4K20me3) and the acetylation of histone H4 at Lys16 (H4K16ac).[15,16] These histone modifications are key factors for heterochromatin organization or chromatin remodelling. Changes in H3K9me3 patterns have also been observed in fibroblasts isolated from another progeriod syndrome mandibuloacral dysplasia (MAD) and in cells derived from old healthy individuals.[7,17] These findings clearly demonstrate that prelamin A accumulation leads to abnormal organization and function of heterochromatin, which may contribute to the phenotypes in progeria.

Mammalian heterochromatin protein 1 (HP1), including HP1α, HP1β, and HP1γ, are non-histone chromatin-associated proteins, which bind to histone H3 that is tri-methylated at lysine 9 (H3K9me3) via their N-terminal chromo domain (CD) to control heterochromatin high-order organization.[18,19] HP1 requires dimerization via their C-terminal chromo shadow domain (CSD) and interacts with many nuclear proteins that possess a conserved PxVxL penta-peptide motif to trigger a variety of

functions, ranging from replication, transcription, chromatin organization, and nuclear architecture, to chromosomal maintenance.[20,21] Via the CD region, HP1 directly or indirectly associates with lamins, such as lamin B receptor (LBR), LAP2β and lamina-associated polypeptides (LAP2α).[22-24] It not only anchors the peripheral heterochromatin to the inner nuclear membrane, but also mediates nuclear envelope reassembly in a dynamic manner.[25]

Progeriod cells are characterized by accumulation of irreparable DNA damages and defective DNA repair.[26] Recently, heterochromatin-mediated DNA damage response (DDR) has been found important for genome integrity; the superstructure of heterochromatin impedes DNA repair as a barrier, and most of heterochromatin components, such as KRAB-associated protein 1 (KAP-1), HP1, play important roles in the heterochromatin DDR.[27-29] ATM phosphorylates KAP-1 at Ser824 (pS824-KAP-1), alters KAP-1 affinity for chromatin, and facilitates heterochromatin remodelling in DDR.[27,30] Recent findings also link HP1 proteins to the DNA damage response. All 3 HP1 isoforms are mobilized and recruited to various types of DNA damage sites.[31,32] In response to DNA damage, HP1β is rapidly mobilized by casein kinase 2 (CK2)-mediated phosphorylation of its CD region at Thr 51 (pT51-HP1β). The phosphorylation disrupts hydrogen bonds that fold the CD around H3K9me3, releasing HP1β from heterochromatin and possibly leading to heterochromatin relaxation.[29] Inhibition of CK2 or a constitutively Thr51 mutant HP1β diminishes γ-H2AX signals.[29] Moreover, KAP-1 directly binds to HP1α CSD region.[27] Cells lacking HP1 fail to form discreet pS824-KAP-1 foci after DNA damage.[33] Previously we have shown that KAP-1 phosphorylation is compromised and leads to delayed DNA damage-induced chromatin remodelling and accelerated senescence in *Zmpste24*-deficient mice.[34] However, it is still unclear whether the defective KAP-1 phosphorylation is the unique regulatory mechanism underlying the genomic instability and accelerated senescence in progeria mice. Therefore it would be interesting to explore the roles of HP1 in mechanisms linking abnormal lamin A, delayed chromatin remodelling, defective DNA repair, and premature aging. In this study, we investigated the effects of prelamin A accumulation on HP1 expression, subcellular distribution, phosphorylation, and their impacts on premature senescence. We found that the level of HP1α associated with the nuclear matrix was significantly increased in *Zmpste24*$^{-/-}$ cells. Upon DNA damage, HP1α phosphorylation was significantly compromised, leading to delayed formation of γ-H2AX foci in *Zmpste24*$^{-/-}$ MEFs. Knocking down HP1α alleviated the delayed DNA damage response and accelerated senescence in *Zmpste24*$^{-/-}$ MEFs. Our findings establish a functional link between prelamin A, HP1α, heterochromatin repair, and early senescence in *Zmpste24*-deficient mice and suggest a potential therapeutic strategy for laminopathy-based premature aging via the intervention of HP1α.

Materials and Methods

Cell culture and drug treatments

Zmpste24$^{-/-}$ mice were generated by Zhou *et al.* previously.[4] Genotyping of mice for the mutant *Zmpste24* allele was performed by PCR as described previously.[15] Mouse embryonic fibroblasts (MEFs) were obtained from 13.5-d *Zmpste24*$^{+/+}$ and *Zmpste24*$^{-/-}$

embryos. Littermate-matched *Zmpste24*$^{+/+}$ and *Zmpste24*$^{-/-}$ MEFs were cultured in complete Dulbecco modified Eagle medium (DMEM) (pH 7.4) supplemented with 10% fetal bovine serum. Early passage (passage 3) of *Zmpste24*$^{-/-}$ MEFs without showing senescence phenotypes were employed in all experiments.15 To induce DNA damage, MEFs were treated with either 4 μM Camptothecin (CPT, Sigma C9911) or DMSO for 1 h. Afterward, CPT was removed by washing 3 times with PBS and replacing with fresh medium.

Antibodies

Commercial available antibodies used in this experiments are as follow: lamin A/C (Santa Cruz Biotechnology, sc-20681, http://www.scbt.com/datasheet-20681-lamin-a-c-h-110-antibody.html), HP1α (Millipore, 05–689, http://www.millipore.com/catalogue/item/05-689; Abcam, ab77256, http://www.abcam.com/hp1-alpha-antibody-chip-grade-ab77256.html), HP1β (Abcam, ab10811, http://www.abcam.com/CBX1-HP1-beta-MAC353-antibody-ChIP-Grade-ab10811.html), HP1γ (Millipore, 05–690, http://www.millipore.com/catalogue/item/05-690), γ-H2AX (Upstate, 05–636, http://www.millipore.com/catalogue/item/05-636), H3K9me3 (Abcam, ab8898, http://www.abcam.com/histone-h3-tri-methyl-k9-antibody-chip-grade-ab8898.html), H3 (Abcam, ab1791, http://www.abcam.com/histone-h3-antibody-chip-grade-ab1791.html), HMGB1 (Cell Signaling, 3935, https://www.cellsignal.com/products/3935.html), P16 (Santa Cruz Biotechnology, sc-81156, http://www.scbt.com/datasheet-81156-p16-1e12e10-antibody.html), α-tubulin (Cell Signaling, 2144, http://www.cellsignal.com/products/2144.html), β-actin (cwbiotech, CW0096A, http://www.cwbiotech.com/en/scart/cproduct.aspx?id=4283). pT50-HP1α polyclonal antibody was made by Abmart (Shanghai, http://www.ab-mart.com/index.php) against the phospho-peptide, C-SEEHN(pT)WEPEK. It was diluted 1:300 for immunoblotting and 1:100 for immunofluorescence staining. Secondary antibodies used are as follows: Horseradish peroxidase (HRP) labeled Goat anti-rabbit (Pierce, 31460, http://www.pierce-antibodies.com/Goat-anti-Rabbit-IgG-H-L-Secondary-Antibody-Polyclonal-31460.html), HRP labeled Goat anti-Mouse IgG (Pierce, 32430 http://www.pierce-antibodies.com/Glutamic-Acid-Decarboxylase-65-antibody-Polyclonal-PA532430.html), HRP labeled Goat anti-Rat IgG (Pierce, 31470, http://www.pierce-antibodies.com/Goat-anti-Rat-IgG-H-L-Secondary-Antibody-Polyclonal-31470.html), HRP labeled Rabbit anti-Goat IgG (Pierce, 31402, http://www.pierce-antibodies.com/Rabbit-anti-Goat-IgG-H-L-Secondary-Antibody-Polyclonal-31402.html), Alexa Fluor 488 donkey anti-goat IgG (H+L) (Invitrogen, A11055s, http://www.lifetechnologies.com/order/catalog/product/A11055), Alexa Fluor 488 donkey anti-rat IgG (H+L) (Invitrogen, A21208, http://www.lifetechnologies.com/order/catalog/product/A21208), Alexa Fluor 488 donkey anti-mouse IgG (H+L) (Invitrogen, A21202, http://www.lifetechnologies.com/order/catalog/product/A21202), Alexa Fluor 555 donkey anti-mouse IgG (H+L) (Invitrogen, A31570, http://www.lifetechnologies.com/order/catalog/product/A31570), Alexa Fluor 594 goat anti-rabbit IgG (H+L) (Invitrogen, A11012,

http://www.lifetechnologies.com/order/catalog/product/A11012). All reagents were used at the dilutions recommended by the manufacturers or mentioned above.

Co-immunoprecipitation

Cell extracts were prepared in modified RIPA buffer (20 mM Tris, pH 7.5, 300 mM NaCl, 0.5% Nonidet P-40, 1% Triton X-100, 1 mM EGTA, 1 mM DTT). Protein A conjugated Sepharose beads (Roche 11719394001) were washed twice with ice-cold PBS and pelleted by centrifugation at 2000 × g for 1 min at 4 °C. Two micrograms of the antibody of interest and lysates from 1 × 107 MEFs were incubated for 2 h at 4 °C with rotation. The antibody conjugate was then incubated with 50 μL of the pre-washed Sepharose beads overnight at 4 °C with rotation. The excess unbound protein was removed by washing 3 times with 500 μL modified RIPA buffer; Sepharose beads were pelleted by centrifugation at 2000 × g for 2 min at 4 °C. Co-immunoprecipitated proteins were eluted off the Sepharose beads by adding 50 μL of 1 × loading buffer (1% SDS, 100 mM DTT, 50 mM Tris, pH 6.8) and boiling for 3 min. The elute was centrifuged at 2000 × g for 4 min, and the supernatant containing co-immunoprecipitated proteins was collected and analyzed by western blotting.

Western blotting

Whole-cell lysate was prepared by suspending the MEFs in 1 volume of suspension buffer (10 mM Tris-HCl, pH 7.5, 0.1 M NaCl, 1mM EDTA, 1 mM DTT, pH 8.0, protease inhibitors), followed by adding 1 volume of Laemmli buffer (0.1M Tris-HCl, pH 7.0, 4% SDS, 20% glycerol,1 mM DTT, protease inhibitors) and boiling for 5 min. Twenty micrograms of total proteins were electrophoresed through 10% SDS polyacrylamide gels and transferred to PVDF membrane (Millipore). The membrane was incubated with primary antibodies overnight at 4 °C, and then probed with appropriate secondary antibodies linked to HRP for 1 h at room temperature. Antibody binding was visualized by enhanced chemiluminiscence kit (Pierce 34095). Relative blot band intensity was measured by ImageJ and normalized to corresponding controls as indicated. For statistical analysis, at least 3 independent immunoblots were quantified and 2-tailed t test was used for P values.

Real-time PCR

Total RNA was extracted with the Trizol® reagent (Invitrogen, 15596-026) according to the manufacturer's protocol. RNA quantity was monitored by UV spectrophotometry and agarose gel electrophoresis. One microgram of total RNA was transcribed to cDNA using the iScript™ cDNA Synthesis Kit (Bio-rad, 70-8891). Quantitative RT-PCR (Q-PCR) was run on the 7500 Fast Real-Time PCR System (Applied Biosystems), with the use of the SsoFast™ EvaGreen Supermix kit (Bio-rad, 172-5200). Mouse HP1α and β-actin primers are as follows: HP1α (232 bp) forward, 5′-GAAAGAAGAC CAAGAGGACA G C-3′; reverse, 5′-TTGTTTCACC CTCCTTCATC T-3′. β-actin (517 bp) forward, 5′-ATATCGCTGC GCTGGTCGTC-3′; reverse, 5′-AGGATGGCGT GAGGGAGAGC-3′. All Q-PCR reactions were performed in triplicate in the final volume 10 μl for 40 cycles according to the following protocol: each cycle at 95 °C for the initial 30 s, then at 95 °C for 5 s, and

60 °C for 5 s. The obtained results were averaged, and gene expression levels were normalized to β-actin.

Subcellular fractionation

MEFs were suspended (4 × 107 cells/ml) in buffer A [10 mM HEPES (pH 7.9), 10 mM KCl, 1.5 mM MgCl2, 0.34 M sucrose, 10% glycerol, 1 mM DTT, complete protease inhibitors (Roche), and 1 mM PMSF (Sigma)]. After the addition of 0.1% Triton X-100, cells were incubated on ice for 5 min. Nuclei were obtained by centrifugation at 1300 × g for 4 min at 4 °C. The supernatant containing the cytosolic extract (S1) was collected by centrifugation at 20 000 × g for 15 min at 4 °C. Nuclei were then washed twice with ice-cold buffer A and lysed in buffer B (3 mM EDTA, 0.2 mM EGTA, 1 mM DTT, complete protease inhibitors [Roche], and 1 mM PMSF [Sigma]) for 5 min on ice. The pellet (P2) containing the chromatin and nuclear matrix protein was obtained by centrifugation at 1700 × g for 4 min at 4 °C. The supernatant consisting of nucleoplasmic protein (S2) was also collected. To obtain nuclear matrix-associated proteins, cell nuclei (P1) were resuspended in buffer A plus 1 mM CaCl2 and digested with 5 units of micrococcal nuclease (MNase, Sigma, N3755) at 37 °C for 5 min; the reaction was stopped by the addition of 1 mM EGTA. By low-speed centrifugation as described above, the pellet obtained after digestion consisted of the nuclease-resistant chromatin and nuclear matrix-associated proteins (P2'); the supernatant contained the nucleoplasmic and nuclease susceptible chromatin-associated proteins (S2'). The fractions were dissolved in 1× loading buffer (1% SDS, 100 mM DTT, 50 mM Tris, pH 6.8) and sonicated for 15 s. Equal amounts were resolved using SDS-PAGE, and the levels of protein were further detected by western blotting.

Immunofluorescence microscopy

MEFs were seeded in 8-chamber slides to 70% confluence, treated with CPT for 1 h and allowed to recover for indicated time. The slides were washed twice with PBS and fixed with 4% paraformaldehyde in PBS for 10 min at 4 °C, followed by 10 min permeation with 0.2% Triton X-100/PBS. The slides were blocked in 1% BSA/PBS with 5% normal serum overnight at 4 °C, and then incubated with primary antibody diluted in 1% BSA/PBS overnight at 4 °C in a humid box. After washing 3 times with PBS, the slides were incubated with FITC- or TRITC-coupled secondary antibodies diluted in 1% BSA/PBS for 40 min at R.T. and then washed 3 times with 1%Tween20/PBS to remove unbound antibodies. The slides were mounted with ProLong Gold antifade reagent with DAPI (Invitrogen, P36935), sealed with nail polish, and analyzed by Olympus Fluoview FV1000 immunofluorescence microscopy. Photos were processed with Photoshop CS®. Focus counting was performed by 100 cells randomly chosen for each experiment. Two-tailed Student t test was used for P values where applied.

RNA interference

HP1α sense and antisense RNA are 5′-GGAUACAGUC UGAGAGUUAT T-3′ and 5′-UAACUCUCAG ACUGUAUCCT T-3′ respectively. Transfection was performed in triplicate in 6-well plates with lipofectamine RNAiMAX Reagent (Invitrogen, 13778-

100) according to the manufacturer's instructions. Forty-eight hours post-transfection, the cells were treated with 4 μM CPT for 1 h, and harvested at indicated times for western blotting and immunofluorescence microscopy analysis as described above.

Senescence-associated β-gal assay

Senescence-associated β-Galactosidase activity was accessed with cellular senescence assay kit (Mirus, MiR2600). Briefly, cells were seeded in 6-well plates, fixed at room temperature for 5 min with 2 mL of 1× fixing solution, washed twice with 1× PBS, and stained with 2 mL of freshly prepared 1× β-Galactosidase detection solution at 37 °C for 16 h in dark room. The cells were washed twice with 1× PBS, overlaid with 70% glycerol/PBS, and photographed. Blue-stained MEFs were counted in more than 200 randomly chosen cells. Two-tailed t test was applied for P values.

Results

The level of HP1α is increased in *Zmpste24*$^{-/-}$ MEFs

HP1 proteins serve as linkers, connecting peripheral heterochromatin to inner nuclear membranes.[24,25] To investigate whether HP1s are involved in defective DNA repair and premature aging, we first examined levels of HP1 isoforms and H3K9me3 by western blotting in *Zmpste24*$^{-/-}$ MEFs and wild-type littermate controls. To eliminate epigenetic alterations induced by cellular senescence, early-passage *Zmpste24*$^{-/-}$ MEFs (passage 3), which have similar proliferative potential as wild-type littermate controls (data not shown and ref. 15), were used throughout this study. Compared with wild-type littermate controls, a more than 40% increase in HP1α level was observed in *Zmpste24*$^{-/-}$ MEFs, whereas HP1β and HP1γ were much less affected (Fig. 1A and B). Consistent with our previous report,35 the level of H3K9me3, a HP1-binding heterochromatin marker, was significantly elevated, whereas levels of H3K9me1 and H3K9me2 were hardly affected (Fig. S1 A and B). To evaluate whether the elevated HP1α protein is attributable to the transcriptional regulation of HP1α by prelamin A, the mRNA level of HP1α was examined by real-time reverse-transcription PCR. As shown, the level of HP1α mRNA was not affected in *Zmpste24*$^{-/-}$ MEFs (Fig. 1C), indicating that prelamin A modulates HP1α in a post-translational manner. Collectively, these data suggest that the presence of prelamin A stabilizes HP1α protein in *Zmpste24*$^{-/-}$ MEFs.

HP1α interacts with prelamin A in *Zmpste24*$^{-/-}$ MEFs

Given that lamin A and prelamin A bind to HP1α and LAP2α in HEK293 cells,36 we reasoned that prelamin A might increase the binding capacity to HP1α, thus stabilizing it. To this end, co-immunoprecipitation (Co-IP) was performed in identical early passage of *Zmpste24*$^{-/-}$ MEFs and wild-type littermate controls to investigate the interaction of endogenous prelamin A and HP1. Since lamin-containing nuclear matrix (NM) is insoluble in RIPA buffer containing 150 mM NaCl, and raising the salt concentration to 500 mM completely abolishes the interaction between A-type lamins and HP1, RIPA buffer containing 350 mM NaCl was used for the Co-IP. As shown in Figure 2A, HP1α, HP1β, and HP1γ were detected in the anti-lamin A/C immunoprecipitates by western blotting. However, the pull-down levels are

comparable between *Zmpste24*$^{-/-}$ MEFs and wild-type littermate controls, suggesting that prelamin A might bind to HP1 isoforms in a similar capacity as lamin A. Reciprocally, endogenous lamin A/prelamin A was detected in the anti-HP1α immunoprecipitates. Interestingly, the anti-HP1α immunoprecipitates also pull down lamin C (Fig. 2B), which is encoded by an alternate splicing variant of LMNA gene and shares the N-terminal 566 aa with lamin A,37 suggesting that HP1 interacts with lamin A/prelamin A through domains beyond C-terminal lamin A-specific region. Nonetheless, these data have roled out the possibility that prelamin A directly regulates HP1 protein stability.

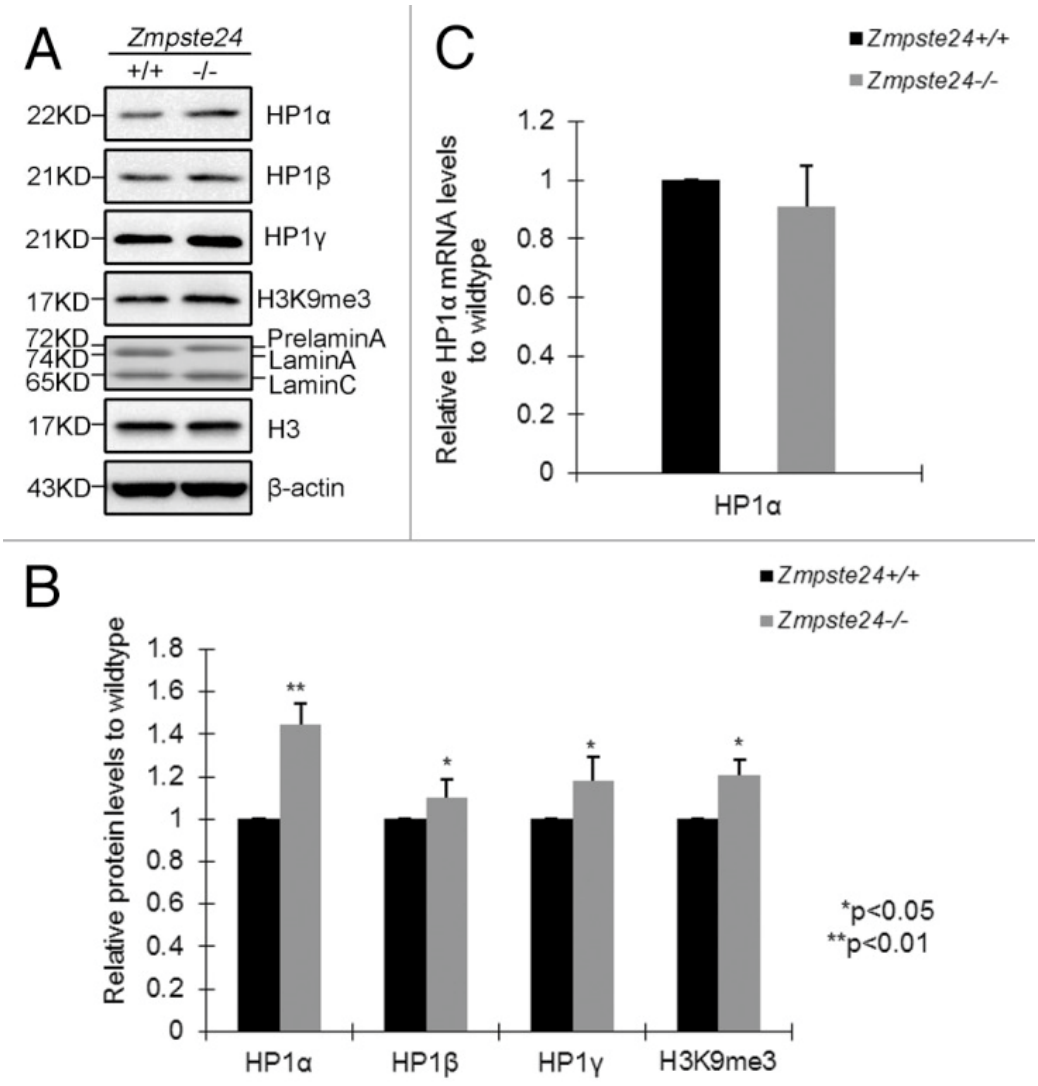

Figure 1. Increased level of HP1α in *Zmpste24*$^{-/-}$ MEFs. (A) Representative immunoblots showing protein levels of HP1α, HP1β, HP1γ, H3K9me3 in *Zmpste24*$^{-/-}$ MEFs and wild-type littermate controls at passage 3. (B) Relative levels of HP1α, HP1β, HP1γ, H3K9me3 in *Zmpste24*$^{-/-}$ MEFs comparing with wild-type littermate controls. Data (mean ± s.e.m.) represent 3 independently derived lines of MEFs in separate experiments. *$P < 0.05$, **$P < 0.01$, 2-tailed Student t test. (C) Real-time RT-PCR analysis of HP1α mRNA expression in *Zmpste24*$^{-/-}$ MEFs and wild-type littermate controls. HP1α mRNA abundance was calculated by $2^{-\Delta\Delta Ct}$ normalized to β-actin. Data represent 3 independently derived lines of MEFs in separate experiments.

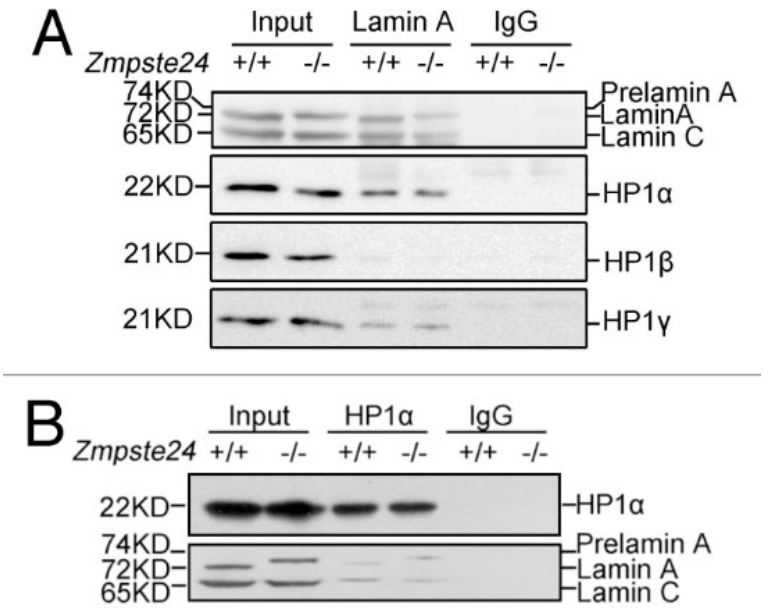

Figure 2. HP1 interacts with endogenous prelamin A in a similar manner as lamin A. (A) Immunoblots showing endogenous HP1α, HP1β, HP1γ in the anti-lamin A/C immunoprecipitates from *Zmpste24*$^{-/-}$ MEFs and wild-type littermate controls. Data represent 1 of 3 independent experiments. (B) Immunoblots showing endogenous lamin A/prelamin A/lamin C in the anti-HP1α immunoprecipitates in *Zmpste24*$^{-/-}$ MEFs and wild-type littermate controls. Data represent 1 of 3 independent experiments.

HP1α is mainly distributed in nuclease-resistant nuclear matrix and fraction in *Zmpste24*$^{-/-}$ MEFs

Accumulation of prelamin A jeopardizes the nuclear lamina and matrix structure, resulting in disturbed heterochromatin organization.[14,15,38] Although prelamin A has similar binding capacity to HP1 as lamin A, it may jeopardize the overall nuclear matrix structure and consequently mis-localize HP1 proteins and, thus, modulate their stability. Therefore, we further investigate whether HP1α is mislocalized in the nuclear matrix fraction of *Zmpste24*$^{-/-}$ MEFs. A well-established subcellular fractionation strategy was applied to separate cell extracts into fractions including cytoplasm (S1), nucleoplasm (S2), chromatin and nuclear matrix (P2), nucleoplasm and nuclease susceptible chromatin (S2'), and micrococcal nuclease (MNase)-resistant nuclear matrix (P2').[16] α-tubulin, β-actin, high-mobility group protein B1 (HMGB1), lamin A/C served as controls for the cytoplasmic, nucleoplasmic, euchromatin-bound, and nuclear matrix fractions, respectively. As expected, in wild-type MEFs, α-tubulin was detected only in cytoplasm fraction, whereas β-actin was present in all cytoplasmic and nuclear fractions (Fig. 3A). For nuclear proteins, lamin A/C was resistant to MNase digestion and remained exclusively in nuclear matrix fraction (P2'). In contrast, the euchromatin-bound protein HMGB1 was absent from the nuclear matrix fraction (P2') and was completely released into nucleoplasmic fraction (S2') after MNase treatment. Although sensitive to MNase, after digestion, HP1 and H3K9me3 were still partially retained in the nuclear matrix fraction (P2') (Fig. 3A). Similarly, HP1 distribution was examined in *Zmpste24*$^{-/-}$ cells; as shown in Figure 3B, the level of HP1α protein retained in the nuclear matrix fraction (P2') of *Zmpste24*$^{-/-}$ MEFs was much higher than that of wild-type controls. Concomitantly, the level of HP1α

released into the nucleoplasm and suspensible chromatin fraction (S2') was much lower in progeriod cells than that in wild-type cells. Likewise, H3K9me3 distribution was shown in a similar manner as HP1α (Fig. 3B). Notably, subcellular distributions of HP1β and HP1γ were not much affected in *Zmpste24*$^{-/-}$ MEFs. Altogether, these findings suggest that the increased HP1α in progeriod cells is mainly distributed in prelamin A-enriched nuclear matrix fraction (P2'), which might mislead the heterochromatin to the dis-organized nuclear matrix, thus disturbing the formation and function of heterochromatin.

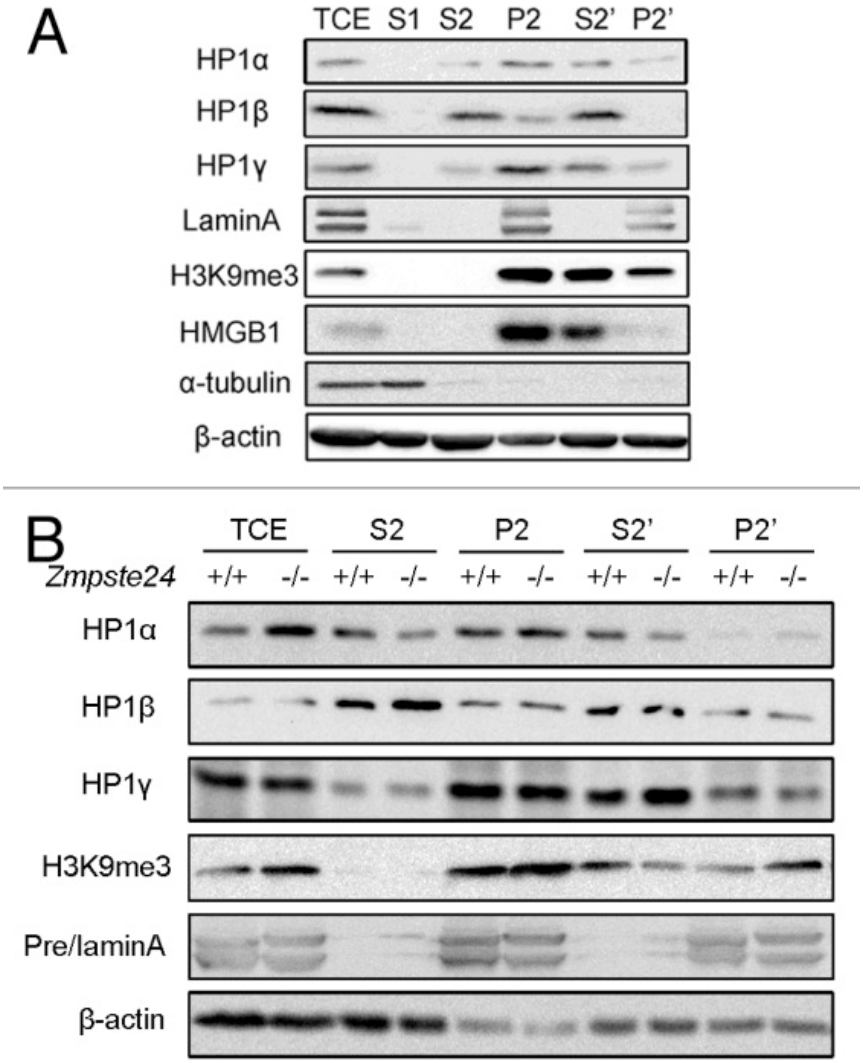

Figure 3. Increased HP1α was mainly localized in nuclease-resistant chromatin and nuclear matrix fraction in *Zmpste24*$^{-/-}$ MEFs. (**A**) Subcellular fractions of MEFs: S1 (cytoplasmic), S2 (nucleoplasmic), P2 (chromatin + nuclear matrix), S2' (nucleoplasmic + nuclease susceptible chromatin), P2' (nuclear matrix + nuclease resistant chromatin), and TCE (total cell extraction) as described in the "Materials and Methods". Representative immunoblots showing the subcellular distribution of HP1α, HP1β, HP1γ, HMGB1 (euchromatin marker), H3K9me3 (heterochromatin marker), and LaminA/C (nuclear matrix marker). (**B**) Immunoblots showing increased levels of HP1α in nuclease-resistant chromatin and nuclear matrix fraction, whereas no significant changes of HP1β and HP1γ in various nuclear fractions. Data represent 1 of 3 independently derived lines of MEFs in separate experiments.

HP1α phosphorylation is compromised following DNA damage in *Zmpste24*$^{-/-}$ MEFs

In addition to heterochromatin mis-organization, sustained DNA damage checkpoint response is another hallmark of progeriod cells, which is a driving factor of cellular senescence.[26] We and others recently found that the irreparable DNA damages accumulated in *Zmpste24*-dificient mice are indeed associated with heterochromatin, indicating a defective heterochromatin repair.[34,35] Recent reports showed that HP1 is mobilized via phosphorylation, which alters heterochromatin organization, and then is recruited to DNA damage sites.[29,32] Therefore we asked whether HP1α phosphorylation is affected in progeriod cells. It has been reported that residues Thr 51 in human HP1β and Thr50 in HP1α are both crucial in regulating the binding of HP1 to H3K9me3 and the remodeling of heterochromatin in response DNA damage.[29] Given the high similarity of chromodomain regions surrounding Thr 51 in HP1β and Thr50 in HP1α in both humans and mice (Fig. S2A), a polyclonal antibody that recognizes mouse HP1α phosphorylated at residue Thr50 (pT50-HP1α) was raised as described in "Materials and Methods". The specificity of the anti-pT50-HP1α antibody was tested by SAP (shrimp alkaline phosphatase) treatment (Fig. S2B). By western blotting, pT50-HP1α dynamics were examined in *Zmpste24*$^{-/-}$ MEFs with Camptothecin (CPT) treatment, a radiomimetic reagent, which induces DSBs into progeriod cells as described before.[39] γ-H2AX was examined as a sensitive marker for the presence of DSBs. CPT treatment induced rapid increase of γ-H2AX level in both *Zmpste24*$^{-/-}$ MEFs and wild-type controls (Fig. 4A). Thereafter, the level of γ-H2AX decreased at 4 h and returned to almost background level at 8 h in wild-type controls, but it remained significantly higher in *Zmpste24*$^{-/-}$ MEFs at 4 and 8 h (Fig. 4A). Although total level of HP1α did not show obvious changes within 8 h, CPT treatment induced a dynamic change of pT50-HP1α in wild-type MEFs, which peaked at 30 min and gradually decreased thereafter (Fig. 4A and B). However, the level of pT50-HP1α was significantly reduced and the kinetics delayed in *Zmpste24*$^{-/-}$ MEFs, whereby it maximized around 2–4 h after CPT treatment (Fig. 4A and B). Of note, the delayed pT50-HP1α kinetics in *Zmpste24*$^{-/-}$ MEFs is consistent with the delayed γ-H2AX level upon CPT treatment. To confirm the delayed pT50-HP1α kinetics after DNA damage in progeriod cells, we further employed immunofluorescence confocal microscopy. Within 30 min post-CPT treatment, pT50-HP1α and γH2AX foci were stochastically distributed throughout the nucleus in both *Zmpste24*$^{-/-}$ and wild-type control cells, and most of them co-localized with each other (Fig. 4C). The number of pT50-HP1α foci maximized around 30 min after DNA damage in wild-type cells; however, this was significantly delayed, until 2 h, in progeriod cells (Fig. 4D). Collectively, these findings confirm defective DNA repair evidenced by defective H2AX phosphorylation in progeriod cells and further imply that delayed pT50-HP1α might lead to defective mobilization of HP1α and cause delayed chromatin remodeling and, therefore, delayed recruitment of DNA damage response factors.

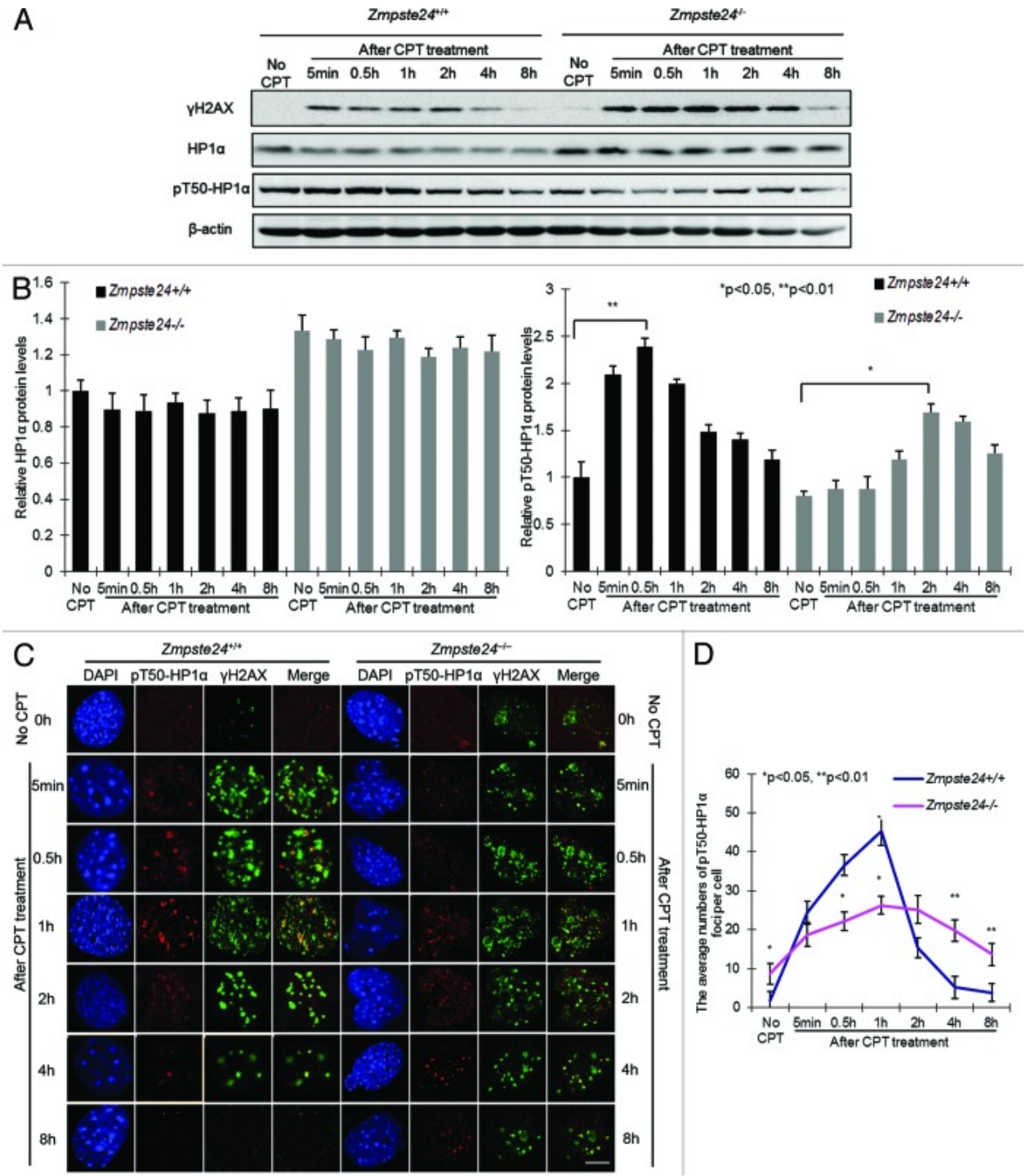

Figure 4. DNA damage-induced pT50-HP1α phosphorylation is compromised in *Zmpste24*$^{-/-}$ MEFs. (**A**) Representative immunoblots showing levels of γH2AX, HP1α and pT50-HP1α at indicated time points in *Zmpste24*$^{-/-}$ MEFs and wild-type littermate controls treated with 4 μM camptothecin (CPT). (**B**) Relative levels of HP1α and pT50-HP1α after CPT treatment in *Zmpste24*$^{-/-}$ MEFs and wild-type littermate controls. Data represent 3 independently derived lines of MEFs in separate experiments. (**C**) Representative photos of immunofluorescence confocal microscopy showing pT50-HP1α and γH2AX foci after CPT treatment at indicated time points. Scale bar, 5 μm. (**D**) The number of pT50-HP1α foci per cell after CPT treatment in *Zmpste24*$^{-/-}$ MEFs and wild-type controls. At least 100 cells were counted. Data represent mean ± s.e.m., $*P < 0.05$, $**P < 0.01$, 2-tailed Student *t* test.

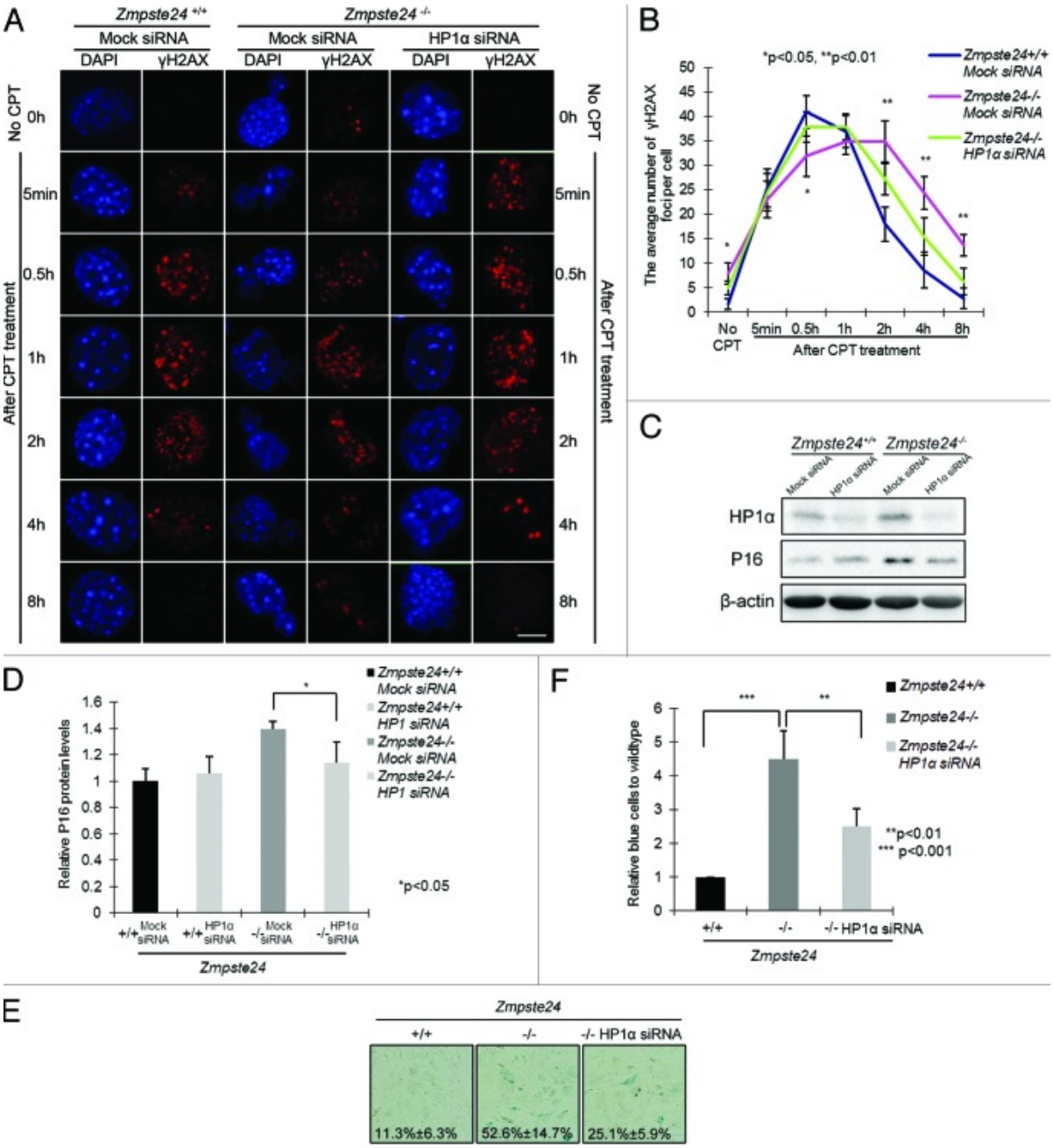

Figure 5. Knocking down HP1α promotes DNA damage response and attenuates cellular senescence in *Zmpste24*$^{-/-}$ MEFs. (**A**) Representative photos showing γH2AX foci at indicated time points in *Zmpste24*$^{-/-}$ MEFs and wild-type littermate controls treated with HP1α siRNA or mock siRNA. Scale bar, 5 μm. (**B**) The number of γH2AX foci per cell at indicated time points in *Zmpste24*$^{-/-}$ MEFs treated with HP1α siRNA. At least 100 cells were counted. Data represent mean ± s.e.m., **P* < 0.05, ***P* < 0.01, 2-tailed Student *t* test. (**C**) Representative immunoblots showing levels of HP1α and P16 in *Zmpste24*$^{-/-}$ MEFs and wild-type littermate controls treated with HP1α siRNA or mock siRNA. (**D**) Quantification of P16 level in (**C**). Data represent mean ± s.e.m., n = 3, **P* < 0.05, 2-tailed Student *t* test. (**E**) Representative photos of SA-β-gal activity showing the blue-stained senescent cells in *Zmpste24*$^{-/-}$ MEFs and wild-type littermate controls at passage 5. (**F**) Quantification of (**E**) showing the percentage of senescent cells. Data represent mean ± s.e.m., n = 3, ** *P* < 0.01, ****P* < 0.001, 2-tailed Student *t* test.

HP1α knockdown attenuates defective DNA damage response and cellular senescence

DNA breaks in heterochromatin can be abrogated by knocking down HP1 or other heterochromatin components.[28] To gain further insight into whether increased HP1α is the critical link between prelamin A and delayed DNA damage response and accelerated aging phenotypes in *Zmpste24*$^{-/-}$ MEFs, we explored if endogenous HP1α knockdown might alleviate the delayed DNA damage response and early onset of cellular senescence in *Zmpste24*$^{-/-}$ MEFs. In cells treated with short interfering RNAs (siRNAs) specifically targeting HP1α, although level of β-actin was quite stable for as long as 48 h, diminished HP1α expression was confirmed (Fig. S3). We next evaluated the effects of HP1α knockdown on γ-H2AX foci after CPT treatment. As shown in Figure 5A and B, a large number of γ-H2AX foci still persisted at 8 h in *Zmpste24*$^{-/-}$ MEFs, and this was significantly reduced in HP1α siRNA-treated *Zmpste24*$^{-/-}$ MEFs. Additionally, HP1α knockdown considerably reduced the expression of cellular senescence marker p16 expression (Fig. 5C and D). When cells were monitored for senescence-associated β-galactosidase (SA-β-gal) activity, the number of positively blue-stained cells dropped from more than 50% in scramble-treated to less than 25% in HP1α siRNA-treated *Zmpste24*$^{-/-}$ MEFs (Fig. 5E and F). Collectively, HP1α knockdown rescues defective DNA repair and attenuates the accelerated cellular senescence in *Zmpste24*$^{-/-}$ MEFs.

Discussion

In this report, we have shown that nuclear matrix-associated HP1α level was remarkably elevated in *Zmpste24*$^{-/-}$ MEFs. Upon DNA damage, a significantly compromised HP1α phosphorylation on Thr50 was observed in *Zmpste24*$^{-/-}$ MEFs, which correlates with the delayed γ-H2AX foci formation. Knocking down HP1α improved γ-H2AX foci formation and rescued cellular senescence in *Zmpste24*$^{-/-}$ MEFs. Our data suggest a critical role of HP1α in prelamin A-regulated genomic instability and premature aging.

Heterochromatin perturbation and epigenetic mis-regulation are hallmarks of progeria.[6,15,17] However, how various components functionally affect heterochromatin dynamics in the presence of prelamin A or progerin remains largely unknown. Here we found that prelamin A accumulation resulted in an increase of HP1α protein level, while the mRNA was hardly affected, suggesting a potential role for prelamin A in stabilizing HP1α protein. It has been shown that lamin A and prelamin A binds to HP1α in vitro, and farnesylated prelamin A showed reduced binding capacity to HP1α compared with the non-farnesylated form and wild-type lamin A.[36] However, a comparable binding affinity of HP1α to prelaminA and lamin A was found in our study, although prelamin A is farnesylated in *Zmpste24*$^{-/-}$ MEFs. One possible interpretation of this seeming discordance is that ectopic farnesylated prelamin A might be functionally different from the endogenous one caused by *Zmpste24* deficiency. Consistent with this notion is the finding that different strategies in generating unfarnesylatable progerin may result in opposite phenotypes in knock-in mouse models.[40-42] It has also been widely accepted that there is reduced of heterochromatin in HGPS cells, supported by decreased H3K9me3, H3K27me3, and

HP1α.[15] However, we have previously shown that prelamin A might elicit functional difference with progerin in addition to the structural differences, *i.e.*, loss of 50 amino acids, which may cause loss of function of lamin A.[35] Interestingly, several reports found that lamin A regulates HP1 stability through inhibition of specific ubiquitin ligase activities, and loss of lamin A accelerates HP1α degradation in $Lmna^{-/-}$ MEFs.[43,44] In this regard, the seemingly contradictory observation might be explained by the structural and functional difference between prelamin A in *Zmpste24*-null cells and progerin in human HGPS cells. The level of HP1α in the presence of progerin could be attributable to a combined gain of function of the partially processed C tail, which elevates the HP1α level, and loss of function of lamin A, which is due to 50-aa-truncation and accelerates the degradation of HP1α. Nevertheless, the lack of difference between prelamin A and lamin A in their binding capacity to HP1α suggests that it is unlikely that prelamin A regulates HP1α stability in a similar manner as it does on Suv39h1. On the other front, HP1, H3K9me3, and its principal methyltransferase Suv39h1 are all enriched in the pericentric heterochromatin region, and it is considered that N-terminal upstream of Suv39h1 CD region possess interaction site with HP1 CSD region, recruiting HP1α to bind H3K9me3 within its CD region.[45] Consistent with our previous report, we observed a remarkably increased level of H3K9me3 in *Zmpste24*-null cells and a significant increase of association of HP1α with the nuclear matrix fraction, wherein H3K9me3 is highly enriched. Therefore, it is also plausible to speculate that prelamin A might interfere with the correct positioning and stability of HP1α/Suv39h1/H3K9me3 heterochromatic complex, thus impairing the localization of pericentric heterochromatin domains at the nuclear periphery and finally resulting in disorganization of heterochromatin.

Although initial studies revealed that HP1 plays a key role in heterochromatin formation and gene silencing, recent studies have highlighted the importance of HP1-mediated chromatin remodeling and DNA damage response. In this study, we found that the level of pT50-HP1α, which co-localizes with γ-H2AX, is compromised in $Zmpste24^{-/-}$ MEFs after DNA damage, suggesting defective mobilization of HP1α and, thereafter, compromised chromatin remodeling. Another heterochromatin protein KAP-1, which promotes heterochromatic DSB repair by ATM-mediated phosphorylation and therefore facilitates the release of KAP-1 and CHD3 from heterochromatin and global chromatin relaxation, directly binds to HP1α CSD.[27,28] We have previously shown that pS824-KAP-1 level is significantly reduced, preventing the release of CHD3 from heterochromatin and global chromatin relaxation in $Zmpste24^{-/-}$ MEFs.[34] We therefore speculate that nuclear matrix fraction enrichment of HP1α in $Zmpste24^{-/-}$ MEFs might be also involved in the retention of KAP-1 on heterochromatin. Notably, the decreased level of pS824-KAP-1 in our previous study is not totally in accordance with the dynamic changes of chromatin relaxation in $Zmpste24^{-/-}$ MEFs. Although the level of pS824-KAP-1 was decreased, it peaked 30 min after DNA damage, which is similar to wild-type cells. Interestingly, although delayed, the chromatin still underwent global relaxation at 2 h and, concomitantly, the recruitment of 53BP1 after irradiation in $Zmpste24^{-/-}$ MEFs, indicating a backup mechanism regulating the late-stage global chromatin relaxation. In this study, we found that the peak level of pT50-HP1α was postponed to 2 h, which correlates well with the delayed relaxation of chromatin in progeriod cells after DNA damage,

implicating that pT50-HP1α could be the backup mechanism mediating chromatin remodeling in progeroid cells.

The rescue of cellular senescence by HP1α knockdown suggests potential links between chromatin remodeling, DNA repair, and premature aging. Interestingly, a recent report by Lattanzi and colleagues showed de-condensation of heterochromatin and enhanced DNA repair efficacy in centenarian fibroblasts and in normal cells treated with rapamycin, highlighting the pivotal roles of chromatin remodeling and DNA repair in aging/longevity.[46] Rapamycin targets mTOR pathways, inhibits DNA damage response (or pseudo-DNA damage response), and therefore slows down cellular senescence.[47-49] In this scenario, it would be interesting to examine whether rapamycin could rescue the defective chromatin remodeling and defective DNA repair in *Zmpste24*-null cells in future study. Nevertheless, our data shed new light into molecular basis of HP1α in heterochromatin mis-organization, delayed DNA damage response, and early senescence in *Zmpste24*-deficient progeria mouse model, providing an additional intervention target for progeria and normal aging.

Acknowledgments

We thank Drs Ashok R Venkitaraman and Venkat Pisupati (Hutchison/MRC Research Centre, Cambridge Univerisity) for providing pT51-HP1β polyclonal antibody. This study was supported by grants from the National Natural Science Foundation of China (NSFC 81070270) and Science and Technology Bureau of Shenzhen City Grants (JC201005280552A). The funders had no role in study design, data collection and analysis, decision to publish, or preparation of the manuscript.

Disclosure of Potential Conflicts of Interest

No potential conflicts of interest were disclosed.

References

1. Eriksson M, Brown WT, Gordon LB, Glynn MW, Singer J, Scott L, Erdos MR, Robbins CM, Moses TY, Berglund P, *et al*. Recurrent de novo point mutations in lamin A cause Hutchinson–Gilford progeria syndrome. Nature. 2003;423:293–8. doi: 10.1038/nature01629.
2. De Sandre-Giovannoli A, Bernard R, Cau P, Navarro C, Amiel J, Boccaccio I, Lyonnet S, Stewart CL, Munnich A, Le Merrer M, *et al*. Lamin a truncation in Hutchinson–Gilford progeria. Science. 2003;300:2055. doi: 10.1126/science.1084125.
3. Navarro CL, De Sandre-Giovannoli A, Bernard R, Boccaccio I, Boyer A, Geneviève D, Hadj-Rabia S, Gaudy-Marqueste C, Smitt HS, Vabres P, *et al*. Lamin A and ZMPSTE24 (FACE-1) defects cause nuclear disorganization and identify restrictive dermopathy as a lethal neonatal laminopathy. Hum Mol Genet. 2004;13:2493–503. doi: 10.1093/hmg/ddh265.
4. Pendás AM, Zhou Z, Cadiñanos J, Freije JM, Wang J, Hultenby K, Astudillo A, Wernerson A, Rodríguez F, Tryggvason K, *et al*. Defective prelamin A processing and muscular and adipocyte alterations in Zmpste24 metalloproteinase-deficient mice. Nat Genet. 2002;31:94–9.
5. Goldman RD, Gruenbaum Y, Moir RD, Shumaker DK, Spann TP. Nuclear lamins: building blocks of nuclear architecture. Genes Dev. 2002;16:533–47. doi: 10.1101/gad.960502.
6. Goldman RD, Shumaker DK, Erdos MR, Eriksson M, Goldman AE, Gordon LB, Gruenbaum Y, Khuon S, Mendez M, Varga R, *et al*. Accumulation of mutant lamin A causes progressive changes in nuclear architecture in Hutchinson–Gilford progeria syndrome. Proc Natl Acad Sci U S A. 2004;101:8963–8. doi: 10.1073/pnas.0402943101.
7. Scaffidi P, Misteli T. Lamin A-dependent nuclear defects in human aging. Science. 2006;312:1059–63. doi: 10.1126/science.1127168.
8. Cao K, Blair CD, Faddah DA, Kieckhaefer JE, Olive M, Erdos MR, Nabel EG, Collins FS. Progerin and telomere dysfunction collaborate to trigger cellular senescence in normal human fibroblasts. J Clin Invest. 2011;121:2833–44. doi: 10.1172/JCI43578.
9. Capell BC, Erdos MR, Madigan JP, Fiordalisi JJ, Varga R, Conneely KN, Gordon LB, Der CJ, Cox AD, Collins FS. Inhibiting farnesylation of progerin prevents the characteristic nuclear blebbing of Hutchinson–Gilford progeria syndrome. Proc Natl Acad Sci U S A. 2005;102:12879–84. doi: 10.1073/pnas.0506001102.
10. Fong LG, Frost D, Meta M, Qiao X, Yang SH, Coffinier C, Young SG. A protein farnesyltransferase inhibitor ameliorates disease in a mouse model of progeria. Science. 2006;311:1621–3. doi: 10.1126/science.1124875.
11. Cao K, Graziotto JJ, Blair CD, Mazzulli JR, Erdos MR, Krainc D, Collins FS. Rapamycin reverses cellular phenotypes and enhances mutant protein clearance in Hutchinson–Gilford progeria syndrome cells. Sci Transl Med. 2011;3:89ra58. doi: 10.1126/scitranslmed.3002346.
12. Blagosklonny MV. Progeria, rapamycin and normal aging: recent breakthrough. Aging (Albany NY) 2011;3:685–91.

13. Cenni V, Capanni C, Columbaro M, Ortolani M, D'Apice MR, Novelli G, Fini M, Marmiroli S, Scarano E, Maraldi NM, *et al*. Autophagic degradation of farnesylated prelamin A as a therapeutic approach to lamin-linked progeria. Eur J Histochem. 2011;55:e36. doi: 10.4081/ejh.2011.e36.
14. Taimen P, Pfleghaar K, Shimi T, Möller D, Ben-Harush K, Erdos MR, Adam SA, Herrmann H, Medalia O, Collins FS, *et al*. A progeria mutation reveals functions for lamin A in nuclear assembly, architecture, and chromosome organization. Proc Natl Acad Sci U S A. 2009;106:20788–93. doi: 10.1073/pnas.0911895106.
15. Shumaker DK, Dechat T, Kohlmaier A, Adam SA, Bozovsky MR, Erdos MR, Eriksson M, Goldman AE, Khuon S, Collins FS, *et al*. Mutant nuclear lamin A leads to progressive alterations of epigenetic control in premature aging. Proc Natl Acad Sci U S A. 2006;103:8703–8. doi: 10.1073/pnas.0602569103.
16. Krishnan V, Chow MZ, Wang Z, Zhang L, Liu B, Liu X, Zhou Z. Histone H4 lysine 16 hypoacetylation is associated with defective DNA repair and premature senescence in Zmpste24-deficient mice. Proc Natl Acad Sci U S A. 2011;108:12325–30. doi: 10.1073/pnas.1102789108.
17. Filesi I, Gullotta F, Lattanzi G, D'Apice MR, Capanni C, Nardone AM, Columbaro M, Scarano G, Mattioli E, Sabatelli P, *et al*. Alterations of nuclear envelope and chromatin organization in mandibuloacral dysplasia, a rare form of laminopathy. Physiol Genomics. 2005;23:150–8. doi: 10.1152/physiolgenomics.00060.2005.
18. Bannister AJ, Zegerman P, Partridge JF, Miska EA, Thomas JO, Allshire RC, Kouzarides T. Selective recognition of methylated lysine 9 on histone H3 by the HP1 chromo domain. Nature. 2001;410:120–4. doi: 10.1038/35065138.
19. Lachner M, O'Carroll D, Rea S, Mechtler K, Jenuwein T. Methylation of histone H3 lysine 9 creates a binding site for HP1 proteins. Nature. 2001;410:116–20. doi: 10.1038/35065132.
20. Brasher SV, Smith BO, Fogh RH, Nietlispach D, Thiru A, Nielsen PR, Broadhurst RW, Ball LJ, Murzina NV, Laue ED. The structure of mouse HP1 suggests a unique mode of single peptide recognition by the shadow chromo domain dimer. EMBO J. 2000;19:1587–97.
21. Thiru A, Nietlispach D, Mott HR, Okuwaki M, Lyon D, Nielsen PR, Hirshberg M, Verreault A, Murzina NV, Laue ED. Structural basis of HP1/PXVXL motif peptide interactions and HP1 localisation to heterochromatin. EMBO J. 2004;23:489–99. doi: 10.1038/sj.emboj.7600088.
22. Duband-Goulet I, Courvalin JC. Inner nuclear membrane protein LBR preferentially interacts with DNA secondary structures and nucleosomal linker. Biochemistry. 2000;39:6483–8. doi: 10.1021/bi992908b.
23. Ye Q, Callebaut I, Pezhman A, Courvalin JC, Worman HJ. Domain-specific interactions of human HP1-type chromodomain proteins and inner nuclear membrane protein LBR. J Biol Chem. 1997;272:14983–9. doi: 10.1074/jbc.272.23.14983.
24. Ye Q, Worman HJ. Interaction between an integral protein of the nuclear envelope inner membrane and human chromodomain proteins homologous to Drosophila HP1. J Biol Chem. 1996;271:14653–6. doi: 10.1074/jbc.271.25.14653.

25. Kourmouli N, Theodoropoulos PA, Dialynas G, Bakou A, Politou AS, Cowell IG, Singh PB, Georgatos SD. Dynamic associations of heterochromatin protein 1 with the nuclear envelope. EMBO J. 2000;19:6558–68. doi: 10.1093/emboj/19.23.6558.
26. Liu B, Wang J, Chan KM, Tjia WM, Deng W, Guan X, Huang JD, Li KM, Chau PY, Chen DJ, *et al*. Genomic instability in laminopathy-based premature aging. Nat Med. 2005;11:780–5. doi: 10.1038/nm1266.
27. Ziv Y, Bielopolski D, Galanty Y, Lukas C, Taya Y, Schultz DC, Lukas J, Bekker-Jensen S, Bartek J, Shiloh Y. Chromatin relaxation in response to DNA double-strand breaks is modulated by a novel ATM- and KAP-1 dependent pathway. Nat Cell Biol. 2006;8:870–6. doi: 10.1038/ncb1446.
28. Goodarzi AA, Noon AT, Deckbar D, Ziv Y, Shiloh Y, Löbrich M, Jeggo PA. ATM signaling facilitates repair of DNA double-strand breaks associated with heterochromatin. Mol Cell. 2008;31:167–77. doi: 10.1016/j.molcel.2008.05.017.
29. Ayoub N, Jeyasekharan AD, Bernal JA, Venkitaraman AR. HP1-beta mobilization promotes chromatin changes that initiate the DNA damage response. Nature. 2008;453:682–6. doi: 10.1038/nature06875.
30. Goodarzi AA, Noon AT, Jeggo PA. The impact of heterochromatin on DSB repair. Biochem Soc Trans. 2009;37:569–76. doi: 10.1042/BST0370569.
31. Luijsterburg MS, Dinant C, Lans H, Stap J, Wiernasz E, Lagerwerf S, Warmerdam DO, Lindh M, Brink MC, Dobrucki JW, *et al*. Heterochromatin protein 1 is recruited to various types of DNA damage. J Cell Biol. 2009;185:577–86. doi: 10.1083/jcb.200810035.
32. Ayoub N, Jeyasekharan AD, Venkitaraman AR. Mobilization and recruitment of HP1: a bimodal response to DNA breakage. Cell Cycle. 2009;8:2945–50. doi: 10.4161/cc.8.18.9486.
33. White D, Rafalska-Metcalf IU, Ivanov AV, Corsinotti A, Peng H, Lee SC, Trono D, Janicki SM, Rauscher FJ., 3rd The ATM substrate KAP1 controls DNA repair in heterochromatin: regulation by HP1 proteins and serine 473/824 phosphorylation. Mol Cancer Res. 2012;10:401–14. doi: 10.1158/1541-7786.MCR-11-0134.
34. Liu B, Wang Z, Ghosh S, Zhou Z. Defective ATM-Kap-1-mediated chromatin remodeling impairs DNA repair and accelerates senescence in progeria mouse model. Aging Cell. 2013;12:316–8. doi: 10.1111/acel.12035.
35. Liu B, Wang Z, Zhang L, Ghosh S, Zheng H, Zhou Z. Depleting the methyltransferase Suv39h1 improves DNA repair and extends lifespan in a progeria mouse model. Nat Commun. 2013;4:1868. doi: 10.1038/ncomms2885.
36. Lattanzi G, Columbaro M, Mattioli E, Cenni V, Camozzi D, Wehnert M, Santi S, Riccio M, Del Coco R, Maraldi NM, *et al*. Pre-Lamin A processing is linked to heterochromatin organization. J Cell Biochem. 2007;102:1149–59. doi: 10.1002/jcb.21467.
37. Stuurman N, Heins S, Aebi U. Nuclear lamins: their structure, assembly, and interactions. J Struct Biol. 1998;122:42–66. doi: 10.1006/jsbi.1998.3987.
38. Maraldi NM, Lattanzi G, Capanni C, Columbaro M, Merlini L, Mattioli E, Sabatelli P, Squarzoni S, Manzoli FA. Nuclear envelope proteins and chromatin arrangement: a pathogenic mechanism for laminopathies. Eur J Histochem. 2006;50:1–8.

39. Liu Y, Wang Y, Rusinol AE, Sinensky MS, Liu J, Shell SM, Zou Y. Involvement of xeroderma pigmentosum group A (XPA) in progeria arising from defective maturation of prelamin A. FASEB J. 2008;22:603–11. doi: 10.1096/fj.07-8598com.
40. Yang SH, Andres DA, Spielmann HP, Young SG, Fong LG. Progerin elicits disease phenotypes of progeria in mice whether or not it is farnesylated. J Clin Invest. 2008;118:3291–300. doi: 10.1172/JCI35876.
41. Davies BS, Barnes RH, 2nd, Tu Y, Ren S, Andres DA, Spielmann HP, Lammerding J, Wang Y, Young SG, Fong LG. An accumulation of non-farnesylated prelamin A causes cardiomyopathy but not progeria. Hum Mol Genet. 2010;19:2682–94. doi: 10.1093/hmg/ddq158.
42. Yang SH, Chang SY, Ren S, Wang Y, Andres DA, Spielmann HP, Fong LG, Young SG. Absence of progeria-like disease phenotypes in knock-in mice expressing a non-farnesylated version of progerin. Hum Mol Genet. 2011;20:436–44. doi: 10.1093/hmg/ddq490.
43. Chaturvedi P, Parnaik VK. Lamin A rod domain mutants target heterochromatin protein 1α and β for proteasomal degradation by activation of F-box protein, FBXW10. PLoS One. 2010;5:e10620. doi: 10.1371/journal.pone.0010620.
44. Chaturvedi P, Khanna R, Parnaik VK. Ubiquitin ligase RNF123 mediates degradation of heterochromatin protein 1α and β in lamin A/C knock-down cells. PLoS One. 2012;7:e47558. doi: 10.1371/journal.pone.0047558.
45. Yamamoto K, Sonoda M. Self-interaction of heterochromatin protein 1 is required for direct binding to histone methyltransferase, SUV39H1. Biochem Biophys Res Commun. 2003;301:287–92. doi: 10.1016/S0006-291X(02)03021-8.
46. Lattanzi G, Ortolani M, Columbaro M, Prencipe S, Mattioli E, Lanzarini C, Maraldi NM, Cenni V, Garagnani P, Salvioli S, *et al*. Lamins are rapamycin targets that impact human longevity: a study in centenarians. J Cell Sci. 2014;127:147–57. doi: 10.1242/jcs.133983.
47. Pospelova TV, Demidenko ZN, Bukreeva EI, Pospelov VA, Gudkov AV, Blagosklonny MV. Pseudo-DNA damage response in senescent cells. Cell Cycle. 2009;8:4112–8. doi: 10.4161/cc.8.24.10215.
48. Demidenko ZN, Zubova SG, Bukreeva EI, Pospelov VA, Pospelova TV, Blagosklonny MV. Rapamycin decelerates cellular senescence. Cell Cycle. 2009;8:1888–95. doi: 10.4161/cc.8.12.8606.
49. Leontieva OV, Lenzo F, Demidenko ZN, Blagosklonny MV. Hyper-mitogenic drive coexists with mitotic incompetence in senescent cells. Cell Cycle. 2012;11:4642–9. doi: 10.4161/cc.22937.

Supporting information

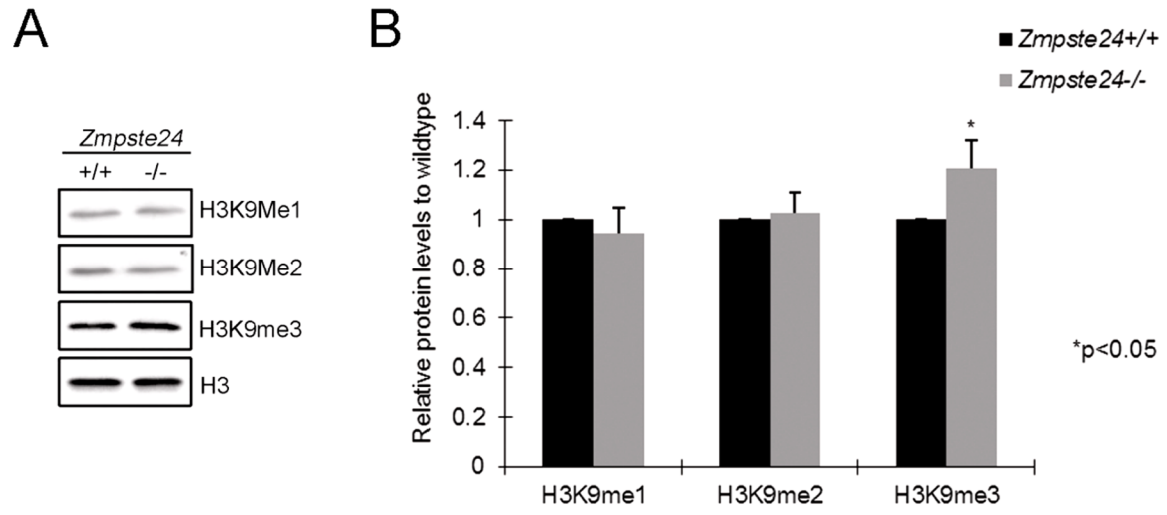

Figure S1. Histone H3K9 methylation profile in *Zmpste24*$^{-/-}$ MEFs. (A) Representative immunoblots showing H3K9me1, H3K9me2 and H3K9me3 levels in *Zmpste24*$^{-/-}$ MEFs and wild-type littermate controls at early passage 3. Histone H3 is internal control. (B) Relative levels of H3K9 methylation in *Zmpste24*$^{-/-}$ MEFs normalized to H3. Data, mean ± s.e.m., represent three independently derived lines of MEFs in separate experiments. **P*<0.05, ***P*<0.01, two tailed student's *t* test.

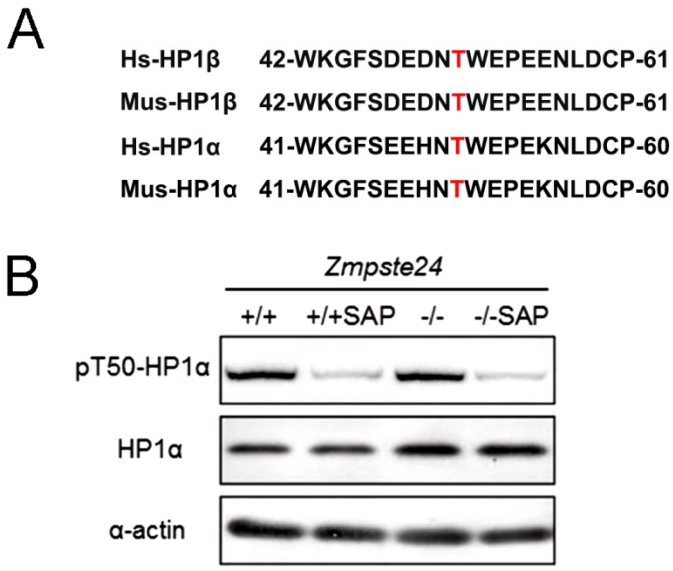

Figure S2. Amino acid sequence surrounding H3K9me3 binding site of HP1α and anti HP1αT50P antibody specificity. (A) Sequence alignment of conserved residues surrounding Thr51 of HP1β and Thr50 of HP1α in human and mouse. (B) Representative immunoblots showing levels of pT50-HP1α and HP1α in *Zmpste24*$^{-/-}$ MEFs and wild-type controls treated with Shrimp Alkaline Phosphatase (SAP).

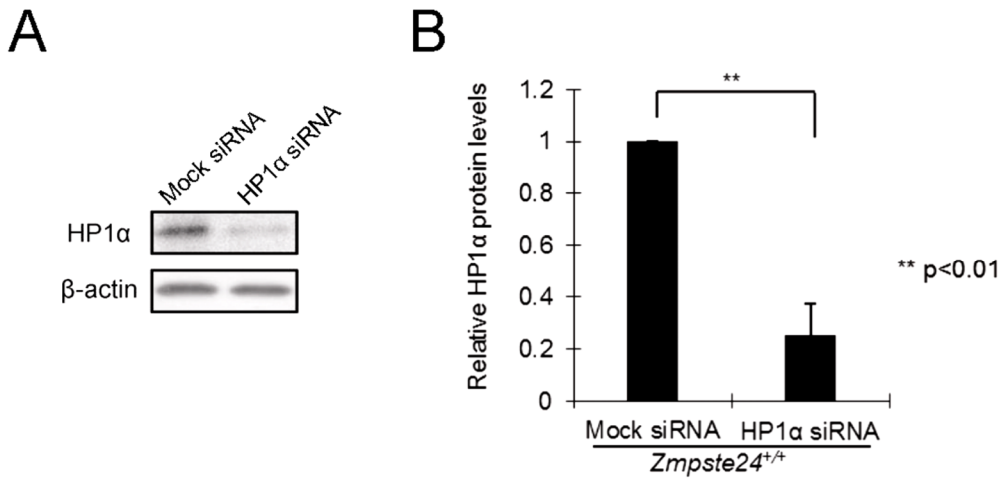

Figure S3. Knocking down HP1α in wild-type control MEFs. (A) Representative immunoblot showing HP1α protein level in cells treated with HP1α siRNA. (B) Quantification of A. Data, mean ± s.e.m. represent three independently derived lines of MEFs in separate experiments. **P*<0.05, ***P*<0.01, two tailed student's *t* test.

Chapter 3

Development of a Lentivirus Vector-based Assay for Non-destructive Monitoring of Cell Fusion Activity

Zeinab Neshati, Jia Liu, Guangqian Zhou, Martin J. Schalij, Antoine A. F. de Vries

Adapted from: PLoS One. 2014;9:e102433.

Abstract

Cell-to-cell fusion can be quantified by endowing acceptor and donor cells with latent reporter genes/proteins and activators of these genes/proteins, respectively. One way to accomplish this goal is by using a bipartite lentivirus vector (LV)-based cell fusion assay system in which the cellular fusion partners are transduced with a flippase-activatable *Photinus pyralis luciferase* (*PpLuc*) expression unit (acceptor cells) or with a ecombinant gene encoding $FLPe^{NLS+}$, a nuclear-targeted and molecularly evolved version of lippase (donor cells). Fusion of both cell populations will lead to the FLPe-dependent generation of a functional *PpLuc* gene. PpLuc activity is typically measured in cell lysates, precluding consecutive analysis of one cell culture. Therefore, in this study the PpLuc-coding sequence was replaced by that of *Gaussia princeps* luciferase (GpLuc), a secretory protein allowing repeated analysis of the same cell culture. In myotubes the spread of $FLPe^{NLS+}$ may be limited due to its nuclear localization signal (NLS) causing low signal outputs. To test this hypothesis, myoblasts were transduced with LVs encoding either $FLPe^{NLS+}$ or an NLS-less version of FLPe ($FLPe^{NLS-}$) and subsequently co-cultured in different ratios with myoblasts containing the FLPe-activatable *GpLuc* expression cassette. At different times after induction of cell-to-cell fusion the GpLuc activity in the culture medium was determined. $FLPe^{NLS+}$ and $FLPe^{NLS-}$ both activated the latent *GpLuc* gene but when the percentage of *FLPe*-expressing myoblasts was limiting, $FLPe^{NLS+}$ generally yielded slightly higher signals than $FLPe^{NLS-}$ while at low acceptor-to-donor cell ratios $FLPe^{NLS-}$ was usually superior. The ability of $FLPe^{NLS+}$ to spread through myofibers and to induce reporter gene expression is thus not limited by its NLS. However, at high FLPe concentrations the presence of the NLS negatively affected reporter gene expression. In summary, a rapid and simple chemiluminescence assay for quantifying cell-to-cell fusion progression based on GpLuc has been developed.

Introduction

During cell-to-cell fusion, plasma membranes of individual cells merge to form a multinucleated structure called a syncytium. Plasma membrane fusion is a crucial event during, for example, fertilization, syncytiotrophoblast production, skeletal muscle formation, bone remodeling, eye lens development and certain forms of tissue repair [1]. In general, cell fusion is a tightly regulated and highly selective process involving specific cell types. Inappropriate cell fusion has been implicated in tumor development and progression [2]. Cell fusion can be easily observed using microscopic techniques and in many studies the extent of cell fusion is expressed as fusion index, which either stands for the percentage of cells with two or more nuclei or the percentage of nuclei present in syncytia [3]. However, without continuous monitoring, it is impossible to decide by microscopy alone whether multinucleation is caused by cell fusion or the result of karyokinesis without cytokinesis. In addition, cells growing on top of each other can be mistaken for syncytia. Furthermore, as fusion index determinations are generally carried out manually, they are laborious, error-prone and often inaccurate. This has led to the development of methods for quantifying cell fusion independent of microscopic inspection. Nearly all these methods are based on systems of two components that interact to create a novel detectable signal only after cell fusion [3]. Mohler and Blau, for example, developed a quantitative cell fusion assay based on functional complementation between two biologically inactive β-galactosidase deletion mutants [4].

Another possibility to produce fusion-dependent signals is by applying site-specific recombination systems such as Cre-loxP and FLP-FRT. In these systems, a latent reporter gene is activated by the action of the site-specific DNA recombinase Cre from bacteriophage P1 or flippase/FLP from *Saccharomyces cerevisiae*, which catalyze the excision and inversion of DNA flanked by 34-base pair (bp) recognition sequences (loxP for Cre and FRT for FLP) in a direct or inverted repeat configuration, respectively [5,6]. Gonçalves *et al.* previously developed a bipartite lentivirus vector (LV)-based cell fusion assay system in which the cellular fusion partners are endowed with a FLP-activatable *Photinus pyralis luciferase* (*PpLuc*) expression unit/‘‘gene switch’’ (acceptor cells) or with a recombinant gene encoding a molecularly evolved version of FLP (FLPe) with a nuclear localization signal (NLS) derived from the simian virus 40 large T antigen (donor cells) [7]. Fusion between acceptor and donor cells led to the FLPe-dependent generation of a functional episomal *PpLuc* expression module. This cell fusion monitoring system was successfully used to study the role of the p38 MAPK signaling pathway in myoblast fusion/myotube formation. However, since PpLuc is a cytoplasmic protein and its substrate D-luciferin is poorly membrane-permeable, this assay requires lysis of the cells prior to luminometry and does not allow repeated analysis of the same cell culture. This prompted us to develop a nondestructive method to quantify cell fusion using the bipartite LV-based cell fusion assay system described by Gonc¸alves and colleagues as starting point.

The key difference between the new and ‘‘old’’ version of the LV-based cell fusion assay system is the replacement of the *PpLuc* open reading frame (ORF) in the ‘‘original’’ gene switch construct by the humanized coding sequence of *Gaussia princeps* luciferase (GpLuc), which is a secretory protein converting the substrate

coelenterazine into coelenteramide plus light. GpLuc also displays a much higher specific luciferase activity than PpLuc and is exceptionally resistant to exposure to heat and strongly acidic and basic conditions [8]. In addition, we hypothesized that in myotubes the spread of nuclear-targeted FLPe ($FLPe^{NLS+}$) beyond the direct surroundings of donor nuclei may be limited due to the presence of the NLS. This would result in the activation of only a fraction of the reporter genes especially in hybrid myotubes containing a relatively low percentage of *FLPe* gene-positive donor nuclei compared to GpLuc-encoding acceptor nuclei. To test this hypothesis, we generated an LV encoding an NLS-less version of FLPe ($FLPe^{NLS-}$) and compared, in myogenic fusion assays, its ability to activate latent *GpLuc* genes with that of $FLPe^{NLS+}$.

Materials and Methods

Plasmids

DNA constructions were carried out with enzymes from Fermentas (Fisher Scientific, Landsmeer, the Netherlands) or from New England Biolabs (Bioké, Leiden, the Netherlands) by using established procedures [9] or following the instructions provided with specific reagents.

To generate a bicistronic self-inactivating (SIN) human immunodeficiency virus type 1 (HIV1) vector shuttle plasmid coding for Streptomyces alboniger puromycin N-acetyl transferase (PurR) and FLPeNLS-, pLV.FLPe.PurR ([7]; GenBank accession number: GU253314; hereinafter referred to as pLV.hCMV-IE.$FLPe^{NLS+}$.IRES.PurR.hHBVPRE; Fig. 1A) was digested with BshT1 and Eco81I and the 9.6-kb DNA fragment containing the vector backbone was purified from agarose gel. The hybridization product of oligodeoxyribonucleotides 5' CCGGTACCATGAGTCAATTTGATATATTATGTAAAAC-ACCACC 3' and 5' TTAGGTGGTGTTTTACATAATATATCAAATTGACTCATGGTA 3' (both from Eurofins MWG Operon, Ebersberg, Germany) was combined with the 9.6-kb BshT16Eco81I fragment of pLV.hCMV-IE.$FLPe^{NLS+}$.IRES.PurR.hHBVPRE by ligation with bacteriophage T4 DNA ligase producing pLV.hCMV IE.$FLPe^{NLS-}$.IRES.PurR.hHBVPRE (Fig. 1B).

To generate a SIN-LV shuttle plasmid carrying a silent *GpLuc* gene that can be activated by FLP, cloning vector pR6K.MCS was digested with XmaJI and NotI, the 2.2-kb DNA fragment containing the vector backbone was purified from agarose gel and combined with the 0.6-kb GpLuc-encoding XmaJI×NotI fragment of phGluc.dBamHI yielding construct pR6K.GpLuc. The cloning vector pR6K.MCS was derived from construct pA1.GFP.A2 ([10]; GenBank accession number: GQ380658) by combining its 2.0-kb SalI×Aflll fragment with the 0.3-kb SalI×Aflll fragment of pMOLUC ([11]; Addgene, Cambridge, MA; plasmid number: 12514). Plasmid phGluc.dBamHI was made from the mammalian expression vector phGluc ([12]; Addgene; plasmid number: 22522) by self-ligation of its 2.9-kb BamHI fragment. The GpLuc ORF was excised from pR6K.GpLuc by digestion with XmaJI and MluI and combined with the 7.2-kb BcuI×MluI fragment of pLV.GS.DsRed.dKpnI to generate pLV.GS.GpLuc.v1 (Fig. 1D). The LV shuttle plasmid pLV.GS.DsRed.dKpnI was derived from pLV.pA+.GS.DsRed ([7]; GenBank accession number: GU253312) by

self-ligation of its 7.9-kb KpnI fragment. The SIN-LV shuttle plasmid pLV.GS.GpLuc.v6 is a derivative of construct pLV.pA+.GS.Luc ([7], hereinafter referred to as pLV.GS.PpLuc), in which the sequences interspersed between the rabbit *β-hemoglobin* gene polyadenylation signal (rHBB pA) and the mouse *metallothionein 1* gene (mMT1) pA (*i.e.* the *PpLuc* ORF and an FRT sequence) are replaced by a synthetic DNA fragment comprising the *GpLuc* ORF and an FRT sequence.

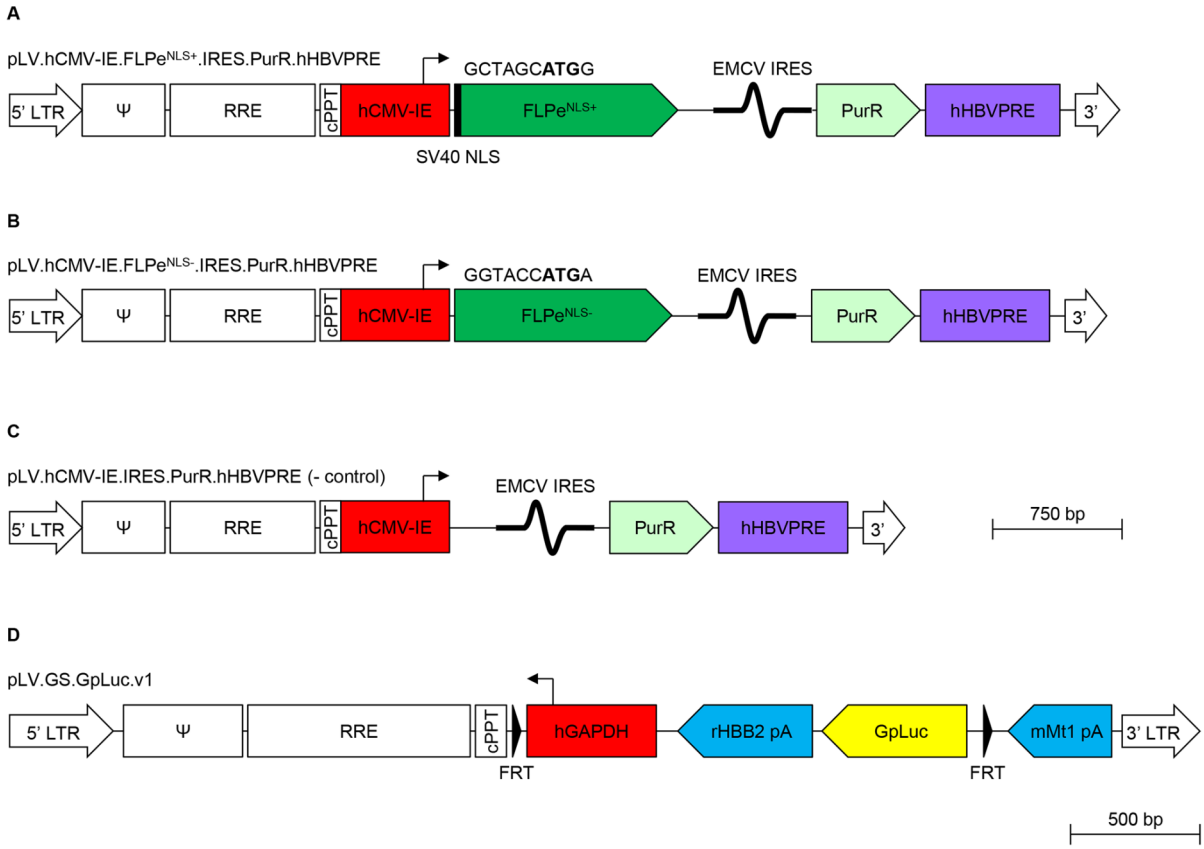

Figure 1. Structure of the LV DNA in the LV shuttle plasmids. (A): pLV.hCMV-IE.FLPe^{NLS+}. IRES.PurR. hHBVPRE (B): pLV.hCMVIE. FLPe^{NLS-}.IRES.PurR.hHBVPRE (C): pLV.hCMV-IE.IRES.PurR.hHBVPRE and (D): pLV.GS.GpLuc.v1. The start codons of the FLPe^{NLS+} and FLPe^{NLS-} ORFs are shown in boldface. 5' LTR, chimeric 5' long terminal repeat containing the Rous sarcoma virus U3 region and the HIV1 R and U5 regions; Ψ, HIV1 packaging signal; RRE, HIV1 Rev-responsive element; cPPT, HIV1 central polypurine tract and termination site; hCMV-IE, human cytomegalovirus *immediate early* gene promoter; FLPe^{NLS+}, molecularly evolved flippase with simian virus 40 (SV40) nuclear localization signal (NLS; black bar); FLPe^{NLS-}, molecularly evolved flippase without NLS; EMCV IRES, encephalomyocarditis virus internal ribosomal entry site; PurR; *Streptomyces alboniger* puromycin N-acetyl transferase-coding sequence; hHBVPRE, human hepatitis B virus posttranscriptional regulatory element; black triangle/FRT, flippase recognition target sequence; hGAPDH, human *glyceraldehyde 3-phosphate dehydrogenase* gene promoter; rHBB2 pA, rabbit β-*hemoglobin* gene polyadenylation signal; GpLuc, *Gaussia princeps* luciferase-coding sequence; mMT1 pA, mouse *metallothionein 1* gene polyadenylation signal; 3' LTR, 3' HIV1 long terminal repeat containing a deletion in the U3 region to render the LV self-inactivating.

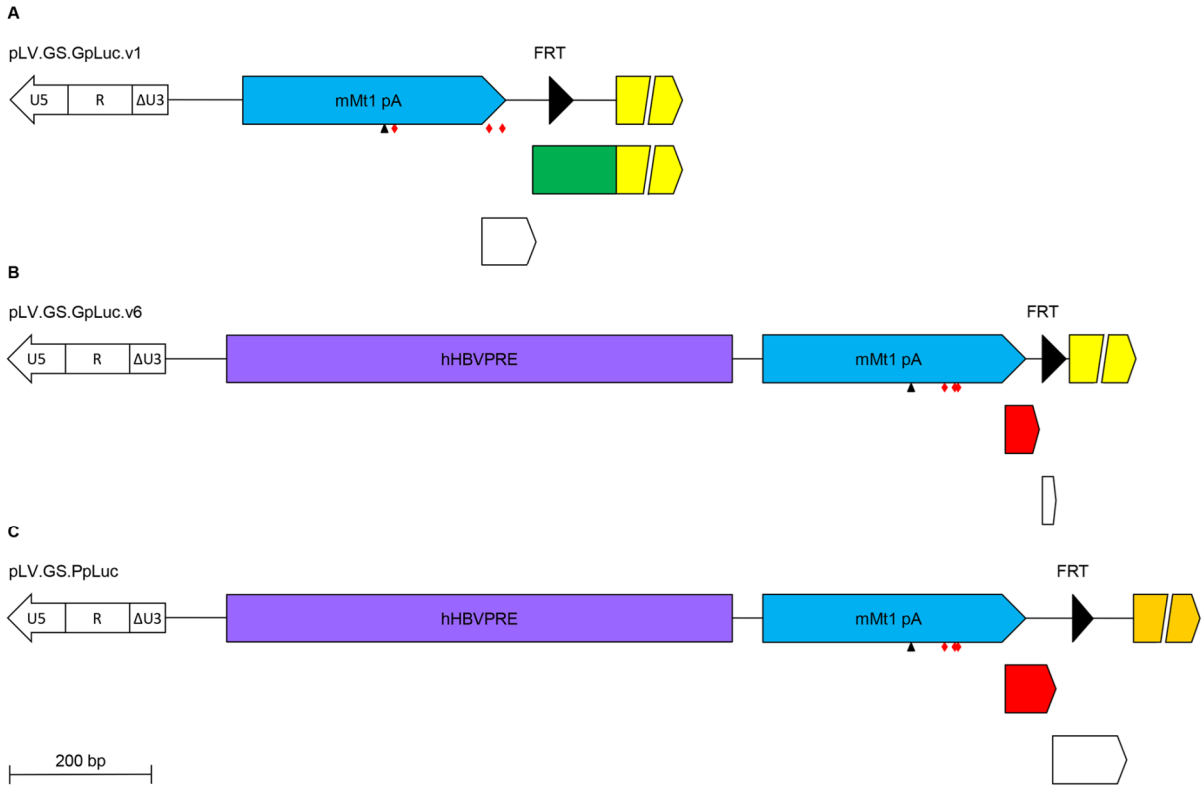

Figure 2. Improved design of the *GpLuc* gene switch cassette. (A–C): Detailed structure of the areas upstream of the *Luc* ORFs in pLV.GS.GpLuc.v1 (A), pLV.GS.GpLuc.v6 (B) and pLV.GS.PpLuc (C) starting at the HIV1 3' LTR. U5, HIV1 LTR unique 5' region; R, HIV1 LTR repeat region; ΔU3, enhancer- and promoterless HIV1 LTR unique 3' region; blue arrow, mouse *metallothionein 1* gene polyadenylation signal (mMT1 pA); small black triangle, AATAAA motif in mMT1 pA; red diamonds, stop codons in frame with Luc ORFs; large black triangle, minimal FRT sequence; light yellow arrow, *GpLuc* ORF; green box, 5' in-frame extension of the *GpLuc* ORF; white arrows, out-of-frame ORFs preceding *Luc* ORFs; red arrows, in-frame ORFs preceding *Luc* ORFs; dark yellow arrow, *PpLuc* ORF.

More details about the genetic makeup of pLV.GS.GpLuc.v1, pLV.GS.GpLuc.v6 and pLV.GS.PpLuc and about the nucleotide sequences located in between the mMT1 pA and *Luc* ORFs of these three SIN-LV plasmids are provided in Figs. 2 and 3. The ligation mixtures were introduced in chemocompetent cells of Escherichia coli strain GeneHogs (Life Technologies Europe, Bleiswijk, the Netherlands) or GT115 (InvivoGen, San Diego, CA). Large-scale plasmid purifications were performed using JETSTAR 2.0 Plasmid Maxiprep kits (Genomed, Löhne, Germany) according to the manufacturer's instructions.

Cells

The culture and differentiation conditions of the murine Bmi1- and human TERT-immortalized human myoblasts (iDMD myoblasts) have been described previously [13].

Viral vectors

The vesicular stomatitis virus G protein-pseudotyped SIN-LVs LV.FLPe^{NLS+}.PurR, LV.FLPe^{NLS-}.PurR, LV.PurR (negative control vector), LV.GS.GpLuc.v1, LV.GS.PpLuc and LV.GS.GpLuc.v6 were generated in 293T cells with the aid of the LV shuttle plasmids pLV.hCMV-IE.FLPe^{NLS+}.IRES.PurR.hHBVPRE, pLV.hCMV-IE.FLPe^{NLS-}.IRES.PurR.hHBVPRE, pLV.CMV. IRES.PURO ([14], hereinafter referred to as pLV.hCMV-IE.IRES.PurR.hHBVPRE; Fig. 1C), pLV.GS.GpLuc.v1, pLV.GS.PpLuc and pLV.GS.GpLuc.v6, respectively. The 293T cells were transfected with one of the LV shuttle constructs and the packaging plasmids psPAX2 (Addgene; plasmid number: 12260) and pLP/VSVG (Life Technologies Europe) at a molar ratio of 2:1:1. To concentrate and purify the LV particles, producer cell supernatants were layered onto 5-ml cushions of 20% (wt/vol) sucrose in phosphate-buffered saline (PBS) and centrifuged at 15,000 rotations per minute for 2 h at 4°C in an SW32 rotor (Beckman Coulter Nederland, Woerden, the Netherlands). Prior to ultracentifugation, producer cell supernatants were clarified by low speed centrifugation and filtration through 0.45-mm pore-sized cellulose acetate filters (Pall Netherlands, Mijdrecht, the Netherlands). For more details about the SIN-LV production method, see [15]. The titers of the resulting LV stocks were determined using the RETROTEK HIV-1 p24 Antigen ELISA kit (ZeptoMetrix, Franklin, MA) following the instructions provided by the manufacturer. To derive functional titers from these measurements a conversion factor of 2.5 transducing units (TUs) per pg of HIV-1 p24 protein was used.

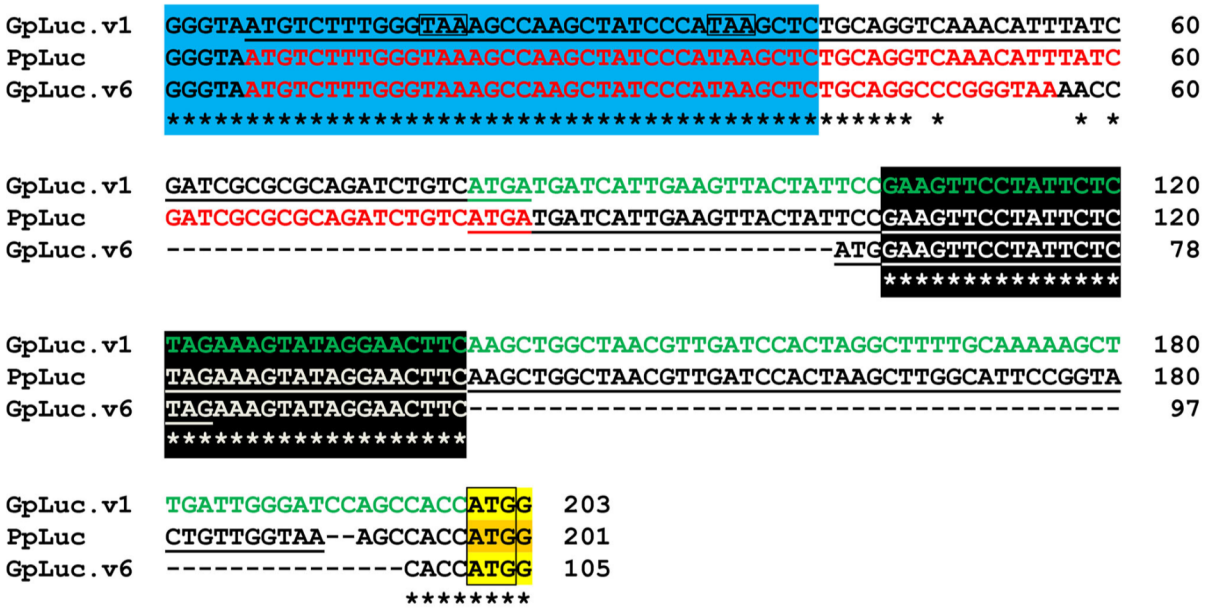

Figure 3. Alignment of the nucleotide sequences immediately upstream of the *Luc* ORFs in pLV.GS.GpLuc.v1, pLV.GS.PpLuc and pLV.GS.GpLuc.v6. Blue box, 3' end of the mMT1 pA; underlined sequences, out-of-frame ORFs preceding *Luc* ORFs; boxed TAA sequences, in-frame stop codons preceding *Luc* ORFs; red letters, in-frame ORFs preceding *Luc* ORFs; green letters, 5' in-frame extension of the *GpLuc* ORF in pLV.GS.GpLuc.v1; black box, minimal FRT sequence; boxed ATG sequences, *Luc* initiation codons; light yellow box, 5' end *GpLuc* ORF; dark yellow box, 5' end *PpLuc* ORF.

Cell transductions

Cryopreserved LV.FLPe^{NLS+}.PurR-transduced iDMD myoblasts ([7]; hereinafter referred to as myoblasts-FLPe^{NLS+}) were thawed and cultured in the presence of puromycin (Life Technologies Europe) at a final concentration of 0.4 µg/ml to prevent transgene silencing. *FLPe^{NLS-}*expressing iDMD myoblasts were generated by overnight (±20 h) exposure of 10^5 cells in a well of a 24-well cell culture plate (Greiner Bio-One, Alphen aan den Rijn, the Netherlands) to 30 TUs of LV.FLPe^{NLS-}.PurR per cell in 500 µl of growth medium in a humidified atmosphere of 5% CO_2/95% air at 37°C. The next day, the cell monolayer was rinsed three times with 1 ml of PBS after which fresh culture medium was added. At 3 days post transduction, the culture of LV.FLPe^{NLS-}.PurR-treated cells (hereinafter referred to as myoblasts-FLPe^{NLS-}) as well as a control culture of untransduced iDMD myoblasts were given medium containing 0.8 µg/ml of puromycin. Within a week, all cells in the culture of untransduced iDMD myoblasts had died while the cells in the LV.FLPe^{NLS-}.PurR-treated culture were nicely expanding. The myoblasts-FLPe^{NLS-} were passaged once a week (split ratio 1:3) in growth medium containing 0.4 µg/ml of puromycin. Myoblasts$^{GS.GLuc}$, myoblasts$^{GS.PLuc}$ and myoblasts$^{GS.GLuc+}$ were generated likewise by exposure of iDMD myoblasts to LV.GS.GpLuc.v1, LV.GS.PpLuc and LV.GS.GpLuc.v6, respectively. Before being used for co-culture experiments, the cells were passaged at least three times to rule out secondary transduction of the *FLPe*-expressing myoblasts in the co-cultures with luciferase-encoding SIN-LVs [16].

Co-culture establishment and maintenance

Co-cultures containing a total number of 2×10^5 cells were established in wells of 24-well culture plates by mixing myoblasts-FLPe^{NLS+} or myoblasts-FLPe^{NLS-} with myoblasts$^{GS.GLuc}$ at the indicated ratios. Following an incubation period of about 72 h when the cell monolayers had reached 90–100% confluency, the growth medium was substituted by 400 µl of either differentiation medium or fresh growth medium. At specified time points thereafter, the culture medium (400 µl) was collected and stored at -80℃ for luciferase assay. The co-cultures were then either terminated or further incubated at 37℃ in a water-saturated atmosphere of 5% CO_2/95% air.

To compare the performance of the newly developed LV.GS.GpLuc.v1-based cell fusion assay system with that of the previously described LV.GS.PpLuc-based cell fusion quantification method [7], myoblasts$^{GS.GLuc}$ or myoblasts$^{GS.PLuc}$ were cocultured with myoblasts-FLPe^{NLS+} in different ratios in 24-well culture plates containing 2×10^5 cells per well. Samples (culture fluid for cultures containing myoblasts$^{GS.GLuc}$ and cell lysates for cultures containing myoblasts$^{GS.PLuc}$) were harvested 96 h and 120 h after induction of myogenic differentiation. Exactly the same approach was used to compare the LV.GS.GpLuc.v1- and LV.GS.GpLuc.v6-based cell fusion assays.

Immunocytology

At different time points after the initiation of differentiation, 1:1 co-cultures of myoblasts-FLPe^{NLS-} and myoblasts$^{GS.GLuc}$ were fixed by incubation for 30 minutes at room temperature (RT) in PBS containing 4% formaldehyde. To permeabilize the cells, they were exposed for 10 minutes at RT to 0.1% Triton X-100 in PBS. Next,

cells were incubated overnight at 4℃ with mouse antiskeletal muscle troponin I (skTnI) primary antibody (HyTest, Turku, Finland; clone 12F10) diluted 1:100 in PBS +0.1% donkey serum (Santa Cruz Biotechnology, Santa Cruz, CA) followed by a 2-h incubation at RT with Alexa Fluor 568-conjugated donkey anti-mouse IgG (H+L) secondary antibody (Life Technologies Europe) diluted 1:400 in PBS +0.1% donkey serum. Counterstaining of nuclei was performed with 10 µg/ml Hoechst 33342 (Life Technologies Europe) in PBS. Cells were washed three times with PBS after fixation, permeabilization and incubation with primary antibody, secondary antibody and DNA-binding fluorochrome. To minimize photobleaching, coverslips were mounted in Vectashield mounting medium (Vector Laboratories, Burlingame, CA). Pictures were taken with a fluorescence microscope equipped with a digital color camera (Nikon Eclipse 80i; Nikon Instruments Europe, Amstelveen, the Netherlands) using NIS Elements software (Nikon Instruments Europe).

Subcellular fractionation and western blotting

Myoblasts-FLPe^{NLS+} and myoblasts-FLPe^{NLS-} were cultured separately in 24-well cell culture plates at a density of 2×10^5 cells per well. Following an incubation period of 72 h when the cell monolayers had reached 90-100% confluency, the growth medium was substituted by 400 µl of either differentiation medium or fresh growth medium. Ninety-six h later, cell fractionation was carried out as described by *Suzuki et al.* [17] with the following modifications. Cell pellets were suspended in 97.5 µl of ice-cold 0.1% NP40 in PBS. One-third of the lysate was removed as ‘‘whole cell lysate’’ and mixed with 5 µl of 10×NuPAGE Sample Reducing Agent and 12.5 µl of 4×NuPAGE LDS Sample Buffer (both from Life Technologies Europe). The rest of the lysate was briefly centrifuged at 4℃ after which 32.5 µl of the supernatant was removed as ‘‘cytosolic fraction’’ and supplemented with 5 µl of 10×NuPAGE Sample Reducing Agent and 12.5 µl of 4×NuPAGE LDS Sample Buffer. The remaining supernatant was removed and the pellet was washed with and suspended in 30 µl PBS, after which 5 µl of 10×NuPAGE

Sample Reducing Agent and 12.5 µl of 4×NuPAGE LDS Sample Buffer were added to produce the ‘‘nuclear fraction’’. Nuclear fractions and whole cell lysates were sonicated for 2 times 10 seconds at 200 Hz using a Soniprep 150 ultrasonic disintegrator (Measuring and Scientific Equipment, London, United Kingdom). After incubating the samples for 1 minute at 100℃, 10 µl of whole cell lysate, 10 µl of cytosolic fraction and 5 µl of nuclear fraction were applied to a NuPAGE Novex 12% Bis-Tris gel (Life Technologies Europe). Following electrophoretic separation, the proteins were transferred to a polyvinylidene difluoride membrane (Amersham Hybond P; GE Healthcare Europe, Diegem, Belgium) by wet electroblotting. Next, the membrane was incubated with 2% ECL AdvanceTM blocking agent (GE Healthcare Europe) in PBS-0.1% Tween 20 (PBST) for 1 h at RT and probed with rabbit anti-FLP (1:200; Diagenode, Seraing, Belgium; CS-169-100), mouse anti-glyceraldehyde 3-phosphate dehydrogenase (GAPDH; 1:10,000; Merck Millipore, Billerica, MA; clone 6C5) or rabbit anti-lamin A/C (1:10,000; Santa Cruz Biotechnology; sc-20681) primary antibodies overnight at 4℃, followed by a 1-h incubation with appropriate horseradish peroxidase-conjugated secondary antibodies (Santa Cruz Biotechnology). GAPDH served as cytoplasmic marker protein and lamin

A/C antibody was used as nuclear marker protein. Target protein signals were visualized using the SuperSignal West Femto Maximum Sensitivity Substrate Kit (Thermo Scientific, Rockford, IL) and chemiluminescence was measured with the ChemiDoc XRS imaging system (Bio-Rad Laboratories, Veenendaal, the Netherlands).

FLPe functionality test
To test the functionality of the FLPe molecules encoded by LV.FLPe^{NLS+}.PurR and LV.FLPe^{NLS-}.PurR, myoblasts$^{GS.GLuc}$ were transduced with LV.FLPe^{NLS+}.PurR, LV.FLPe^{NLS-}.PurR or LV.PurR. Myoblasts$^{GS.GLuc}$ were seeded in a 24-well cell culture plate at a density of 10^5 cells per well and exposed for 20 h to 75 µl per well of concentrated vector stock diluted in growth medium to a final volume of 500 µl. Next, the cell monolayers were rinsed three times with 1 ml of PBS after which 400 µl fresh growth medium was added. At 24 h after the removal of the inoculum, the culture medium was collected and transiently stored at -80°C for subsequent analysis of luciferase activity. The cells were overlaid with 400 ml of fresh growth medium, which was harvested 24 h later for storage at -80°C until luciferase activity measurement.

Luciferase assay
After thawing the GpLuc-containing samples on ice, 50 µl of each sample was transferred to a well of a white opaque 96-well flat-bottom microtiter plate (OptiPlate-96; PerkinElmer, Groningen, the Netherlands) for chemiluminescence measurements. The native coelenterazine (Promega Benelux, Leiden, the Netherlands) stock solution (5 mg/ml in acidified methanol) was diluted 1,000 times in phenol red-free Dulbecco's modified Eagle's medium (Life Technologies Europe) and equilibrated for 1 h in the dark at RT before starting the measurements. The luciferase activity was measured at RT with the aid of a Wallace 1420 VICTOR 3 multilabel plate reader with automatic injection system (PerkinElmer). Immediately after automated addition of 20 ml of substrate to a well, substrate and sample were mixed by shaking for 1 second (double orbital, 0.1 mm, normal speed). PpLuc activity was measured in cell lysates as previously described [7]. For each condition, three independent samples were measured in three series of measurements.

Statistical analysis
Different experimental groups were compared using the independent samples t-test. Differences among means were considered significant at $P \leq 0.05$. Graphs were prepared in GraphPad Prism version 5 (GraphPad Software, La Jolla, CA).

Results

Microscopic analysis of cell fusion kinetics
Cultured myoblasts can be prompted to fuse with each other by withdrawing mitogens from the culture medium. This causes a time-dependent accumulation of nuclei in syncytial structures called myotubes or myosacs depending on whether these structures are elongated or rounded. To get a first impression of the cell-to-cell fusion kinetics of the genetically modified iDMD myoblasts, 1:1 co-cultures of myoblasts-

FLPe^{NLS-} and myoblasts$^{GS.GLuc}$ were exposed to myogenic differentiation conditions. As shown in the upper panel of Fig. 4, the myoblasts started to fuse 48 h after serum withdrawal resulting in the formation of myotubes/sacs. Both the percentage of nuclei present in myotubes/sacs as well as the size of the syncytia increased with time until 120 h following serum removal, after which the cells started to detach from the surface of the culture plates. The fusion process was accompanied by the accumulation of sarcomeric proteins as evinced by the results of the skTnI-specific immunostaining depicted in the lower panel of Fig. 4.

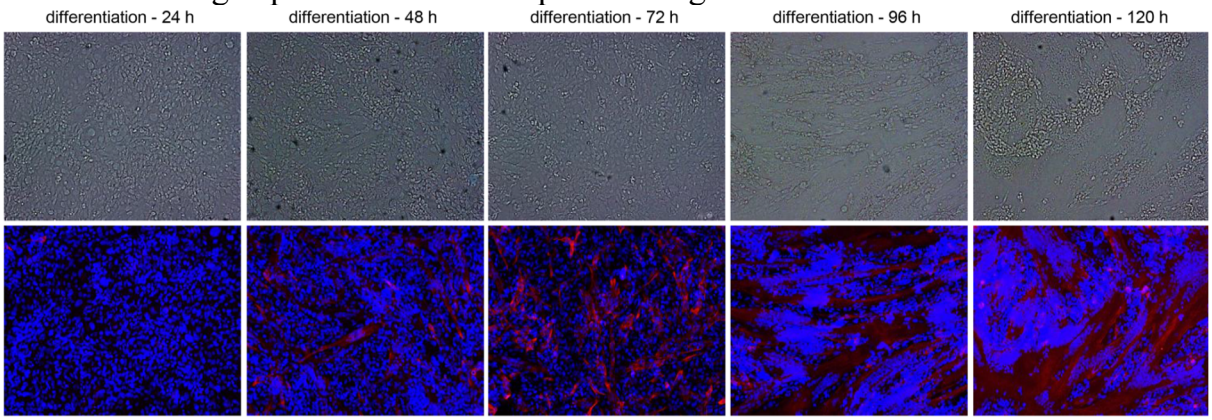

Figure 4. Microscopic analysis of cell fusion kinetics in 1:1 co-cultures of myoblasts-FLPe^{NLS-} and myoblasts$^{GS.GLuc}$ after maintenance for 72 h in growth medium and subsequent exposure to differentiation medium. At 24, 48, 72, 96 or 120 h after initiation of differentiation the cells were fixed and immunostained for skTnI (red fluorescence). The blue fluorescence corresponds to nuclei labeled with the karyophilic dye Hoechst 33342. The upper and lower row of pictures show phase-contrast images and fluoromicrographs, respectively. The first syncytia appeared at ±48 h after serum removal. The cell cultures displayed a time-dependent increase in frequency and size of myotubes/sacs until the cells started to detach from the surface of the culture plates. In parallel cultures of myoblasts kept in normal growth medium the cells remained firmly attached to their support and only few small syncytia were observed at late times after culture initiation (data no shown).

Immunodetection of FLPe in LV.FLPe$^{NLS+/-}$.PurR transduced iDMD myoblasts

To compare FLPe protein level and intracellular distribution between myoblasts-FLPe^{NLS+} and myoblasts-FLPe^{NLS-}, western blot analysis was performed on whole cell lysates as well as on nuclear and cytosolic cell fractions (Fig. 5A). As expected from the presence at its amino terminus of the SV40 NLS, FLPeNLS+ (predicted molecular weight: 49.7 kilodaltons) had a slightly lower gel mobility than FLPeNLS- (predicted molecular weight: 48.6 kilodaltons). Both under growth and differentiation conditions, the steady-state level of FLPeNLS+ was considerably higher than that of FLPe^{NLS-} even though the nucleotide sequences upstream of the FLPe start codon are very similar and both proteins contain a ‘‘destabilizing’’ amino acid residue (serine in FLPe^{NLS-} versus alanine in FLPe^{NLS+}; [18]) immediately downstream of the initiator methionine. Fig. 5A also reveals that a larger fraction of FLPe^{NLS+} molecules than of FLPe^{NLS-} molecules also reveals that a larger fraction of FLPe^{NLS+} molecules than of FLPe^{NLS-} molecules resides in the nucleus (nuclear-to-cytosolic ratios under differentiation conditions of 8.4 and 3.1, respectively) consistent with the presence in FLPe^{NLS+} of an SV40 NLS.

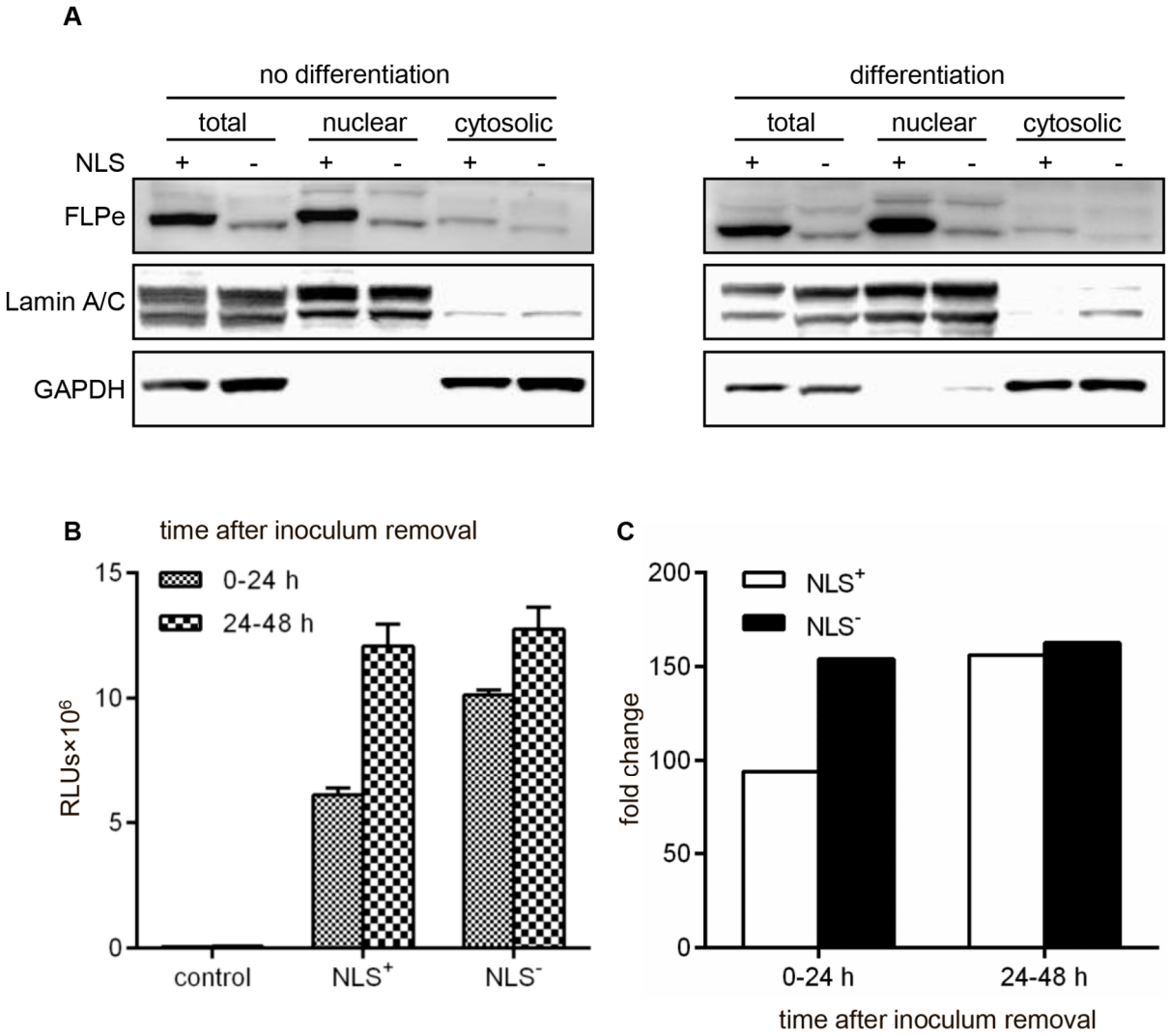

Figure 5. Analysis of FLPe$^{NLS+/-}$ level, intracellular localization and enzymatic activity. (A): Western blotting analysis of whole protein lysates, nuclear cell fractions and cytosolic cell fractions of myoblasts-FLPe^{NLS+} (+) and of myoblasts-FLPe^{NLS-} (-) maintained in growth medium (no differentiation) or exposed to differentiation conditions for 96 h (differentiation). (B): Luciferase activity measurements in culture media of myoblasts$^{GS.GLuc}$ transduced with LV.FLPe^{NLS+}.PurR, LV.FLPe^{NLS-}.PurR or LV.PurR (negative control vector) representing different intervals (*i.e.* 0–24 h and 24–48 h) post transduction. Bars show mean 6 standard error of the mean (n = 3). (C): Fold change in luciferase activity calculated on the basis of the data presented in (B). The average light production by samples of LV.PurR-transduced myoblasts$^{GS.GLuc}$ was the denominator and the mean of the RLUs produced by LV.FLPe^{NLS+}.PurR-transduced myoblasts$^{GS.GLuc}$ (NLS$^+$) or by LV.FLPe^{NLS-}.PurR-transduced myoblasts$^{GS.GLuc}$ (NLS$^-$) was the numerator. NLS, nuclear localization signal; FLPe, molecularly evolved flippase; GAPDH, glyceraldehyde 3-phosphate dehydrogenase; RLUs, relative light units.

Assessment of FLPe$^{NLS+/-}$ functionality

To investigate the functionality of the FLPe molecules encoded by LV.FLPe^{NLS+}.PurR and LV.FLPe^{NLS-}.PurR, myoblasts$^{GS.GLuc}$ were transduced with either of these FLPe-encoding SIN-LVs or with LV.PurR (negative control vector). Production of functional recombinases by the FLPe-encoding SIN-LVs should result in activation of

the *GpLuc* gene switch cassettes incorporated into the genomes of the myoblasts$^{GS.GLuc}$ and the secretion of active GpLuc molecules in their culture medium (Fig. 6). Analysis of the culture media harvested at 24 h after vector removal showed strong luciferase activity in the samples derived from the LV.FLPe^{NLS+}.PurR- and LV.FLPe^{NLS-}.PurR-transduced myoblasts$^{GS.GLuc}$, while hardly any luciferase activity was detected in the culture medium of LV.PurR-transduced myoblasts$^{GS.GLuc}$ (Fig. 5B). During the next 24-h interval the luciferase activity in the culture media of LV.FLPe^{NLS+}.PurR- and LV.FLPe^{NLS-}.PurR-transduced myoblasts$^{GS.GLuc}$ further increased whereas the luciferase activity in the negative control samples remained very low. As a result, luciferase activity was 94/154- and 156/162-fold higher in 0-24 h and 24-48 h culture medium of LV.FLPe^{NLS+}.PurR- and LV.FLPe^{NLS-}.PurR-transduced myoblasts$^{GS.GLuc}$, respectively, than in the corresponding culture media of LV.PurR-infected cells (Fig. 5C). These findings confirm the presence of FLP recombinase-activatable *GpLuc* expression units in myoblasts$^{GS.GLuc}$ and demonstrate that LV.FLPe^{NLS+}.PurR and LV.FLPe^{NLS-}.PurR both code for functional FLPe molecules.

Validation of the LV.FLPe$^{NLS+/-}$.PurR/LV.GS.GpLuc-based cell fusion assay system

To compare the ability of FLPe^{NLS+} and FLPe^{NLS-} to activate the *GpLuc* gene switch upon cell fusion, myoblasts$^{GS.GLuc}$ were cocultured with myoblasts-FLPe^{NLS+} or myoblasts-FLPe^{NLS-} at different ratios (*i.e.* 95:5, 90:10, 75:25, 50:50, 25:75, 10:90 and 5:95). Monocultures of myoblasts-FLPe^{NLS+}, myoblasts-FLPe^{NLS-} or myoblasts$^{GS.GLuc}$ exposed to growth or differentiation medium and co-cultures of FLPe-expressing myoblasts and myoblasts$^{GS.GLuc}$ maintained in growth medium served as negative controls. Based on the results of the microscopic analysis of cell fusion activity (Fig. 4), the culture medium was harvested 96 h after induction of myogenic differentiation. It should be noted, however, that the kinetics of cell fusion progression slightly differed between individual experiments probably reflecting small differences in the myoblast populations used for different experiments. Luciferase activity in the medium of the fusogenic cell cultures depended on the ratio of myoblasts$^{GS.GLuc}$ and myoblasts-FLPe, showed a similar trend for myoblasts-FLPe^{NLS+} -and myoblasts-FLPe^{NLS-} containing co-cultures and was highest when co-cultures contained 50-95% myoblasts$^{GS.GLuc}$ (Fig. 7A). The peak of GpLuc activity was reached at myoblast$^{GS.GLuc}$:myoblast-FLPe ratios of 90:10 and 75:25 for myoblasts-FLPe^{NLS+} and myoblasts-FLPe^{NLS-}, respectively (Fig. 7A). Interestingly, at low myoblast$^{GS.GLuc}$:myoblast-FLPe ratios (*i.e.* 10:90 and 5:95) the luciferase activity was significantly higher for myoblasts-FLPe^{NLS-} than for myoblasts-FLPe^{NLS+} (Fig. 7A). Myoblast cultures kept under growth conditions and myoblast-FLPe monocultures maintained in differentiation medium yielded luminescence signals close to or at background levels. The monocultures of myoblasts$^{GS.GLuc}$ did, however, secrete detectable amounts of GpLuc under differentiation conditions although the signal intensity was much lower than that produced by serum-deprived co-cultures containing 50–90% myoblasts$^{GS.GLuc}$. For the co-cultures containing 50-90% myoblasts$^{GS.GLuc}$ shifting from growth to differentiation medium resulted in a >100-fold increase in luciferase activity (Fig. 7B).

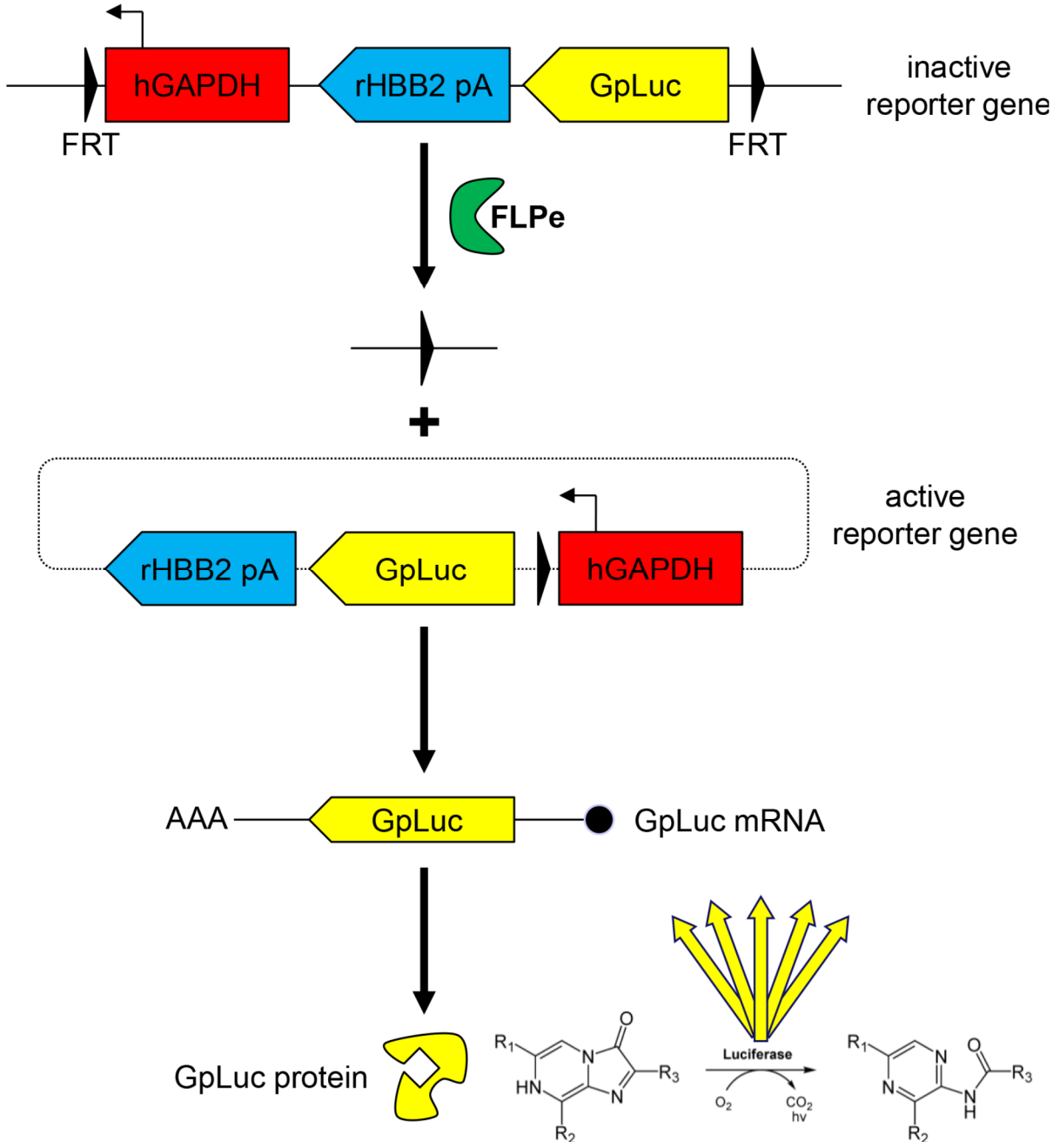

Figure 6. Schematic overview of the activation of the *GpLuc* gene switch cassette. Recognition of the FRT sites in chromosomally integrated copies of the LV.GS.GpLuc genome by FLPe leads to the activation of the latent *GpLuc* gene through the formation of circular episomes positioning the *hGAPDH* gene promoter upstream of the *GpLuc* ORF. Black triangle/FRT, flippase recognition target sequence; hGAPDH, human *glyceraldehyde 3-phosphate dehydrogenase* gene promoter; rHBB2 pA, rabbit *β-hemoglobin* gene polyadenylation signal; GpLuc, *Gaussia princeps* luciferase-coding sequence; FLPe, molecularly evolved flippase.

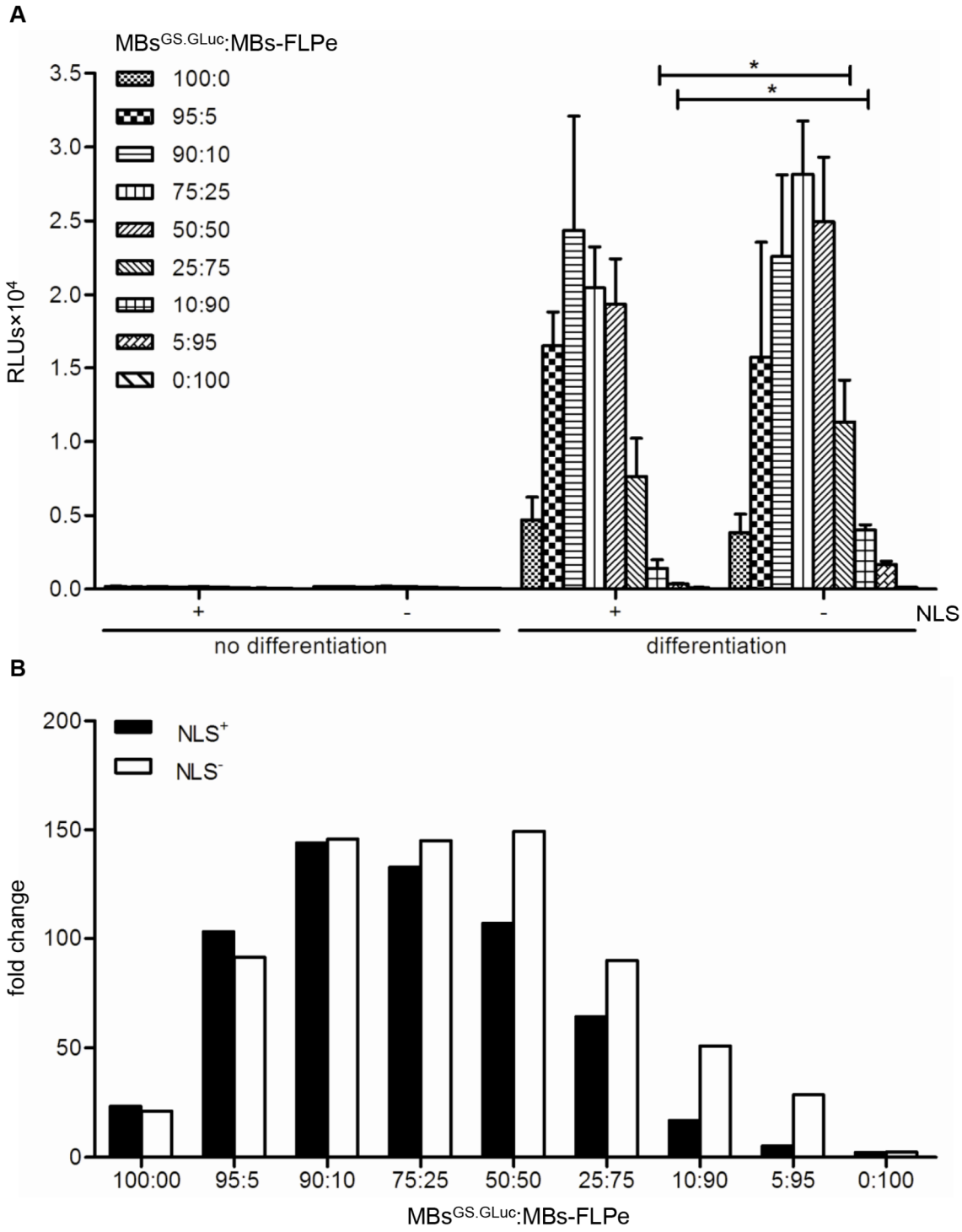

Figure 7. Validation of the LV.FLPe$^{NLS+/-}$.PurR/LV.GS.GpLuc.v1-based cell fusion assay system. (A): Luminometric analysis of culture medium of myoblasts$^{GS.GLuc}$ co-cultured with myoblasts-FLPe^{NLS+} (+) or with myoblasts-FLPe^{NLS-} (-) at the indicated ratios. At 72 h after cell seeding, the culture fluid in each well was replaced by fresh culture medium with (no differentiation) or without (differentiation conditions) serum. Nighty-six h later the culture media were collected and subjected to luciferase activity measurements. Bars represent mean ± standard error of the mean (n = 3). (B): Fold change in luciferase activity calculated on the basis of the data presented in (A). For each culture composition the average light production under growth conditions was the denominator and the mean of the RLUs produced under differentiation conditions was the numerator. RLUs, relative light units; MBs$^{GS.GLuc}$, myoblasts$^{GS.GLuc}$; MBs-FLPe, myoblasts-FLPe; NLS, nuclear localization signal.

Use of the LV.FLPe$^{NLS+/-}$.PurR/LV.GS.GpLuc-based cell fusion assay system to analyse cell fusion progression

To investigate the utility of the LV.FLPe$^{NLS+/-}$.PurR/LV.GS.GpLuc-based cell fusion assay system to follow cell fusion progression, myoblasts$^{GS.GLuc}$ were mixed with myoblasts-FLPe^{NLS+} or with myoblasts-FLPe^{NLS-} at a ratio of 50:50. After the cell cultures had become nearly confluent, they were either given fresh growth medium or exposed to differentiation medium. This was followed by the periodic collection of culture fluid for luciferase measurements using two different approaches. In one experiment, the culture medium was left on the cells for different time periods (*i.e.* from 0-24, 0-36, 0-48, 0-60, 0-72, 0-84, 0-96, 0-108 and 0-120 h) before being harvested for luminometry (‘‘cumulative assay’’; Fig. 8). In the other experiment, the culture fluid was refreshed every 24 h and the amount of biologically active luciferase that had been secreted between 0-24, 24-48, 48-72, 72-96 and 96-120 h after the start of the differentiation process was determined (‘‘kinetics assay’’; Fig. 9). As shown in Fig. 8A, following an initial slow increase, the luciferase activity in the culture medium of the serum-deprived co-cultures rose sharply at late times (>72 h) after initiation of differentiation. Co-cultures of myoblasts$^{GS.GLuc}$ and myoblasts-FLPe^{NLS-} produced better results than the combination of myoblasts$^{GS.GLuc}$ and myoblasts-FLPe^{NLS+} (Fig. 8A,B) in spite of the much higher FLPe concentration in myoblasts-FLPe^{NLS+} than in myoblasts- FLPe^{NLS-} (Fig. 5A). These findings were corroborated by the data derived from the ‘‘kinetics assay’’ (Fig. 9).

On the basis of the previous results, another experiment was carried out in which we directly compared the performance of FLPe^{NLS+} and FLPe^{NLS-} at different myoblast$^{GS.GLuc}$:myoblast-FLPe ratios (*i.e.* 95:5, 75:25, 25:75 and 5:95) and different time points (*i.e.* 72, 96 and 120 h after serum withdrawal). The culture medium was refreshed just before the start of the first sampling interval (*i.e.* at 48 h after serum removal) and after each round of sample collection. This experiment confirmed that at high myoblast$^{GS.GLuc}$:myoblast-FLPe ratios FLPe^{NLS-} was nearly as efficient as FLPe^{NLS+} at inducing reporter gene expression while at low myoblast$^{GS.GLuc}$:myoblast-FLPe ratios FLPe^{NLS-} gave rise to more RLUs (Fig. 10A) and to higher signal-to-noise ratios (Fig. 10B). In accordance with the experiment presented in Fig. 7, the co-cultures consisting of 75% myoblasts$^{GS.GLuc}$ and 25% myoblasts-FLPe yielded the highest signals both in absolute (Fig. 10A) and relative (Fig. 10B) terms. Also in line with the previous experiments was the finding that most GpLuc accumulation takes place between 96 and 120 h after serum removal.

Comparison of LV.GS.GpLuc.v1- and LV.GS.PpLuc-based cell fusion assay systems

In the next experiment, a direct comparison was made between the previously described LV.GS.PpLuc-based quantitative cell fusion assay system [7] and the new LV.GS.GpLuc-based method to quantify cell-to-cell fusion. Consistent with the much higher light output of GpLuc than of PpLuc [8], LV.GS.GpLuc yielded up to 23-fold higher signals than LV.GS.PpLuc (Fig. 11A). However, the LV.GS.PpLuc-based cell fusion assay system appeared to be approximately twice as sensitive as its LV.GS.GpLuc-based counterpart at detecting myoblast-to-myoblast fusion at 120 h after initiation of differentiation (Fig. 11B). The difference in sensitivity between the

GS.GpLuc.v1- and LV.GS.PpLuc-based cell fusion assay systems was even bigger for the samples collected at 96 h after serum removal especially at the lowest two myoblast$^{GS.Luc}$:myoblast-FLPe^{NLS+} ratios (*i.e.* when FLPe levels are highest).

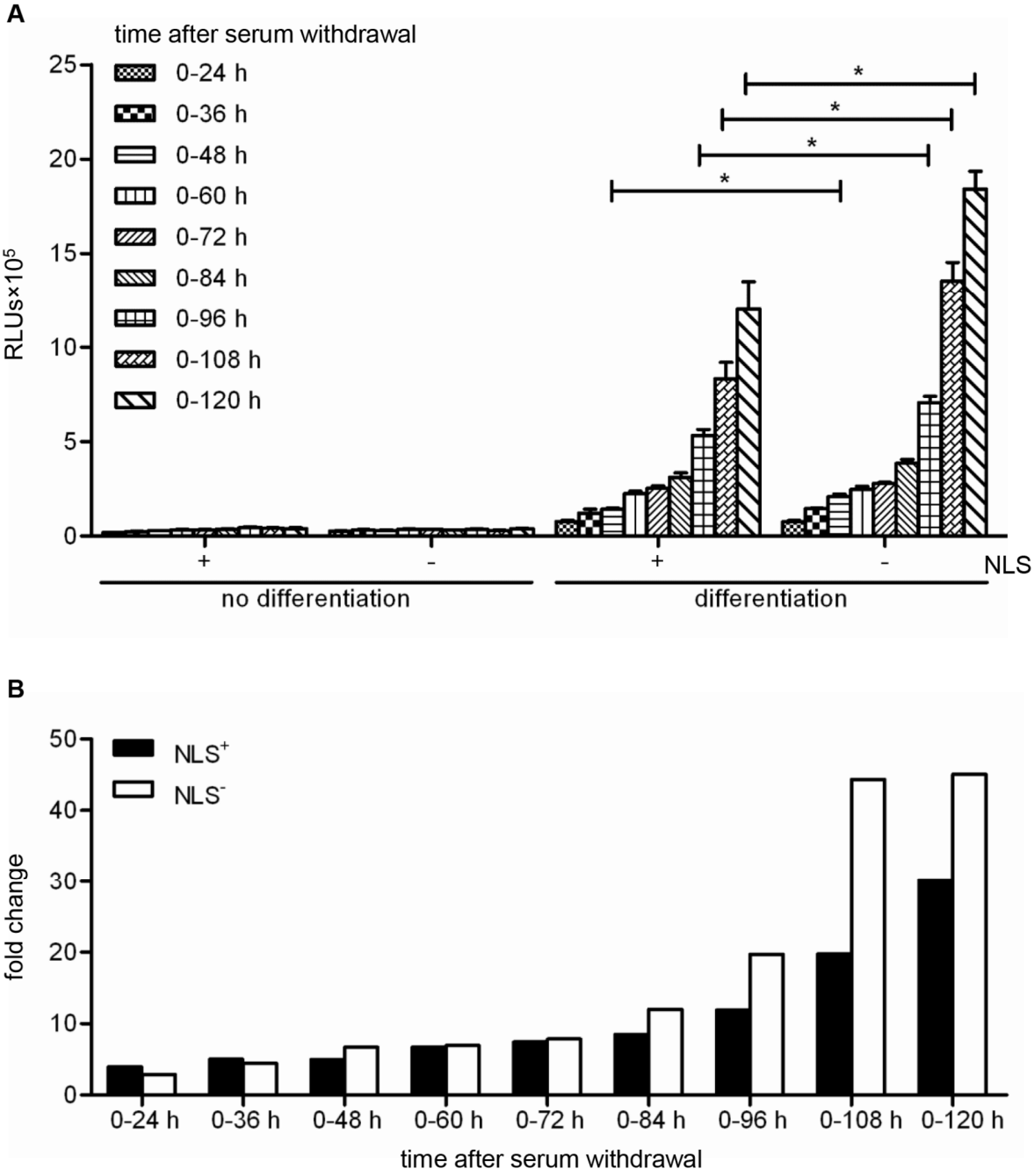

Figure 8. Analysis of GpLuc accumulation in proliferating and differentiating 1:1 co-cultures of myoblasts$^{GS.GLuc}$ and either myoblasts-FLPe^{NLS+} or myoblasts-FLPe^{NLS-}. (A): Luminometric analysis of culture medium of co-cultures of 50% myoblasts$^{GS.GLuc}$ and 50% myoblasts-FLPe^{NLS+} (+) or 50% myoblasts-FLPe^{NLS-} (2). At 72 h after cell seeding, the culture fluid was replaced by fresh culture medium with (growth conditions, no differentiation) or without (differentiation conditions) serum, which was left on the cells for the indicated periods of time. Bars represent mean ± standard error of the mean (n = 3). (B): Fold change in luciferase activity calculated on the basis of the data presented in (A). For each sampling time the average light production under growth conditions was the denominator and the mean of the RLUs produced under differentiation conditions was the numerator. RLUs, relative light units; NLS, nuclear localization signal.

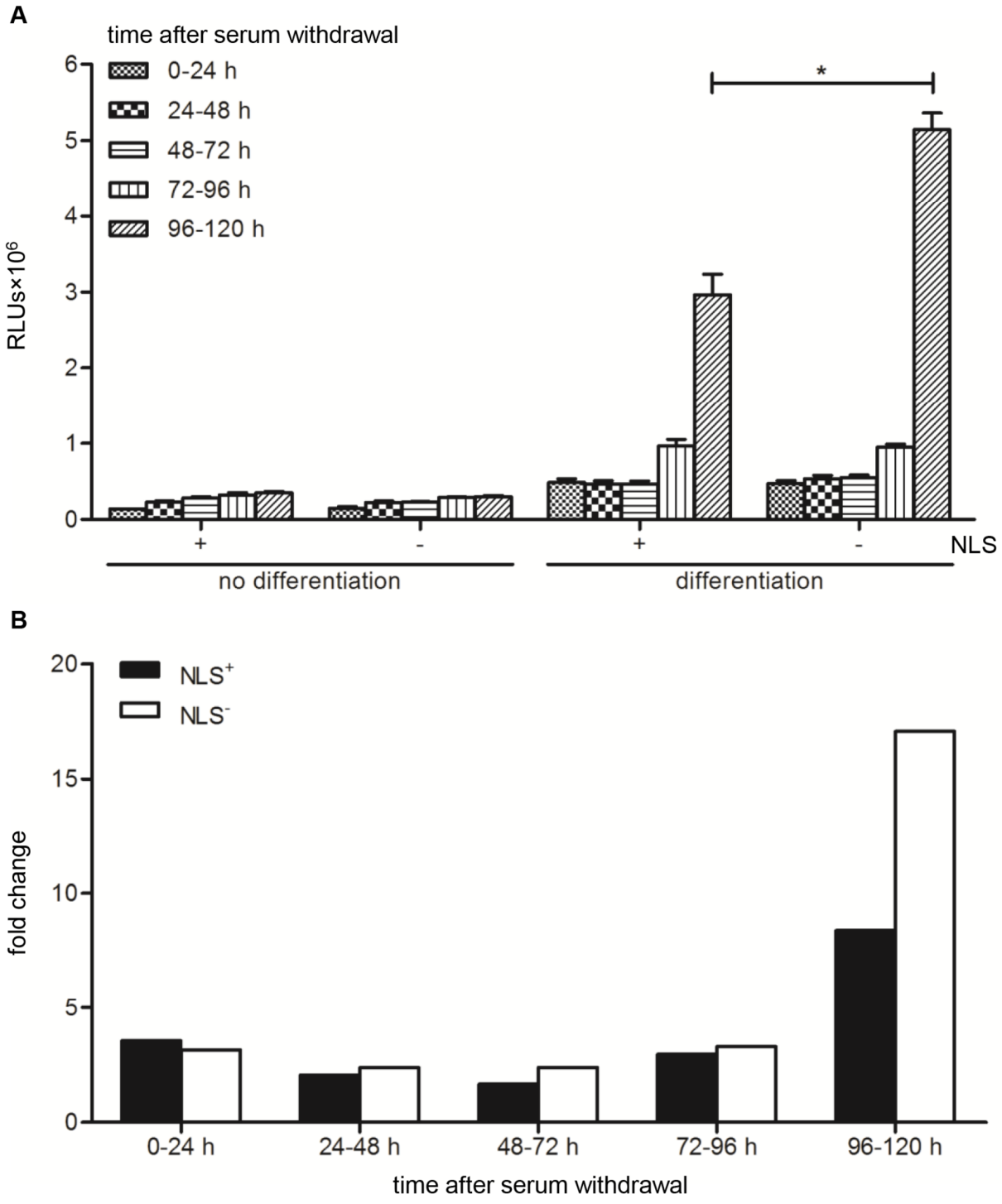

Figure 9. Analysis of GpLuc secretion in proliferating and differentiating 1:1 co-cultures of myoblasts$^{GS.GLuc}$ and either myoblasts-FLPe^{NLS+} or myoblasts-FLPe^{NLS-}. (A): Luminometric analysis of culture medium of co-cultures of 50% myoblasts$^{GS.GLuc}$ and 50% myoblasts-FLPe^{NLS+} (+) or 50% myoblasts-FLPe^{NLS-} (2). At 72 h after cell seeding, the culture fluid was replaced by fresh culture medium with (growth conditions, no differentiation) or without (differentiation conditions) serum, which was left on the cells for the indicated 24-h time intervals. Bars represent mean ± standard error of the mean (n = 3). (B): Fold change in luciferase activity calculated on the basis of the data presented in (A). For each sampling time the average light production under differentiation conditions was the numerator. RLUs, relative light units; NLS, nuclear localization signal.

Improvement of the GS.GpLuc-based cell fusion assay system

The results presented in Figs. 7 and 11 identify the FLP-independent increase in GpLuc production when shifting from growth to differentiation medium as the main contributor to the reduced signal-to-noise ratio of the LV.GS.GpLuc-based cell fusion assay system as compared to its LV.GS.PpLuc-based counterpart. In search for a possible explanation for the high background signal produced by LV.GS.GpLuc.v1 in comparison to LV.GS.PpLuc, we compared their genetic organization upstream of the *Luc* start codon. As shown in Figs. 2 A,B and 3 the *PpLuc* ORF in LV.GS.PpLuc is preceded by an out-of-frame ORF (uORF) starting with 2 ATG codons in a favourable context for translational initiation [19] and ending with a highly efficient stop codon [20] separated by only 7 nucleotides from the *PpLuc* initiation codon. This specific genetic makeup will be effective in supressing any *PpLuc* expression directed by mRNAs with 5' ends located upstream of the second ATG codon in the uORF. Oppositely, in LV.GS.GpLuc.v1 the previously mentioned tandem of ATG codons are in-frame with the *GpLuc* initiation codon allowing the synthesis of an N-terminally extended GpLuc fusion protein. Located further upstream of the *GpLuc* ORF in LV.GS.GpLuc.v1 is an out-of-frame ORF with suboptimal start and stop codons. LV.GS.GpLuc.v1 thus offers much more possibilities for ''leaky'' *Luc* expression than LV.GS.PpLuc. To solve this problem, we designed LV.GS.GpLuc.v6. In this construct, the distance between the mMT1 pA and *GpLuc* ORF is kept very short to minimize the chance of creating transcriptional start sites in the intervening region. As an additional measure to limit leaky *GpLuc* expression, LV.GS.GpLuc.v6 contains a 21-bp uORF starting immediately upstream of the FRT sequence and ending with an efficient stop codon provided by the FRT sequence. Between the stop codon of the uORF and the *PpLuc* initiation codon only 20 nucleotides are present comprising the remainder of the FRT sequence and an optimal start site for *GpLuc* translation.

LV.GS.GpLuc.v6 was used to generate myoblasts$^{GS.GLuc+}$ carrying the optimized *GpLuc* gene switch cassette. Next, the performance of the LV.GS.GpLuc.v1- and LV.GS.GpLuc.v6- based cell fusion assay systems was compared in an experiment with the same setup as used for the comparison of LV.GS.GpLuc.v1 with LV.GS.PpLuc except for the omission of the 1:1 myoblast$^{GS.GLuc(+)}$:myoblast-FLPe^{NLS+} ratio. Luciferase activity in 0-96 h and 0-120 h culture medium of serum-deprived myoblast$^{GS.GLuc+}$ monocultures was ±3-fold lower than in culture medium of differentiating myoblast$^{GS.GLuc}$ monocultures (Fig. 12), demonstrating the effectiveness of the new gene switch design to inhibit leaky *GpLuc* expression. However, since the improved gene switch design also reduced FLPe-dependent signal output the fold increase in GpLuc activity during myogenic differentiation of myoblast$^{GS.GLuc(+)}$:myoblast-FLPe^{NLS+} co-cultures was quite similar for LV.GS.GpLuc.v1 and LV.GS.GpLuc.v6 (Fig. 12B). Still, in comparison to LV.GS.GpLuc.v1 for LV.GS.GpLuc.v6 a much larger part of the increase in GpLuc activity observed in differentiating myoblast$^{GS.GLuc(+)}$:myoblast-FLPe^{NLS+} co-cultures is attributable to cell fusion.

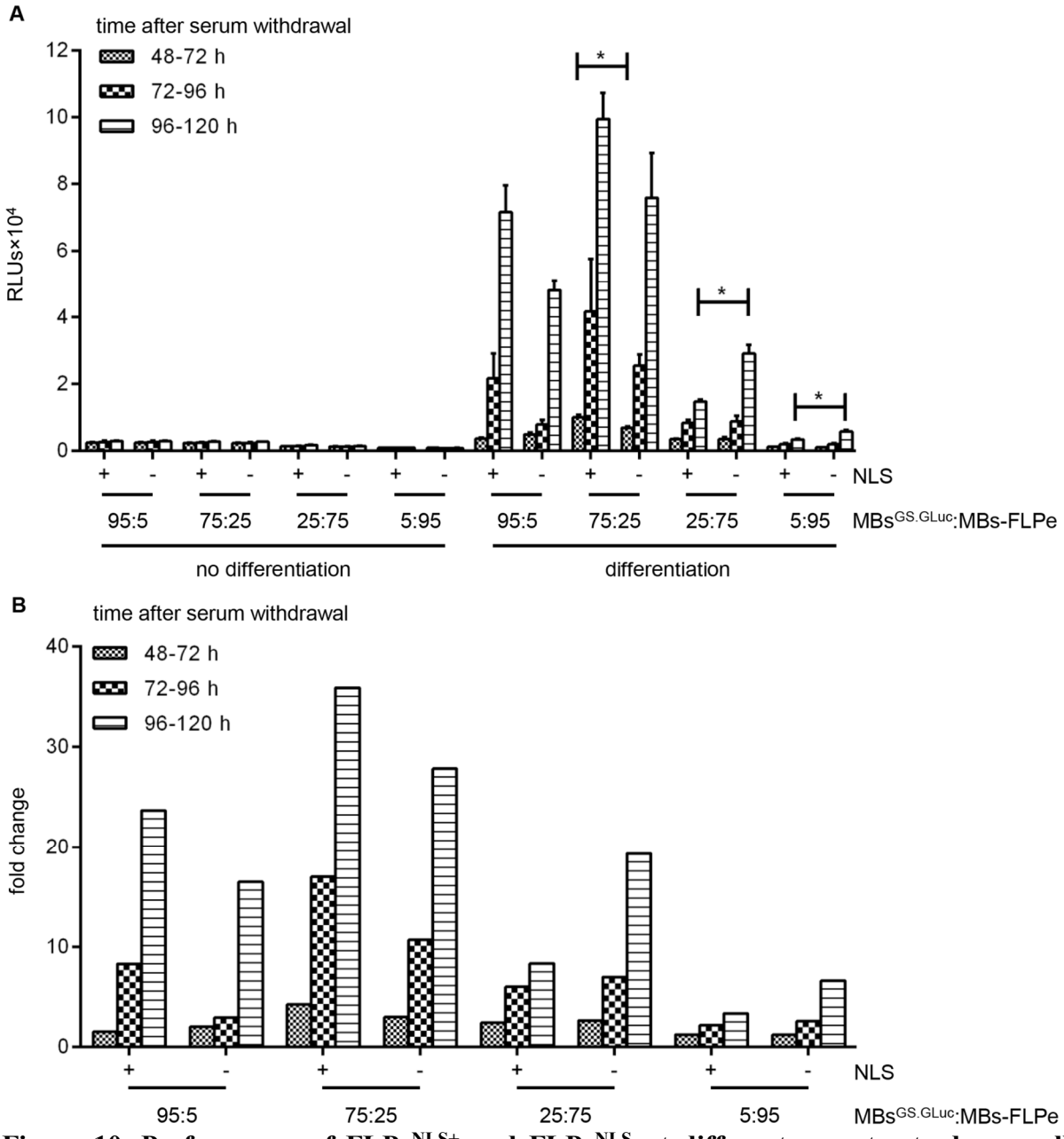

Figure 10. Performance of FLPe^{NLS+} and FLPe^{NLS-} at different acceptor-to-donor cell ratios and time points. (A): GpLuc release by proliferating or differentiating co-cultures of myoblasts$^{GS.GLuc}$ and myoblasts-FLPe^{NLS+} (+) or myoblasts-FLPe^{NLS-} (-) at different time intervals after culture initiation. Myoblasts$^{GS.GLuc}$ and myoblasts-FLPe were seeded in different ratios (*i.e.* 95:5%, 75:25%, 25:75% and 5:95%). At 72 h after cell seeding, the culture fluid was replaced by fresh culture medium with (growth conditions, no differentiation) or without (differentiation conditions) serum. Fourthy-eight h later the culture medium was refreshed once again. Twenty-four h later the culture fluid was harvested for luciferase activity measurement and replaced by the same volume of fresh culture medium. This procedure was repeated every 24 h until 120 h after the first medium change. Bars represent mean ± standard error of the mean (n = 3). (B): Fold change in luciferase activity calculated on the basis of the data presented in (A). For each experimental condition the average light production under growth conditions was the denominator and the mean of the RLUs produced under differentiation conditions was the numerator. RLUs, relative light units; MBs$^{GS.GLuc}$, myoblasts$^{GS.GLuc}$; MBs-FLPe, myoblasts-FLPe; NLS, nuclear localization signal.

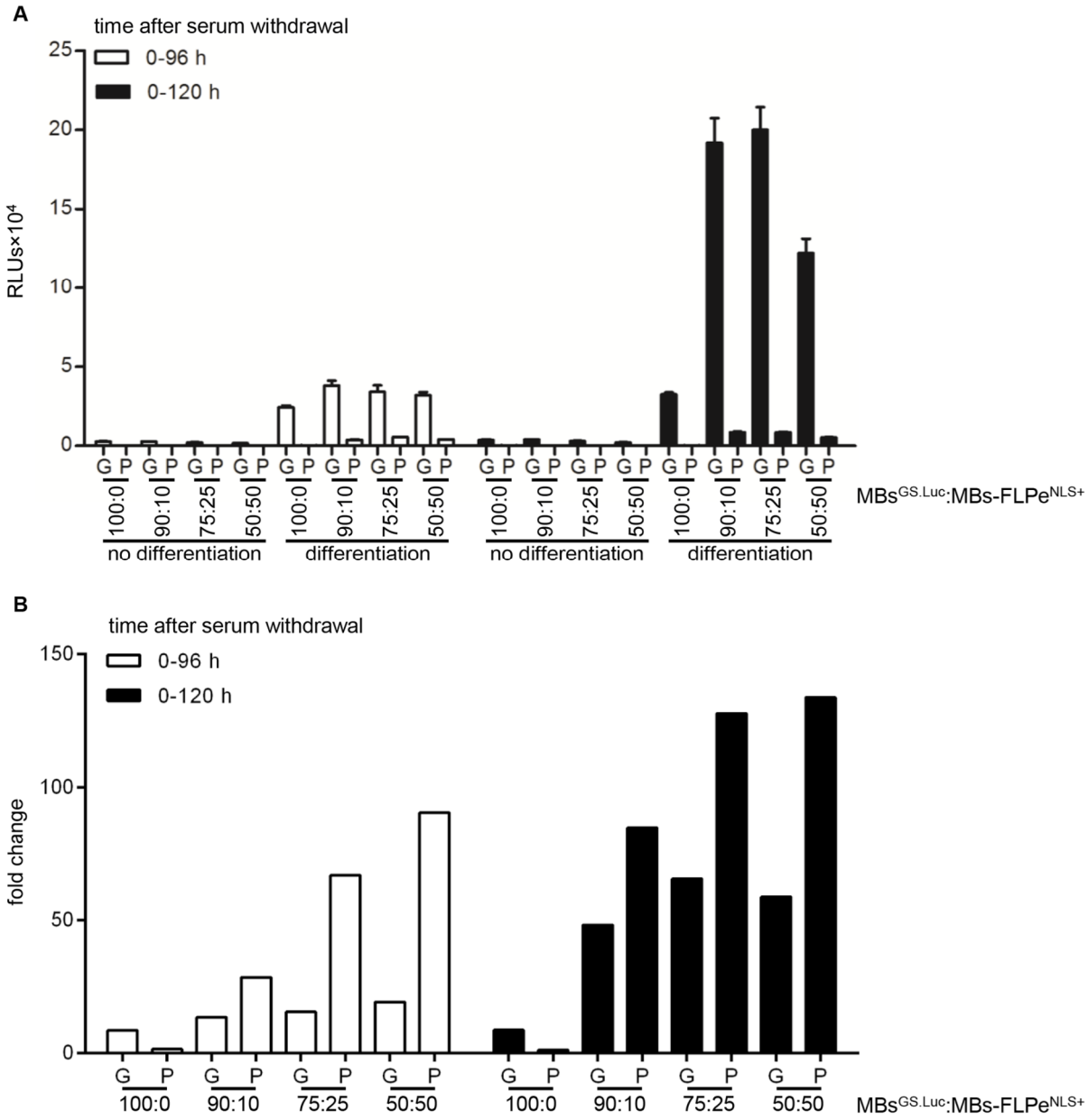

Figure 11. Comparison of LV.GS.GpLuc.v1- and LV.GS.PpLuc-based cell fusion assay systems. (A): GpLuc and PpLuc production by proliferating or differentiating co-cultures of myoblasts$^{GS.GLuc}$ or myoblasts$^{GS.PLuc}$ with myoblasts-FLPe^{NLS+} at different times after culture initiation. Cells were seeded in different ratios (*i.e.* 100:0%, 90:10%, 75:25% and 50:50%). At 72 h after cell seeding the culture fluid was replaced by fresh culture medium with (growth conditions, no differentiation) or without (differentiation conditions) serum. Ninety-six h and 120 h later samples (culture fluid for cultures containing myoblasts$^{GS.GLuc}$ and cell lysates for cultures containing myoblasts$^{GS.PLuc}$) were harvested for luciferase activity measurements. Bars represent mean 6 standard error of the mean (n = 3). (B): Fold change in luciferase activity calculated on the basis of the data presented in (A). For each experimental condition the average light production under growth conditions was the denominator and the mean of the RLUs produced under differentiation conditions was the numerator. RLUs, relative light units; G, LV.GS.GpLuc.v1-based cell fusion assay; P, LV.GS.PpLuc-based cell fusion assay; MBsGS.Luc, myoblasts$^{GS.GLuc}$ or myoblasts$^{GS.PLuc}$; MBs-FLPe^{NLS+}, myoblasts-FLPe^{NLS+}.

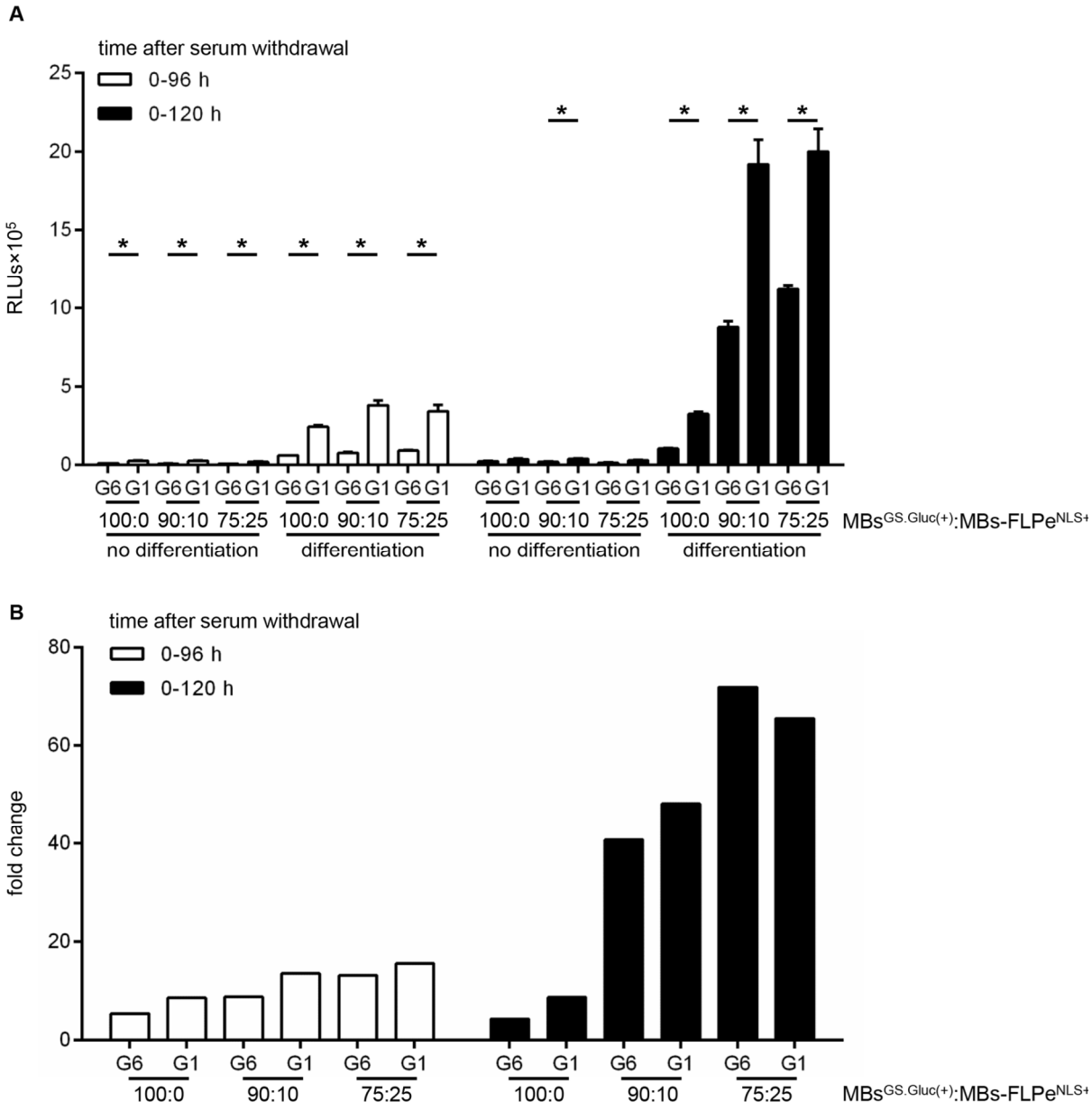

Figure 12. Comparison of LV.GS.GpLuc.v1- and LV.GS.GpLuc.v6-based cell fusion assay systems. (A): GpLuc production by proliferating or differentiating co-cultures of myoblasts$^{GS.GLuc}$ or myoblasts$^{GS.GLuc+}$ with myoblasts-FLPe^{NLS+} at different times after culture initiation. Cells were seeded in different ratios (*i.e.* 100:0%, 90:10% and 75:25%). At 72 h after cell seeding the culture fluid was replaced by fresh culture medium with (growth conditions, no differentiation) or without (differentiation conditions) serum. Ninety-six h and 120 h later culture medium collected for luciferase activity measurement. Bars represent mean ± standard error of the mean (n = 3). (B): Fold change in luciferase activity calculated on the basis of the data presented in (A). For each experimental condition the average light production under growth conditions was the denominator and the mean of the RLUs produced under differentiation conditions was the numerator. RLUs, relative light units; G1, LV.GS.GpLuc.v1-based cell fusion assay; G6, LV.GS.GpLuc.v6-based cell fusion assay; MBs$^{GS.GLuc(+)}$, myoblasts$^{GS.GLuc}$ or myoblasts$^{GS.GLuc+}$; MBs-FLPe^{NLS+}, myoblasts-FLPe^{NLS+}.

Discussion

Apart from being involved in the formation and maintenance of skeletal muscles, bones and the placenta, cell-to-cell fusion plays an important role in numerous other biological processes like fertilization. It has also been implicated in the initiation and progression of cancer [2] and as a driving force in evolution [21]. Moreover, cell-to-cell fusion has been of great value to establish the chromosomal location of specific genes [22], can be used to induce cellular reprogramming [23,24] and is indispensable for generating hybridomas [25]. The involvement of cell-to-cell fusion in a large variety of biological processes and its diverse biotechnological applications have prompted investigations into the mechanisms of cell fusion and the contribution of specific factors to this process. Instrumental to this research is the availability of robust assays to determine cell fusion kinetics and extent. However, most of the existing quantitative cell fusion assays do not allow consecutive analysis of the same cells/tissue. Accordingly, in this paper a new quantitative assay is presented to monitor cell-to-cell fusion. This assay is based on the activation of a latent *GpLuc* gene after fusion of cells containing this latent reporter gene with cells encoding a recombinase that activates the dormant *GpLuc* gene. The extent of cell-to-cell fusion is subsequently quantified by simply measuring the enzymatic activity of the luciferase molecules secreted by the cellular fusion products. To the best of our knowledge this is the first assay that allows quantification of cell fusion activity by medium sampling.

To validate the new cell fusion assay it was used to monitor the formation of myotubes/sacs in cultures of serum-deprived human myoblasts. In these experiments, several parameters were varied including the acceptor-to-donor cell ratio and the sample regimen(s) of the cell culture medium. In general, transgene expression increased with increasing fractions of myoblasts$^{GS.GLuc}$ up to the point at which the number of active/nuclear FLPe molecules became limiting (*i.e.* at myoblast$^{GS.GLuc}$:myoblast-FLPe ratios of 90:10 for FLPe^{NLS-} and of 95:5 for FLPe^{NLS+}; Fig. 7).

At high myoblast$^{GS.GLuc}$:myoblast-FLPe ratios LV.FLPe^{NLS+} was slightly more effective than LV.FLPe^{NLS-} in activating the latent *GpLuc* gene most likely due to fact that under differentiation conditions myoblasts-FLPe^{NLS+} contain ±5-fold more nuclear FLPe molecules than myoblasts-FLPe^{NLS-} (Fig. 5A). In contrast, at low myoblast$^{GS.GLuc}$:myoblast-FLPe ratios (*i.e.* when FLPe is no longer limiting) LV.FLPe^{NLS-} consistently outperformed LV.FLPe^{NLS+} (Figs. 7 and 10). Collectively, these findings suggest that its NLS does not noticeably hamper the spreading of FLPe^{NLS+} through myofibers/sacs but that high nuclear FLPe levels may somehow limit reporter gene expression. A possible explanation for the higher *GpLuc* expression in differentiating cocultures containing large percentages of myoblasts-FLPe^{NLS-} in comparison to those with large fractions of myoblasts-FLPe^{NLS+} may be the more frequent occurrence of secondary recombination events in the latter co-cultures leading to the deactivation of functional *GpLuc* expression modules.

While monocultures of myoblasts$^{GS.GLuc}$ maintained in growth medium displayed very little if any leaky *GpLuc* expression, considerable amounts of GpLuc were produced by myoblast$^{GS.GLuc}$ monocultures exposed to differentiation medium.

There are several possible explanations for this finding. Firstly, growth and differentiation medium may differently affect light output *e.g.* by (i) causing different levels of coelenterazine "auto-oxidation", (ii) containing different concentrations of chemiluminescence inhibi- tors or (iii) absorbing blue light to a different extent. Possibilities (i) and (iii) can be ruled out since mixing of coelenterazine substrate solution with fresh or myoblasts-FLPe^{NLS+}-conditioned growth or differentiation medium produced very similar signals (data not shown). This leaves us with the possibility that transcription termination by the mMT1 pA incorporated into the gene switch constructs is not very efficient or that differentiation conditions somehow stimulate transcription initiation in the region located in between the mMT1 pA and the *Luc* ORFs. For LV.GS.PpLuc and LV.GS.GpLuc.v6 the resulting transcripts may not lead to substantial luciferase production due to the presence of "decoy" ORFs immediately upstream of the *Luc* initiation codons (Figs. 2 and 3). A similar favorable situation does not exist for LV.GS.GpLuc.v1, which may explain the high background signals produced by this construct under differentiation conditions. Even though the luciferase activity in culture medium of differentiating myoblast$^{GS.GLuc+}$ monocultures is ±3-fold lower than in culture medium of differentiating myoblast$^{GS.GLuc}$ monocultures LV.GS.GpLuc.v6 still gives rise to a higher background signal under differentiation conditions than LV.GS.PpLuc (compare Fig. 11 with 12). Considering that the sequences in between the mMT1 pA and the *Luc* start codon in LV.GS.PpLuc and LV.GS.GpLuc.v1 are nearly identical this may suggest that the GpLuc-coding sequence itself is the source of the relatively high luciferase activity detected in medium of differentiating LV.GS.GpLuc monocultures. If so, the problem could be overcome by switching to another secretory luciferase (*e.g. Vargula hilgendorfii luciferase* [26], Lucia luciferase (InvivoGen Europe, Toulouse, France) or secretory NanoLuc [27]). Also the fact that GpLuc is a secretory protein with a long half-life (66 days in culture medium) [28] while Ppluc has a relatively short half-life (±2 hours in cells) [29] may contribute to the higher background signals associated with LV.GS.GpLuc.v1 and LV.GS.GpLuc.v6 than with LV.GS.PpLuc.

Taken together, in this paper a new assay to quantify (the progression of) cell-to-cell fusion activity is described. Due to its nondestructive nature allowing repeated sampling of the same specimen, this assay will be an attractive alternative to existing quantitative cell fusion assays based on (i) light microscopic assessment of multinucleation, (ii) fluorescence dequenching, (iii) fluorescence resonance energy transfer, (iv) biochemical complementation or (v) activation of reporter genes different from *GpLuc* including *LacZ* and *PpLuc* [3]. Other advantages of the LV.FLPe$^{NLS+/-}$.PurR/LV.GS.GpLuc-based cell fusion assay include the simplicity and speed of the analytical procedures and the ability to combine it with (immuno)cytology, real-time microscopy, cell function assays and other methods to study cell behavior.

The sensitivity of the current assay could be improved by changing the human *glyceraldehyde 3-phosphate dehydrogenase* (*hGAPDH*) gene promoter driving *GpLuc* expression for a promoter with higher activity in the cell type(s) under investigation. In addition, the sequences interspersed between the 39 long terminal repeat (LTR) and the *GpLuc* initiation codon of LV.GS.GpLuc.v6 may be further optimized to minimize leaky *GpLuc* expression.

Acknowledgments

The authors thank Martijn Rabelink (Department of Molecular Cell Biology, Leiden University Medical Center) for titrating the LV preparations.

References

1. Shinn-Thomas JH, Mohler WA (2011) New insights into the mechanisms and roles of cell-cell fusion. Int Rev Cell Mol Biol 289: 149-209.
2. Lu X, Kang Y (2009) Cell fusion as a hidden force in tumor progression. Cancer Res 69: 8536-8539.
3. Shinn-Thomas JH, Scranton VL, Mohler WA (2008) Quantitative assays for cell fusion. Methods Mol Biol 475: 347-361.
4. Mohler WA, Blau HM (1996) Gene expression and cell fusion analyzed by lacZ complementation in mammalian cells. Proc Natl Acad Sci USA 93: 12423–12427.
5. Holkers M, de Vries AA, Gonc¸alves MA (2006) Modular and excisable molecular switch for the induction of gene expression by the yeast FLP recombinase. Biotechniques 41: 711-713.
6. Turan S, Bode J (2011) Site-specific recombinases: from tag-and-target- to tagand-exchange-based genomic modifications. FASEB J 25: 4088-4107.
7. Gonc¸alves MA, Janssen JM, Holkers M, de Vries AA (2010) Rapid and sensitive lentivirus vector-based conditional gene expression assay to monitor and quantify cell fusion activity. PLoS One 5: e10954.
8. Tannous BA, Kim DE, Fernandez JL, Weissleder R, Breakefield XO (2005) Codon-optimized Gaussia luciferase cDNA for mammalian gene expression in culture and in vivo. Mol Ther 11: 435-443.
9. Sambrook J, Russell DW (2001) Molecular cloning: a laboratory manual. New York: Cold Spring Harbor Laboratory Press.
10. van Nierop GP, de Vries AA, Holkers M, Vrijsen KR, Gonc¸alves MA (2009) Stimulation of homology-directed gene targeting at an endogenous human locus by a nicking endonuclease. Nucleic Acids Res 37: 5725-5736.
11. Feng T, Li Z, Jiang W, Breyer B, Zhou L, *et al*. (2002) Increased efficiency of cloning large DNA fragments using a lower copy number plasmid. Biotechniques 32: 992, 994, 996 passim.
12. Pastrana DV, Tolstov YL, Becker JC, Moore PS, Chang Y, *et al*. (2009) Quantitation of human seroresponsiveness to Merkel cell polyomavirus. PLoS Pathog 5: e1000578.
13. Cudre´-Mauroux C, Occhiodoro T, KÖnig S, Salmon P, Bernheim L, *et al*. (2003) Lentivector-mediated transfer of Bmi-1 and telomerase in muscle satellite cells yields a Duchenne myoblast cell line with long-term genotypic and phenotypic stability. Hum Gene Ther 14: 1525-1533.
14. Uil TG, de Vrij J, Vellinga J, Rabelink MJ, Cramer SJ, et al. (2009) A lentiviral vector-based adenovirus fiber-pseudotyping approach for expedited functional assessment of candidate retargeted fibers. J Gene Med 11: 990-1004.
15. Ramkisoensing AA, Pijnappels DA, Swildens J, Goumans MJ, Fibbe WE, et al. (2012) Gap junctional coupling with cardiomyocytes is necessary but not sufficient for cardiomyogenic differentiation of cocultured human mesenchymal stem cells. Stem Cells 30: 1236-1245.
16. Ramkisoensing AA, de Vries AA, Schalij MJ, Atsma DE, Pijnappels DA (2012) Brief report: Misinterpretation of coculture differentiation experiments by unintended

labeling of cardiomyocytes through secondary transduction: delusions and solutions. Stem Cells 30: 2830-2834.
17. Suzuki K, Bose P, Leong-Quong RY, Fujita DJ, Riabowol K (2010) REAP: A two minute cell fractionation method. BMC Res Notes 3: 294.
18. Gonda DK, Bachmair A, Wu¨nning I, Tobias JW, Lane WS, et al. (1989) Universality and structure of the N-end rule. J Biol Chem 264: 16700-16712.
19. Kozak M (1986) Point mutations define a sequence flanking the AUG initiator codon that modulates translation by eukaryotic ribosomes. Cell 44: 283-292.
20. McCaughan KK, Brown CM, Dalphin ME, Berry MJ, Tate WP (1995) Translational termination efficiency in mammals is influenced by the base following the stop codon. Proc Natl Acad Sci USA 92: 5431-5435.
21. Sinkovics JG (2011) Horizontal gene transfers with or without cell fusions in all categories of the living matter. Adv Exp Med Biol 714: 5-89.
22. Grzeschik KH (1986) The role of somatic cell genetics in human gene mapping. Experientia 42: 1128-1137.
23. Sanges D, Lluis F, Cosma MP (2011) Cell-fusion-mediated reprogramming: pluripotency or transdifferentiation? Implications for regenerative medicine. Adv Exp Med Biol 713: 137-159.
24. Serov OL, Matveeva NM, Khabarova AA (2011) Reprogramming mediated by cell fusion technology. Int Rev Cell Mol Biol 291: 155-190.
25. Ko¨hler G, Milstein C (1975) Continuous cultures of fused cells secreting antibody of predefined specificity. Nature 256: 495-497.
26. Maguire CA, Bovenberg MS, Crommentuijn MH, Niers JM, Kerami M, et al. (2013) Triple bioluminescence imaging for in vivo monitoring of cellular processes. Mol Ther Nucleic Acids 2: e99.
27. Hall MP, Unch J, Binkowski BF, Valley MP, Butler BL, et al. (2012) Engineered luciferase reporter from a deep sea shrimp utilizing a novel imidazopyrazinone substrate. ACS Chem Biol 7: 1848-1857.
28. Tannous BA (2009) Gaussia luciferase reporter assay for monitoring biological processes in culture and in vivo. Nat Protoc 4: 582-591.
29. Ignowski JM, Schaffer DV (2004) Kinetic analysis and modeling of firefly luciferase as a quantitative reporter gene in live mammalian cells. Biotechnol Bioeng 86: 827-834.

Chapter 4

Generation and primary characterization of iAM-1, conditionally immortalized atrial myocytes with preserved cardiomyogenic differentiation capacity

Liu J, Volkers L, Jangsangthong W, Bart CI, Engels MC, Zhou G, Schalij MJ, Ypey DL, Pijnappels DA, de Vries AAF

Adapted from: Cardiovasc Res. 2018. doi: 10.1093/cvr/cvy134.

Abstract

Aims: The generation of homogeneous cardiomyocyte populations from fresh tissue or stem cells is laborious and costly. A potential solution to this problem would be to establish lines of immortalized cardiomyocytes. However, as proliferation and (terminal) differentiation of cardiomyocytes are mutually exclusively processes, their permanent immortalization causes loss of electrical and mechanical functions. We therefore aimed at developing conditionally immortalized atrial myocyte (iAM) lines allowing toggling between proliferative and contractile phenotypes by a single-component change in culture medium composition.

Methods and results: Freshly isolated neonatal rat atrial cardiomyocytes (AMs) were transduced with a lentiviral vector conferring doxycycline-controlled expression of simian virus 40 large T antigen. Under proliferative conditions (*i.e.* in the presence of doxycycline), the resulting cells lost most cardiomyocyte traits and doubled every 38 hours. Under differentiation conditions (*i.e.* in the absence of doxycycline), the cells stopped dividing and spontaneously reacquired a phenotype very similar to that of primary AMs in gene expression profile, sarcomeric organization, contractile behaviour, electrical properties and response to ion channel-modulating compounds (as assessed by patch-clamp and optical voltage mapping). Moreover, differentiated iAMs had much narrower action potentials and propagated them at >10-fold higher speeds than the widely used murine atrial HL-1 cells. High-frequency electrical stimulation of confluent monolayers of differentiated iAMs resulted in reentrant conduction resembling atrial fibrillation, which could be terminated by tertiapin treatment, just like in monolayers of primary AMs.

Conclusion: Through controlled expansion and differentiation of AMs, large numbers of functional cardiomyocytes were generated with properties far superior to the differentiated progeny of existing cardiomyocyte lines. iAMs provide an attractive new model system for studying cardiomyocyte proliferation, differentiation, metabolism and (electro)physiology and to investigate cardiac diseases, regeneration and drug responses, without using animals.

Nonstandard abbreviations and acronyms

AMs	neonatal rat atrial cardiomyocytes
AF	atrial fibrillation
ANP	atrial natriuretic peptide
AP	action potential
APD	action potential duration
CV	conduction velocity
Cx43	connexin 43
dox	doxycycline
eGFP	enhanced green fluorescent protein
iAMs	conditionally immortalized AMs
IFM	immunofluorescence microscopy
LT	large T
LUMC	Leiden University Medical Center
LV	lentiviral vector
Mlc2a	atrial regulatory myosin light chain
Mlc2v	ventricular regulatory myosin light chain
pAMs	primary AMs
pVMs	primary neonatal rat ventricular cardiomyocytes
PSC-CMCs	cardiomyocytes derived from pluripotent stem cells
RMP	resting membrane potential
RT-qPCR	reverse transcription-quantitative polymerase chain reaction
SV40	simian virus 40

Introduction

Due to the limited availability of human heart tissue and the low mitotic activity of postnatal human cardiomyocytes, cardiac research has strongly relied on experiments in animals[1,2] or with primary cardiomyocytes of animal origin[3,4]. The increasing opposition to the use of animals for biomedical research has fuelled the search for alternative models of human cardiac disease.

Recently, cardiomyocytes derived from pluripotent stem cells (PSC-CMCs) have emerged as new models for studying different aspects of cardiac disease. Despite the great potential of PSC-CMCs as cardiac model systems, they have some serious drawbacks that need to be overcome before becoming a practical alternative to the use of laboratory animals. Both the generation of PSCs and the production of homogeneous populations of cardiomyocytes from these cells is a laborious, time-consuming and costly endeavour of varying efficiency, which requires properly timed treatment of the starting material with different cocktails of expensive growth factors and small molecules[5]. Moreover, PSCs greatly differ in their ability to differentiate into cardiomyocytes and typically yield phenotypically heterogeneous populations of immature cardiac muscle cells[6,7]. The latter feature is limiting the use of PSC-CMCs in studying cardiac physiology and pathology, *e.g.* it has been proven difficult to establish homogeneous (confluent) monolayers of these cells for cardiac arrhythmia research by high-resolution optical mapping[8].

As another approach to reduce laboratory animal use in cardiac research, cardiomyocyte lines have been generated using cardiac muscle cells from rodents and humans as starting material and the simian virus 40 (SV40) large T (LT) antigen to induce cell proliferation[9-15]. Unfortunately, all cardiomyocyte lines generated thus far, including the widely used HL-1 cell line, display large structural and functional deficits in comparison to the primary cells from which they were derived.

In an attempt to overcome the paucity of cell lines with robust cardiomyogenic differentiation capacity, we developed a new strategy to selectively and conditionally immortalize cardiomyocytes. Given our special interest in atrial fibrillation (AF) as the most common heart rhythm disorder in clinical practice[16], the recent discovery by members of our research group that neonatal rat atrial cardiomyocytes (AMs) possess a constitutively active acetylcholine-dependent K^+ current playing an important role in the development of AF[17] and the relatively low cell yields obtained from enzymatically dissociated neonatal rat atria, AMs were chosen as starting material. These cells were transduced with a single lentiviral vector (LV) allowing myocyte-restricted doxycycline (dox)/tetracycline-dependent LT expression followed by their clonal expansion in the presence of dox. The resulting monoclonal cell lines were characterized by cell proliferation assays, reverse transcription-quantitative polymerase chain reaction (RT-qPCR) analysis, phase-contrast and immunofluorescence microscopy (IFM), western blotting, optical voltage mapping The response of the cells to cardiac ion channel inhibitors and their ability to integrate with pAMs were also investigated. Altogether, our data show that we have generated cardiomyocyte lines that (i) outperform all existing lines of cardiac muscle cells in terms of cardiomyogenic differentiation ability, (ii) have great potential as models for fundamental and applied cardiac research and (iii) depending on the specific

application, may provide easy-to-use and cost-effective alternatives for PSC-CMCs and for cardiomyocytes freshly isolated from animals.

Methods

Detailed methods are available in Supplementary material online.

Animal experiments

All animal experiments were approved by the Animal Experiments Committee of Leiden University Medical Center (LUMC) and conformed to the Guide for the Care and Use of Laboratory Animals as stated by the US National Institutes of Health.

Cardiac cell culture

Neonatal rat cardiomyocytes were isolated and cultured essentially as described[18].

LV production

LV particles were produced using a previously published method[18]. The molecular structure of the shuttle plasmid used for the production of the LT-encoding LV is depicted in *Figure 1A*.

Molecular analyses

The primer pairs used for transcriptome analysis by RT-qPCR are shown in *Table S1* (see Supplementary material online).

Details about the antibodies used for western blotting and immunostaining of formaldehyde-fixed cells are presented in *Table S2* (see Supplementary material online).

Apoptosis was studied using Alexa Fluor-568-conjugated annexin V.

Electrophysiological studies

Optical voltage mapping using di-4-ANEPPS as fluorescent voltage indicator was performed essentially as described previously[19]. A detailed description of the whole-cell patch-clamp studies can be found in the Supplementary material online.

Statistical analyses

Data were derived from a specified number (N) of observations from 3 different cell cultures. Unless otherwise stated, data were expressed as mean±standard deviation (SD) and SDs were represented by error bars. All data were analysed with the nested ANOVA test using the Real Statistics Resource Pack software (release 5.1, copyright 2013 – 2017, Charles Zaiontz, www.real-statistics.com). For comparisons involving >2 experimental groups, this test was followed by Bonferroni *post-hoc* analysis. Results were considered statistically significant at P values <0.05. Statistical significance was expressed as follows: *: P<0.05, **: P<0.01, ***: P<0.001, ****: P<0.0001.

Results

Conditional immortalization of AMs

Low-density cardiomyocyte-enriched cultures of primary cells isolated from the atria of 2-day-old Wistar rats were transduced with LV particles containing a dox-inducible LT expression unit based on the monopartite lentiviral Tet-on system developed by Szulc *et al.*[20]. LT expression in this LV system was driven by the strong hybrid striated muscle-specific MHCK7 promoter[21] (*Figure 1A*) to minimize the likelihood of inadvertently immortalizing the ±12% non-cardiomyocytes present in the primary atrial cell cultures[17] (data not shown).

In the presence of dox, cells started to divide forming clearly discernible colonies at 1-3 weeks post-transduction (*Figure 1B*). Nine of >80 cell clones were randomly selected for testing the dox dependency of their proliferation ability. Cells of all 9 clones were actively dividing in the presence of dox and stopped doing so in its absence. To investigate whether these clones contained excitable cells, confluent monolayers were established, maintained in dox-free culture medium for 9 days and examined by optical voltage mapping. Following 1-Hz electrical stimulation, 7 of the 9 clones produced excitatory waves spreading from the pacing electrode to the opposite site of the culture dishes. Of these 7 clones, clone #5 showed the shortest action potential (AP) duration (APD) and highest conduction velocity (CV) and was therefore picked for further investigation. Western blot analysis and IFM showed expression of LT in this clone to be tightly and effectively controlled by dox (*Figure 1C-E*).

Comparison of the light microscopic morphology of the conditionally immortalized AMs (iAMs) with those of primary AMs (pAMs) revealed that the surface area of proliferating iAMs did not significantly differ from that of pAMs at culture day 1 (*Figure 2A and E*). Also, in near-confluent monolayers, iAMs that were kept for 9 days in dox-free medium closely resembled pAMs at culture day 9 in both size and appearance (*Figure 2A*).

In the presence of dox, 72.2±8.1% of iAMs stained positive for the proliferation marker Ki-67, which percentage dramatically decreased upon dox removal (*Figure 2B and F*). Consistently, in the presence of dox, iAMs proliferated with an average doubling time of 38 h, whereas under differentiation conditions (*i.e.* in the absence of dox), the cell number slightly decreased with time (*Figure 2G*). As expected, in primary atrial cell cultures, the percentage of α-actinin$^+$ cells expressing Ki-67 was very low indicating that the large majority of proliferating Ki-67$^+$ cells in these cultures are non-cardiomyocytes (*Figure 2C and F*). Probing iAM cultures with fluorescently labelled annexin V for the presence of surface-exposed phosphatidylserine as marker of apoptosis revealed low signals in proliferating cultures, which slightly increased under differentiation conditions (*Figure 2D and H*) but did not noticeably differ from those in 9-day-old pAM cultures (*Figure 2D and H*).

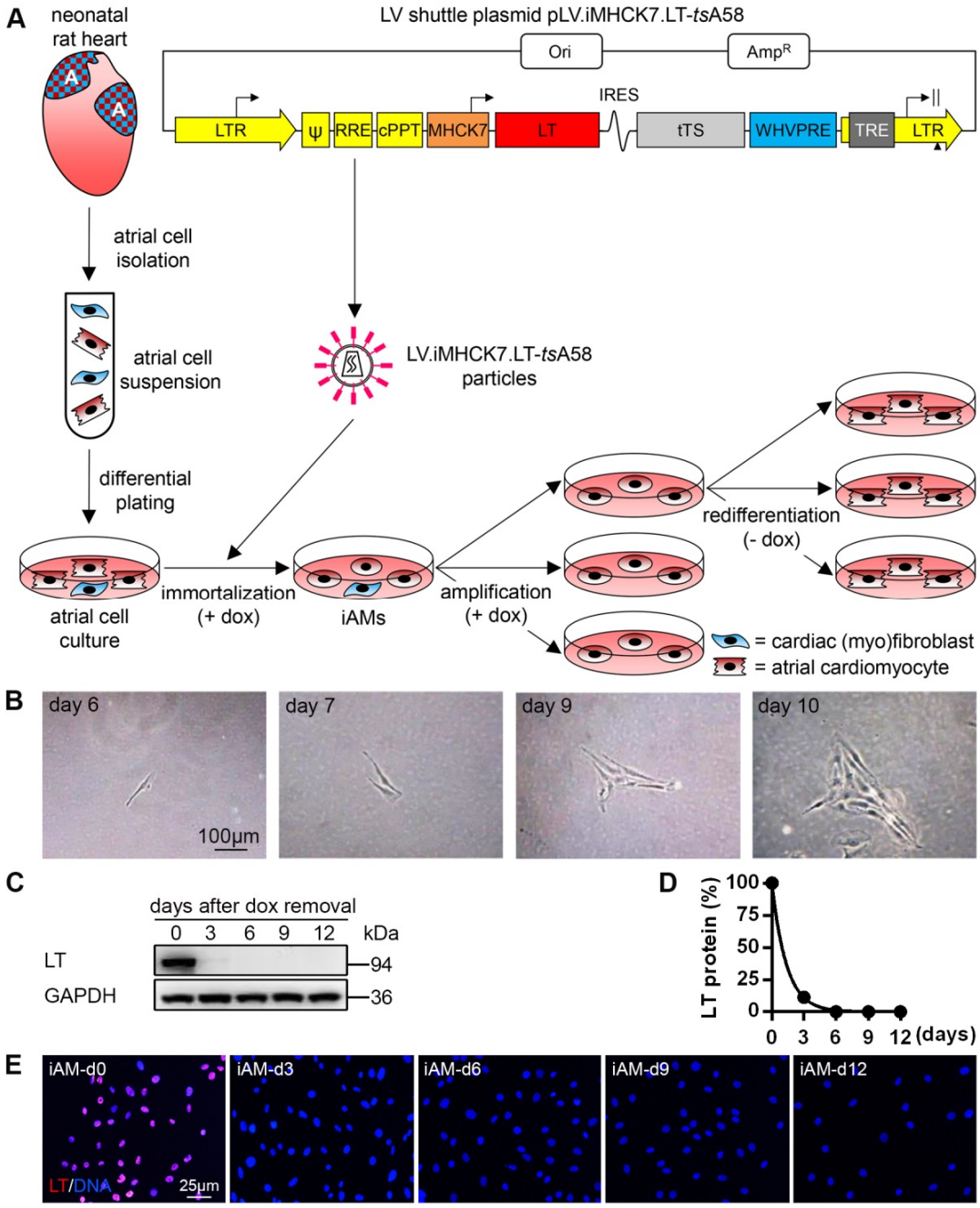

Figure 1. Conditional immortalization of pAMs. (*A*) Scheme of the procedure used for the reversible immortalization, amplification and subsequent redifferentiation of pAMs. A, atrium. Ori, bacterial origin of replication. Amp^R, *Escherichia coli* ß-lactamase gene. LTR, human immunodeficiency virus type 1 (HIV1) long terminal repeat. Ψ, HIV1 packaging signal. RRE, HIV1 Rev-responsive element. cPPT, HIV1 central polypurine tract and termination site. MHCK7, chimeric striated muscle-specific promoter[21]. LT, coding sequence of the temperature-sensitive mutant LT protein *ts*A58[33]. IRES, encephalomyocarditis virus internal ribosome entry site. tTS, coding sequence of the hybrid tetracycline-controlled transcriptional repressor TetR-KRAB[34]. WHVPRE, woodchuck hepatitis virus posttranscriptional regulatory element. TRE, tetracycline-responsive promoter element consisting of 7 repeats of a 19 nucleotide tetracycline operator (*tetO*) sequence. (*B*) Bright-field images of a single cell in a pAM culture showing dox-dependent clonal expansion. (*C-E*) Analysis by western blotting (*C, D*) and immunocytology (*E*) of LT protein expression in iAM cultures before (day 0) and 3, 6, 9 and 12 days after dox removal.

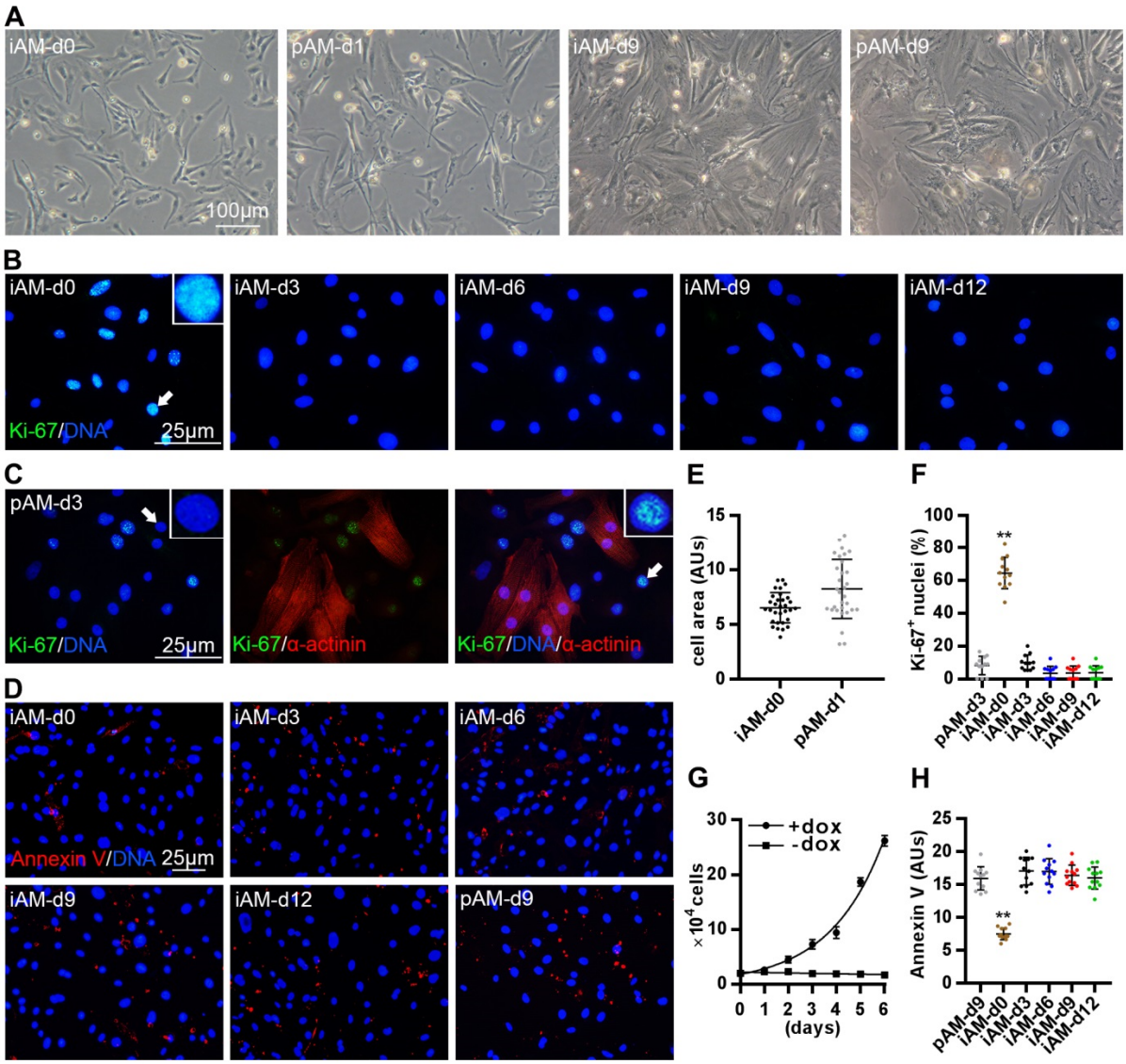

Figure 2. Morphology, proliferative activity and apoptosis analysis of iAMs. (*A*) Bright-field images of proliferating iAMs (*i.e.* iAM-d0) and iAM-d9 and of pAMs at culture day 1 (pAM-d1) and 9 (pAM-d9). (*B*) Fluorescence images of proliferating iAMs and of iAMs at different days after dox removal immunostained for the proliferation marker Ki-67. The arrow is pointing at the nucleus shown at a higher magnification in the inset. (*C*) Fluoromicrograph of a 3-day-old pAM (pAM-d3) culture that was not subjected to mitomycin C treatment following double immunostaining for Ki-67 and sarcomeric α-actinin. The Ki-67^{+}/α-actinin^{-} cells observed in this culture mainly result from uninhibited proliferation of cardiac fibroblasts (data not shown). Arrows are pointing at the nuclei shown at a higher magnification in the insets. (*D*) Fluorescence images of proliferating iAMs, of iAMs at different days after dox removal and of a 9-day-old, mitomycin C-treated pAM (pAM-d9) culture labelled with Alexa Fluor-568-conjugated annexin V to assess externalization of phosphatidylserine as indicator of apoptosis. (*E*) Quantification of cell surface area of iAM-d0 and of pAM-d1. Data are presented as mean±SD, N=30 cells per experimental group, each consisting of 3 cell preparations. For statistical analysis, the nested ANOVA test was used. (*F*) Graph showing the percentage of Ki-67^{+} nuclei in proliferating iAM cultures, in iAM cultures at different days after dox removal and among the cardiomyocytes (*i.e.* α-actinin^{+} cells) in pAM-d3 cultures. Data are presented as mean±SD, N=12 cell cultures per experimental group from 3 individual preparations. Statistics was done

using the nested ANOVA test with Bonferroni *post-hoc* correction. (*G*) Quantification of cell numbers in iAM cultures with or without dox. Data are presented as mean±SD, N=3. (*H*) Quantification of cell surface-bound annexin V in proliferating iAM cultures, in iAM cultures at different days after dox removal and in mitomycin C-treated pAM-d9 cultures. Data are presented as mean±SD, N=12 cell cultures per experimental group from 3 individual preparations. Statistics was done using the nested ANOVA test with Bonferroni *post-hoc* correction. AUs, arbitrary units. $^{**}P<0.01$ vs pAM cultures.

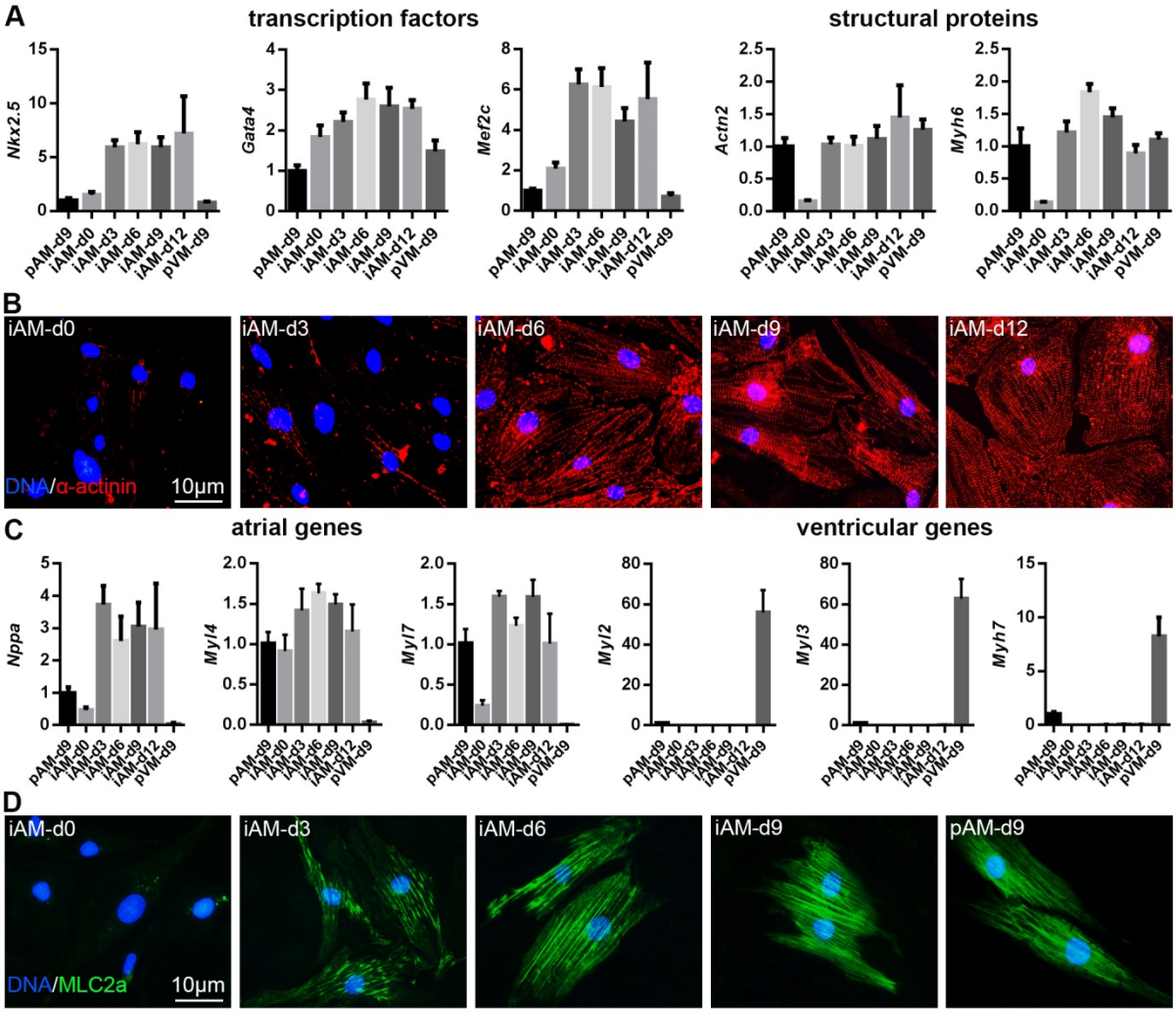

Figure 3. Cardiomyogenic differentiation potential of iAMs. (*A, C***)** Analysis by RT-qPCR of the expression of the cardiac transcription factor genes *Nkx2.5*, *Gata4* and *Mef2c*, the cardiac sarcomeric protein genes *Actn2* and *Myh6* **(***A***),** the "atrial" genes *Nppa*, *Myl4* and *Myl7* and the "ventricular" genes *Myl2*, *Myl3* and *Myh7* **(***C***)** in pAMs and pVMs at day 9 of culture and in iAMs on the indicated days of differentiation. mRNA levels are expressed relative to those in 9-day-old pAM (pAM-d9) cultures, which were set at 1. Data are presented as mean±SD, N=3. The low abundance of "atrial" transcripts in pAM samples is most likely due to the presence of some ventricular myocytes in these samples. Similarly, the pVM cultures may have contained low numbers of atrial myocytes. Alternatively, pAMs may express "ventricular" genes at low levels and pVMs may display low-level expression of "atrial" genes. (*B, D*) Fluorescence images of proliferating iAMs and of iAMs at different days after dox removal immunostained for sarcomeric α-actinin (red, *B*) or the atrial regulatory myosin light chain MLC2a (green, *D*). pAMs and pVMs at culture day 9 served as positive and negative control for the MLC2a immunostaining, respectively. Cell nuclei have been visualized by staining with Hoechst 33342 (blue).

Cardiomyogenic differentiation potential of iAMs

The expression of cardiac marker genes in proliferating and differentiating iAM cultures was assessed by RT-qPCR analysis and compared with that of pAMs and of primary neonatal rat ventricular cardiomyocytes (pVMs) at culture day 9. Previous experience has shown that at this particular time point, the primary cardiomyocytes are optimally adapted to the *in vitro* environment and still in an advanced state of differentiation[17-19,22,23]. Expression of the *Nkx2.5*, *Gata4* and *Mef2c* genes, which encode early cardiac transcriptional regulators, was higher in proliferating (*i.e.* day 0) iAMs than in pAMs and pVMs and rapidly increased soon after dox removal (*Figure 2A*). Expression of the sarcomeric protein-encoding *Actn2* and *Myh6* genes, on the other hand, was lower in day 0 iAMs than in pAMs and s. Transcription of these genes also showed a rapid increase under differentiation conditions to very similar levels as in pAMs and pVMs (*Figure 3A*).

To study myofibrillogenesis, cells were immunostained for sarcomeric α-actinin (*Figure 3B*). At the immortalized stage, α-actinin expression in iAMs was low and in most cells the protein was diffusely spread throughout the cytoplasm. However, in a few cells, α-actinin showed a punctate staining pattern with the protein clustering in spherical or short elongated structures. At day 3 of differentiation, α-actinin formed longer structures with a dot-like appearance reminiscent of immature myofibrils. Myofibril assembly nearly reached completion at day 6 after dox removal, with most of the α-actinin displaying the Z-line staining pattern typical of cardiomyocytes. At the later stages of differentiation (*i.e.* at days 9 and 12 after dox removal), myofibrils underwent further maturation resulting in cells with highly organized sarcomeres.

After dox removal, mRNA levels of the atrial natriuretic peptide (ANP)-encoding *Nppa* gene, the atrial essential myosin light chain-encoding *Myl4* gene and the atrial regulatory myosin light chain (*i.e.* Mlc2a)-encoding *Myl7* gene were moderately (*Myl4*) to strongly (*Nppa* and *Myl7*) upregulated in iAMs (*Figure 3C*). Moreover, neither in the absence nor in the presence of dox, iAMs expressed detectable amounts of transcripts encoding ventricular regulatory myosin light chain (*i.e.* Mlc2v; *Myl2* gene), ventricular essential myosin light chain (*Myl3* gene) or β-myosin heavy chain (*Myh7* gene; *Figure 3C*). The RNA samples of 9-day-old pAM cultures contained high amounts of ‘’atrial” mRNA while ”ventricular” transcripts were barely detectable in these samples (*Figure 3C*). For the RNA samples from the 9-day-old pVM cultures the opposite was true, *i.e.* they contained high amounts of *Myl2*, *Myl3* and *Myh7* transcripts but hardly any *Nppa*, *Myl4* or *Myl7* mRNA (*Figure 3C*). Collectively, these data indicate that iAMs reacquire properties of atrial rather than ventricular cardiomyocytes when cultured in dox-free medium (*Figure 3C*). Mlc2a immunostaining confirmed these findings and showed gradual incorporation of this protein into sarcomeres indiscernible from those in pAMs that had been cultured for 9 days (*Figure 3D*). iAMs started to exhibit spontaneous contractions from day 6 of differentiation (Supplementary material online, *Movie I*) demonstrating sarcomere functionality. The immunostainings for α-actinin and Mlc2a also revealed that the spontaneous differentiation of iAMs in the absence of dox is a highly synchronous event occurring in essentially all cells at approximately the same time.

Electrophysiological properties of iAMs

RT-qPCRs targeting genes encoding cardiac ion channels showed an increase in the mRNA levels of *Scn5a*/$Na_v1.5$, *Cacna1c*/$Ca_v1.2$, *Kcnj3*/$K_{ir}3.1$, *Kcnj5*/$K_{ir}3.4$ and *Kcnj11*/$K_{ir}6.2$ during the early stages of iAM differentiation, which, later in the differentiation process, dropped to approximately equal levels as in pAMs at culture day 9 (Supplementary material online, *Figure S1A-E*). A similar differentiation-dependent trend in expression levels was observed for *Kcnd3*/$K_v4.3$ and *Kcnh2*/$K_v11.1$ but in these cases transcript levels at the late stages of iAM differentiation were higher than those in day 9 pAMs (Supplementary material online, *Figure S1F and G*). The iAMs did not express detectable amounts of *Kcnj2*/$K_{ir}2.1$ at any stage in the differentiation process in contrast to pAMs that had been cultured for 9 days (Supplementary material online, *Figure S1H*). However, *Kcnj2* expression in pAMs was much lower than in pVMs at culture day 9. Transcript levels of the pacemaker channel genes *Hcn2* and *Hcn4* showed dynamic changes during the cardiomyogenic differentiation of iAMs (Supplementary material online, *Figure S1I* and *J*). Proliferating iAMs expressed more *Hcn2* mRNA than pAMs at day 9 of culture but this difference largely disappeared following 12 days of cardiomyogenic differentiation of the iAMs. The *Hcn4* mRNA level in proliferating iAMs was lower than in pAMs at culture day 9 but showed a gradual increase during the first 9 days of iAM differentiation to suddenly drop afterwards. RT-qPCR analysis of *Ryr2* and *Atp2a2*/Serca2 transcripts showed an increase in the expression of these Ca^{2+}-handling protein genes early during iAM differentiation. From day 3 of differentiation onwards, *Ryr2* and *Atp2a2* mRNA levels in iAMs remained constant and were very similar (*Ryr2*) or 2- to 3-fold higher (*Atp2a2*) than in pAMs at culture day 9 (Supplementary material online, *Figure S1K* and *L*).

Since spreading of APs through cardiac tissue critically depends on the presence of intercellular conduits, iAM cultures at different stages of differentiation were immunostained for the gap junction protein connexin 43 (Cx43). As shown in *Figure 4A*, Cx43 was first observed in iAMs at 3 days after dox removal and its amounts gradually increased as the cells further differentiated. Initially, Cx43 was mainly detected in the perinuclear region (*i.e.* at the site of biosynthesis) but at days 9 of differentiation, most Cx43 was found in punctate patterns at the interfaces between iAMs. To investigate the functionality of these gap junctional plaques, confluent monolayers of differentiated iAMs were subjected to 1-Hz electrical point stimulation, which caused the cells to contract at the pacing frequency (Supplementary material online, *Movie II*). This result was corroborated by optical voltage mapping, which showed uniform radial spreading of excitatory waves from the site of electrical point stimulation in iAM cultures at day 9 of differentiation (Supplementary material online, *Movie III*). Additional optical voltage mapping experiments revealed a gradual increase in CV (*Figure 4B* and *D*; Supplementary material online, *Movie III*) and decrease in APD (*Figure 4C, E* and *F*) with ongoing iAM differentiation. As a matter of fact, CV and APD at 30 and 80% repolarization (APD_{30} and APD_{80}, respectively) did not significantly differ between iAM cultures at differentiation days 9 and 12 and 9-day-old pAM cultures. These data suggest that upon dox removal, iAMs differentiate into AMs with electrophysiological properties strongly resembling those of pAMs.

To investigate the ionic basis of the similar electrophysiological properties of pAMs and cardiomyogenically differentiated iAMs as measured by optical voltage, we conducted patch-clamp experiments on these cardiomyocytes. The resting membrane potentials (RMP) of pAMs and iAMs in monolayer culture did not significantly differ (-64.5±1.2 mV, N=15 vs -67.5±1.6 mV, N=13), while single-cell recordings showed pAMs to have a more negative RMP (-62.8±1.8 mV, N=14) than iAMs (-46.0±1.9 mV, N=27; Supplementary material online, Figure S2A). In spite of the measured difference in RMP between single pAMs and single iAMs, both cell types were excitable and produced APs with very similar characteristics under the same stimulation conditions (Supplementary material online, Figure S2B and Table S3). Of all the AP parameters assessed only the upstroke velocity and the overshoot were somewhat smaller for the iAMs in comparison to the pAMs (Supplementary material online, Table S3). In voltage-clamp experiments, we found that the main membrane current responsible for the excitability of both cell types is a fast voltage-activated transient Na+ current (consistent with the expression of Scn5a in these cells, Supplementary material online, Figure S1A), which occurred in these cells as a dominant current component (see Supplementary material online, Figure S2B, D and E). Although these patch-clamp results fit with the optical mapping data, we were puzzled by the similar RMPs for pAM and iAM monolayers, given the undetectable *Kcnj2* expression in cardiomyogenically differentiated iAMs (Supplementary material online, *Figure S1H*) and the presumed difference in the inward rectifier current between pAMs and iAMs (I_{K1}; Supplementary material online, *Figure S2B*). This apparent discrepancy was resolved by showing, with the aid of ouabain, that the electrogenic Na^+/K^+ ATPase plays a vital role in generating hyperpolarized RMPs in both pAMs and iAMs (Supplementary material online, *Figure S3*).

To investigate their ability to form a functional cardiac syncytium with pAMs, iAMs were labelled with enhanced green fluorescent protein (eGFP) by lentiviral transduction. Next, 1:1 co-cultures of pAMs treated at day 1 of culture with mitomycin C and eGFP-labelled iAMs were established and subsequently kept for 8 days in dox-free culture medium. The co-cultures were compared with iAM monocultures at day 9 of differentiation and with 9-day-old, mitomycin C-treated pAM cultures. (Supplementary material online, *Figure S4A*). Cx43 immunostaining of the co-cultures revealed the presence of gap junctions between iAMs and pAMs (Supplementary material online, *Figure S4B*). Optical voltage mapping showed uniform radial spreading of APs from the pacing electrode at roughly the same speed in all 3 culture types (Supplementary material online, *Figure S4C* and *D*) suggesting proper electrical integration of differentiated iAMs in co-cultures with pAMs.

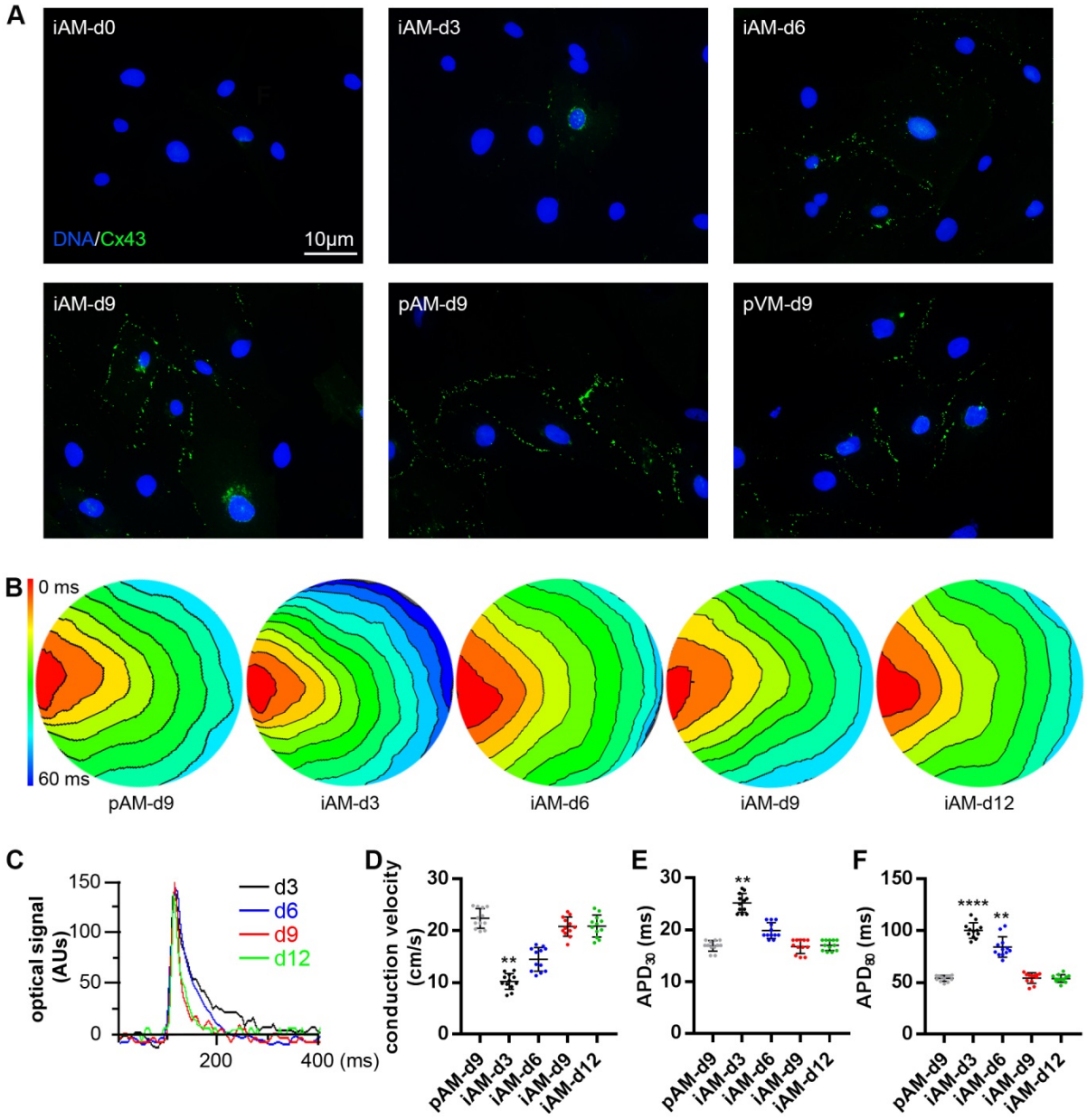

Figure 4. Electrophysiological properties of iAMs. (*A*) Fluorescence images of proliferating iAMs and of iAMs at different days after dox removal immunostained for Cx43 (green) showing its differentiation-dependent accumulation at the sarcolemma in gap junctional plaques. As positive controls for the Cx43 immunostaining, 9-day-old pAM and pVM cultures were included. Hoechst 33342 (blue) staining shows cell nuclei. (*B-F*) Optical voltage mapping of confluent iAM and 9-day-old pAM (pAM-d9) monolayers following 1-Hz electrical point stimulation. (*B, C*) Typical activation maps (*B*; isochrones are separated by 6 ms) and optical signal traces (*C*) of iAM cultures at different days after dox removal showing an increase in CV and a decrease in APD with advancing iAM differentiation. (*D-F*) Quantification of CV (*D*), APD_{30} (*E*) and APD_{80} (*F*) in pAM-d9 cultures and in iAM cultures at 3, 6, 9 and 12 days of differentiation. Data are presented as mean±SD, N=12 cell cultures per experimental group from 3 individual preparations. Statistics was done using the nested ANOVA test with Bonferroni *post-hoc* correction. AUs, arbitrary units. $^{**}P<0.01$ and $^{****}P<0.0001$ vs pAM-d9 cultures.

Comparison of the electrophysiological properties of iAMs and HL-1 cells

The electrophysiological properties of iAM clone #5 were compared with those of the widely used HL-1 cell line, which was derived from the AT-1 mouse atrial myocyte tumour lineage[11]. To this end, confluent monolayers of iAMs at day 9 of differentiation and optimally maintained confluent cultures of HL-1 cells were subjected to optical voltage mapping following 1-Hz pacing. The CV in the HL-1 cultures was ±20-fold lower than in the iAM cultures (*Figure 5A* and *B*; *Movie III*) and HL-1 cells displayed greatly prolonged APs as compared to differentiated iAMs (*Figure 5C*) characterized by a very slow upstroke. These data clearly demonstrate that differentiated iAMs possess electrophysiological properties superior to those of HL-1 cells.

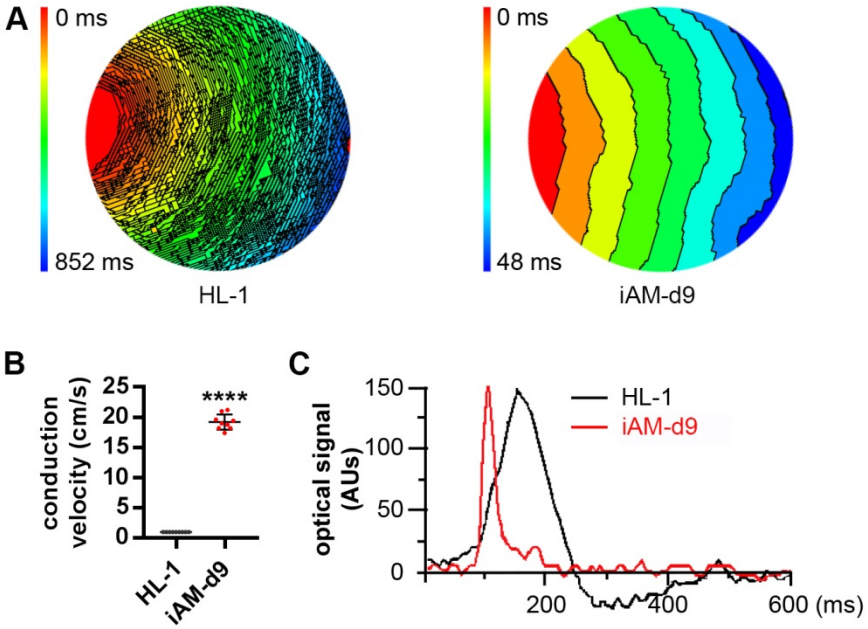

Figure 6. Comparison by optical voltage mapping and 1-Hz electrical point stimulation of the electrophysiological properties of confluent monolayers of iAMs at day 9 of differentiation (iAM-d9) with those of HL-1 cells. Typical activation maps (*A*, 6-ms isochrone spacing) showing a much slower CV (*B*) and optical signal traces (*C*) showing a much longer APD for the HL-1 cells as compared to the iAM-d9. Data are presented as mean±SD, N=9 cell cultures per group from 3 individual preparations. For statistical analysis, the nested ANOVA test was used. AUs, arbitrary units. ****$P<0.001$.

iAMs as *in vitro* model of AF

Our research group previously developed an *in vitro* model of AF based on high-frequency electrical stimulation of confluent pAM cultures. The resulting reentrant circuits, or so-called rotors, could be terminated by prolonging APD of the pAMs using the $K_{ir}3.x$-specific inhibitor tertiapin[17]. To determine whether confluent cultures of iAMs at different stages of differentiation would display similar behaviour, they were burst paced in the absence or presence of 100 nM tertiapin. While rotors could be readily induced in iAM cultures from differentiation day 6 onwards (*Figure 6A-C*; Supplementary material online, *Movie IV*), reentry could not be established in iAM cultures at day 3 of differentiation (*Figure 6C*). Reentry inducibility, the number of rotors per culture and rotor frequency increased with the time after dox removal

(*Figure 6C-E*). After treatment with tertiapin, iAMs that had been cultured for 9 days without dox showed a strong increase in APD (*Figure 6F-H*). Moreover, in the presence of tertiapin it was no longer possible to induce reentry in confluent monolayers of iAMs at day 6, 9 or 12 of differentiation by burst pacing (*Figure 6C-F*). The fact that tertiapin treatment only slightly reduced the CV in confluent monolayers of iAMs at day 9 of differentiation (from 20.5 to 19.8 cm/s; *Figure 6I*) suggests that Kir3.x channel activity is not the major determinant of iAM excitability at the monolayer level.

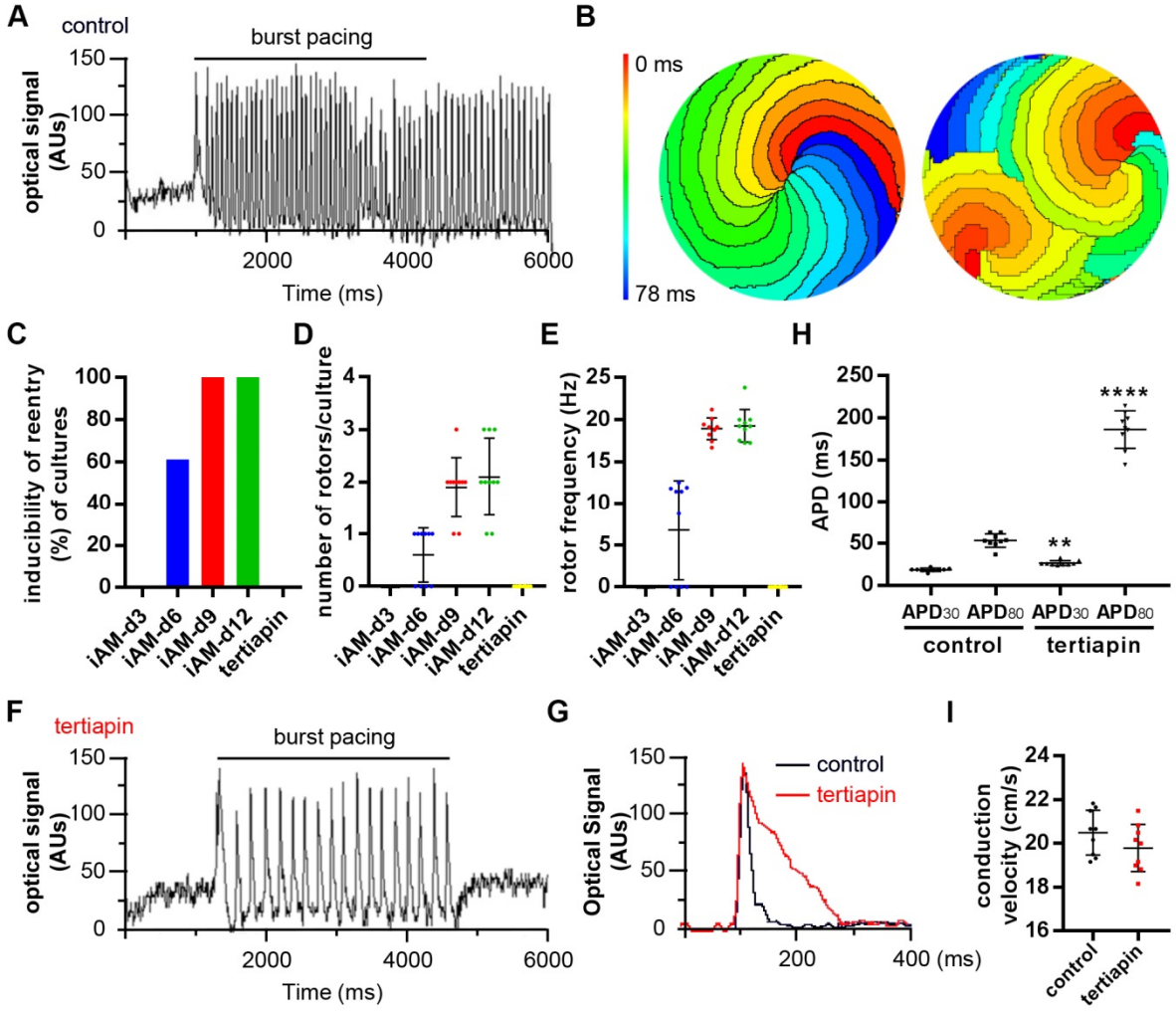

Figure 5. Suitability of iAMs as *in vitro* AF model assessed by optical voltage mapping. (*A, F*) Typical optical signal traces of mock- (*A*) and tertiapin (*F*)-treated iAMs at day 9 of differentiation (iAM-d9) after high-frequency (10-50 Hz) electrical point stimulation. (*B*) Activation maps (6-ms isochrone spacing) of iAM-d9 cultures showing 1 (left) or 2 (right) reentrant circuits. (*C-E*) Inducibility of reentry (*C*), arrhythmia complexity (*D*) and quantification of rotor frequency (*E*) in iAM cultures at 3, 6, 9 and 12 days of differentiation. (*G*) Typical optical AP records of mock- (black) and tertiapin (red)-treated iAM-d9 following 1-Hz pacing. (*H-I*) Quantification of APD_{30}, APD_{80} (*H*) and CV (*I*) of mock- and tertiapin-treated iAM-d9. Data are presented as mean±SD, N=9 cell cultures per experimental group from 3 individual preparations. Statistics was done using the nested ANOVA test with Bonferroni *post-hoc* correction. $^{**}P<0.01$ and $^{****}P<0.0001$ vs control cultures.

Discussion

Until now, all attempts to generate lines of cardiomyocytes that can give rise to cells with electrical and contractile properties approaching those of the starting material have failed. Indeed, all cardiomyocyte lines reported to date display large structural and functional deficits compared to the primary cardiomyocytes from which they were derived[11,13,15,24]. In this study, we have solved this problem and describe the generation of monoclonal lines of conditionally immortalized neonatal rat atrial myocytes with preserved cardiomyogenic differentiation capacity. This was accomplished by transducing pAMs with an LV directing myocyte-selective and dox-dependent expression of the SV40 LT antigen. Culturing of the resulting cells in medium with dox caused their rapid expansion, while in dox-free culture medium, the amplified cells spontaneously and synchronously differentiated into fully functional (*i.e.* excitable and contractile) AMs that were successfully used to develop a monolayer model of AF, for investigating the APD-prolonging effects of toxins (tertiapin, *Figure 6*). To provide our iAMs with a unique and easy-to-remember identifier, we have dubbed the progeny of iAM clone #5 the iAM-1 cell line.

Properties of iAMs

RT-qPCR analysis of iAMs in different stages of differentiation (*Figure 3* and Supplementary material online, *Figure S1*) shows a rapid increase in mRNA levels of cardiac transcription factors, ion channels, Ca^{2+}-handling proteins and sarcomeric proteins shortly after dox removal. At later stages of differentiation, these mRNA levels generally either stay fairly constant (as for the genes encoding cardiac transcription factors, sarcomeric and Ca^{2+}-handling proteins and ANP) or decline again to the approximate mRNA levels of pAMs (*Scn5a*, *Cacna1c*, *Hcn2*, *Kcnj3*, *Kcnj11*) and/or proliferating iAMs (*Scn5a*, *Cacna1c*, *Kcnd3*, *Kcnh2*, *Kcnj3*). These findings are consistent with the notion that upon dox removal iAMs rapidly engage in a cardiomyogenic differentiation program with the concomitant upregulation of genes needed to build a functional cardiomyocyte. To complement the RT-qPCR data, we recently initiated an RNA-seq study focussing on transcriptomes of iAMs at different stages of cardiomyogenic differentiation and subsequent dedifferentiation. The results of this study will be presented elsewhere.

Following their differentiation in the absence of dox, iAMs acquire properties of atrial rather than ventricular myocytes as evinced by the high-level expression in differentiated iAMs of "atrial" genes including *Nppa*, *Myl4*, *Myl7*, *Kcnj3* and *Kcnj5*[17] and the lack of expression of the "ventricular" *Myl2*, *Myl3* and *Myh7* genes[25]. Moreover, following 1-Hz pacing, differentiated iAMs display rapid contractions that strongly resemble those of pAMs but are quite different from the slower contractions of pVMs (Supplementary material online, *Movie II* and data not shown). Consistently, the average APD_{30} and APD_{80} of differentiated iAMs do not significantly differ from those of pAMs (*Figure 4E* and *F*, respectively; Supplementary material online, *Table S3*) but are much shorter than the average APD_{30} and APD_{80} of pVMs (Supplementary material online, Figure S5). Collectively, these findings indicate that although LT expression results in the dedifferentiation and proliferation of AMs, the cells retain

some kind of epigenetic memory causing them to spontaneously differentiate into atrial myocytes upon dox removal.

RMPs of iAMs and pAMs

pAM and iAM monolayers had similar RMPs *(Figure S2A*). Although RMP measurements of single cells are less reliable than those of cell clusters, because the voltage is measured from a high-resistance source (R_m>100 MΩ) after establishing gigaseal, the RMPs of single pAMs and pAM monolayers did not significantly differ (*Figure S2A*). However, the RMP of single iAMs was significantly depolarized compared to that of iAM monolayers (*Figure S2A*). Further experiments as part of a dedicated patch-clamp study are needed to determine the precise cause for this difference, which may, however, relate to the lack of *Kcnj2* expression in cardiomyogenically differentiated iAMs (*Figure S1H*) together with technical difficulties to perform meaningful RMP measurements in neonatal/immature (atrial) cardiomyocytes due to their high plasma membrane resistance[26,27].

Our finding that the electrogenic Na^+/K^+ ATPase plays an important role in the generation of the RMP of AMs is of particular interest, because it ensures a sufficiently negative RMP for the maintenance of excitability of iAMs in monolayer cultures, in the absence of *Kcnj2* expression. The great importance of the Na^+/K^+ pump for establishing physiological Na^+ and K^+ gradients is widely recognized in the electrophysiology of adult cardiomyocytes. Decreased activity of the Na^+/K^+ pump under ischaemic conditions causes the loss of physiological K^+ and Na^+ gradients with consequent RMP depolarization and other effects favouring arrhythmogenesis[28]. However, as stated in many physiology textbooks, a direct contribution of the electrogenic action of the Na^+/K^+ pump to the RMP of adult cardiomyocytes is often considered as relatively small compared to the pump's indirect electrogenic effect, *i.e.* its ability to create transmembrane K^+ and Na^+ gradients. This may be understood by considering the Na^+/K^+ pumps in the plasma membrane as a low conductance pathway with a negative reversal potential determined by their ATP-driven action[29,30]. This implies that the direct electrogenic effects of pump currents will, at the same current densities, be more prominent in high-resistance (~1 GΩ) cardiomyocytes like the AMs than in lower-resistance (~100 MΩ) cardiomyocytes like adult rat ventricular cardiomyocytes[31]. Possibly, no/low expression of inward rectifier K^+ channels in iAMs and an important role for the Na^+/K^+ ATPase activity in setting the RMP is characteristic for young (atrial) myocytes or a sign of incomplete differentiation of these cells. Developmental increases in I_{K1} are not uncommon and have previously been reported for ventricular cardiomyocytes of various rodent species[32].

Because of the dominance of voltage-activated Na^+ channels in the voltage-clamp recordings of both pAMs and iAMs, we ascribed the excitability of iAMs mainly to those channels. However, AMs also express, though at much lower levels, voltage-activated Ca^{2+} channels[33] (Supplementary material online, *Figure S1B*), which may be expected to contribute to pAM and iAM excitability. How these Ca^{2+} channels compare in their contribution to excitability in pAMs and iAMs deserves further experimental work. The same applies to the contributions of outward rectifier K^+ currents to the excitability of pAMs and iAMs, and to the realisation of the RMP of single iAMs in general.

Possible applications of iAMs

Long-term culture of iAMs did not significantly reduce their proliferation rate in the presence of dox and the sarcomeric organization and contractile behaviour of iAMs from different passages at day 9 of differentiation were indistinguishable (data not shown). Moreover, no progressive cell flattening, nuclear enlargement, development of senescence-associated heterochromatin foci or other signs of senescence were observed during the first 55 population doublings of the cells. Assessment of the electrophysiological properties of confluent monolayers of differentiated iAMs by optical voltage mapping after 25, 40 and 55 population doublings revealed no significant differences in APD or CV (see Supplementary material online, *Figure S6*). Also, differentiated iAMs resume cell division following addition of dox to the culture medium and redifferentiate again into atrial myocytes following subsequent dox removal (data not shown). iAMs therefore provide a virtually unlimited supply of cardiomyocytes for fundamental research but may also prove very useful for: (i) the development of acquired disease models, (ii) identifying new therapeutic targets, (iii) screening of drugs and toxins, (iv) testing of new treatment modalities (*e.g.* gene and cell therapy), (v) production of biopharmaceuticals in bioreactors or encapsulated cell/tissue grafts and (vi) the improvement of tissue engineering approaches. The recent rapid progress in genome editing technologies[34] will further expand the applicability of iAMs allowing them to be used as models for studying key aspects of inherited cardiomyopathies.

A highly attractive feature of the iAMs is that they spontaneously undergo cardiomyogenic differentiation in a synchronous and near quantitative manner in standard culture medium without dox. Contrarily, generation of cardiomyocytes from embryonic or induced PSCs requires their properly timed treatment with various cocktails of growth factors and small molecules[5]. This typically yields phenotypically heterogeneous populations of mostly immature cardiomyocytes contaminated with variable percentages of non-cardiomyocytes. Consequently, to obtain relatively pure populations of PSC-CMCs various different enrichment procedures have been developed[35]. Production of more or less homogeneous populations of cardiomyocytes from PSCs thus is a laborious, time-consuming and costly endeavour as compared to the straightforward generation of atrial myocytes from iAMs. This may explain why there are very few reports on the use of PSC-CMCs to investigate cardiac arrhythmias in monolayer cultures by optical mapping[8], while such experiments are easily performed with differentiated iAM monolayers (*Figure 4-6* and Supplementary material online, *Figure S3-9*). Also, in contrast to PSC-CMCs, iAMs offer the possibility to study the molecular mechanisms involved in the transition of a differentiated cardiomyocyte that is no longer able to undergo cytokinesis into an actively dividing cell. This is particularly relevant given the growing interest in the regeneration of mammalian hearts from within by stimulating cardiomyocytes surrounding the site(s) of cardiac injury to multiply themselves through cell division[36,37]. Current findings regarding the molecular changes accompanying the reactivation of cardiomyocyte proliferation should be interpreted with caution due to the presence of other cell types (*e.g.* cardiac fibroblasts and inflammatory cells) in most test materials. iAMs do not suffer from this drawback making them a potentially

highly useful model system to study the mechanisms underlying cell cycle reentry and progression of cardiomyocytes.

Optical voltage mapping of other clones of excitable iAMs yielded very similar results although not all of them reached the same maximum CV and minimum APD as clone #5 (*e.g.* clone #1 and #6; Supplementary material online, *Figure S7A-C* and *D-F*, respectively). An intriguing finding of this study is the difference in electrophysiological properties between the differentiated progeny of different iAM clones, which extends to iAM clones not presented in this study. The cause(s) of this heterogeneity is/are unclear given the fact that cardiomyogenically differentiated cells with a similarly high level of sarcomeric organization still differed in electrophysiological behaviour (data not shown). Therefore, besides a different propensity to mature, other factors might explain the electrophysiological differences between individual iAM clones. Different iAM clones may, for instance, be derived from different parts of the atria (*e.g.* left or right atrium, epi- or endocardial atrium) or represent different subtypes of atrial myocytes (*i.e.* nodal, bundle and working cells). Also, the number and location of the chromosomal insertion sites of the LV genomes and the cell's epigenetic status at the moment of immortalization may have contributed to the observed heterogeneity in electrophysiological properties between different iAM clones.

Although single-cell patch-clamp analysis can yield a wealth of information about the electrophysiological behaviour of individual cells and has been widely used to estimate the risk of drug-induced proarrhythmia, the technique does not directly assess proarrhythmic potential and is of limited use for studying arrhythmia mechanisms. Optical mapping, on the other hand, allows investigation of normal and disturbed cardiac electrical impulse propagation in a direct manner with high spatial and temporal resolution[38,39]. As demonstrated by the experiments described *in Figure 4-6* and *Figure S4, S7-9* (see Supplementary material online), confluent iAM cultures are well-suited for optical mapping studies. In combination with their large proliferation capacity, this opens perspectives for developing high-throughput analyses based on the iAM lines and/or future lines of other cardiomyocytes generated with our conditional immortalization method.

Comparison between HL-1 and iAM-1 cells

Of all AM lines generated to date, the murine AM line HL-1 has the most differentiated phenotype and is therefore most widely used. Side-by-side comparison of the electrophysiological properties of confluent monolayers of differentiated iAM-1 cells and HL-1 cells by optical voltage mapping (*Figure* 5 and *Movie III*) showed an average CV for the HL-1 cultures of 1 cm/s, which is about 20-fold lower than that of differentiated iAM-1 cell cultures and in line with previous reports[24]. Since Ma *et al*[40]. reported a resting membrane potential of −77.7±0.4 mV for HL-1 cells at an extracellular K^+ concentration of 4 mM, the low CV in confluent HL-1 cell monolayers does not seem to result from a high percentage of cardiac fast Na^+ channels being in an inactivated state. The large difference in CV between both cell types thus conceivably relates to the fact that confluent HL-1 monolayers are a blend of proliferating cells without cardiomyocyte functionality, which are electrically coupled to cells that phenotypically resemble embryonic atrial myocytes[11]. Conversely,

in the iAM cultures at 9 days of differentiation virtually all cells are in a similar advanced stage of differentiation forming a highly conductive cardiac syncytium (*Figure 4, 5* and Supplementary material online, *Figure S4, S5, S7-9*). Gap junctional coupling between undifferentiated and differentiated cells may also explain the apparent discrepancy between the broad optical voltage traces of HL-1 cells in monolayer cultures versus the short APDs recorded for single HL-1 cells following whole-cell current clamping[24].

Conclusion

By employing a monopartite LV system allowing inducible expression of the SV40 LT antigen in cardiomyocytes, we have generated lines of iAMs with (functional) properties superior to those of all existing cardiomyocyte lines, none of which yields cells that approach the structural and functional maturity of dox-deprived iAMs. This is especially true for differentiated iAM-1 monolayers, which show homogeneous AP propagation at much higher speeds than obtained with other lines of cardiac muscle cells. The broad applicability of the iAMs was illustrated by their use (i) to study the cardiac ion channel-modulatory activity of toxins and drugs and (ii) as AF model. Since iAMs undergo a highly coordinated and precisely timed cardiomyogenic differentiation process, they might also be ideally suited to study specific aspects of cardiac muscle cell formation and maturation. Finally, because differentiation of iAMs into electrically and mechanically active cardiomyocytes that phenotypically resemble atrial myocytes of newborn rats occurs spontaneously (*i.e.* without the need for complex treatment regimens with expensive [bio]chemicals), iAMs may provide an easy-to-use and cost-effective system to address specific fundamental and applied cardiac research.

Funding

This study received financial support from the Netherlands Heart Institute (ICIN grant 230.148-04 to A.A.F.d.V.), the Royal Netherlands Academy of Arts and Sciences (Chinese Exchange Programme grant 10CDP007 to A.A.F.d.V.), and Ammodo (to D.A.P. and A.A.F.d.V.). Additional support came from the research programme More Knowledge with Fewer Animals (MKMD) with project number 114022503 (to A.A.F.d.V.), which is (partly) financed by the Netherlands Organisation for Health Research and Development (ZonMw) and the Dutch Society for the Replacement of Animal Testing (dsRAT) and from the Chinese Scholarship Council (to J.L.).

Acknowledgements

We thank Brian Bingen, Zeinab Neshati and Iolanda Feola, Niels Harlaar and Annemarie Kip from LUMC's Laboratory of Experimental Cardiology for their help with establishing AM cultures, LV production, generating movie files and RT-qPCR experiments, respectively. We are indebted to Bianca Brundel and Deli Zhang (Department of Physiology, Institute for Cardiovascular Research, VU University Medical Center) for supplying HL-1 cells.

Conflict of interest

None declared.

References

1. Hasenfuss G. Animal models of human cardiovascular disease, heart failure and hypertrophy. *Cardiovasc Res* 1998;**39**:60-76.
2. Robinson N, Souslian L, Gallegos RP, Rivard AL, Dalmasso AP, Bianco RW. *Animal models for cardiac research.* In: Iaizzo PA. Handbook of Cardiac Anatomy, Physiology, and Devices. 3rd ed. Cham: Springer International Publishing, 2015:469-491.
3. Mitcheson JS, Hancox JC, Levi AJ. Cultured adult cardiac myocytes: future applications, culture methods, morphological and electrophysiological properties. *Cardiovasc Res* 1998;**39**:280-300.
4. Parameswaran S, Kumar S, Verma RS, Sharma RK. Cardiomyocyte culture - an update on the in vitro cardiovascular model and future challenges. *Can J Physiol Pharmacol* 2013;**91**:985-998.
5. Spater D, Hansson EM, Zangi L, Chien KR. How to make a cardiomyocyte. *Development* 2014;**141**:4418-4431.
6. Karakikes I, Ameen M, Termglinchan V, Wu JC. Human induced pluripotent stem cell-derived cardiomyocytes: insights into molecular, cellular, and functional phenotypes. *Circ Res* 2015;**117**:80-88.
7. Veerman CC, Kosmidis G, Mummery CL, Casini S, Verkerk AO, Bellin M. Immaturity of human stem-cell-derived cardiomyocytes in culture: fatal flaw or soluble problem? *Stem Cells Dev* 2015;**24**:1035-1052.
8. Herron TJ. Calcium and voltage mapping in hiPSC-CM monolayers. *Cell Calcium* 2016;**59**:84-90.
9. Steinhelper ME, Lanson NA Jr, Dresdner KP, Delcarpio JB, Wit AL, Claycomb WC, Field LJ. Proliferation in vivo and in culture of differentiated adult atrial cardiomyocytes from transgenic mice. *Am J Physiol* 1990;**259**:H1826-1834.
10. Jahn L, Sadoshima J, Greene A, Parker C, Morgan KG, Izumo S. Conditional differentiation of heart- and smooth muscle-derived cells transformed by a temperature-sensitive mutant of SV40 T antigen. *J Cell Sci* 1996;**109 (Pt 2)**:397-407.
11. Claycomb WC, Lanson NA Jr, Stallworth BS, Egeland DB, Delcarpio JB, Bahinski A, Izzo NJ Jr. HL-1 cells: a cardiac muscle cell line that contracts and retains phenotypic characteristics of the adult cardiomyocyte. *Proc Natl Acad Sci U S A* 1998;**95**:2979-2984.
12. Rybkin II, Markham DW, Yan Z, Bassel-Duby R, Williams RS, Olson EN. Conditional expression of SV40 T-antigen in mouse cardiomyocytes facilitates an inducible switch from proliferation to differentiation. *J Biol Chem* 2003;**278**:15927-15934.
13. Davidson MM, Nesti C, Palenzuela L, Walker WF, Hernandez E, Protas L, Hirano M, Isaac ND. Novel cell lines derived from adult human ventricular cardiomyocytes. *J Mol Cell Cardiol* 2005;**39**:133-147.
14. Goldman BI, Amin KM, Kubo H, Singhal A, Wurzel J. Human myocardial cell lines generated with SV40 temperature-sensitive mutant tsA58. *In Vitro Cell Dev Biol Anim* 2006;**42**:324-331.
15. Zhang Y, Nuglozeh E, Toure F, Schmidt AM, Vunjak-Novakovic G.

Controllable expansion of primary cardiomyocytes by reversible immortalization. *Hum Gene Ther* 2009;**20**:1687-1696.
16. Lip GY, Fauchier L, Freedman SB, Van Gelder I, Natale A, Gianni C, Nattel S, Potpara T, Rienstra M, Tse HF, Lane DA. Atrial fibrillation. *Nat Rev Dis Primers* 2016;**2**:16016.
17. Bingen BO, Neshati Z, Askar SF, Kazbanov IV, Ypey DL, Panfilov AV, Schalij MJ, de Vries AA, Pijnappels DA. Atrium-specific Kir3.x determines inducibility, dynamics, and termination of fibrillation by regulating restitution-driven alternans. *Circulation* 2013;**128**:2732-2744.
18. Feola I, Teplenin A, de Vries AA, Pijnappels DA. Optogenetic engineering of atrial cardiomyocytes. *Methods Mol Biol* 2016;**1408**:319-331.
19. Bingen BO, Engels MC, Schalij MJ, Jangsangthong W, Neshati Z, Feola I, Ypey DL, Askar SF, Panfilov AV, Pijnappels DA, de Vries AA. Light-induced termination of spiral wave arrhythmias by optogenetic engineering of atrial cardiomyocytes. *Cardiovasc Res* 2014;**104**:194-205.
20. Szulc J, Wiznerowicz M, Sauvain MO, Trono D, Aebischer P. A versatile tool for conditional gene expression and knockdown. *Nat Methods* 2006;**3**:109-116.
21. Salva MZ, Himeda CL, Tai PW, Nishiuchi E, Gregorevic P, Allen JM, Finn EE, Nguyen QG, Blankinship MJ, Meuse L, Chamberlain JS, Hauschka SD. Design of tissue-specific regulatory cassettes for high-level rAAV-mediated expression in skeletal and cardiac muscle. *Mol Ther* 2007;**15**:320-329.
22. Majumder R, Engels MC, de Vries AA, Panfilov AV, Pijnappels DA. Islands of spatially discordant APD alternans underlie arrhythmogenesis by promoting electrotonic dyssynchrony in models of fibrotic rat ventricular myocardium. *Sci Rep* 2016;**6**:24334.
23. Yu Z, Liu J, van Veldhoven JP, AP IJ, Schalij MJ, Pijnappels DA, Heitman LH, de Vries AA. Allosteric modulation of Kv11.1 (hERG) channels protects against drug-induced ventricular arrhythmias. *Circ Arrhythm Electrophysiol* 2016;**9**:e003439.
24. Dias P, Desplantez T, El-Harasis MA, Chowdhury RA, Ullrich ND, Cabestrero de Diego A, Peters NS, Severs NJ, MacLeod KT, Dupont E. Characterisation of connexin expression and electrophysiological properties in stable clones of the HL-1 myocyte cell line. *PLoS One* 2014;**9**:e90266.
25. Lompre AM, Nadal-Ginard B, Mahdavi V. Expression of the cardiac ventricular alpha- and beta-myosin heavy chain genes is developmentally and hormonally regulated. *J Biol Chem* 1984;**259**:6437-6446.
26. Horváth A, Lemoine MD, Löser A, Mannhardt I, Flenner F, Uzun AU, Neuber C, Breckwoldt K, Hansen A, Girdauskas E, Reichenspurner H, Willems S, Jost N, Wettwer E, Eschenhagen T, Christ T. Low Resting Membrane Potential and Low Inward Rectifier Potassium Currents Are Not Inherent Features of hiPSC-Derived Cardiomyocytes. *Stem Cell Reports*;**10**:822-833.
27. Dawodu AA, Monti F, Iwashiro K, Schiariti M, Chiavarelli R, Puddu PE. The shape of human atrial action potential accounts for different frequency-related changes in vitro. *Int J Cardiol* 1996;**54**:237-249.
28. Carmeliet E. Cardiac ionic currents and acute ischemia: from channels to arrhythmias. *Physiol Rev* 1999;**79**:917-1017.

29. Gadsby DC, Nakao M. Steady-state current-voltage relationship of the Na/K pump in guinea pig ventricular myocytes. *J Gen Physiol* 1989;**94**:511-537.
30. Läuger P. Electrogenic ion pumps. 1991.
31. Ypey DL, van Meerwijk WPM, Umar S, Pijnappels DA, Schalij MJ, van der Laarse A. Depolarization-induced automaticity in rat ventricular cardiomyocytes is based on the gating properties of L-type calcium and slow Kv channels. *Eur Biophys J* 2013;**42**:241-255.
32. Itoh H. *Electrophysiological simulation of developmental changes in action potentials of cardiomyocytes.* In: Arjunan SNV, Dhar PK, Tomita, M. E-Cell System: Basic Concepts and Applications. New York: Springer-Verlag, 2013: 75-88.
33. Avila G, Medina IM, Jiménez E, Elizondo G, Aguilar CI. Transforming growth factor-β1 decreases cardiac muscle L-type Ca^{2+} current and charge movement by acting on the $Ca_V1.2$ mRNA. *Am J Physiol Heart Circ Physiol* 2007;**292**:H622-H631.
34. Maggio I, Goncalves MA. Genome editing at the crossroads of delivery, specificity, and fidelity. *Trends Biotechnol* 2015;**33**:280-291.
35. Schwach V, Passier R. Generation and purification of human stem cell-derived cardiomyocytes. *Differentiation* 2016;**91**:126-138.
36. Foglia MJ, Poss KD. Building and re-building the heart by cardiomyocyte proliferation. *Development* 2016;**143**:729-740.
37. Uygur A, Lee RT. Mechanisms of Cardiac Regeneration. *Dev Cell* 2016;**36**:362-374.
38. Herron TJ, Lee P, Jalife J. Optical imaging of voltage and calcium in cardiac cells & tissues. *Circ Res* 2012;**110**:609-623.
39. Himel HD IV, Bub G, Lakireddy P, El-Sherif N. Optical imaging of arrhythmias in the cardiomyocyte monolayer. *Heart Rhythm* 2012;**9**:2077-2082.
40. Ma L, Zhang X, Chen H. TWIK-1 two-pore domain potassium channels change ion selectivity and conduct inward leak sodium currents in hypokalemia. *Sci Signal* 2011;**4**:ra37.
41. Loeber G, Tevethia MJ, Schwedes JF, Tegtmeyer P. Temperature-sensitive mutants identify crucial structural regions of simian virus 40 large T antigen. *J Virol* 1989;**63**:4426-4430.
42. Deuschle U, Meyer WK, Thiesen HJ. Tetracycline-reversible silencing of eukaryotic promoters. *Mol Cell Biol* 1995;**15**:1907-1914.

Supporting information

Supplemental methods

Construction of plasmids

DNA constructions were carried out with enzymes from Fermentas (Thermo Fisher Scientific, Breda, the Netherlands) or from New England Biolabs (Bioke´, Leiden, the Netherlands) and with oligodeoxyribonucleotides from Eurofins MWG Operon (Ebersberg, Germany) using established procedures or following the instructions provided with specific reagents.

To generate a thermosensitive version of the oncogenic simian virus 40 (SV40) large T (LT) antigen (mutant *ts*A58 also known as *ts*A438A-V[1]), plasmid pAT153.SV40ori(-)[2] was incubated with PvuII and the 4.3-kb digestion product was recircularized with bacteriophage T4 DNA ligase to generate pAT153.SV40ori(-).dPvuII. pAT153.SV40ori(-).dPvuII was subsequently cut with HindIII and PvuII and the large digestion product of 4.3 kb was combined with the hybridization product of oligodeoxyribonucleotides 5' CTGTGCTTCTAGAATTATGTGGGGGGAA 3' and 5' AGCTTTCCCCCCACATAATTCTAGAAGCACAG 3' (underlined nucleotides represent the mutant LT codon and its complement) producing pAT153.SV40ori(-).dPvuII.LT-*ts*A58. Next, pAT153.SV40ori(-)dPvuII.LT-*ts*A58 was linearized with PvuII and the 4.3-kb digestion product was ligated to the 2.0-kb PvuII fragment of pAT153.SV40ori(-) to generate pAT153.SV40ori(-).LT-*ts*A58. pAT153.SV40ori(-).LT-*ts*A58 was used as template in a polymerase chain reaction (PCR) with VELOCITY DNA polymerase (GC Biotech, Alphen aan den Rijn, the Netherlands) and primers 5' AGGTTTAAACTACGGGATCCGTGCACCATGGATAAAGTTTTAAACAGAGA GGA 3' and 5' CCGAATTCTTTATGTTTCAGGTTCAGGG 3' (underlined nucleotides represent the LT initiation codon and the complement of its termination codon) to amplify the LT-coding sequence. The resulting PCR fragment was inserted into plasmid pJET1.2/blunt using the CloneJET PCR cloning kit (Thermo Fisher Scientific) to generate pJet1.2.LT-*ts*A58. pJet1.2.LT-*ts*A58 was incubated with MssI and EcoRI and the 2.5-kb digestion product was combined with the 11.0-kb MssI×EcoRI fragment of lentiviral vector (LV) shuttle plasmid pLV.iMHCK7 to generate pLV.iMHCK7.LT-*ts*A58 (*Figure 1A*). pLV.iMHCK7 is a derivative of pLVET-tTR-KRAB[3] (Addgene, Cambridge, MA; plasmid number: 116444) in which the human *EEF1A1* gene promoter and the *Aequorea victoria* enhanced green fluorescent protein (eGFP)-coding sequence were replaced by the striated muscle-specific MHCK7 promoter[4] and a small polylinker containing unique SpeI, MssI, PstI and EcoRI restriction enzyme recognition sequences.

LV shuttle plasmid pLV.MHCK7.eGFP is a derivative of construct pLV.MHCK7.eYFP.WHVPRE[5], in which the coding sequence for the *Aequorea victoria* enhanced yellow fluorescent protein and the woodchuck hepatitis virus posttranscriptional regulatory element (WHVPRE) are replaced by the eGFP open reading frame and a mutated shortened version of the WHVPRE designated WHVoPRE[6].

LV production

To generate vesicular stomatitis virus G protein-pseudotyped particles of LV.iMHCK7.LT-*ts*A58, subconfluent monolayers of 293T cells were transfected with LV shuttle construct pLV.iMHCK7.LT-*ts*A58 and the packaging plasmids psPAX2 (Addgene; plasmid number: 12260) and pLP/VSVG (Thermo Fisher Scientific) at a molar ratio of 2:1:1. The 293T cells were cultured in high-glucose Dulbecco's modified Eagle's medium (DMEM; Life Technologies Europe, Bleiswijk, the Netherlands, catalogue number: 41966) with 10% foetal bovine serum (FBS; Life Technologies Europe). The transfection mixture, which consisted of 35 µg of plasmid DNA and 105 µg of polyethyleneimine (Polysciences Europe, Eppelheim, Germany) in 2 ml of 150 mM NaCl per 175-cm^2 cell culture flask (Greiner Bio-One, Alphen aan den Rijn, the Netherlands), was directly added to the culture medium. The next morning, the transfection medium was replaced by 15 ml of fresh high-glucose DMEM supplemented with 5% FBS and 25 mM HEPES-NaOH (pH 7.4). At ±48 hours after the start of the transfection procedure, the culture supernatants were harvested and cleared from cellular debris by centrifugation at room temperature (RT) for 10 minutes at 3,750×*g* and subsequent filtration through 0.45-µm pore-sized, 33-mm diameter polyethersulfone Millex-HP syringe filters (Millipore, Amsterdam, the Netherlands). To concentrate and purify the LV particles, 30 ml of vector suspension in a 38.5-ml polypropylene ultracentrifuge tube (Beckman Coulter Nederland, Woerden, the Netherlands) was underlayed with 5 ml of 20% (wt/vol) sucrose in phosphate-buffered saline (PBS) and centrifuged for 120 minutes at 4°C with slow acceleration and without braking at 15,000 revolutions per minutes in an SW32 rotor (Beckman Coulter Nederland). Next, the supernatants were discarded and the pellets were suspended in PBS-1% bovine serum albumin (BSA; Sigma-Aldrich, St. Louis, MO) by overnight incubation with gentle shaking at 4°C. The concentrated vector suspension was divided on ice in 50 µl aliquots for storage at -80°C. LV.MHCK7.eGFP particles were generated using the same procedure except for the use of pLV.MHCK7.eGFP instead of pLV.iMHCK7.LT-*ts*A58 as LV shuttle plasmid.

Animal experiments

All animal experiments were approved by the Animal Experiments Committee of Leiden University Medical Center and conformed to the Guide for the Care and Use of Laboratory Animals as stated by the US National Institutes of Health.

Isolation and culture of cardiomyocytes

Cardiomyocytes were isolated from neonatal Wistar rat hearts and cultured as detailed elsewhere[7]. Briefly, rats were anaesthetized with 4-5% isoflurane inhalation. After adequate anaesthesia had been confirmed by the absence of pain reflexes, hearts were excised. Atria and ventricles were separated from the hearts, minced and dissociated by 2 subsequent 30-minute treatments with collagenase type I (Worthington Biochemical, Lakewood, NJ) and DNase I (Sigma-Aldrich). Cells were pelleted by centrifugation for 10 minutes at RT and 160×*g* and suspended in Ham's F10 medium (Life Technologies Europe, catalogue number: 11550) supplemented with 100 units/mL of penicillin and 100 µg/mL of streptomycin (Life Technologies Europe) and with 10% heat-inactivated FBS and 10% heat-inactivated horse serum (HS; Life

Technologies Europe). Next, cell suspensions were transferred to Primaria culture dishes (Corning Life Sciences, Amsterdam, the Netherlands) and incubated for 120 minutes at 37°C in a humidified atmosphere of 5% CO_2 to allow preferential attachment of non-cardiomyocytes. The unattached cells (mainly atrial myocytes AMs or ventricle myocytes VMs) were collected, passed through a cell strainer (70-µm mesh pore size; BD Biosciences, Breda, the Netherlands) and seeded at a density of 2×10^3 cells/cm^2 in a 6-well cell culture plate (Corning Life Sciences) coated with fibronectin from bovine plasma (Sigma-Aldrich) for immortalization purposes or on bovine fibronectin-coated glass coverslips in 24-well cell culture plates (Greiner Bio-One) at a density between 2×10^4 and 8×10^5 cells/well for comparative studies. LV.iMHCK7.LT-*ts*A58-transduced cells and primary AMs (pAMs) were subsequently maintained in a 1:1 mixture of low-glucose DMEM (Life Technologies Europe, catalogue number: 22320) and Ham's F10 medium (DMEM/F10) supplemented with 5% heat-inactivated HS, 1× penicillin-streptomycin, 2% BSA and sodium ascorbate to a final concentration of 0.4 mM and in DMEM/F10 with 10% heat-inactivated FBS and 100 ng/ml doxycycline (dox) or no dox as indicated, respectively. Culture medium was replaced daily (pAMs and pVMs) or every 2-3 days (immortalized AMs).

For the isolation and culture of neonatal rat ventricular cardiomyocytes (pVMs) the same method was used as for pAMs except that ventricular instead of atrial tissue of newborn rats served as starting material.

HL-1 cells were cultured in 25-cm^2 cell culture flasks (Corning Life Sciences) for regular passaging and on round glass coverslips (diameter of 15 mm) for optical mapping purposes essentially as described in the MEA Application Note: HL-1 Cardiac Cell Line of Multi Channel Systems (Reutlingen,Germany; http://www.multichannelsystems.com/sites/multichannelsystems.com/files/documents/applications/MEA-Application%20Note_HL-1.pdf).

The best performing line of conditionally immortalized AMs (iAMs) has been designated iAM-1. Inquiries about this cell line and other iAM lines can be send to iAM-1@hartlongcentrum.nl.

Transduction of pAMs and generation of iAM clones

At day 1 of culture, pAMs were transduced with LV.iMHCK7.LT-*ts*A58. The next day, the inoculum was replaced by culture medium containing 100 ng/ml dox to induce LT expression. The cells were given fresh culture medium every other day. After 1 week of culture, the transduced cells were trypsinized and plated at a low density of 10~20 cells/cm^2 in a 100-mm diameter cell culture dish (Greiner Bio-One) to generate single-cell clones. After 2-3 weeks, individual cell colonies were picked and expanded in the presence of dox. To investigate their spontaneous cardiomyogenic differentiation ability, iAMs were cultured in the absence of dox for 3, 6, 9 and 12 days and characterized by a combination of molecular biological, cell biological, immunological and electrophysiological techniques.

To facilitate their identification in co-cultures with pAMs, iAM-1 cells were eGFP-labelled using the LV designated LV.MHCK7.eGFP and passaged multiple times in the presence of dox before use as donor cells to avoid carry-over of functional LV.MHCK7.eGFP particles[8].

Western blotting

Western blotting was carried out as detailed before[9]. After blocking, the membranes were incubated overnight at 4°C with primary mouse monoclonal antibodies directed against LT (1:2,000; Santa Cruz Biotechnology, Dallas, TX, catalogue number: sc-147) or glyceraldehyde 3-phosphate dehydrogenase (GAPDH; loading control; 1:100,000; Millipore, catalogue number: MAB374) and then probed with goat anti-mouse IgG secondary antibodies linked to horseradish peroxidase (1:15,000; Santa Cruz Biotechnology) for 1 hour at RT. Chemiluminescence was produced using the SuperSignal West Femto maximum sensitivity substrate (Thermo Fisher Scientific), captured by a ChemiDoc XRS imaging system (Bio-Rad Laboratories, Veenendaal, the Netherlands) and analysed by Quantity One software (Bio-Rad Laboratories) using the GAPDH signals for normalization purposes.

Immunocytology

Immunostaining of cultured cells was performed as previously described[10] using the following primary antibodies at a dilution of 1:200 in PBS containing 0.1% normal donkey serum (NDS; Sigma-Aldrich): mouse anti-LT (Santa Cruz Biotechnology, catalogue number: sc-147), rabbit anti-Ki-67 (Abcam, Cambridge, United Kingdom, catalogue number: ab15580), mouse anti-α-actinin (Sigma-Aldrich, catalogue number: A7811), rabbit anti-atrial myosin light chain 2 (MLC2a)[11] and rabbit anti-connexin 43 (Cx43; Sigma-Aldrich, catalogue number: C6219). Bound antigens were detected using Alexa 488-conjugated donkey anti-rabbit IgG (H+L) (Thermo Fisher Scientific, catalogue number: A21206) and Alexa 568-coupled donkey anti-mouse IgG (H+L) (Thermo Fisher Scientific, catalogue number: A10037). These secondary antibodies were diluted 1:400 in PBS. Hoechst 33342 (10 μg/μl; Thermo Fisher Scientific) was used to counterstain nuclei. Stained cells were visualized using a digital colour camera-equipped fluorescence microscope (Nikon Eclipse 80i; Nikon Instruments Europe, Amstelveen, the Netherlands).

Analysis of cell proliferation and programmed cell death

To assess their proliferation rate, iAMs were cultured at low density in medium with or without 100 ng/ml dox. At different days after culture initiation, cells were collected in PBS, mixed at a ratio of 1:1 with 0.4% Trypan Blue (VWR International, Amsterdam, the Netherlands) in PBS and briefly incubated at RT after which viable cells were counted using a haemocytometer. To distinguish proliferating from non-proliferating cells, monolayer cultures of AMs were immunostained with Ki-67-specific antibodies.

To study apoptosis, cells were incubated with Alexa Fluor-568-conjugated annexin V (Thermo Fisher Scientific, catalogue number: A13202) as described before[10]. pAMs treated for 24 hours with 1 μM of the chemotherapeutic agent doxorubicin (Sigma-Aldrich) served as positive control for the apoptosis assay.

Quantitative analyses of cell surface area, the percentage of Ki-67$^+$ cardiomyocytes and cell surface-bound annexin V were performed with the Java-based image processing program Image J (version 1.50i, National Institutes of Health, Bethesda, MD).

Reverse transcription-quantitative PCR (RT-qPCR)

RT-qPCR was performed as previously reported[10]. Briefly, iAMs were seeded at a density of 8×10^5 cells/well in 24-well cell culture plates and cultured for 1 day in medium containing 100 ng/ml dox. The next day, cells were either lysed in TRIzol Reagent (Thermo Fisher Scientific) and total RNA was isolated using the RNeasy Mini kit (QIAGEN Benelux, Venlo, the Netherlands) or kept for 3, 6, 9 or 12 days in culture medium without dox prior to cell lysis and RNA extraction. The RNA was reverse transcribed with the iScript cDNA synthesis kit (Bio-Rad Laboratories) and gene expression levels were determined by PCR using the Bioline SensiFAST SYBR No-ROX kit (GC biotech) and intron-spanning primer pairs (*Table S1*). Due to the high nucleotide sequence identity of the pacemaker channel genes, *Hcn2* and *Hcn4* mRNA levels were determined using TaqMan primer/probe sets Rn01408572_mH andRn00572232_m1), respectively, together with TaqMan Universal Master Mix II (all from Thermo Fisher Scientific). PCR amplifications were performed in a CFX96 Touch Real-Time PCR Detection System (Bio-Rad Laboratories) or in a QuantStudio 5 Real-Time PCR System (Thermo Fisher Scientific). Per target gene 3 independent experiments were performed consisting of 3 samples per experiment. Quantitative analyses were based on the $2^{-\Delta\Delta CT}$ method using CFX Manager software (Bio-Rad Laboratories). PCR amplifications of the rat 18S rRNA gene (*Rn18s*) were included for normalization purposes.

Optical voltage mapping

For studying action potential (AP) propagation in confluent monolayer cultures, cells were seeded at a density of 8×10^5 cells/well in 24-well cell culture plates onto bovine fibronectin-coated round glass coverslips (diameter of 15 mm) and subjected to optical voltage mapping using di-4-ANEPPS (Thermo Fisher Scientific) as fluorescent voltage indicator as described previously[5]. The measurements were carried out at 37°C on 9-day-old pAM and pVM cultures and on iAMs that had been maintained for 0, 3, 6, 9 and 12 days in dox-free medium. Optical signals were captured using a MiCAM ULTIMA-L imaging system (SciMedia, Costa Mesa, CA). Optical traces were analysed using Brain Vision Analyzer 1208 software (Brainvision, Tokyo, Japan). To minimize noise artefacts, calculations were based on the average of the signals at a selected pixel and its eight nearest neighbours. Conduction velocity (CV) and AP duration (APD) at different percentages of repolarization were determined using cardiomyocyte cultures showing uniform AP propagation and 1:1 capture after 1-Hz local electrical stimulation with an epoxy-coated bipolar platinum electrode delivering square 10-ms, 8-V suprathreshold electrical impulses via a STG 2004 stimulus generator and MC Stimulus II software (both from Multi Channel Systems). Burst pacing with a cycle length of 20-100 ms was used to induce reentry. The effects of tertiapin (100 nM, Alomone Labs), astemizole (100 nM, a gift of Zhiyi Yu), carbachol (2 μM, Alcon, Gorinchem, the Netherlands) and ouabain (100 -400 μM, Sigma-Aldrich) were investigated by pipetting them directly into the medium and dispersing them by gentle shaking, followed by optical mapping. To facilitate APD comparison, the amplitude of the optical signal traces was normalized for all samples within a given experiment.

Patch-clamping

Whole-cell patch-clamp recordings were conducted on single iAMs and pAMs (2.5×10^4 cells/2-cm^2 well) and on iAM and pAM monolayers (8×10^5 cells/2-cm^2 well) seeded on fibronectin-coated glass coverslips. The monolayer measurements were carried out using 9-day-old cultures of freshly isolated pAMs or iAMs that were cultured for 9 days in the absence of dox. For single-cell measurements, freshly isolated pAMs were cultured for 2-3 days before patch-clamping. Single-cell patch-clamping of iAMs was done 1-3 days after low-density replating of monolayer cells that had been maintained for 8-9 days without dox unless indicated otherwise. For patch-clamp experiments, pAMs and iAMs were submerged in a Tyrode bath solution containing (in mM): 126 NaCl, 11 glucose, 10 HEPES, 5.4 KCl, 1 $MgCl_2$, and 1.8 $CaCl_2$ (adjusted to pH 7.40 with NaOH). Patch recordings were conducted 15-60 minutes later at 20-23°C. Data acquisition was done using an inverted Zeiss Axiovert 35 microscope (Carl Zeiss, Oberkochen, Germany), an MPC-200 multi-micromanipulator system (Sutter Instrument, Novato, CA) and a conventional patch-clamp rig consisting of a CV-7B head stage, MultiClamp 700B amplifier and a Digidata 1440A A/D converter (Axon CNS, Molecular Devices, Sunnyvale, CA). Patch pipettes were fabricated from borosilicate glass capillaries with an inner and outer diameter of 1.17 and 1.5 mm, respectively (Harvard Apparatus, Kent, United Kingdom), using a vertical puller (P-30; Sutter Instrument). Pipette tips were fire-polished and had typical tip resistances for single cell and monolayer measurements of 2-4 and 4-7 MΩ, respectively, when filled with a solution containing (in mM): 80 potassium DL-aspartate, 40 KCl, 8 NaCl, 5.5 glucose, 5 HEPES, 5 EGTA, 1 $MgCl_2$, 4 Mg-ATP, and 0.1 Na_3-GTP (adjusted to pH 7.20 with KOH). The plasma membrane resistance (R_m) of single pAMs and iAMs at their resting membrane potential (RMP) was approximately 1.1 and 0.9 GΩ, respectively. The effects of carbachol (2 μM) and ouabain (100 and 300 μM) were investigated via local drug perfusion while continuously monitoring the RMP. For fast Na^+ current analysis, signals induced by 50-ms depolarizing pulses in 10-mV increments starting from a holding potential of -80 mV in the absence and presence of 10 μM tetrodotoxin (TTX, Alomone Labs, Jerusalem, Israel) were digitally subtracted. Voltage clamp recordings were ≥75% compensated for pipette series resistance and capacitive transients. Throughout the experiments, the current and voltage outputs of the amplifier were continuously sampled at 10 kHz after low-pass filtered at 4 kHz with a four-pole Bessel filter. Data acquisition was carried out using pCLAMP 10.7 software (Axon CNS, Molecular Devices).

Current densities were determined by normalizing peak current amplitudes to cell capacitance. Voltage dependence of activation was analysed by fitting the data with a single Boltzmann equation, $I = \mathrm{I_{max}}/(1 + e^{-(\frac{V-V½}{k})})$, where V is the variable test potential, $V_{1/2}$ the voltage of half-maximum activation, k the slope factor, and I_{max} the normalized maximum amplitude of the Na^+ current. All data were corrected for liquid junction potentials. Data analysis was done using Clampfit 10.7 (Axon CNS, Molecular Devices), Excel (version 2010, Microsoft, Redmond, WA) and Prism 7 (Graphpad Software, La Jolla, CA).

Atrial tissue culture and iAM injection in cultured atrial tissue

Atrial tissue from neonatal rats was used as graft recipient of iAMs. Two-day-old Wistar rats were anaesthetized by 4-5% isoflurane inhalation and adequate anaesthesia was confirmed by the absence of reflexes. After the chest was opened and the inferior vena cava was cut off with scissors, the right atrium was punctured with a 19-gauge needle. The heart was perfused through this needle with pre-warmed and oxygenated PBS containing 10 IU/ml heparin (LEO Pharma, Amsterdam, the Netherlands) to flush out the blood. Two and a half µl of growth factor-reduced Matrigel (BD Biosciences) was mixed with 2.5 µl cell suspension containing 5×10^4 iAMs and injected into the bilateral atrial free walls using a 25-µl syringe equipped with a 33-gauge needle (Hamilton Robotics, Reno, NV).

Subsequently, the atrial tissue including the injected area was excised and cultured with the following modifications. The atrial tissue was placed with the endocardial surface down onto the semi-porous polytetrafluoroethylene membrane (0.4 µm pore size) of a PICM0RG50 cell culture insert (Millipore) in a 35-mm diameter Petri dish containing 1 ml sterilized Tyrode's solution (TS; 136 mM NaCl, 5.4 mM KCl, 10 mM MgH_2PO_4, 1 mM MgH_2PO_4, 10 mM glucose, 0.9 mM $CaCl_2$) of RT and gradually warmed to 37°C. Next, the TS was replaced with 1 ml pre-warmed low-glucose DMEM supplemented with 1% heat-inactivated FBS, 1× penicillin-streptomycin, 1× B-27 supplement minus antioxidants (Life Technologies Europe) and 5 µM Z-Asp-2,6-dichlorobenzoyloxymethylketone (Santa Cruz Biotechnology) and the tissue was kept at 37°C in humidified 95% air-5% CO_2 (culture conditions) until histological examination. Culture medium was replaced every 2 days.

Whole tissue staining and confocal microscopy

Neonatal rat atrial tissue was quickly washed 3 times with PBS and fixed by incubation for 30 minutes at 4°C in buffered 4% formaldehyde (Added Pharma, Oss, the Netherlands) followed by 3 quick washes with PBS and a 5-minute wash with PBST (0.1% Triton X-100 Sigma-Aldrich in PBS). Next, aspecific binding sites were blocked by incubation for 1 hour at RT with 10% NDS in PBST. After two 10-minute washes with PBST, samples were incubated overnight at 4°C with primary antibodies directed against sarcomeric α-actinin to detect cardiomyocytes (mouse IgG1, clone EA-53; Sigma-Aldrich) or against eGFP to detect iAMs (rabbit IgG, polyclonal; Thermo Fisher Scientific, catalogue number: A11122) and diluted 1:200 in PBS-1% FBS. After 3 quick and four 15-minute washes with PBS, the tissues were incubated with appropriate Alexa Fluor 488/568-conjugated secondary antibodies of donkey origin (1:200 dilution in PBS containing 1% FBS) for 4 hours at 4°C followed by another sequence of 3 short and 4 long washes with PBS. Nuclear counterstaining was performed by incubating the cells for 10 minutes at RT with 10 µg/ml Hoechst 33342 followed by 3 washes with PBS. Coverslips were mounted in Vectashield mounting medium (Vector Laboratories, Burlingame, CA). Images were acquired with a Leica TCS SP8 confocal laser scanning microscope (Leica Microsystems, Rijswijk, the Netherlands). For Z plane reconstruction, we acquired confocal stacks with a step size of 0.3 µm and analysed the resulting images using Leica Application Suite AF Lite software (Leica Microsystems).

Plasmid DNA transfection of iAMs.

For monitoring the transfection efficiency of iAMs with plasmid DNA, we used the eGFP-encoding mammalian expression plasmid pU.CAG.eGFP. One day before transfection, iAMs were seeded at a density of 4.8×10^5 cells per well in a 24-well cell culture plate and maintained in iAM culture medium with dox. The next day, the cells were transfected with Lipofectamine 3000 reagent (Thermo Fisher Scientific) according to the manufacturer's instructions. To this end, 50 µl of plasmid DNA-lipid complexes containing 500 ng of pU.CAG.eGFP DNA, 1 µl of P3000 reagent and 1.5 µl of Lipofectamine 3000 reagent diluted in Opti-MEM I reduced serum medium (Thermo Fisher Scientific) were added per well to 500 µl of iAM culture medium without dox. At the indicated times after the start of the transfection procedure, the cells were processed for flow cytometry using a BD Accuri flow cytometer (BD Biosciences), (immuno)fluorescence microscopy and optical voltage mapping. For the cells that were analysed at day 9 post-transfection, the transfection medium was replaced with regular iAM culture medium without dox 2 days after the addition of the lipoplexes.

Statistical analyses

Data were derived from a specified number (N) of observations from 3 different cell cultures. Unless otherwise stated, data were expressed as mean±standard deviation (SD) and SDs were represented by error bars. All data were analysed with the nested ANOVA test using the Real Statistics Resource Pack software (release 5.1, copyright 2013 – 2017, Charles Zaiontz, www.real-statistics.com). For comparisons involving >2 experimental groups, this test was followed by Bonferroni *post-hoc* analysis. Results were considered statistically significant at P values <0.05. Statistical significance was expressed as follows: *: $P<0.05$, **: $P<0.01$, ***: $P<0.001$, ****: $P<0.0001$.

Supplemental results

Excitability of iAMs

Short depolarizing current-clamp stimulations of single cells (10-20 ms, 100-300 pA, holding potential: -80 mV) were sufficient to evoke APs in pAMs (*Figure S2B*, left panel) and in a fraction of iAMs (*Figure S2B*, right panel). The fraction of these so-called excitable iAMs gradually increased from ±35% at day 3 of culture in the absence of dox to ±90% at day 9 and 12 after the initiation of the differentiation process by dox removal (*Figure S2C*).

The shapes of the pAM and iAM APs were similar based on the nearly identical APDs at 30 and 80% repolarization (APD_{30} and APD_{80}, respectively). Also, the while the AP amplitudes of iAMs did not significantly differ from those of pAMs although iAMs had a smaller upstroke velocity and overshoot than pAMs (*Table S3*). Thus, overall, the excitability properties of pAMs and cardiomyogenically differentiated iAMs were rather similar.

To investigate the ionic basic of the APs generated by iAMs, whole-cell membrane current was recorded using voltage steps applied from a holding potential of -90 mV to test potentials ranging from -130 through +70 mV. In pAMs (*Figure S2B*, left panel), the whole-cell current evoked by hyperpolarizing potentials was

inward and stationary and had the properties of an inward rectifier K^+ current[12]. The magnitude of this current gradually declined to zero when increasing the potentials from -130 to -70 mV. Depolarization beyond a holding potential of -70 mV elicited a large, fast transient inward current with a time course typical of a fast voltage-activated Na^+ current, as in Ramos-Mondragon *et al.*[13], and consistent with mRNA expression of *Scn5a* (*Figure S1A*). Upon further depolarization, the fast inward current became smaller and gradually gave way to a tiny outward current which, based on its electrophysiological characteristics and the RT-qPCR data, likely represents an outward rectifier K^+ current. As shown in the right panel of *Figure S2B*, excitable iAMs displayed a similar total inward current as pAMs but a much stronger total outward current and no obvious inwardly rectifying K^+ current (*i.e.* I_{K1}), consistent with the absence of detectable *Kcnj2* expression in iAMs (*Figure S1H*). Since I_{K1} is important for maintaining a stable negative RMP[12], optical voltage mapping and patch-clamp studies were conducted to determine the role of the atrium-specific acetylcholine-activated K^+ channels (*i.e.* $K_{ir}3.1$ and $K_{ir}3.4$) and the electrogenic Na^+/K^+ pump in regulating the RMP of cardiomyogenically differentiated iAMs (*Figure S3*).

First, we applied the muscarinic receptor agonist carbachol to maximize $I_{K,ACh}$ currents in confluent pAM and cardiomyogenically differentiated iAM monolayers. Carbachol had no effect on the CV (*Figure S3A* and *D*) or RMP of the iAM (-67.5±2.5 mV vs -67.1±2.6 mV in control cultures, N=8) and pAM (-64.5±1.9 mV vs -64.3±1.7 mV, N=7) monolayers (*Figure S3B* and *E*). Also, no carbachol effect was measured in single pAMs (*Figure S3F*). However, iAMs dissociated from cardiomyogenically differentiated monolayers and subsequently cultured as single cells for 1-3 days showed a hyperpolarizing shift of -16.9±2.6 mV in the RMP after carbachol administration (*Figure S3C*), thereby approaching the RMP of pAMs.

To determine the role of the Na^+/K^+ ATPase in maintaining a hyperpolarized RMP, its activity was inhibited in a graded manner by exposing pAM and cardiomyogenically differentiated iAM monolayers to increasing concentrations of ouabain. After ouabain administration, the CV decreased dose-dependently in both the pAM and iAM monolayers, although the iAM cultures seemed somewhat more sensitive to ouabain than the pAM cultures. Also, monolayers subjected to 300 and 400 μM ouabain showed partial or full conduction block in optical mapping experiments (*Figure S3G* and *J*). These findings are consistent with the patch-clamp results, which showed a dose-dependent depolarizing effect of ouabain on the RMP of the monolayers (*Figure S3H, I, K* and *L*) due to both electrogenic effects and changes in the intracellular ion concentrations. To specifically investigate the electrogenic effects of the Na^+/K^+ pump, we performed single-cell patch-clamp measurements, because in these experiments the intra- and extracellular ion concentrations are fixed by the composition of the pipette and bath solutions, respectively. Since this gave a similar depolarizing effect of ouabain on the RMPs of pAMs and iAMs as found in the monolayer studies, we conclude that the Na^+/K^+ pump plays an important electrogenic role in maintaining a negative RMP in iAMs as well as pAMs. This result explains why iAM monolayers despite the lack of detectable *Kcnj2* expression (*Figure S1H*) are able to generate a stable hyperpolarized RMP to maintain excitability. Furthermore, the RMPs of single iAMs are less stable and more vulnerable to the

measurement conditions of the whole-cell patch-clamp (*Figure S2A*)[14], but are easily repolarized by (full) activation of $K_{ir}3.x$ channels.

In conclusion, the electrogenic contribution of the Na^+/K^+ pump to their RMP allows iAMs to display similar excitability properties as pAMs linked to the presence of similarly strong voltage-activated Na^+ currents.

iAMs as *in vitro* model for studying ion channel-drug interactions

Drug-induced ventricular arrhythmias due to inadvertent blockade of the $K_v11.1$ channel represents a major safety concern in drug development[15]. RT-qPCR analysis showed that the *Kcnh2*/$K_v11.1$ gene is highly expressed in iAMs peaking at 6 days after the initiation of differentiation. At this time, *Kcnh2* transcripts were 16-fold more abundant in iAMs than in pAMs at culture day 9 (N=3, $P<0.01$; *Figure S1G*). Double immunostaining of these cells for $K_v11.1$ and sarcomeric α-actinin showed that both cell types expressed the $K_v11.1$ protein and that it was concentrated around the nucleus and at the sarcolemma (*Figure S8A*). To test whether iAMs could be used to identify unintended $K_v11.1$ blockers, the effect of exposing iAMs at day 6 of differentiation to 100 nM of the antihistamine astemizole, which was previously shown to efficiently and selectively block the $K_v11.1$ channel[16], was studied by optical voltage mapping. Astemizole significantly increased APD at 40 and 90% repolarization (APD_{40} and APD_{90}, respectively) from 21.5±1.0 and 88.7±5.4 ms in vehicle-treated cultures to 30.2±2.1 and 110.9±4.2 ms in cultures containing 100 nM astemizole (N=6, $P<0.01$; *Figure S8B and C*) without affecting CV (14.8±2.8 cm/s vs 14.5±1.1 cm/s in control cultures; N=6, P=0.57; *Figure S8D and E*). These data demonstrate the presence of a detectable I_{Kr} in differentiating iAMs and show the utility of AM cultures as *in vitro* model to investigate the AP-prolonging effects of $K_v11.1$ blockers.

Plasmid DNA transfection of iAMs

The practical applicability of iAMs would benefit greatly from them being well transfectable with plasmid DNA. We hence tested whether iAMs would be amenable to plasmid DNA transfection with Lipofectamine 3000. Near-confluent cultures of proliferating iAMs were lipofected with the eGFP-encoding mammalian expression plasmid pU.CAG.eGFP in dox-free medium and transgene expression was assessed by direct fluorescence microscopy and flow cytometry at 2 and 9 days after dox removal (*Figure S9A and B*). At 2 days post-transfection, approximately 50% of the iAMs were $eGFP^+$, which percentage did not decrease following incubation of the cells in dox-free medium for 7 more days. Importantly, transfected cells differentiated equally well into functional cardiomyocytes as their non-transduced counterparts judged from the results of α-actinin immunostaining (*Figure S9C*) and optical voltage mapping (*Figure S9D*) of the iAM cultures at 9 day after transfection.

Engraftment of iAMs into viable neonatal rat atrium

To investigate their ability of engraftment, we developed a transplantation model to study the engraftment of iAMs in neonatal rat atrium (*Figure S10A*). eGFP-labelled iAMs were cultured for 2 days in dox-free medium to initiate cardiomyogenic differentiation and subsequently injected into the atrium. Following iAM injection, the

atrium was excised and kept in culture for 6 days. The presence of spontaneous contractions at the end of the culture period demonstrated that the atrial tissue was still viable after 6 days of culture (Supplementary material online, *Movie V*). Confocal laser scanning microscopy of the tissue after fixation at the end of the culture period revealed the presence of $eGFP^+$ cells throughout the atrium (*Figure S10B*). Immunostaining for α-actinin showed that many of the $eGFP^+$ cells possessed highly organized sarcomeres (*Figure S10B*), whose length (*i.e.* distance between 2 Z-lines) did not significantly differ from that of pAMs (*Figure S10C*). Collectively, these data provide evidence for the cardiomyogenic differentiation and structural integration of transplanted iAMs into atrial tissue.

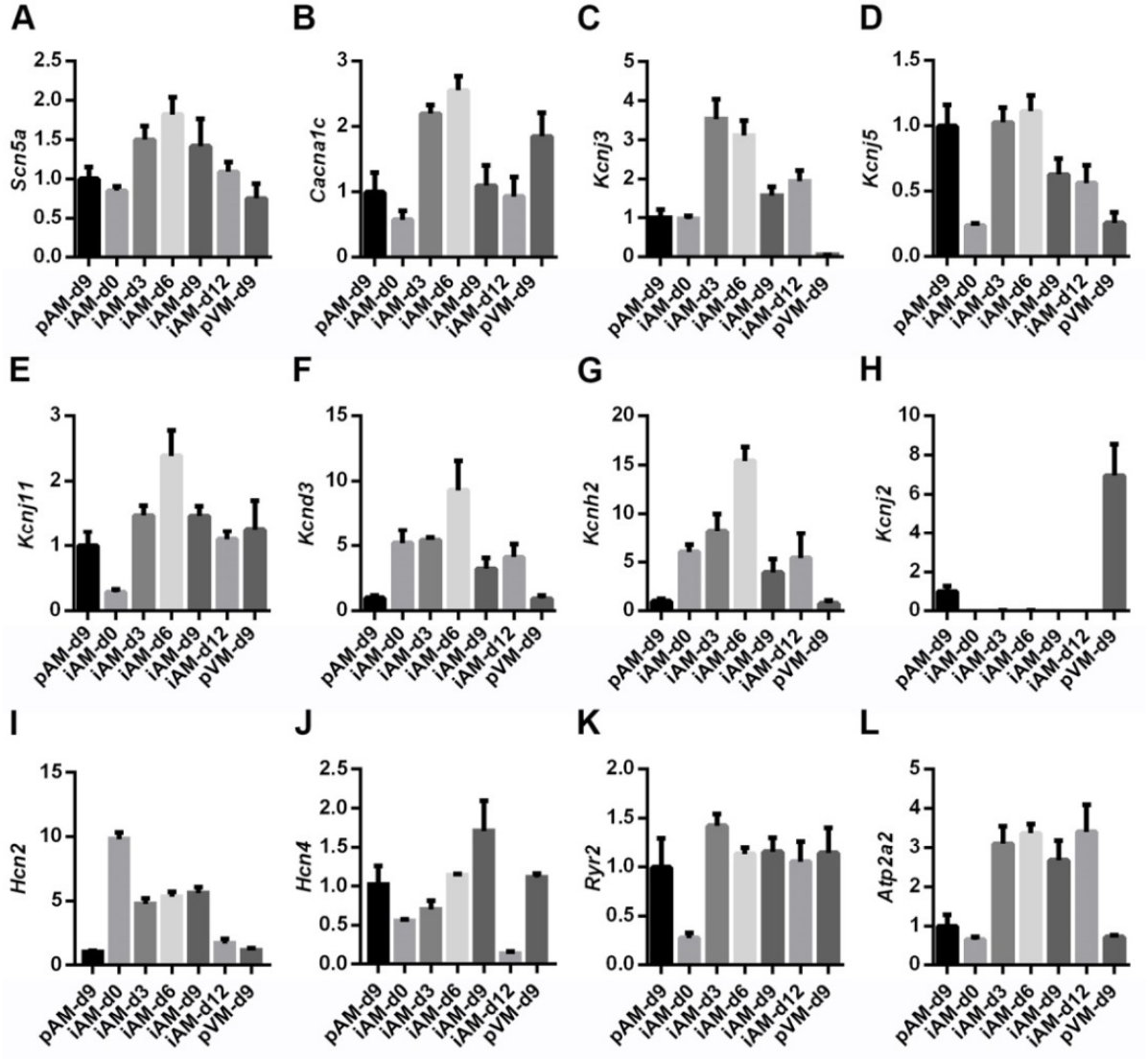

Figure S1. Analysis by RT-qPCR of the expression of the cardiac ion channel genes *Scn5a* (*A*), *Cacna1c* (*B*), *Kcnj3* (*C*), *Kcnj5* (*D*), *Kcnj11* (*E*), *Kcnd3* (*F*), *Kcnh2* (*G*), *Kcnj2* (*H*), *Hcn2* (*I*) and *Hcn4 (J)* and the cardiac Ca^{2+}-handling protein genes *Ryr2* (*K*) and *Atp2a2* (*L*) in pAMs and pVMs at day 9 of culture and in iAMs on the indicated days of differentiation. mRNA levels are expressed relative to those in 9-day-old pAM (pAM-d9) cultures, which were set at 1. Data are presented as mean±SD, N=3 individual preparations.

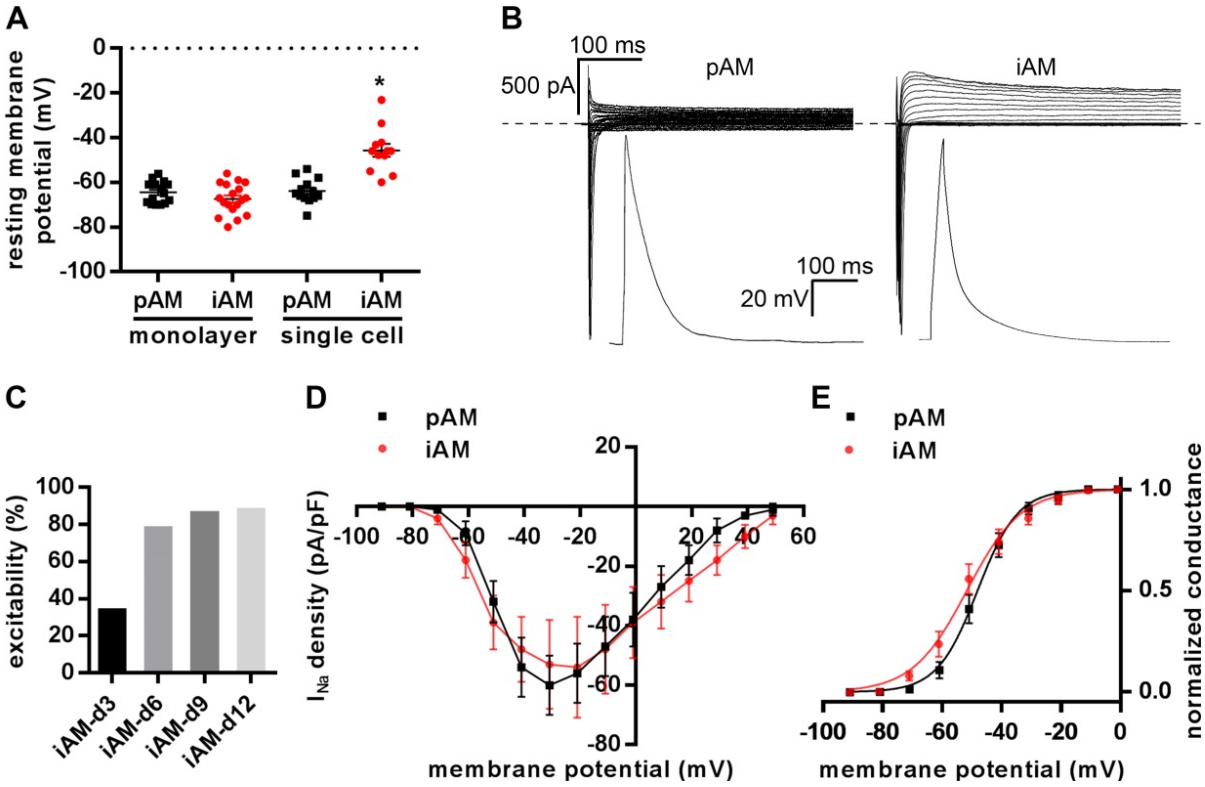

Figure S2. Single-cell patch-clamp analysis of pAMs and cardiomyogenically differentiated iAMs. *(A)* RMP of pAM monolayers (-64.5±1.2 mV, N=15), iAM monolayers (-67.5±1.6 mV, N=18), single pAMs (-63.9±1.5 mV, N=13) and single iAMs (-45.7±2.9 mV, N=12). (*B*) Whole-cell membrane current traces and APs of a pAM at culture day 3 (left) and an iAM kept in the absence of dox for 12 days (right). Before starting the measurement, the cells were clamped at a holding potential of -80 mV. (*C*) Graph showing the percentage of excitable iaCMCs at 3, 6, 9 and 12 days of differentiation. N=9, 9, 7 and 8 for iaCMC-d3, iaCMC-d6, iaCMC-d9 and iaCMC-d12, respectively. (*D*) $Na_v1.5$ I-V relationship and I_{Na} current (*i.e.* TTX-sensitive current) densities in single pAMs and iAMs. Current density was obtained by normalizing peak Na^+ currents to cell capacitance. (*E*) Steady-state of $Na_v1.5$ activation. pAM V½=-48.2±2.4 mV, slope factor=6.8±1.0 (N=5); iAM V½=-51.7±2.5 mV, slope factor=9.1±1.1 (N=6). Peak current densities and steady-state activation of single pAMs and iAMs were similar. Data are presented as mean±SEM. Statistics was done using the nested ANOVA test. *P<0.05.

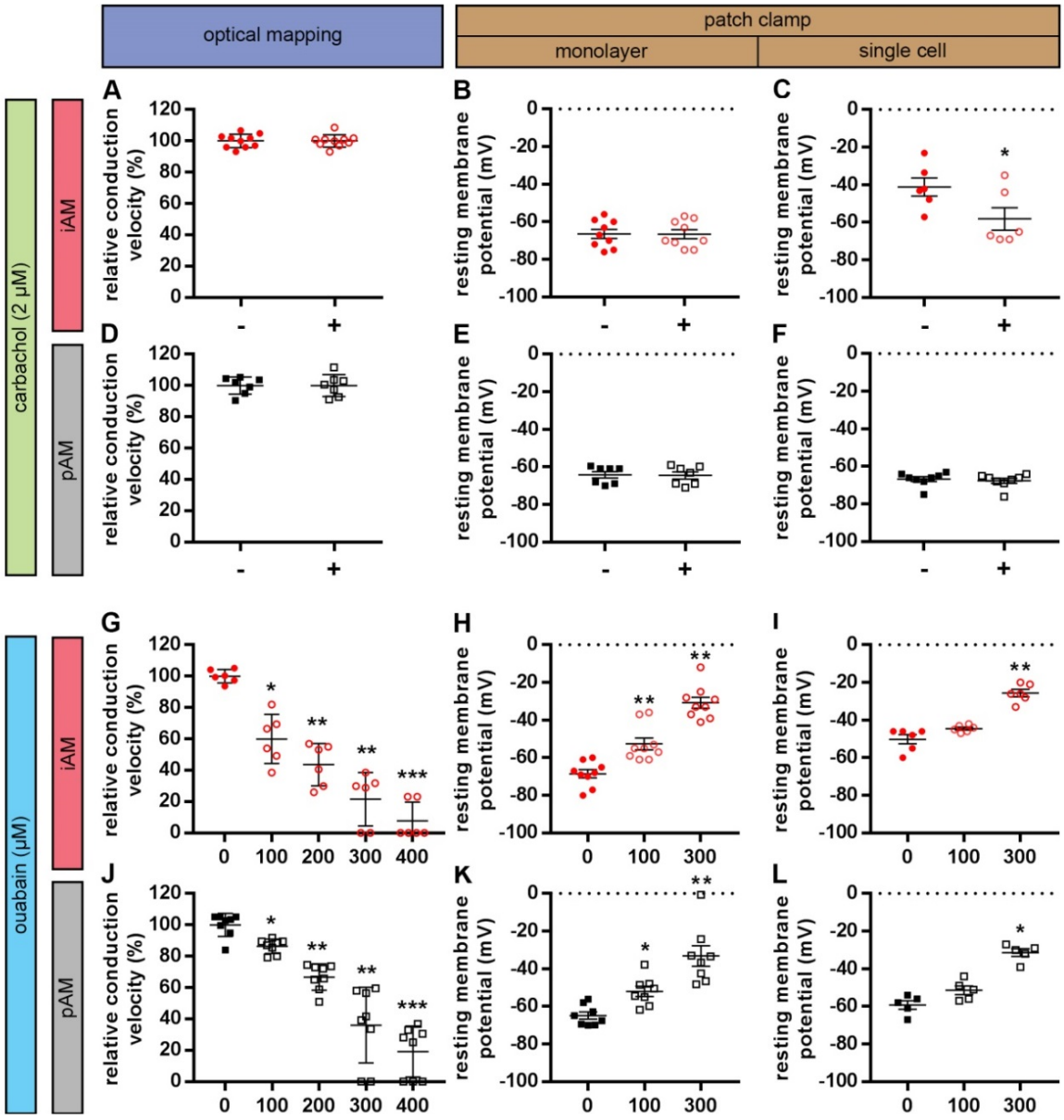

Figure S3. Electrophysiological analyses of pAM and iAM monolayers and single cells using optical voltage mapping and whole-cell patch-clamp recordings. Administration of 2 µM of carbachol to 9-day-old pAM monolayers and cardiomyogenically differentiated iAM monolayers did not affect the CV of (*A*) iAM (N=10) and (*D*) pAM monolayers (N=7). Consistently, patch-clamp recordings showed no shift in the RMP of (*B*) iAM (N=9) and (*E*) pAM (N=7) monolayers after carbachol treatment. Also carbachol had no effect on the RMP of single 2-3 day-old pAMs (N=8). However, iAMs dissociated from monolayers that had maintained for 9 days in the absence of dox showed a significant shift in the RMP (-16.9±2.6 mV, N=6) towards more negative potentials upon exposure to 2 µM carbachol. Statistics was done using the nested ANOVA test. Analysis by optical voltage mapping and whole-cell patch-clamp of cardiomyogenically differentiated iAM monolayers (*G*, N=6; and *H*, N=9) and single cells (*I*, N=6), as well as pAM monolayers (*J*, N=8; and K, N=8) and single cells (*L*, N=5) subjected to increasing concentrations of ouabain showed a significant dose-dependent decrease in CV and a depolarization of the RMP. Thus, the Na^+/K^+ ATPase plays a crucial role in maintaining a stable negative RMP in both pAMs and iAMs. Statistics was done using the nested ANOVA test with Bonferroni *post-hoc* correction. Optical voltage mapping data are presented as mean±SD, patch-clamp data as mean±SEM. **P*<0.05, ***P*<0.01 and ****P*<0.001.

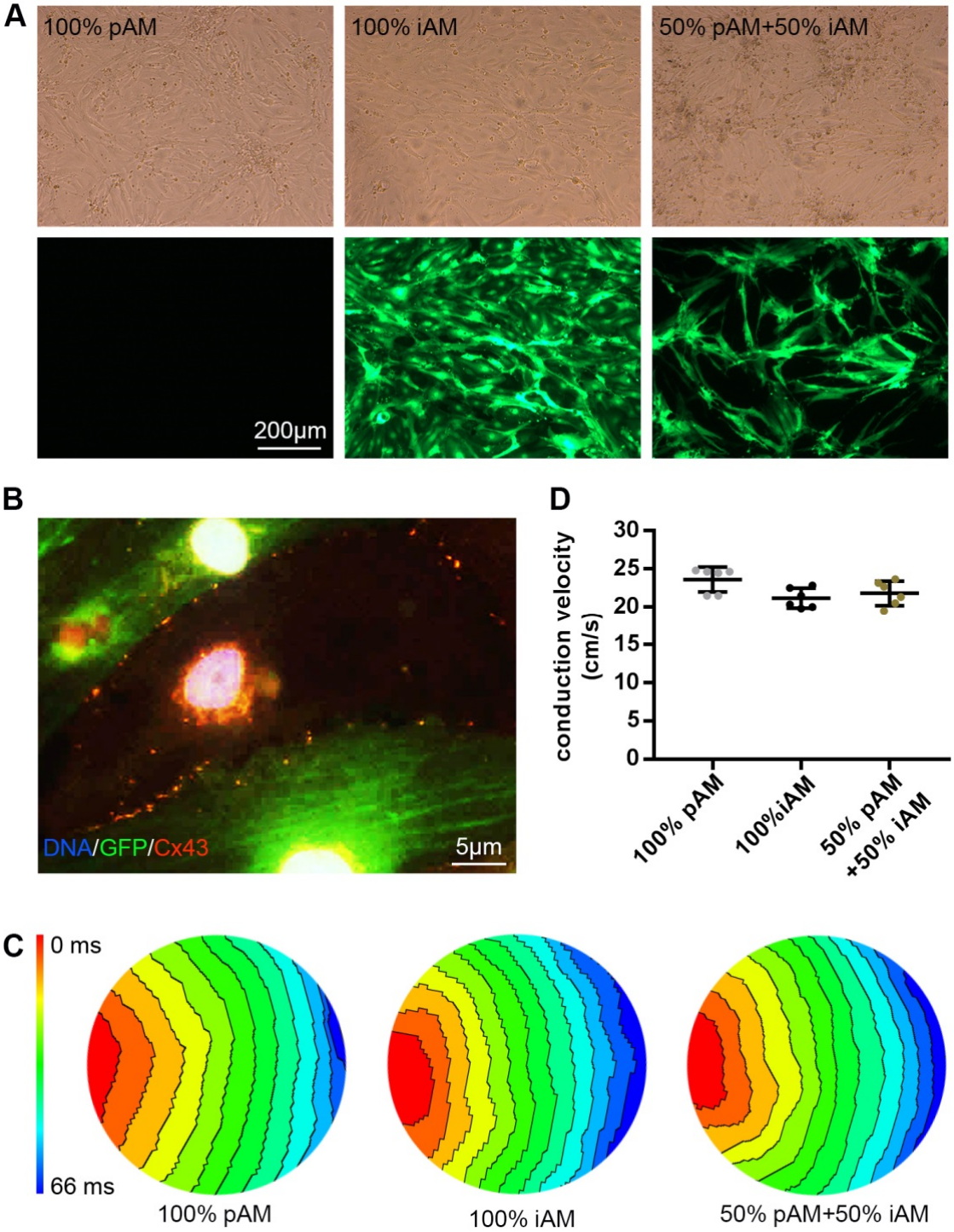

Figure S4. Comparison by optical voltage mapping and 1-Hz electrical point stimulation of the electrophysiological properties of confluent 9-day-old cultures of pAMs, dox-deprived eGFP-labelled iAMs (eGFP-iAMs) and 50% pAMs-50% eGFP-iAMs. (*A*) Bright field images (upper panel) and fluorescence images (lower panel) of each culture type. (*B*) Fluorescence image of 9-day-old pAM/eGFP-iAM co-culture immunostained for Cx43 (red) showing its presence at interfaces between iAMs (green) and pAMs. Cell nuclei have been visualized by staining with Hoechst 33342 (blue). (*C, D*) Activation maps (*C*; isochrones are separated by 6 ms) and CV quantification (*D*) reveal no significant different in the speed of AP propagation between the 3 culture types. Data are presented as mean±SD, N=6 cell cultures per group from 3 individual preparations. Statistics was done using the nested ANOVA test with Bonferroni *post-hoc* correction.

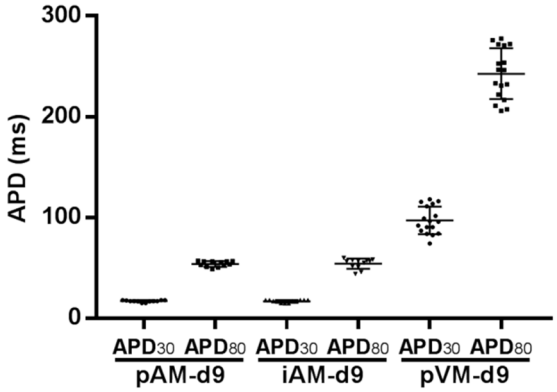

Figure S5. Comparison by optical voltage mapping and 1-Hz electrical point stimulation of APD_{30} and APD_{80} of pAMs and pVMs in 9-day-old cultures with those of iAMs at day 9 of differentiation showing that the pVMs have much longer APDs than the atrial myocytes. Data are presented as mean±SD, N=12 cell cultures per group from 4 individual preparations.

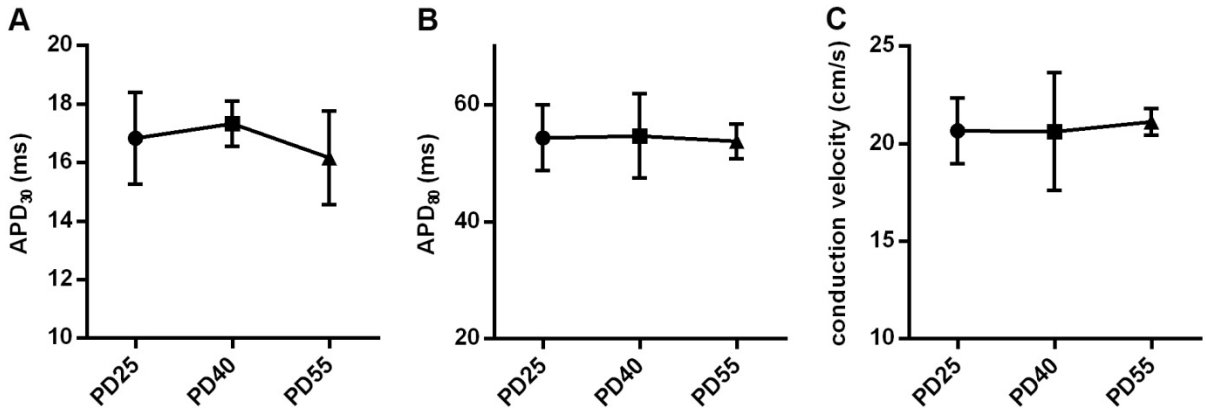

Figure S6. Comparison by optical voltage mapping and 1-Hz electrical point stimulation of the electrophysiological properties of iAMs at day 9 of differentiation (iAM-d9) that, after being cryopreserved, went through 25, 40 or 55 passage doublings (PDs) prior to dox removal. CV (*A*), APD_{30} (*B*) and APD_{80} (*C*) did not significantly differ between iAM-d9 of different PD. Data are presented as mean±SD, N=12 cell cultures per group from 4 individual preparations. Statistics was done using the nested ANOVA test with Bonferroni *post-hoc* correction.

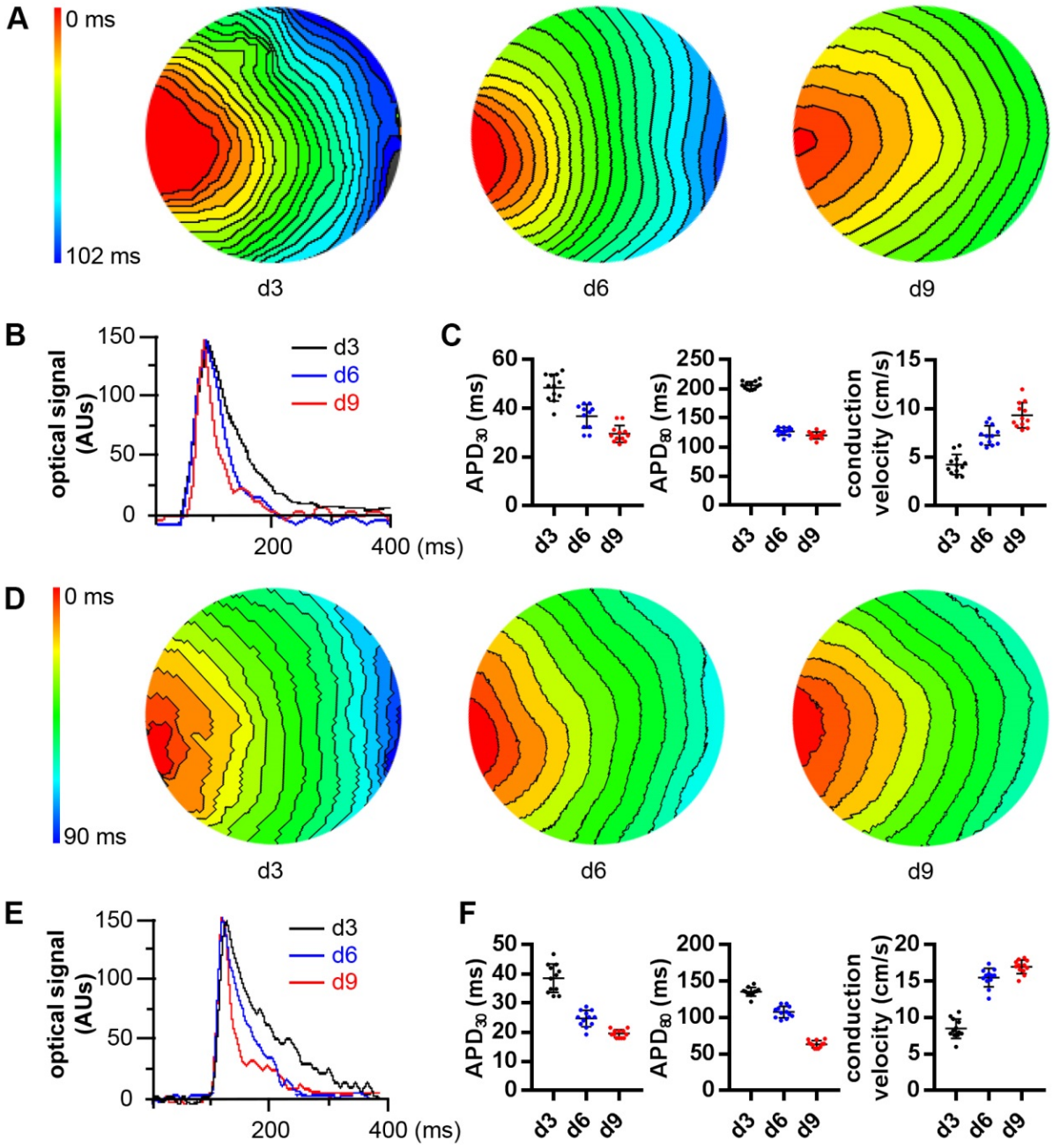

Figure S7. Characterization by optical voltage mapping and 1-Hz electrical point stimulation of confluent monolayers of iAM clones #1 (*A-C*) and #6 (*D-F*). Typical activation maps (*A, D*; isochrones are separated by 6 ms) and optical signal traces (*B, E*) acquired at different days after dox removal showing an increase in CV and a decrease in APD with advancing iAM differentiation. (*C, F*) Quantification of CV, APD_{30} and APD_{80} at 3, 6 and 9 days of iAM differentiation. Data are presented as mean±SD, N=12 cell cultures per group from 3 individual preparations. AUs, arbitrary units.

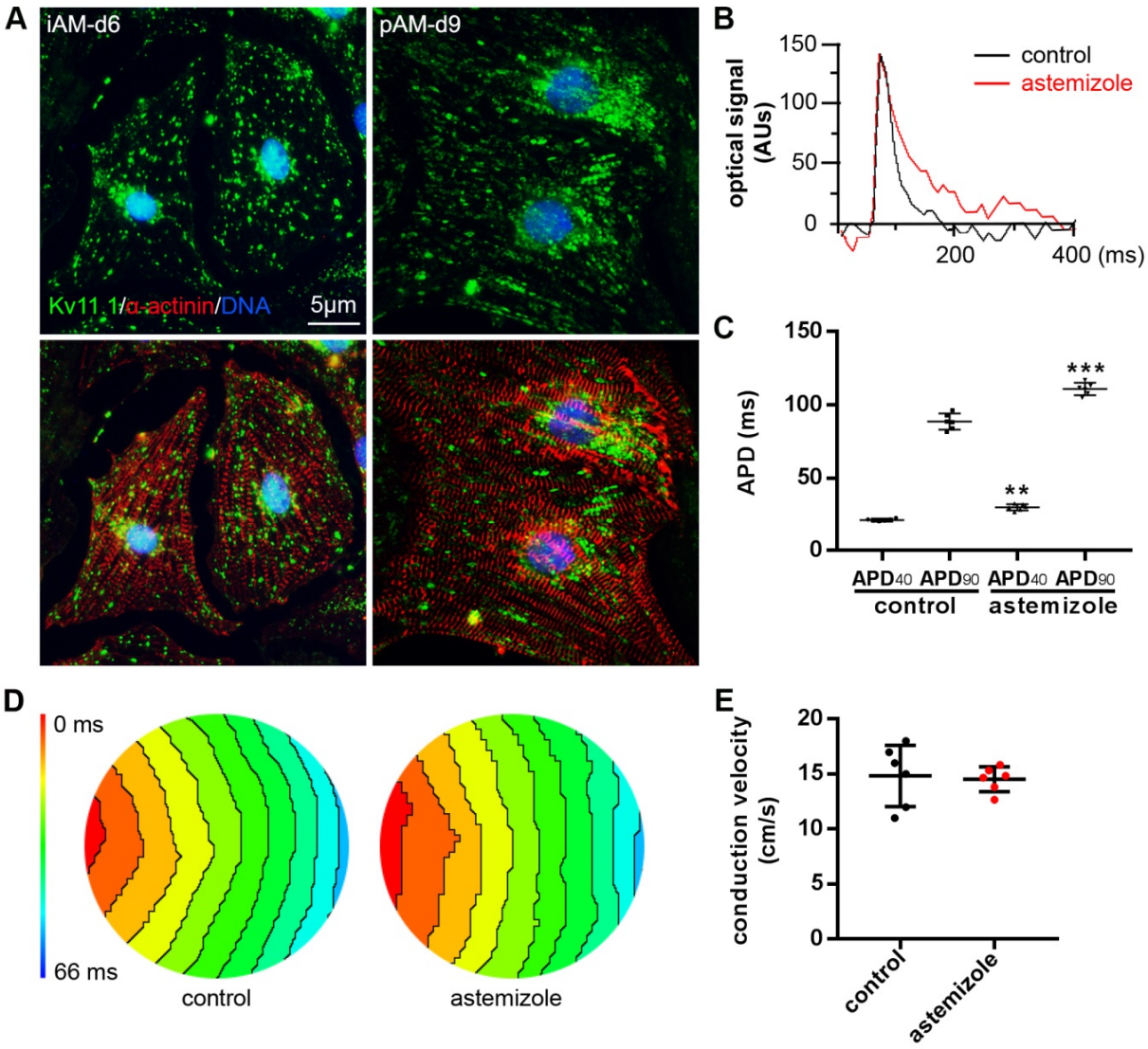

Figure S8. Suitability of iAMs as *in vitro* model to assess the I_{Kr}-blocking potential of drugs by optical voltage mapping. (*A*) Immunofluorescence analysis of $K_v11.1$ protein expression in iAM-d6 cultures and in 9-day-old pAM cultures. (*B-E*) Optical signal traces (*B*), quantitative analyses of APD_{40} and APD_{90} (*C*), activation maps (*D*) and CV (*E*) following 1-Hz pacing of iAM-d6 cultures exposed for 30 minutes to 100 nM astemizole or vehicle (control). Data are presented as mean±SD, N=6 cell cultures per group from 3 individual preparations. For statistical analysis, the nested ANOVA test was used. AUs, arbitrary units. $^{**}P<0.01$ vs control cultures.

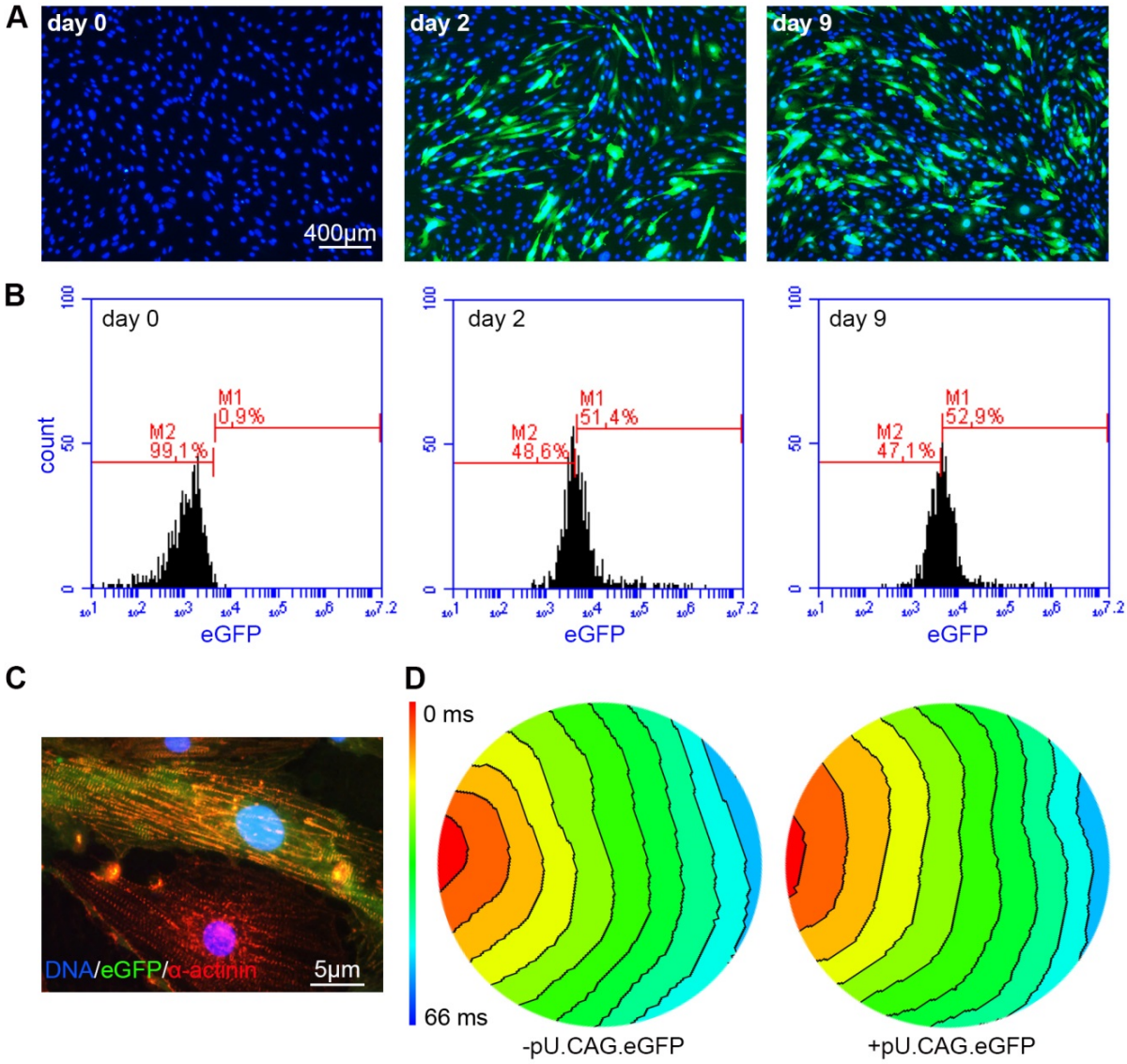

Figure S9. Transient transfection of iAMs with plasmid DNA. (*A*) Direct fluorescent images of iAMs immediately prior to lipofection (day 0) with the eGFP-encoding mammalian expression plasmid pU.CAG.eGFP (left panel) and following maintenance, after transfection, for 2 or 9 days in culture medium without dox (middle and right panel, respectively). (*B*) Quantification, by flow cytometry, of the percentage of $eGFP^+$ cells in the cultures shown in (*A*). (*C*) Fluoromicrograph of an iAM culture that was transfected with pU.CAG.eGFP, subsequently maintained for 9 days in dox-free culture medium and finally immunostained for sarcomeric α-actinin. (*D*) Activation maps (6-ms isochrone spacing) of untransfected (-pU.CAG.eGFP) and pU.CAG.eGFP-transfected (+pU.CAG.eGFP) iAM cultures kept for 9 days in dox-free culture medium.

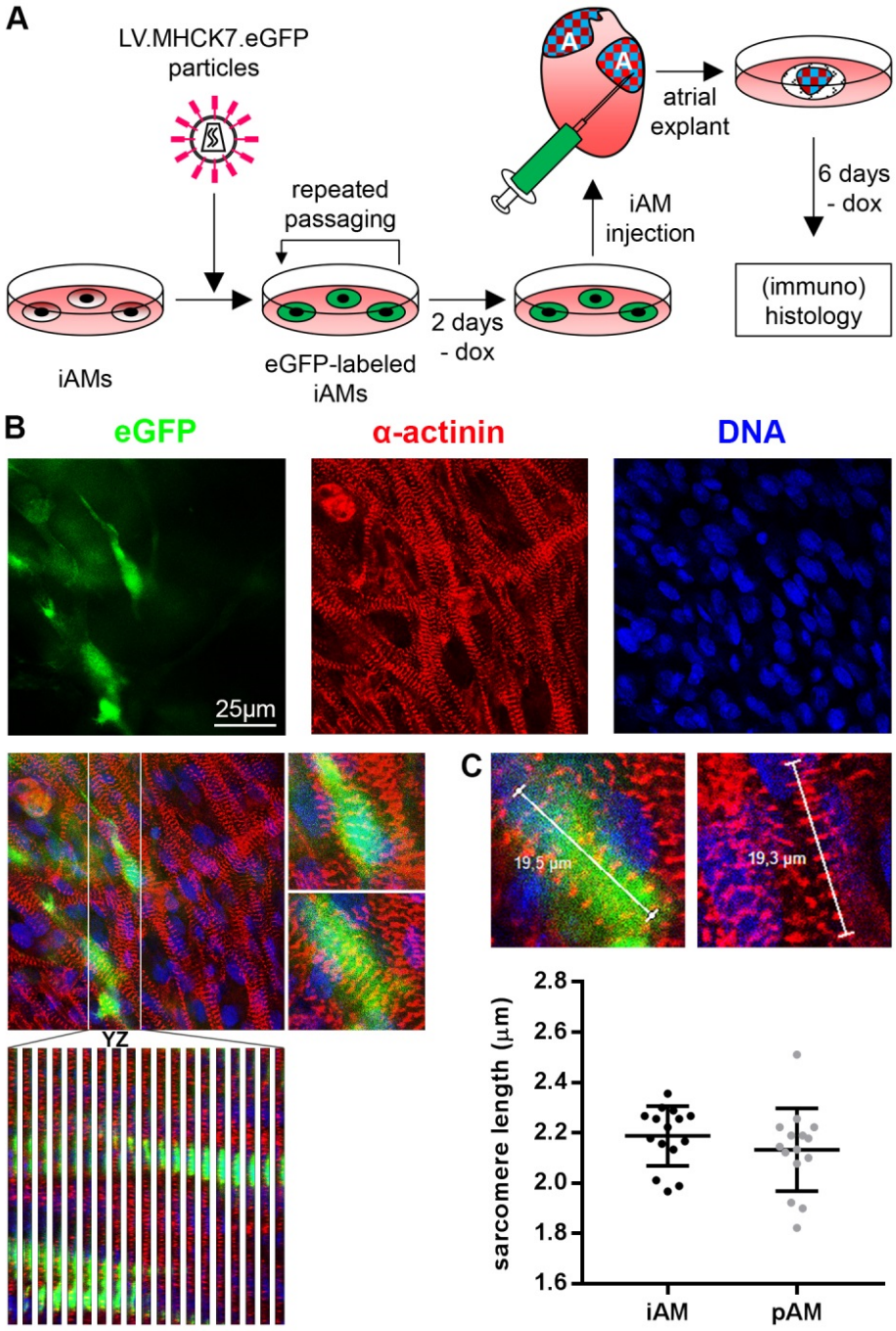

Figure S10. Structural integration of iAMs into neonatal rat atrium. (*A***)** Experimental design to assess the engraftment and cardiomyogenic differentiation potential of iAMs following their injection into neonatal rat atrium. A, atrium. **(***B***)** Analysis by confocal laser scanning fluorescence microscopy of the presence and phenotype of eGFP-labelled iAMs following double immunostaining for eGFP (green) and sarcomeric α-actinin (red) and labelling of cell nuclei with Hoechst 33342 (blue). The 2 small panels in the middle row represent higher magnifications of the upper 2 $eGFP^+$ cells in the adjacent larger panel. A series of YZ reconstructions of the $eGFP^+$ cell-rich zone in this panel (area demarcated by white lines) is shown in the bottom panel. **(***C***)** Sarcomere lengths of endogenous pAMs and of iAMs that underwent cardiomyogenic differentiation following intra-atrial injection. Data are presented as mean±SD, N=15 cells per experimental group from 3 individual preparations. For statistical analysis, the nested ANOVA test was used.

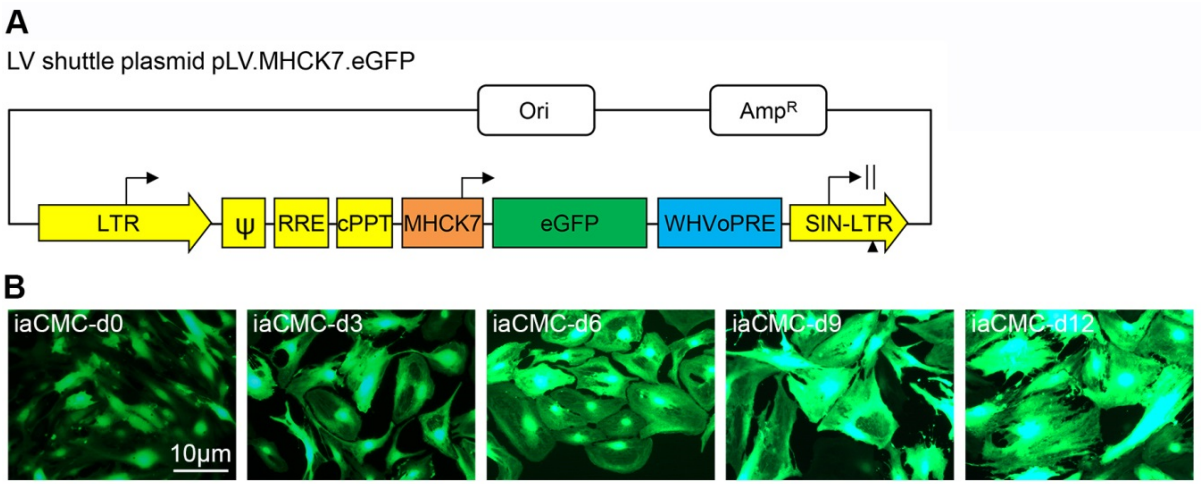

Figure S11. Activity of the MHCK7 promoter in proliferating iAMs and in iAMs at different days after initiation of cardiomyogenic differentiation. (*A*) Map of LV shuttle plasmid pLV.MHCK7.eGFP eGFP, eGFP-coding sequence. WHVoPRE, optimized version of the WHVPRE[6], SIN-LTR, 3' long terminal repeat containing a 400-bp deletion in unique region 3 rendering the corresponding LV self-inactivating[17]. For an explanation of the other abbreviations, see *Figure 1A*. (*B*) Fluoromicrographs of LV.MHCK7.eGFP-transduced iAMs showing an increase in MHCK7 promoter activity, as evinced by an increase in eGFP fluorescence, with advancing iAM differentiation.

Movies

Movie I. iAM culture at 6 days after dox removal showing spontaneously contracting cells.

Movie II. iAM culture at 9 days after dox removal showing rhythmic contractions evoked by 1-Hz electrical point stimulation.

Movie III. Optical voltage recordings showing spreading of action potentials in a 9-day-old pAM culture, iAM cultures at 3 and 9 days after dox removal and an HL-1 culture following 1-Hz electrical point stimulation. The movie is played at 1/8th of the normal speed.

Movie IV. iAM culture at 9 days after dox removal showing reentrant conduction provoked by high-frequency electrical point stimulation. The movie is played at 1/8th of the normal speed.

Movie V. Neonatal rat atrial tissue injected with eGFP-labelled iAMs and kept in culture for 6 days showing spontaneous contractions.

Supplemental discussion

For most parenchymal cell types including cardiomyocytes, proliferation and (terminal) differentiation are mutually exclusive processes. Permanent LT expression, as occurs in the AT-1[18], HL-1[19] and AC[20] lines therefore does not allow the generation of homogeneous populations of differentiated cells. For HL-1 cells, this problem was partially overcome by culturing them in a highly specialized medium promoting their cardiomyogenic differentiation[21]. In order to control LT activity, Jahn *et al.* [22] and Goldman *et al.*[23] relied on a temperature-sensitive version of the LT antigen (*i.e.* LT mutant *ts*A58) to immortalize neonatal rat and human foetal cardiomyocytes, respectively. Culturing of the neonatal rat cardiomyocytes at the non-permissive temperature of 39°C promoted their cardiomyogenic differentiation but still didn't yield excitable cells with well-developed sarcomeres whereas the human foetal cardiomyocytes failed to express cardiac differentiation markers at both the restrictive and permissive temperature. As an alternative method to control LT activity, Rybkin *et al.* generated transgenic mice containing an LT expression cassette under the control of cardiac-specific transcriptional regulatory elements of the murine *Nkx2.5* gene from which the LT-coding sequence could be excised using Cre recombinase. Cells isolated from the subendocardial tumor-like structures in the hearts of these animals could be serially passaged >50 times without showing obvious signs of senescence. Following removal of the LT-coding sequence by transduction with an adenovirus vector expressing Cre recombinase, the cells developed sarcomeres and some of them produced weak and slow Ca^{2+} transients after electrical stimulation. This, however, only occurred in low-serum medium containing insulin, transferrin and selenium or after ectopic expression of cardiomyogenic factors and did not result in the generation of contractile cells. Zhang *et al.*[24] also relied on the Cre-LoxP site-specific recombination system to generate lines of conditionally immortalized pVMs. Cre-mediated removal of the LT expression module and exposure to cardiomyogenic differentiation conditions did, however, not give rise to excitable or contractile cells.

The aforementioned immortalization strategy in which the immortalization gene is flanked with recombinase recognition sites to allow its excision following cell amplification thereby facilitating redifferentiation of the cells has some inherent disadvantages. Firstly, immortalization and subsequent deimmortalization of the cells requires two consecutive genetic manipulations. Secondly, due to the specific nature of the recombinase-mediated excision reaction, repeated switching between proliferative and differentiated cell states is impractical making deimmortalization essentially an irreversible process. Thirdly, recombinase-mediated excision reactions are never complete. Consequently, after recombinase treatment of a cell population there will always be a small fraction of cells that have retained the immortalization gene. As these cells will have a proliferative advantage, they will gradually "overgrow" the deimmortalized cells in the culture.

These drawbacks and the poor cardiomyogenic differentiation capacity of the deimmortalized cardiac muscle cell lines generated by Rybkin *et al.*[25] and Zhang *et al.*[24] prompted us to test another conditional immortalization strategy in an attempt to generate (fully) differentiation-competent cardiomyocyte lines. By transducing pAMs with an LV directing myocyte-selective and dox-dependent expression of the SV40

LT antigen, we succeeded to establish lines of cardiomyocytes showing rapid expansion in the presence of dox, while in its absence, the cells spontaneously and synchronously differentiated into fully functional *(i.e.* excitable and contractile) AMs.

As primary cultures of pAMs inevitably contain some non-cardiomyocytes (mainly cardiac fibroblasts), the myocyte-specific MHCK7 promoter[4,5] was chosen to drive LT expression to avoid the fortuitous generation of non-cardiomyocyte clones. The success of this strategy critically depended on the MHCK7 promoter remaining active following the dedifferentiation of the AMs. Comparison of MHCK7 promoter activity in proliferating and differentiating AMs (*Figure S11*) showed that this was indeed the case. Cardiomyogenic differentiation led to an increase in the transcriptional activity of this promoter, consistent with the upregulation of cardiac transcription factor gene expression (*Figure 3A*). Nonetheless, LT expression was not detectable in differentiated iAMs either by western blotting or by IFM (*Figure 1C-E*). Concordantly, expression of the proliferation marker Ki-67 quickly ceased in the absence of dox (*Figure 2B and F*) indicating that soon after dox removal LT levels became too low to stimulate cell division.

Table S1 Primer pairs used for gene expression analysis

Gene	Forward primer	Reverse primer
Actn2	GGCTATGAGGAATGGCTATTGA	AAGTAGGGCTCGAACTTCC
Atp2a2	TGACCCACGAGCTGTTAATC	GGTGTTCTCTCCTGTTCTGT
Cacna1c	CAAGGTGGTACACGAAGCTCA	ACAGTGCTGCCCCTGGAGTA
Gata4	GGCTCTCTGGGAAACTGG	GAGGTGCCTAGTCCTTGC
Kcnd3	CAACTTTAGCAGGATCTACCATC	AGAGCTTCATTGAGGAGTCCA
Kcnh2	TAGCCTCCTCAACATCCC	CCATGTCTGCACTTAGCC
Kcnj2	GGATCTTACATGCTTCTGTAACC	CAGAGAACTTGTCCTGTTGC
Kcnj3	ACAGCCACATGGTCTCC	CCAGTTCAAGTTGGTCAAGG
Kcnj5	GGTTGTGGTCATACTAGAAGGG	GCAGTCATATCTGCCTTGGG
Kncj11	GGAAGACCCGGAGGTAATAAG	CTCCACTCAGCTATCCTTCAC
Mef2c	GATTCAGATCACGAGGATTATGG	GTGCTGTTGAAGATGATCAGG
Myh6	CTACCAGATCCTGTCCAACAA	GCACATCAAAGGCGCTATC
Myh7	CACCAAGAGGGTCATCCAATA	CCAAATCGGGAGGAGTTATCA
Myl2	TTTGAGCAGACCCAGATCC	ACGTGTCCCTTAGGTCATTC
Myl3	GCTCTGGGACAGAATCCTAC	TCTTGGAGTTGAGCTCTTCC
Myl4	TCAGGGACTCTGCCTTTG	CCTCTTTGAATTCTTCGATCTGG
Myl7	TCAATGTTCGAGCAAGCC	CTGACTTGCAGATGATTCCG
Nkx2.5	CTCCCACCTTTAGGAGAAGG	CGAGGCATCAGGTTAGGTC
Nppa	CCAAGGGCTTCTTCCTCTTC	CTCATCTTCTACCGGCATCTTC
Rn18s	GTAACCCGTTGAACCCCATT	CCATCCAATCGGTAGTAGCG
Ryr2	AACTGGCCTTTGATGTTGGC	AATATGAGGTCGTCTCCAACCC
Scn5a	CCATTGTGCCCTGACGAACCTTA	GCTGCCTCCAGCTTCCACACA

Table S2 Antibodies

Antigen	Host	Dilution	Supplier	Catalogue number
LT	mouse	1:2,000 (WB) 1:200 (IC)	Santa Cruz Biotechnology	sc-147
GAPDH	mouse	1:100,000 (WB)	Millipore	MAB374
Ki-67	rabbit	1:200 (IC)	Abcam	Ab15580
Sarcomeric α-actinin	mouse	1:200 (IC)	Sigma-Aldrich	A7811
MLC2a	rabbit	1:200 (IC)	Non-commercial source	
Cx43	rabbit	1:200 (IC)	Sigma-Aldrich	C6219
K_v11.1	rabbit	1:200 (IC)	Millipore	AB5930
eGFP	rabbit	1:200 (IC)	Thermo Fisher Scientific	A11122
Antigen	**Host**		**Supplier**	**Conjugate**
Mouse IgG	goat	1:15,000 (WB)	Santa Cruz Biotechnology	Horseradish peroxidase
Rabbit IgG (H+L)	donkey	1:400 (IC)	Thermo Fisher Scientific	Alexa 488
Mouse IgG (H+L)	donkey	1:400 (IC)	Thermo Fisher Scientific	Alexa 568

WB, western blotting; IC, immunocytology.

Table S3 AP properties of pAMs and iAMs

	pAM (N=13)	iAM (N=15)
Upstroke velocity (mV/ms)	19.1±1.9	11.4±1.2**
AP amplitude (mV)	108.3±4.0	94.4±2.3
Overshoot (mV)	23.8±3.7	13.9±2.4*
APD_{30} (ms)	20.5±2.6	19.5±1.3
APD_{80} (ms)	74.2±9.5	70.0±6.9

Data represent mean±standard error of the mean (SEM). Statistical analysis was done using the nested ANOVA test. *P<0.05; **P<0.01

Supplemental references

1. Loeber G, Tevethia MJ, Schwedes JF, Tegtmeyer P. Temperature-sensitive mutants identify crucial structural regions of simian virus 40 large T antigen. *J Virol* 1989;**63**:4426-4430.
2. Dinsart C, Cornelis JJ, Klein B, van der Eb AJ, Rommelaere J. Transfection with extracellularly UV-damaged DNA induces human and rat cells to express a mutator phenotype towards parvovirus H-1. *Mol Cell Biol* 1984;**4**:324-328.
3. Szulc J, Wiznerowicz M, Sauvain MO, Trono D, Aebischer P. A versatile tool for conditional gene expression and knockdown. *Nat Methods* 2006;**3**:109-116.
4. Salva MZ, Himeda CL, Tai PW, Nishiuchi E, Gregorevic P, Allen JM, Finn EE, Nguyen QG, Blankinship MJ, Meuse L, Chamberlain JS, Hauschka SD. Design of tissue-specific regulatory cassettes for high-level rAAV-mediated expression in skeletal and cardiac muscle. *Mol Ther* 2007;**15**:320-329.
5. Bingen BO, Engels MC, Schalij MJ, Jangsangthong W, Neshati Z, Feola I, Ypey DL, Askar SF, Panfilov AV, Pijnappels DA, de Vries AA. Light-induced termination of spiral wave arrhythmias by optogenetic engineering of atrial cardiomyocytes. *Cardiovasc Res* 2014;**104**:194-205.
6. Schambach A, Bohne J, Baum C, Hermann FG, Egerer L, von Laer D, Giroglou T. Woodchuck hepatitis virus post-transcriptional regulatory element deleted from X protein and promoter sequences enhances retroviral vector titer and expression. *Gene Ther* 2006;**13**:641-645.
7. Feola I, Teplenin A, de Vries AA, Pijnappels DA. Optogenetic engineering of atrial cardiomyocytes. *Methods Mol Biol* 2016;**1408**:319-331.
8. Ramkisoensing AA, De Vries AA, Schalij MJ, Atsma DE, Pijnappels DA. Brief report: Misinterpretation of coculture differentiation experiments by unintended labeling of cardiomyocytes through secondary transduction: delusions and solutions. *Stem Cells* 2012;**30**:2830-2834.
9. Majumder R, Engels MC, de Vries AA, Panfilov AV, Pijnappels DA. Islands of spatially discordant APD alternans underlie arrhythmogenesis by promoting electrotonic dyssynchrony in models of fibrotic rat ventricular myocardium. *Sci Rep* 2016;**6**:24334.
10. Yu Z, Liu J, van Veldhoven JP, AP IJ, Schalij MJ, Pijnappels DA, Heitman LH, de Vries AA. Allosteric modulation of Kv11.1 (hERG) channels protects against drug-induced ventricular arrhythmias. *Circ Arrhythm Electrophysiol* 2016;**9**:e003439.
11. Kubalak SW, Miller-Hance WC, O'Brien TX, Dyson E, Chien KR. Chamber specification of atrial myosin light chain-2 expression precedes septation during murine cardiogenesis. *J Biol Chem* 1994;**269**:16961-16970.
12. Tristani-Firouzi M, Chen J, Mitcheson JS, Sanguinetti MC. Molecular biology of K+ channels and their role in cardiac arrhythmias1. *Am J Med* 2001;**110**:50-59.
13. Ramos-Mondragón R, Vega AV, Avila G. Long-term modulation of Na+ and K+ channels by TGF-β1 in neonatal rat cardiac myocytes. *Pflugers Arch* 2011;**461**:235-247.
14. Wilson JR, Clark RB, Banderali U, Giles WR. Measurement of the membrane

potential in small cells using patch clamp methods. *Channels* 2011;**5**:530-537.
15. Kannankeril P, Roden DM, Darbar D. Drug-induced long QT syndrome. *Pharmacol Rev* 2010;**62**:760-781.
16. Delpon E, Valenzuela C, Tamargo J. Blockade of cardiac potassium and other channels by antihistamines. *Drug Saf* 1999;**21 Suppl 1**:11-18; discussion 81-17.
17. Zufferey R, Dull T, Mandel RJ, Bukovsky A, Quiroz D, Naldini L, Trono D. Self-inactivating lentivirus vector for safe and efficient in vivo gene delivery. *J Virol* 1998;**72**:9873-9880.
18. Steinhelper ME, Cochrane KL, Field LJ. Hypotension in transgenic mice expressing atrial natriuretic factor fusion genes. *Hypertension* 1990;**16**:301-307.
19. Claycomb WC, Lanson NA, Jr., Stallworth BS, Egeland DB, Delcarpio JB, Bahinski A, Izzo NJ, Jr. HL-1 cells: a cardiac muscle cell line that contracts and retains phenotypic characteristics of the adult cardiomyocyte. *Proc Natl Acad Sci U S A* 1998;**95**:2979-2984.
20. Davidson MM, Nesti C, Palenzuela L, Walker WF, Hernandez E, Protas L, Hirano M, Isaac ND. Novel cell lines derived from adult human ventricular cardiomyocytes. *J Mol Cell Cardiol* 2005;**39**:133-147.
21. White SM, Constantin PE, Claycomb WC. Cardiac physiology at the cellular level: use of cultured HL-1 cardiomyocytes for studies of cardiac muscle cell structure and function. *Am J Physiol Heart Circ Physiol* 2004;**286**:H823-829.
22. Jahn L, Sadoshima J, Greene A, Parker C, Morgan KG, Izumo S. Conditional differentiation of heart- and smooth muscle-derived cells transformed by a temperature-sensitive mutant of SV40 T antigen. *J Cell Sci* 1996;**109 (Pt 2)**:397-407.
23. Goldman BI, Amin KM, Kubo H, Singhal A, Wurzel J. Human myocardial cell lines generated with SV40 temperature-sensitive mutant tsA58. *In Vitro Cell Dev Biol Anim* 2006;**42**:324-331.
24. Zhang Y, Nuglozeh E, Toure F, Schmidt AM, Vunjak-Novakovic G. Controllable expansion of primary cardiomyocytes by reversible immortalization. *Hum Gene Ther* 2009;**20**:1687-1696.
25. Rybkin, II, Markham DW, Yan Z, Bassel-Duby R, Williams RS, Olson EN. Conditional expression of SV40 T-antigen in mouse cardiomyocytes facilitates an inducible switch from proliferation to differentiation. *J Biol Chem* 2003;**278**:15927-15934.

Chapter 5

Generation of conditionally immortalized brown pre-adipocytes with preserved adipogenic capacity

Jia Liu, Sander Kooijman, Eline N. Kuipers, Hetty C. M. Sips, Patrick C. N. Rensen, Martin J. Schalij, Daniël A. Pijnappels,Antoine A.F. de Vries

To be submit

Abstract

Brown adipose tissue (BAT) is regarded as a potential target to treat obesity and associated metabolic disorders because of its capacity to take up and combust glucose and fatty acids for thermoregulation. However, its cellular and molecular investigation has been hampered due to high cellular heterogeneity and a limited availability of cell material. In this study, monoclonal lines of conditionally immortalized brown preadipocytes (iBPAs) were generated, using mouse BAT as starting material. These cell lines retain long-term proliferation as well as adipogenic capacity. RT-qPCR analyses showed that brown fat markers including uncoupling protein 1 (Ucp1) were highly expressed in brown fat cells differentiated from iBPAs. Furthermore, the differentiated cells responded to β3-adrenergic stimulation by increasing glycerol release and *Ucp1* expression. iBPA-derived brown fat cells may represent an easy-to-use model system for fundamental and applied research into BAT.

Introduction

Obesity results from energy intake exceeding expenditure and is a major risk factor for metabolic disorders. A positive energy balance leads to storage of excess energy mainly in adipose tissue[1,2]. In mammals, two major types of functionally distinct adipose tissue exist, *i.e.* white adipose tissue (WAT) and brown adipose tissue (BAT)[3]. WAT is specialized in storing energy in the form of triglycerides[4-6], while brown adipocytes dissipate energy for heat production by uncoupling the electron transport chain from ATP synthesis through expression of uncoupling protein 1 (UCP1)[4,7-11]. As a result, BAT represents a therapeutic target to enhance energy expenditure and combat obesity and related metabolic disorders[2,12,13].

The development of therapeutic strategies based on BAT is hampered by the lack of proper brown adipocyte cell culture models. As mature adipocytes are post-mitotic and thus unable to multiply themselves *in vitro*, the formation of sufficient brown adipocytes for experiments requires proliferation and differentiation of adipocyte precursors. Over the last years, a number of different murine brown preadipocyte (BPA) lines have been generated such as BFC-1[14], HB2[15], HIB 1B[16,17] and T37i[18]. Although these cell lines have been helpful in increasing the understanding of adipocyte biology, they all possess some inherent disadvantages limiting their usefulness as model systems to study the properties of brown fat. BCF-1 cells are spontaneously immortalized cells derived from interscapular BAT but do not express detectable amounts of *Ucp1* following differentiation even after adrenergic stimulation with isoproterenol[19]. HB2 cells are brown preadipocytes isolated from the interscapular BAT of p53 knockout mice, while HIB 1B and T37i cells were derived from transgenic mice expressing the simian virus 40 (SV40) large T (LT) antigen using constitutively active, lineage-restricted promoters to drive transgene expression. While these transgenic cells all express *Ucp1* following adipogenic differentiation and proper stimulation, their gene expression profiles may not accurately recapitulate that of native brown fat cells as both p53 and LT have been shown to affect formation of brown adipocytes[20,21]. Moreover, continuous proliferation pressure due to permanent immortalization may alter the differentiation capacity of BPAs causing their differentiated progeny to functionally differ from primary brown fat cells. Indeed, HB2 cells display a passage number-dependent decrease in the ability to express *Ucp1* following adipogenic differentiation and adrenergic stimulation[15]. These drawbacks prompted us to generate conditionally immortalized monoclonal BPA (iBPA) lines of mice by using a lentiviral vector (LV) expressing LT in a doxycycline (dox)/tetracycline-dependent manner to control cell proliferation[22]. The resulting monoclonal cell lines were characterized in terms of their dox-dependent LT expression level and proliferation capacity and their ability to undergo adipogenic differentiation in the presence of insulin and rosiglitazone using multilocular lipid droplet formation and expression of brown fat marker genes as read-out systems. Finally, the effects of adrenergic stimulation on the glycerol secretion and *Ucp1* mRNA expression of adipogenically differentiated iBPAs was studied.

Materials and Methods

Construction of plasmids

DNA constructions were carried out with enzymes from Fermentas (Thermo Fisher Scientific, Breda, the Netherlands) or from New England Biolabs (Bioke´, Leiden, the Netherlands) and with oligodeoxyribonucleotides from Sigma-Aldrich (Zwijndrecht, the Netherlands) using established procedures or following the instructions provided with specific reagents.

Plasmid pAT153.SV40ori(-)*ts*A58, which codes for the temperature-sensitive mutant of the oncogenic SV40 LT antigen designated *ts*A58[23], was used as template in a polymerase chain reaction (PCR) with VELOCITY DNA polymerase (GC Biotech, Alphen aan den Rijn, the Netherlands) and primers 5' AAGGATCCGTGCACCATGGATAAAGTTTTAAACAGAGAGGA 3' and 5' CCGAATTCTTTATGTTTCAGGTTCAGGG 3' (the LT initiation codon and the complement of its termination codon are underlined). The resulting PCR fragment was inserted into plasmid pJET1.2/blunt using the CloneJET PCR cloning kit (Thermo Fisher Scientific) to generate pJet1.2.LT-*ts*A58. pJet1.2.LT-*ts*A58 was incubated with BamHI and EcoRI and the 2.5-kb digestion product was combined with the 11.5-kb BamHI×EcoRI fragment of SIN-LV shuttle plasmid pLVET.tTS.dEcoRI to generate pLV.ihEEF1A1.LT-*ts*A58. pLVET.tTS.dEcoRI is a derivative of pLVET-tTR-KRAB[22] (Addgene, Cambridge, MA; plasmid number: 116444). It was made by digestion of pLVET-tTR-KRAB with EcoRI and NheI and ligation of the resulting 1.6-kb fragment encoding the encephalomyocarditis virus internal ribosomal entry site and the tetracycline-controlled transrepressor protein TetR-KRAB[24] to the 10.8-kb EcoRI×BcuI fragment of pLVET-tTR-KRAB.

LV production

LV production was carried out as detailed before[25]. To generate vesicular stomatitis virus G protein-pseudotyped particles of LV.ihEEF1A1.LT-*ts*A58, subconfluent monolayers of 293T cells were transfected with LV shuttle construct pLV.ihEEF1A1.LT-*ts*A58 and the packaging plasmids psPAX2 (Addgene; plasmid number: 12260) and pLP/VSVG (Thermo Fisher Scientific) at a molar ratio of 2:1:1. The 293T cells were cultured in high-glucose Dulbecco's modified Eagle's medium (DMEM; Life Technologies Europe, Bleiswijk, the Netherlands; catalogue number: 41966) with 10% fetal bovine serum (FBS; Life Technologies Europe). The transfection mixture consisted of 35 µg of plasmid DNA and 105 µg of polyethyleneimine (Polysciences Europe, Eppelheim, Germany) in 2 ml of 150 mM NaCl per 175-cm^2 cell culture flask (Greiner Bio-One, Alphen aan den Rijn, the Netherlands) and was directly added to the culture medium. The next morning, the transfection medium was replaced by 15 ml of fresh high-glucose DMEM supplemented with 5% FBS and 25 mM HEPES-NaOH (pH 7.4). At ± 48 hours after the addition of plasmid DNA to the producer cells , the culture supernatants were harvested and cleared from cellular debris by centrifugation at room temperature (RT) for 10 min at 3,750×*g* and subsequent filtration through 0.45-µm pore-sized, 33-mm diameter polyethersulfone Millex-HP syringe filters (Millipore, Amsterdam, the Netherlands). To concentrate and purify the LV particles, 30 ml of vector suspension

in a 38.5-ml polypropylene ultracentrifuge tube (Beckman Coulter Nederland, Woerden, the Netherlands) was underlayed with 5 ml of 20% (wt/vol) sucrose in phosphate-buffered saline (PBS) and spun for 120 min at 4°C with slow acceleration and without braking at 15,000 revolutions per min in an SW32 rotor (Beckman Coulter Nederland). Next, the supernatants were removed and the pellets were suspended in PBS-1% bovine serum albumin (BSA; Sigma-Aldrich, St. Louis, MO) by overnight incubation with gentle shaking at 4°C. The concentrated vector suspension was divided on ice in 50 µl aliquots for storage at -80°C.

Isolation and culture of primary murine BPAs

Primary murine BPAs were isolated from the interscapular BAT depot of 4-week-old male C57Bl/6J mice (Charles River Laboratories International, Wilmington, MA). Isolated tissue was minced with scissor into 3- to 4-mm pieces, washed once with DMEM/F-12 GlutaMAX (Thermo Fisher Scientific; catalogue number: 10565018) and incubated in DMEM/F-12 GlutaMAX containing 1 mg/mL collagenase type I (Thermo Fisher Scientific; catalog number: 17018029) at 37°C for 45 min. After centrifugation and resuspension in growth medium (DMEM/F-12 GlutaMAX supplemented with 10% heat-inactivated FBS, 100 U/mL penicillin and 100 µg/mL streptomycin), cells were filtered through a 200-µm pore-sized nylon filter (Sefar, Lochem, the Netherlands; catalogue number: 03-200/39) and seeded into a culture flask. Growth medium was replaced the following day and then every other day.

Transduction of primary murine BPAs and generation of lines of conditionally immortalized mouse BPAs

At passage two, *i.e.* after approximately 8 population doublings (PDs), the primary murine BPAs were transduced with LV.ihEEF1a1.SV40-LT-*ts*A58. The next day, the inoculum was replaced by growth medium containing 100 ng/ml dox (Sigma-Aldrich) to induce LT expression. The cells were subsequently given fresh growth medium with dox every other day. After 1 week of culture, the transduced cells were trypsinized and plated at a low density of 10~20 cells/cm^2 to allow formation of single-cell clones. Two to 3 weeks later, individual cell colonies were picked and separately expanded in the presence of dox.

Culture, differentiation and adrenergic stimulation of murine iBPAs

Murine BPA clones were cultured in growth medium supplemented with 100 ng/mL dox. Growth medium was replaced every other day and cells were split 1:8 after reaching approximately 70% confluency. For differentiation, cells were allowed to grow confluent and 2 days later exposed to growth medium containing 5.6 nM bovine insulin (Sigma-Aldrich; catalogue number: I0305000), 25 µg/mL sodium ascorbate (Sigma-Aldrich; catalogue number: A-7631) and 1 µM of the peroxisome proliferator-activated receptor γ agonist rosiglitazone (Sigma-Aldrich; catalogue number: R2408), 10 mM HEPES (adjusted to pH 7.40 with NaOH). This so-called adipogenic differentiation medium was replaced every other day and the various clones were screened for their adipogenic capacity, *i.e.* their ability to develop multilocular lipid droplets and to express the brown fat marker gene *Ucp1*. Next, differentiated BPAs were stimulated with 1 µM of the broad-spectrum adrenoreceptor agonist noradrenalin

(NA), 10 μM of the highly selective β3 adrenoreceptor agonist CL316243 or vehicle (PBS) for 8 hours. Subsequently, supernatant was collected for colorimetric determination of glycerol production (INstruchemie, Delfzijl, the Netherlands) and cells were lysed in TriPure (Roche Life Science, Almere, the Netherlands) for RNA and protein analysis as described below.

Analysis of cell proliferation

To draw growth curves, the primary murine BPAs and conditionally immortalized cells were subcultured 1:4 and 1:8 on reaching confluency so that each passage corresponded to 2 and 3 PDs, respectively. To assess their proliferation rate and dependence on the activity of SV40 LT antigen, the murine iBPAs were cultured at low density in medium with or without 100 ng/ml dox. At different days after culture initiation, cells were collected in medium and counted using an Accuri flow cytometer (BD Biosciences, Breda, the Netherlands).

Western blotting

Western blotting was carried out as detailed before[26]. After blocking, the membranes were incubated overnight at 4°C with primary mouse monoclonal antibodies directed against LT (1:2,000; Santa Cruz Biotechnology, Dallas, TX; catalogue number: sc-147) or glyceraldehyde 3-phosphate dehydrogenase (GAPDH; loading control; 1:100,000; Millipore; catalogue number: MAB374) and then probed with goat anti-mouse IgG secondary antibodies linked to horseradish peroxidase (1:15,000; Santa Cruz Biotechnology) for 1 hour at RT. Chemiluminescence was produced using the SuperSignal West Femto maximum sensitivity substrate (Thermo Fisher Scientific), captured by a ChemiDoc XRS imaging system (Bio-Rad Laboratories, Veenendaal, the Netherlands) and analysed by Quantity One software (Bio-Rad Laboratories) using the GAPDH signals for normalization purposes.

Immunocytology

Cells were processed for immunostaining as previously described[27]. Detection of LT was done with the same primary antibody as used for the analysis of LT expression by western blotting. Actively replicating were detected using polyclonal rabbit anti-Ki-67 antibodies (Abcam, Cambridge, United Kingdom; catalogue number: ab15580), The primary antibodies were diluted 1:200 in PBS containing 0.1% normal donkey serum (Sigma-Aldrich) and left on the cells overnight at 4°C. Bound antigens were detected using Alexa 488-conjugated donkey anti-rabbit IgG (H+L) (Thermo Fisher Scientific; catalogue number: A21206) and Alexa 568-coupled donkey anti-mouse IgG (H+L) (Thermo Fisher Scientific; catalogue number: A10037). These secondary antibodies were diluted 1:400 in PBS. Hoechst 33342 (10 μg/μl; Thermo Fisher Scientific) was used to counterstain nuclei. Stained cells were visualized using a digital color camera-equipped fluorescence microscope (Nikon Eclipse 80i; Nikon Instruments Europe, Amstelveen, the Netherlands).

RNA isolation, cDNA synthesis and reverse transcription-quantitative PCR (RT-qPCR) analysis

Every other day, starting from day 0 to day 14 of differentiation, cells (n=4 cultures per time point and experimental group) were lysed in TriPure. After RNA extraction, cDNA synthesis was performed using M-MLV reverse transcriptase (Promega Benelux, Leiden, the Netherlands; catalogue number: M1705), random primers, dNTPs and RNasin ribonuclease inhibitor (all from Promega Benelux) and 1 µg of input RNA. Real-time PCR was carried out on a CFX96 PCR machine (Bio-Rad Laboratories, Veenendaal, the Netherlands) using GoTaq qPCR master mix (Promega Benelux; catalogue number: A6002). mRNA expression was normalized to that of the ribosomal protein-encoding housekeeping gene *Rplp0*, also known as *36b4*. Data was expressed as means ± standard error of the mean (SEM) of arbitrary units determined using the $2^{-\Delta CT}$ method. The intron-spanning primer pairs used are listed in Table 1.

Table 1 – List of primer sequences for RT-qPCR

Gene	Forward primer	Reverse primer
Rplp0	GGACCCGAGAAGACCTCCTT	GCACATCACTCAGAATTTCAATGG
Fabp4	ACACCGAGATTTCCTTCAAACTG	CCATCTAGGGTTATGATGCTCTTCA
Lpl	CCCTAAGGACCCCTGAAGAC	GGCCCGATACAACCAGTCTA
Ppargc1a	TGCTAGCGGTTCTCACAGAG	AGTGCTAAGACCGCTGCATT
Pparg	GTGCCAGTTTCGATCCGTAGA	GGCCAGCATCGTGTAGATGA
Prdm16	ACTTTGGATGGGAGCAGATG	CTCCAGGCTCGATGTCCTTA
Ucp1	TCAGGATTGGCCTCTACGAC	TGCATTCTGACCTTCACGAC

Statistical analysis

Data are represented as mean ± SEM. Effect of adrenergic stimuli on BPAs was analysed by two-way ANOVA with Dunnet's *post hoc* test. GraphPad Prism version 6.0 (GraphPad Software, La Jolla, CA) was used for all calculations. Differences at P values < 0.05 were considered statistically significant.

Results

Generation of iBPAs

Since primary BPAs gradually become senescent and stop proliferating at about PD18 (*Figure 1B*), the cells were transduced with an LV conferring dox-dependent expression of the betapolyomavirus oncoprotein LT (*Figure 1A*) and kept in dox-containing culture medium. In contrast to untransduced control cells (nBPAs) , the LT-expressing BPAs kept proliferating at the same speed for at least 60 PDs without showing any conspicuous signs of senescence (*Figure 1B*). To directly compare their proliferation rate and morphology, equal numbers of nBPAs and transduced BPAs (tBPAs) from PD18 were plated at a cell density corresponding to a confluency of 20% and cultured in medium without (nBPAs, tBPAs) or with (tBPAs) dox. Four days later microscopic images were taken. Whereas the cell density of the nBPAs remained

constant, the confluency of the dox-treated tBPA cultures increased to approximately 40 and 90% in the absence and presence of dox, respectively (*Figure 1C*). Moreover, after transduction, the cells maintained a fibroblast-like morphology (*Figure 1C*). Western blot analysis and immunofluorescence microscopy confirmed LT expression in tBPAs but not in nBPAs (*Figure 1D and E*). Taken together, the expression of LT enabled BPAs to continuously proliferate and bypass senescence, therefore, we named these cells immortalized BPAs (iBPAs).

iBPAs are clonogenic and possess long-term inducible expansion capacity

From over 50 rapidly growing cell clones, clone #6 was picked to further study the long-term dox-dependent proliferation capacity of iBPAs since it was one of the most adipogenic clones (see below). First, LT expression of clone #6 cells of PD40 and PD100 before (day 0) and after (day 2, 4, 6 and 8) dox removal were compared by western blotting and immunofluorescence staining. Both PD40 and PD100 cells displayed dox-inducible LT expression, *i.e.* LT was highly expressed in the presence of dox, and LT levels gradually dropped in its absence, being no longer detectable at 6 days after dox removal (*Figure 2A, B and C*). Moreover, quantitative analysis of the western blot data showed no statistically significant difference in LT levels between PD40 and PD100 iBPAs cultured in the presence, or for different days, in the absence of dox (*Figure 2B and C*). Consistently, iBPAs of PD40 and PD100 possessed very similar dox-inducible proliferation capacity as shown by immunostaining for the cellular proliferation marker Ki-67 (Supplementary Figure 1). In the presence of dox, cells proliferated with an average doubling time of 19 hours, whereas in the absence of dox, the cell number slightly increased up to day 4 and then stayed constant in both PD40 as well as PD100 iBPAs (*Figure 2D*). The small increase in the number of iBPAs during the first 4 days after dox removal, which is also evident in Fig. 1C, is likely due to the slow decline of the LT level following transgene silencing. To sum up, iBPAs maintain a high proliferation rate for at least 100 PDs.

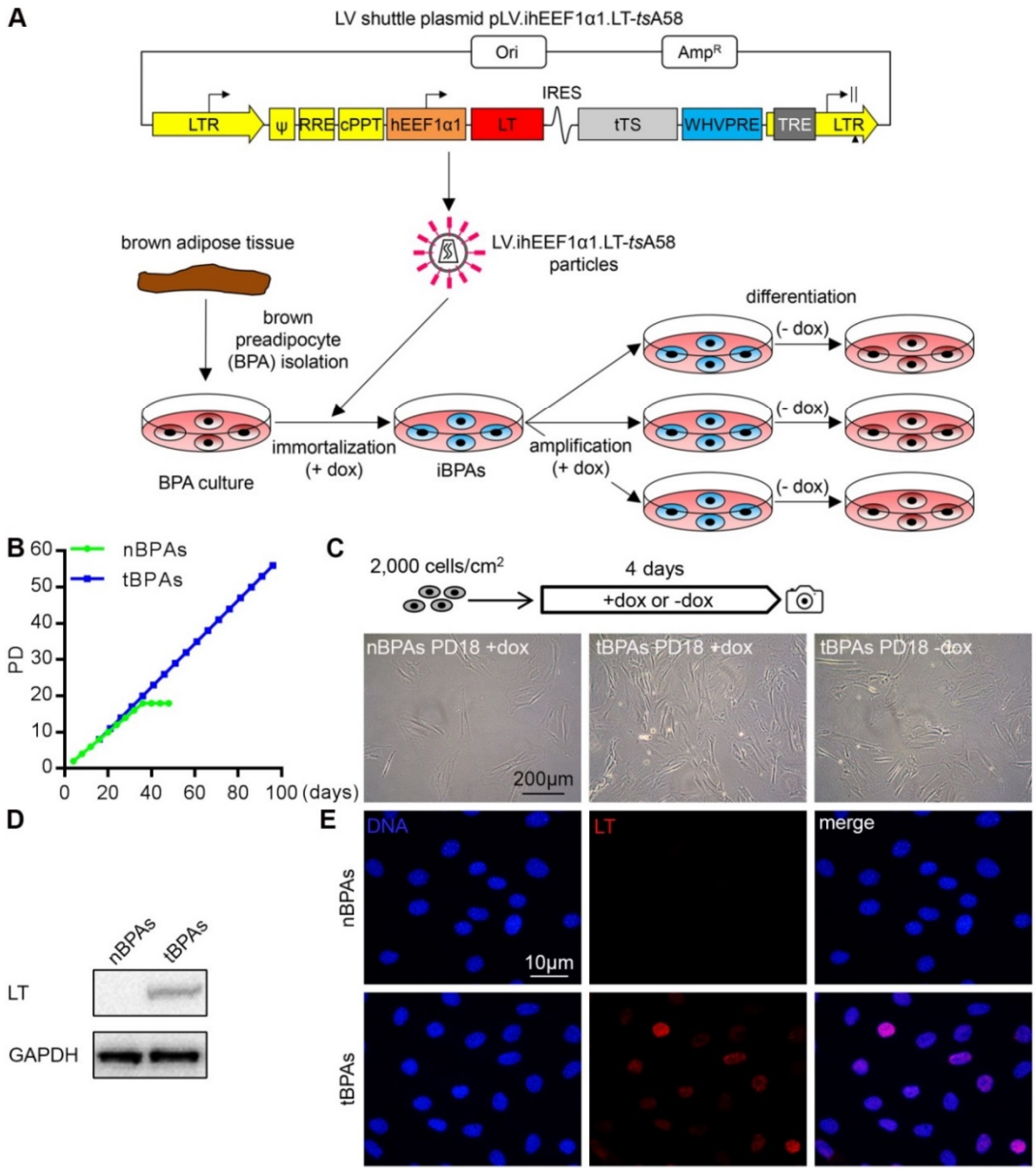

Figure 1. Conditional immortalization of BPAs

(A) Schematic representation of LV shuttle plasmid and protocol to generate conditionally immortalized BPAs. Ori, bacterial origin of replication. Amp^R, *Escherichia coli ß-lactamase* gene. LTR, human immunodeficiency virus type 1 (HIV1) long terminal repeat. Ψ, HIV1 packaging signal. RRE, HIV1 Rev-responsive element. cPPT, HIV1 central polypurine tract and termination site. hEEF1α1, human *eukaryotic translation elongation factor 1A1* gene promoter. LT, coding sequence of the temperature-sensitive mutant LT protein tsA58[34]. IRES, encephalomyocarditis virus internal ribosome entry site. tTS, coding sequence of the hybrid tetracycline-controlled transcriptional repressor TetR-KRAB[24]. WHVPRE, woodchuck hepatitis virus posttranscriptional regulatory element. TRE, tetracycline-responsive promoter element consisting of 7 repeats of a 19-nucleotide tetracycline operator (tetO) sequence. (B) Growth curves of nBPAs and tBPAs. The tBPAs continued to expand after the nBPAs had become senescent. Cells were cultured in the presence of dox. (C) Microscopic images showing the cell density and morphology at PD18 of nBPAs cultured with dox and of tBPAs cultured with or without dox. (D, E) Confirmation of LT expression in dox-exposed tBPAs (PD 18) by western blot and immunofluorescence staining. In both cases, dox-treated nBPAs of PD 18 served as negative controls.

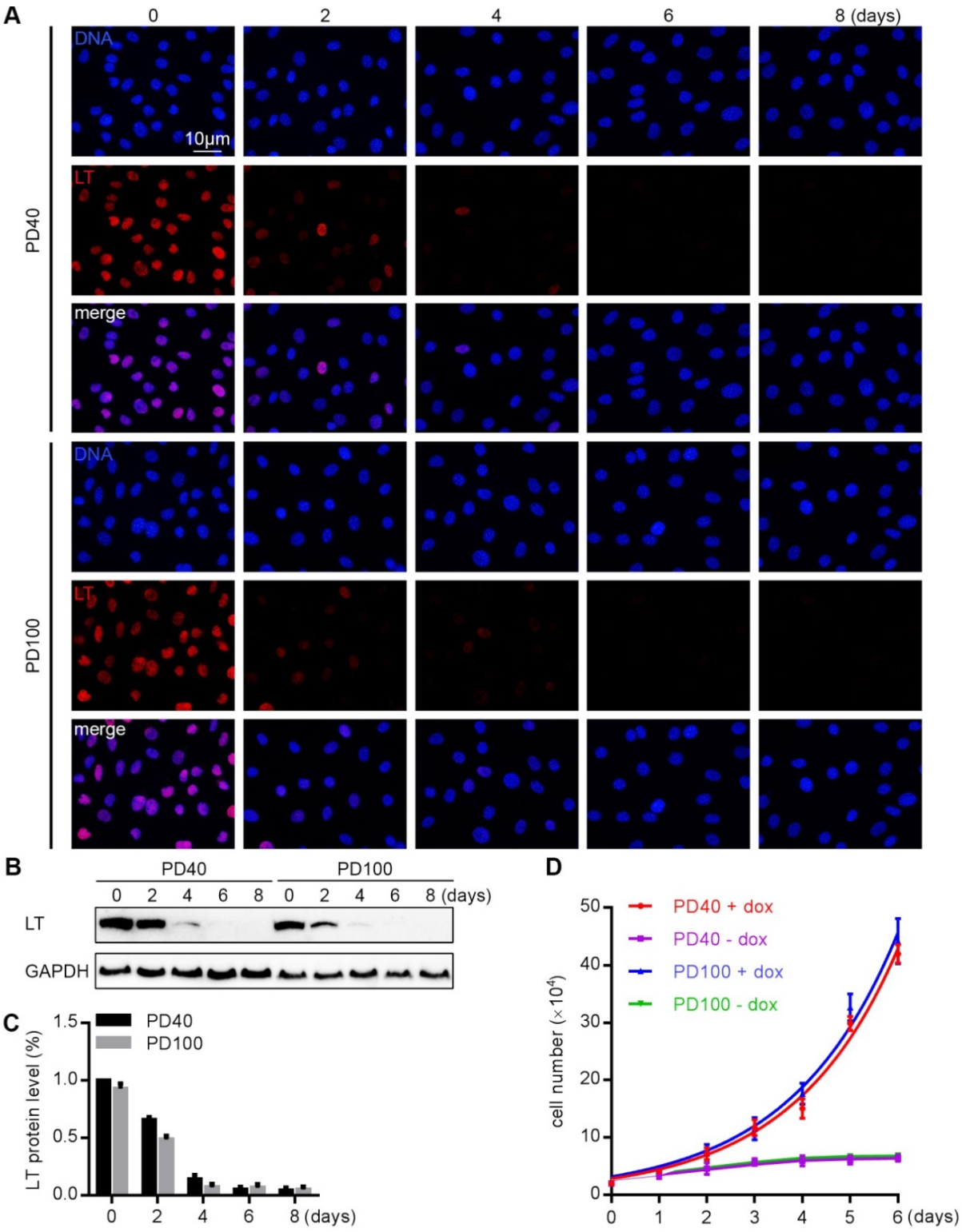

Figure 2. Dox-dependent LT expression and proliferation of iBPAs.
(A) Fluorographs of clone #6 iBPAs of PB40 and PD100 stained with the DNA binding dye Hoechst 33342 (blue) and for the SV40 LT protein (red) before (0) and at 2, 4, 6 and 8 days after dox removal. (B, C) Western blot analysis of LT expression of clone #6 iBPAs at PD40 and PD100 before (0) and at 2, 4, 6 and 8 days after dox removal. (D) Quantification of cell numbers in PD40 and PD100 cultures of clone #6 iBPAs exposed for the indicated days to medium with or without dox.

iBPAs possess adipogenic capacity

In order to assess the adipogenic capacity, cells from each clone were cultured in growth medium and when these clonal preadipocyte cell lines reached 100% confluence, dox was removed from the culture at which time point the cells were induced to differentiate to brown adipocytes under adipogenic culture conditions for 14 days (*Figure 3A*). Clone #6 and #7 cells were most adipogenic based on the extent of lipid droplet formation and *Ucp1* expression level (Supplementary Figure 2). To better characterize the adipogenic potential of these two clones, microscopic images of cell cultures subjected to adipogenic differentiation conditions were taken every two days. The cells of both clones gradually accumulated small lipid droplets acquiring the multilocular typical for brown fat cells and after 14 days of adipogenic differentiation > 90% of the cells was lipid-laden (*Figure 3B*). PD40 iBPAs were further analysed by RT-qPCR to assess the expression of brown adipocyte markers in the time course of differentiation. The unique brown fat marker *Ucp1* showed a robust induction at the RNA level starting at day 4 of adipogenic differentiation for both clones (*Figure 3C*). *Ucp1* peaked at differentiation day 12 for clone #6 and at differentiation day 10 for clone #7 (*Figure 3C*). The transcriptional coactivators PR domain containing 16 (*Prdm16, Figure 3D*) and peroxisome proliferator-activated receptor gamma coactivator 1-α (*Ppargc1a, Figure 3E*), the peroxisome proliferator-activated receptor γ (*Pparg, Figure 3F*), fatty acid binding protein 4 (*Fabp4, Figure 3G*) and lipoprotein lipase (*Lpl, Figure 3H*) followed similar patterns of expression, *i.e.* expression of all these markers was induced from the start of adipogenic differentiation and, except for *Lpl*, peaked at differentiation day 12. Based on these data, we conclude that following conditional immortalization primary murine BPAs retain their adipogenic capacity and that optimal differentiation of iBPAs is reached at 12-14 days after initiation of adipogenesis.

Extensive proliferation reduces the adipogenic capacity of iBPAs

There is no reduction in the adipogenic capacity of iBPAs at least until PD64 (data not shown). To study what would happen afterwards, clone #6 and #7 cells at PD100 were exposed to adipogenic differentiation medium and the expression patterns of the brown fat marker genes were assessed. After 100 doublings, only approximately 30% of the cells contained multiple lipid droplets at differentiation day 14 (Supplementary Figure 3) indicating incompletely preservation of adipogenic capacity. Moreover, the expression of *Ucp1* in clone #6 cells was up to 50-fold lower at PD100 than at PD40. However, exposure to adipogenic differentiation medium still resulted in an approximately 1000-fold upregulation of *Ucp1* expression at differentiation day 12 (*Figure 4A*). In contrast, clone #7 cells of PD100 showed hardly any increase in *Ucp1* expression following adipogenic stimulation (*Figure 4A*). Both clone #6 and #7 cells showed a clear increase in the expression of the other brown fat marker genes after exposure to adipogenic differentiation conditions (*Figure 4B-F*). However, for all these gene, expression was lower at PD100 than at PD40, except for *Lpl*, which was higher expressed at PD100 (*Figure 4G*). Moreover, the expression of these genes did not peak at day 12 of differentiation as observed at PD40, but earlier. In conclusion, late passage iBPAs differentiate less well into brown adipocytes than early passage iBPAs based on lipid droplet formation and brown fat marker gene expression.

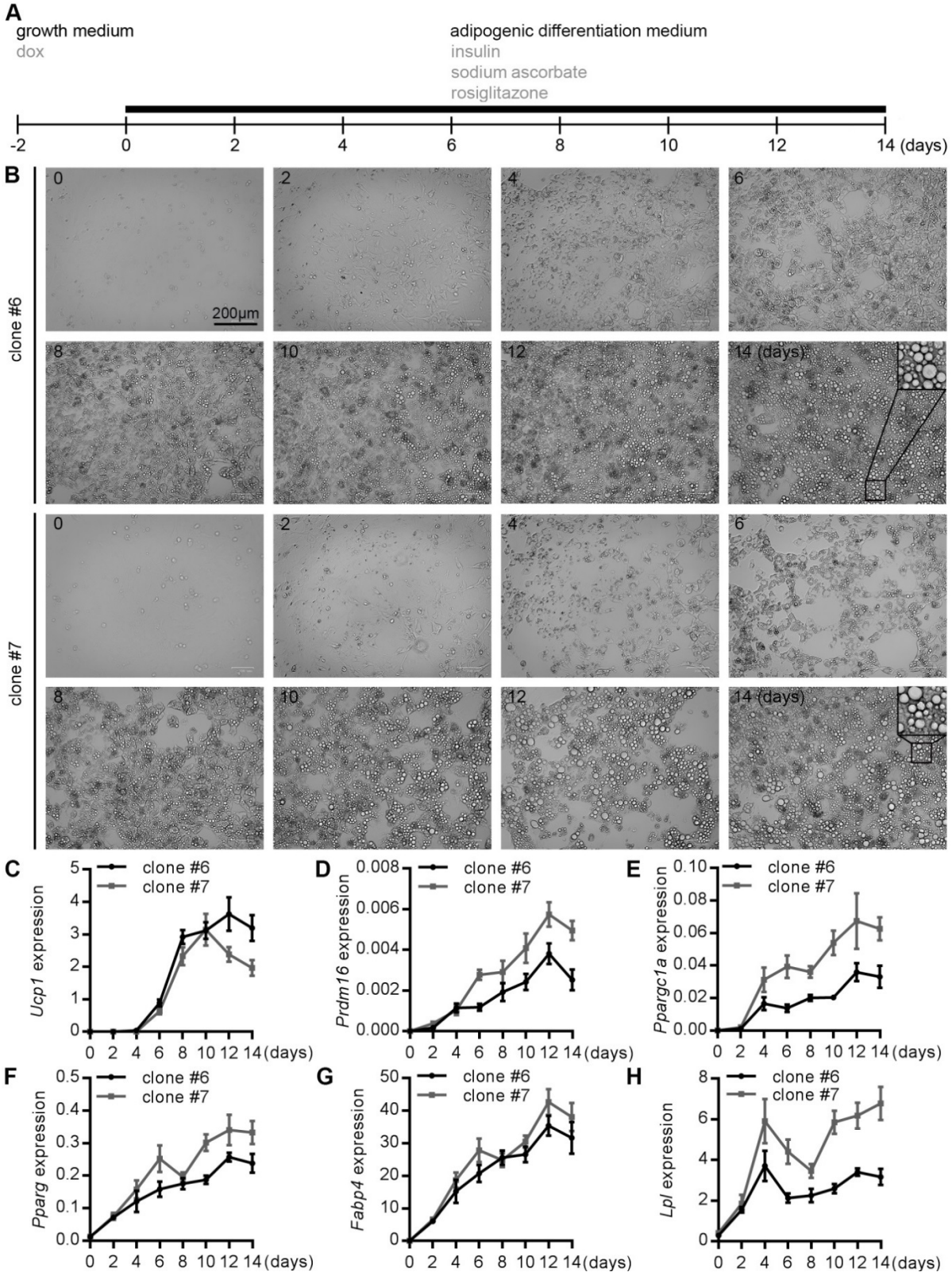

Figure 3. Comparison of the adipogenic potential of 2 different iBPA clones. (A) Protocol used to differentiate iBPAs towards brown adipocytes. (B) Phase contrast images showing the morphological changes associated with the adipogenic differentiation of clone #6 and #7 iBPAs of PD40. (C) RT-qPCR analysis of *Ucp1*, *Prdm16*, *Ppargc1a*, *Pparg*, *Fabp4* and *Lpl* gene expression in clone #6 and #7 iBPAs at PD40 on the indicated days of adipogenic differentiation normalized to *Rplp0* expression. Data are presented as means ± SEM (n=4).

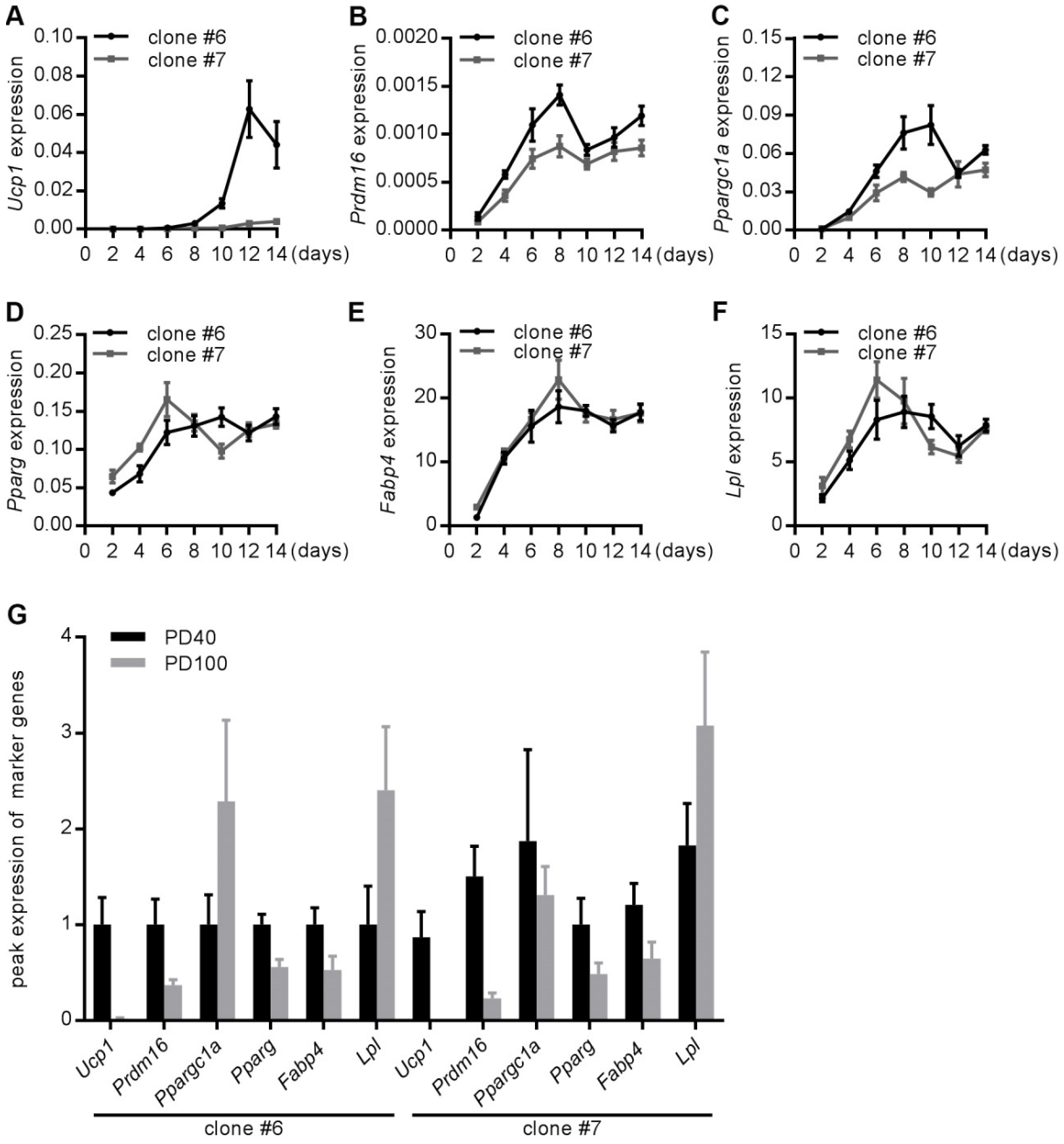

Figure 4. Adipogenic potential of massively amplified iBPA clones.
(A-F) RT-qPCR analysis of *Ucp1, Prdm16, Ppargc1a, Pparg, Fabp4* and *Lpl* gene expression in clone #6 and #7 iBPAs at PD100 on the indicated days of adipogenic differentiation normalized to *Rplp0* expression. (G) Peak expression of the selected marker genes in clone #6 and #7 iBPAs at PD40 and PD100 during adipogenic differentiation. Gene expression levels are expressed relative to those of clone #6 at PD40, which were set at 1. Data are presented as means ± SEM (n=4).

β3-adrenoceptor agonists stimulate lipolysis in adipogenically differentiated iBPAs

To investigate the response of adipogenically differentiated iBPAs to adrenergic stimulation, the cells were stimulated with the general adrenergic agonist NA[28] or with the specific β3 adrenoceptor agonist CL316243[29,30]and glycerol release was quantified. The glycerol concentration in the culture medium was significantly increased upon 8 hours of stimulation with NA (+1659%, $P < 0.001$ for clone #6, +2028%, $P < 0.001$ for clone #7) and CL316243 (+1647%, $P < 0.001$ for clone #6, +1598%, $P < 0.001$ for clone #7) pointing to increased intracellular lipolysis (*Figure 5A*). Furthermore, *Ucp1* expression was determined after 8 hours of NA and CL316243 incubation. Consistent with the increased lipolysis, *Ucp1* expression was significantly increased after NA (+231%, $P < 0.001$ for clone #6, +121%, $P < 0.05$ for clone #7) or CL316243 (+155%, $P < 0.01$ for clone #6, +181%, $P < 0.01$ for clone #7) stimulation in both clones (*Figure 5B*). Together, these data demonstrate that the iBPAs are responsive to β3-adrenergic stimulation.

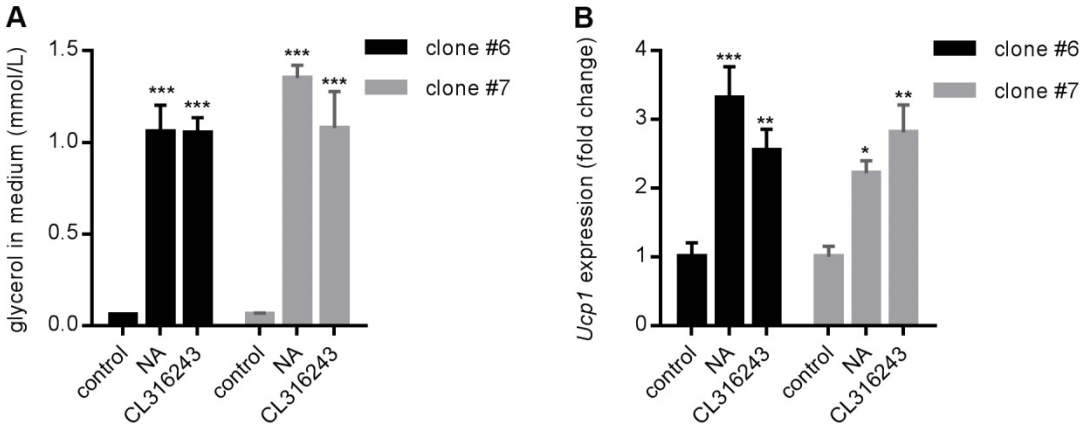

Figure 5. Effect of adrenergic stimulation on *Ucp1* expression and lipolysis of adipogenically differentiated iBPAs. (A, B) Clone #6 and #7 iBPAs of PD46 at differentiation day 12 were stimulated with 1 μM NA or 10 μM CL316243 for 8 hour after which glycerol release in the supernatant (A), and *Ucp1* RNA levels (B) were measured. Data are means ± SEM (n=4).

Discussion

Monoclonal lines of BPAs with inducible proliferation ability

Permanent immortalization of BPAs has been proven to be an effective tool to study brown adipocyte biology and responses to pharmacological treatments[14-18]. However, the rapid loss of robust adipogenic capacity during cell amplification and the potential effects of exogenous expression of immortalization genes such as LT on BPAs remain unresolved issues using this approach. In this study, we developed a system enabling the robust and tightly controlled expansion of monoclonal populations of BPAs by endowing the cells with a dox-regulated SV40 LT expression module. The presence of dox in the culture medium induced LT expression and caused rapid iBPA expansion, while removing dox released the proliferation pressure and prepared the cells for subsequent adipogenic differentiation. Our monoclonal iBPA lines allow synchronous adipogenic differentiation of BPAs, providing a clear advantage in the assessment of differentiation stage-dependent gene expression profiles and epigenetic changes. Moreover, the use, in previous studies, of permanent immortalization gene expression to generate BPA lines poses a problem to their application in transplantation experiments, whereas the tightly controlled LT expression system used in this study created an opportunity for this iBPAs to become a transplantable cell source. Also, recent studies have shown that mature brown adipocytes retain proliferative capacity[28,29], although the mechanism(s) involved is/are largely unknown. It will hence be of interest to investigate what happens when adipogenically differentiated iBPAs are re-exposed to dox. If this would cause them to start dividing again, it might (i) provide a good model system to gain more insight into the pathways involved in BAT hyperplasia and (ii) allow dox-dependent regulation of the size of the brown fat compartment *in vivo*.

LT expression in adipocyte differentiation

Mature lipid-filled adipocytes are post-mitotic, requiring BPAs to exit the cell cycle for terminal differentiation. This may limit the differentiation potential of BPA lines with permanent immortalization gene expression. In addition, studies have shown that LT inhibits white adipogenesis but facilitates brown adipogenesis by inactivation of the pRB pathway[20,30,31]. A better understanding of the role of LT in adipogenesis will help to further understand the mechanisms of brown adipogenesis as well as the conversion of white into brown fat cells and *vice versa*. iBPAs are unique in their ability to vary the timing of LT expression and therefore pocket protein activity in relation to the moment of adipogenic stimulation. This property makes iBPAs particularly attractive for studying the role of cell cycle regulators including those directly targeted by LT in BPA differentiation.

Long-term differentiation capacity of iBPAs

iPBAs retained full adipogenic capacity for at least 64 PDs, implying that $> 10^{19}$ brown adipocytes could be generated from a single preadipocyte. This provides an abundant cell source for cell-based disease modelling and raises the possibility to endow mice with extra brown fat tissue via cell transplantation. This brown fat tissue could be provided with new properties by *ex vivo* genetic engineering thereby creating

additional opportunities for fundamental and applied research. Beyond 64 PDs, the cells show a less pronounced differentiated brown adipocyte phenotype based on the reduced expression of *Ucp1* and other brown fat markers at PD100 in comparison to PD40. The reason could be that proliferation of iBPAs causes gradual loss of the epigenetic modifications required for maintaining their cell type-specific memory[32,33], resulting in a progressive decrease in adipogenic capacity upon repeated passaging.

Difference in adipogenic capacity between diffent iBPA clones

As shown in Supplementary Figure 2, different iBPA clones differ in their ability to differentiate into brown fat cells. The reason for this is unclear but it may have to do with (i) some (intrinsic) heterogeneity of the starting material and/or (ii) the number and location of the chromosomally integrated transgenes. A comparison of the transcriptional signatures of iBPAs from a single source but with different adipogenic capacity may be help to broaden the understanding of the molecular pathways orchestrating brown fat formation.

Conclusion

In this study, we established lines of conditionally immortalized murine brown preadipocytes with long-term proliferation ability (at least 100 PDs) and adipogenic capacity (at least 64 PDs). Following adipogenesis , these cells displayed a multilocular appearance, gene expression signature and metabolic capacity alike brown adipocytes. The generated cell lines could have many applications and, for example, be used to investigate BPA proliferation and differentiation, brown (pre)adipocyte metabolism and regulation of *Ucp1* activity and thermogenesis, for brown (pre)adipocyte-based disease modelling and for BPA transplantation studies.

References

1. Cypess AM, Lehman S, Williams G, Tal I, Rodman D, Goldfine AB, Kuo FC, Palmer EL, Tseng YH, Doria A, Kolodny GM, Kahn CR. Identification and importance of brown adipose tissue in adult humans. *N Engl J Med* 2009;**360**:1509-1517.
2. Tseng YH, Cypess AM, Kahn CR. Cellular bioenergetics as a target for obesity therapy. *Nat Rev Drug Discov* 2010;**9**:465-482.
3. Bauer-Kreisel P, Goepferich A, Blunk T. Cell-delivery therapeutics for adipose tissue regeneration. *Adv Drug Deliv Rev* 2010;**62**:798-813.
4. Townsend K, Tseng YH. Brown adipose tissue: Recent insights into development, metabolic function and therapeutic potential. *Adipocyte* 2012;**1**:13-24.
5. Tang W, Zeve D, Suh JM, Bosnakovski D, Kyba M, Hammer RE, Tallquist MD, Graff JM. White fat progenitor cells reside in the adipose vasculature. *Science* 2008;**322**:583-586.
6. Rodeheffer MS, Birsoy K, Friedman JM. Identification of white adipocyte progenitor cells in vivo. *Cell* 2008;**135**:240-249.
7. Zhang H, Schulz TJ, Espinoza DO, Huang TL, Emanuelli B, Kristiansen K, Tseng YH. Cross talk between insulin and bone morphogenetic protein signaling systems in brown adipogenesis. *Mol Cell Biol* 2010;**30**:4224-4233.
8. Kajimura S, Seale P, Kubota K, Lunsford E, Frangioni JV, Gygi SP, Spiegelman BM. Initiation of myoblast to brown fat switch by a PRDM16-C/EBP-beta transcriptional complex. *Nature* 2009;**460**:1154-1158.
9. Cannon B, Nedergaard J. Developmental biology: Neither fat nor flesh. *Nature* 2008;**454**:947-948.
10. Seale P, Bjork B, Yang W, Kajimura S, Chin S, Kuang S, Scime A, Devarakonda S, Conroe HM, Erdjument-Bromage H, Tempst P, Rudnicki MA, Beier DR, Spiegelman BM. PRDM16 controls a brown fat/skeletal muscle switch. *Nature* 2008;**454**:961-967.
11. Schulz TJ, Tseng YH. Brown adipose tissue: development, metabolism and beyond. *Biochem J* 2013;**453**:167-178.
12. Stanford KI, Goodyear LJ. The therapeutic potential of brown adipose tissue. *Hepatobiliary Surg Nutr* 2013;**2**:286-287.
13. Cohen P, Levy JD, Zhang Y, Frontini A, Kolodin DP, Svensson KJ, Lo JC, Zeng X, Ye L, Khandekar MJ, Wu J, Gunawardana SC, Banks AS, Camporez JP, Jurczak MJ, Kajimura S, Piston DW, Mathis D, Cinti S, Shulman GI, Seale P, Spiegelman BM. Ablation of PRDM16 and beige adipose causes metabolic dysfunction and a subcutaneous to visceral fat switch. *Cell* 2014;**156**:304-316.
14. Forest C, Doglio A, Ricquier D, Ailhaud G. A preadipocyte clonal line from mouse brown adipose tissue. Short- and long-term responses to insulin and beta-adrenergics. *Exp Cell Res* 1987;**168**:218-232.
15. Irie Y, Asano A, Canas X, Nikami H, Aizawa S, Saito M. Immortal brown adipocytes from p53-knockout mice: differentiation and expression of uncoupling proteins. *Biochem Biophys Res Commun* 1999;**255**:221-225.
16. Klaus S, Choy L, Champigny O, Cassard-Doulcier AM, Ross S, Spiegelman B,

Ricquier D. Characterization of the novel brown adipocyte cell line HIB 1B. Adrenergic pathways involved in regulation of uncoupling protein gene expression. *J Cell Sci* 1994;**107 (Pt 1)**:313-319.
17. Kozak UC, Held W, Kreutter D, Kozak LP. Adrenergic regulation of the mitochondrial uncoupling protein gene in brown fat tumor cells. *Mol Endocrinol* 1992;**6**:763-772.
18. Zennaro MC, Le Menuet D, Viengchareun S, Walker F, Ricquier D, Lombes M. Hibernoma development in transgenic mice identifies brown adipose tissue as a novel target of aldosterone action. *J Clin Invest* 1998;**101**:1254-1260.
19. Forest C, Doglio A, Casteilla L, Ricquier D, Ailhaud G. Expression of the mitochondrial uncoupling protein in brown adipocytes. Absence in brown preadipocytes and BFC-1 cells. Modulation by isoproterenol in adipocytes. *Exp Cell Res* 1987;**168**:233-246.
20. Hansen JB, Jørgensen C, Petersen RK, Hallenborg P, De Matteis R, Bøye HA, Petrovic N, Enerbäck S, Nedergaard J, Cinti S. Retinoblastoma protein functions as a molecular switch determining white versus brown adipocyte differentiation. *Proceedings of the National Academy of Sciences* 2004;**101**:4112-4117.
21. Molchadsky A, Ezra O, Amendola PG, Krantz D, Kogan-Sakin I, Buganim Y, Rivlin N, Goldfinger N, Folgiero V, Falcioni R, Sarig R, Rotter V. p53 is required for brown adipogenic differentiation and has a protective role against diet-induced obesity. *Cell Death Differ* 2013;**20**:774-783.
22. Szulc J, Wiznerowicz M, Sauvain MO, Trono D, Aebischer P. A versatile tool for conditional gene expression and knockdown. *Nat Methods* 2006;**3**:109-116.
23. Liu J, Volkers L, Jangsangthong W, Bart CI, Engels MC, Zhou G, Schalij MJ, Ypey DL, Pijnappels DA, de Vries AAF. Generation and primary characterization of iAM-1, a versatile new line of conditionally immortalized atrial myocytes with preserved cardiomyogenic differentiation capacity. *Cardiovasc Res* acceptted.
24. Deuschle U, Meyer WK, Thiesen HJ. Tetracycline-reversible silencing of eukaryotic promoters. *Mol Cell Biol* 1995;**15**:1907-1914.
25. Feola I, Teplenin A, de Vries AA, Pijnappels DA. Optogenetic engineering of atrial cardiomyocytes. *Methods Mol Biol* 2016;**1408**:319-331.
26. Majumder R, Engels MC, de Vries AA, Panfilov AV, Pijnappels DA. Islands of spatially discordant APD alternans underlie arrhythmogenesis by promoting electrotonic dyssynchrony in models of fibrotic rat ventricular myocardium. *Sci Rep* 2016;**6**:24334.
27. Yu Z, Liu J, van Veldhoven JP, AP IJ, Schalij MJ, Pijnappels DA, Heitman LH, de Vries AA. Allosteric modulation of Kv11.1 (hERG) channels protects against drug-induced ventricular arrhythmias. *Circ Arrhythm Electrophysiol* 2016;**9**:e003439.
28. Okamatsu-Ogura Y, Fukano K, Tsubota A, Nio-Kobayashi J, Nakamura K, Morimatsu M, Sakaue H, Saito M, Kimura K. Cell-cycle arrest in mature adipocytes impairs BAT development but not WAT browning, and reduces adaptive thermogenesis in mice. *Scientific reports* 2017;**7**:6648.
29. Fukano K, Okamatsu-Ogura Y, Tsubota A, Nio-Kobayashi J, Kimura K. Cold

exposure induces proliferation of mature brown adipocyte in a ß3-adrenergic receptor-mediated pathway. *PloS one* 2016;**11**:e0166579.
30. Cherington V, Morgan B, Spiegelman BM, Roberts TM. Recombinant retroviruses that transduce individual polyoma tumor antigens: effects on growth and differentiation. *Proceedings of the National Academy of Sciences* 1986;**83**:4307-4311.
31. Higgins C, Chatterjee S, Cherington V. The block of adipocyte differentiation by a C-terminally truncated, but not by full-length, simian virus 40 large tumor antigen is dependent on an intact retinoblastoma susceptibility protein family binding domain. *J Virol* 1996;**70**:745-752.
32. Avgustinova A, Benitah SA. Epigenetic control of adult stem cell function. *Nature Reviews Molecular Cell Biology* 2016.
33. Wagner W. Implications of long-term culture for mesenchymal stem cells: genetic defects or epigenetic regulation? *Stem Cell Res Ther* 2012;**3**:54.
34. Loeber G, Tevethia MJ, Schwedes JF, Tegtmeyer P. Temperature-sensitive mutants identify crucial structural regions of simian virus 40 large T antigen. *J Virol* 1989;**63**:4426-4430.

Supporting information

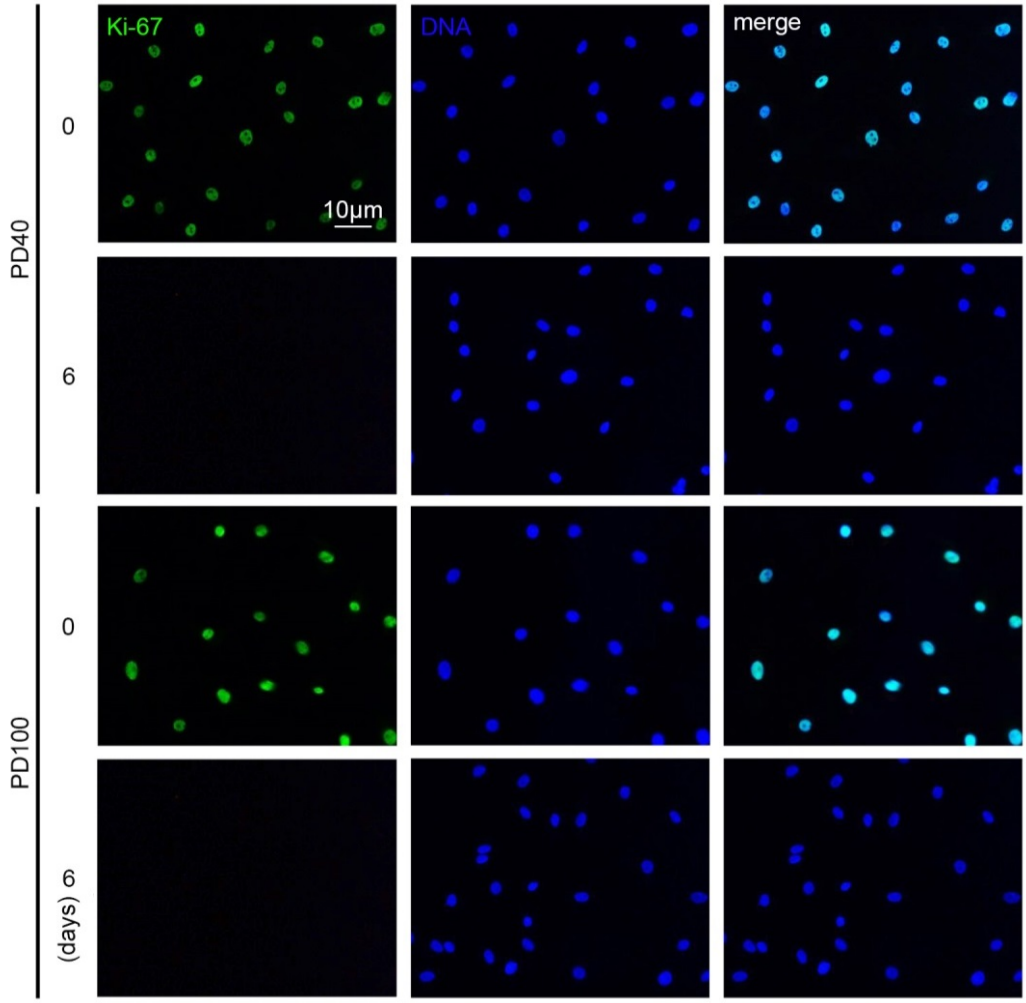

Supplementary Figure 1. Fluorescence images of iBPAs maintained in growth medium before (0) and at 6 days after dox removal immunostained for the proliferation marker Ki-67 (green). Nuclei are visualized with Hoechst 33342 (blue).

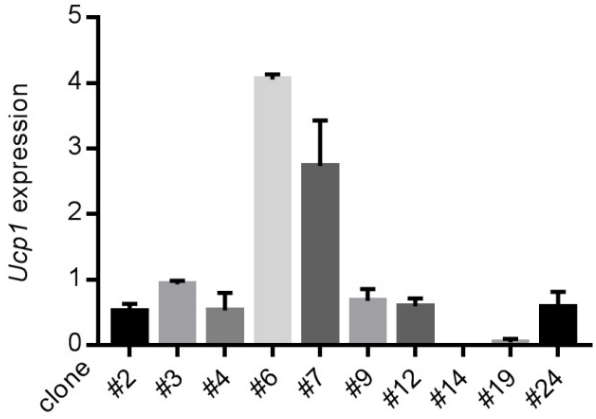

Supplementary Figure 2. RT-qPCR analysis of *Ucp1* expression in 10 different iBPA clones on differentiation day 12 normalized to *Rplp0* expression. Data are presented as means ± SEM (n=4).

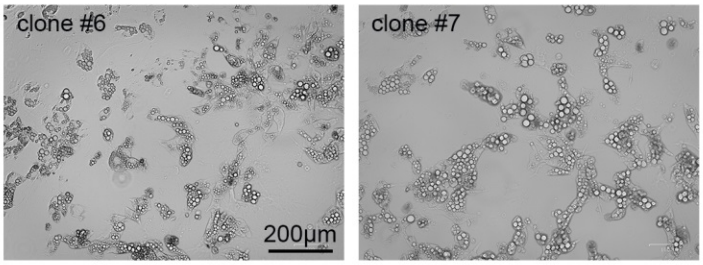

Supplementary Figure 3. Light microscopic images showed the morphology of clone #6 and #7 iBPAs at PD100 on differentiation day 12.

Chapter 6

Allosteric Modulation of $K_v11.1$ (hERG) Channels Protects against Drug-Induced Ventricular Arrhythmias

Zhiyi Yu*; Jia Liu*; Jacobus P.D. van Veldhoven; Adriaan P. IJzerman; Martin J. Schalij; Daniël A. Pijnappels; Laura H. Heitman#; Antoine A. F. de Vries#

*,#Equal contribution

Adapted from: Circ Arrhythm Electrophysiol. 2016;9:e003439.

Abstract

Background-Ventricular arrhythmias due to unintentional blockade of the $K_v11.1$ (hERG) channel are a major safety concern in drug development. In past years, several highly prescribed drugs have been withdrawn for their ability to cause such proarrhythmia. Here, we investigated whether the proarrhythmic risk of existing drugs could be reduced by $K_v11.1$ allosteric modulators.

Methods and Results-Using [^{3}H]dofetilide binding assays with membranes of human $K_v11.1$-expressing HEK293 cells, two existing compounds (VU0405601 and ML-T531) and a newly synthesized compound (LUF7244) were found to be negative allosteric modulators of dofetilide binding to the $K_v11.1$ channel with LUF7244 showing the strongest effect at 10μM. The $K_v11.1$ affinities of typical blockers (*i.e.*, dofetilide, astemizole, sertindole and cisapride) were significantly decreased by LUF7244. Treatment of confluent neonatal rat ventricular myocyte (NRVM) monolayers with astemizole or sertindole caused heterogeneous prolongation of action potential (AP) duration and a high incidence of early afterdepolarizations upon 1-Hz electrical point stimulation, occasionally leading to unstable, self-terminating tachyarrhythmias. Pretreatment of NRVMs with LUF7244 prevented these proarrhythmic effects. NRVM monolayers treated with LUF7244 alone displayed electrophysiological properties indistinguishable from those of untreated NRVM cultures. Prolonged exposure of NRVMs to LUF7244 or LUF7244 plus astemizole did not affect their viability, excitability and contractility as assessed by molecular, immunological and electrophysiological assays.

Conclusion-Allosteric modulation of the $K_v11.1$ channel efficiently suppresses drug-induced ventricular arrhythmias in-vitro by preventing potentially arrhythmogenic changes in AP characteristics, raising the possibility to resume the clinical use of unintended $K_v11.1$ blockers via pharmacological combination therapy.

Introduction

Drug-induced ventricular arrhythmias (DiVAs) are a frequently encountered clinical problem, which has resulted in restricted use or market withdrawal of existing cardiac and non-cardiac drugs and still represents a major obstacle for the development of new drugs.[1] Inhibition of the rapid component of the delayed rectifier K^+ current (I_{Kr}) has been identified as the major culprit in the development of DiVAs. The consequential slowing of cardiac repolarization, manifested in the surface electrocardiogram as a prolongation of the QT interval, increases the likelihood of early afterdepolarizations (EADs), which may give rise to ectopic beats. Drug-induced I_{Kr} blockade also increases spatial dispersion of repolarization and refractoriness thereby further increasing proarrhythmic risk.[2] Together these electrophysiological alterations promote the development of a special type of polymorphic ventricular arrhythmias known as "Torsades de Pointes" (TdPs), which mostly resolve spontaneously but occasionally degenerate into fatal ventricular fibrillation.[3] The K_v11.1 protein, which is encoded by the KCNH2 gene (also known as ether-à-go-go–related gene 1 [ERG or ERG1]), represents the pore-forming α-subunit of the I_{Kr} channel.[4] Several structural features of K_v11.1 render the central cavity of the I_{Kr} channel particularly susceptible to blockade by a heterogeneous collection of chemical compounds including various non-cardiac drugs (e.g., astemizole, sertindole and cisapride).

An obvious strategy to reduce the proarrhythmic risk of drugs with unintended I_{Kr}-blocking effects is by lowering their K_v11.1 affinities via chemical modifications. Alternatively, supplementary drugs that decrease the proarrhythmic risk of inadvertent K_v11.1 blockers can be developed potentially allowing (i) reintroduction of medicines previously recalled from the market because of their K_v11.1-related cardiotoxicity and (ii) admission of new drugs with fortuitous I_{Kr}-blocking activity. Paradoxically, screening of drugs for possible I_{Kr}-blocking side effects has resulted in the serendipitous discovery of various K_v11.1 activators.[5] Besides their potential usefulness in treating inherited long QT syndrome (LQTS), these K_v11.1 activators may also be used to counteract K_v11.1 blockade-associated DiVAs. Indeed, Kang *et al*. showed that the action potential (AP) duration (APD)-prolonging effect of the I_{Kr}-blocking, class III antiarrhythmic drug dofetilide could be counterbalanced by the first identified synthetic K_v11.1 activator designated RPR260243.[6] However, due to their APD-shortening effect, K_v11.1 activators may induce short QT syndrome.[5] Recently, Potet *et al*. described a compound designated VU0405601 that upon pretreatment significantly reduced the APD-prolonging effect of dofetilide in Langendorff-perfused rabbit hearts and dose-dependently mitigated the K_v11.1-blocking effects of seven different drugs in HEK293 cells stably overexpressing the human KCNH2 gene (HEK293K_v11.1 cells).[7] VU0405601 exerted its effects on the K_v11.1 channel in whole-cell voltage-clamp experiments using HEK293K_v11.1 cells only when applied extracellularly. This suggests that VU0405601 binds to the extracellular domain of the K_v11.1 channel rather than to its central cavity leading us to hypothesize that VU0405601 counteracts the APD-prolonging effect of K_v11.1 blockers by an allosteric mechanism.

Allosteric modulators bind their targets at a site topologically different from that of the endogenous ligand. From this so-called allosteric site they generally display higher selectivity across receptor subtypes and thus provide a safer pharmacological profile than ligands binding to the orthosteric site.[8] Notably, since the $K_v11.1$ channel does not have an endogenous ligand, the authors refer to the site where typical blockers (*i.e.*, dofetilide and astemizole) bind as the orthosteric site. Whereas allosteric modulators targeting ligand-gated ion channels and G protein-coupled receptors have been well established as research tools and therapeutic agents,[8-10] little progress has been made in the discovery and clinical development of such compounds for voltage-gated ion channels.

In this study, in-vitro radioligand binding assays were used to investigate whether two previously reported compounds (*i.e.*, VU0405601[7] and ML-T531[11]) and a new compound designated LUF7244 could allosterically modulate binding of the potent $K_v11.1$ blocker dofetilide to the channel's central cavity.[12,13] Radioligand binding assays were also employed to study LUF7244's influence on the interaction between (i) the $K_v11.1$ channel and three different blockbuster drugs (*i.e.*, astemizole, sertindole and cisapride) that have been withdrawn from the market due to their $K_v11.1$-related cardiotoxicity[14] and (ii) astemizole and its intended target, the human histamine H_1 receptor (hH_1R, see **Data Supplement**). The radioligand binding assays were complemented with optical voltage mapping experiments in confluent monolayers of neonatal rat ventricular myocytes (NRVMs). These experiments were performed in the absence and presence of LUF7244 and/or any of the three blockbuster drugs. Electrophysiological parameters analyzed included conduction velocity (CV), APD at 40 and 90% repolarization (APD_{40} and APD_{90}, respectively), APD dispersion and EAD incidence. In addition, the effects of LUF7244 alone and together with astemizole on the viability, excitability and contractility of NRVMs were investigated (see **Data Supplement**). The results of this study indicate that negative allosteric modulation of the $K_v11.1$ channel may provide a safe and effective means to prevent the proarrhythmic effects of I_{Kr} blockers that bind to the channel's central cavity.

Materials and Methods

Radioligand Binding Studies

Radioligand displacement assays and kinetic dissociation assays were performed on membranes of HEK293K_v11.1 cells using [^{3}H]dofetilide as radioligand essentially as described before.[15]

Isolation and Culture of NRVMs

NRVMs were isolated from the hearts of neonatal rats and cultured as previously detailed.[16] The use of these animals was approved by the Animal Experiments Committee of Leiden University Medical Center and conformed to the Guide for the Care and Use of Laboratory Animals as stated by the US National Institutes of Health.

Immunocytochemical Analyses

NRVMs were plated on fibronectin-coated, 15-mm diameter round glass coverslips at a density of 4×10^4 cells. At day 9 of culture, the cells were washed with ice-cold phosphate-buffered saline (PBS), fixed in buffered 4% formaldehyde and permeabilized with 0.1% Triton X-100 in PBS. Next, the cells were double-immunostained for Kv11.1 and α-actinin. Incubation with primary antibodies (diluted 1:200 in PBS-0.1% normal donkey serum) and corresponding donkey Alexa Fluor 488/568-conjugated secondary antibodies (1:400 dilution) lasted for 2 hours. To visualize their nuclei, the cells were incubated with 10µg/mL Hoechst 33342 in PBS. After each processing step, the cells were washed with PBS. Coverslips were mounted in VECTASHIELD mounting medium. Photomicrographs were obtained using a Nikon Eclipse 80i digital color camera-equipped fluorescence microscope.

Reverse Transcription-Quantitative Polymerase Chain Reaction Analyses

Total RNA extracted from NRVMs and from neonatal rat cardiac fibroblasts (NRCFs; maintained in NRVM medium) using the QIAGEN RNeasy Mini kit was reverse transcribed with the Bio-Rad iScript cDNA synthesis kit and the resulting cDNA was amplified by PCR using the Bioline SensiFAST SYBR No-ROX kit. PCR amplifications of rat Kcnh2- and rat 18S rRNA (Rn18s)-specific cDNA (for primer sequences, see **Data Supplement**) were carried out in a CFX96 Touch Real-Time PCR detection system (Bio-Rad) using a 2-step cycling protocol (20-40 cycles of 95°C 10 sec, 60°C 30 sec) after a 5-minute incubation at 95°C. Quantitative analyses were based on the $2^{-\Delta\Delta CT}$ method using CFX Manager software (Bio-Rad).

Optical Mapping Experiments

Optical mapping experiments were done in confluent monolayers of NRVMs using the potentiometric dye di-4-ANEPPS as voltage indicator following previously described methods.[17] To validate the experimental model, cells were incubated for 20 minutes in culture medium containing 0, 10, 30, 100 or 300nM of the hH_1R antagonist and unintended K_v11.1 blocker astemizole and dimethylsulfoxide (DMSO) at a final concentration of 0.03%. In a subsequent experiment, NRVM cultures were first exposed for 30 minutes to 10µM LUF7244 or its solvent (*i.e.*, culture medium containing 0.1% DMSO). Next, astemizole (final concentration of 100nM) or vehicle

was added to the culture medium raising the DMSO concentration to 0.13%. Following an incubation period of 30 minutes at 37°C, optical recordings were started in the continued presence of the appropriate vehicle/drug combinations.

Data Analysis

Radioligand binding assay data were analyzed with GraphPad Prism 5.0 (GraphPad Software, San Diego, CA). Half maximal inhibitory concentrations (*i.e.*, IC_{50} values), apparent inhibitory binding constants (K_i values), dissociation rate constants (k_{off}) and half maximal effective concentrations (*i.e.*, EC_{50} values) were calculated as previously described.[18] Values obtained from the radioligand binding assays are from three different experiments each consisting of two independent samples. Data are expressed as mean±standard error of the mean (SEM) for the radioligand binding assays or as mean±standard deviation (SD) for the optical voltage mapping experiments.

See the **Data Supplement** for more details about the materials and experimental procedures.

Results

Characterization of Allosteric Modulators of [^{3}H]Dofetilide Binding to the K_v11.1 Channel

The interaction of two previously reported ligands VU405601 and ML-T531 as well as the newly designed and synthesized compound LUF7244 (**Figure 1A**) with the human K_v11.1 channel was studied in different [^{3}H]dofetilide binding assays. As shown in **Figure 1B** and **Table I** in the **Data Supplement**, all three compounds reduced [^{3}H]dofetilide binding to the K_v11.1 channel with relatively low affinities, *i.e.*, with IC_{50} values of 7.8±0.4μM, 12±1μM and 3.9±0.7μM for VU0405601, ML-T531 and LUF7244, respectively. Moreover, all displacement curves demonstrated Hill coefficients different from unity (*i.e.*, -1.1±0.03 for ML-T531, -1.2±0.01 for VU0405601 and -1.3±0.1 for LUF7244), implying that VU0405601, ML-T531 and LUF7244 might not competitively displace [^{3}H]dofetilide from the K_v11.1 channel but may bind elsewhere to the channel protein to allosterically modulate radioligand binding.

Subsequently, single-point dissociation assays were performed to screen for allosteric effects of these compounds on the binding of [^{3}H]dofetilide to the K_v11.1 channel. At a concentration of 10μM, VU0405601, ML-T531 and LUF7244 significantly increased the dissociation of [^{3}H]dofetilide from the K_v11.1 channel, indicating that these compounds are negative allosteric modulators of dofetilide binding to the channel (**Figure 1C** and **Table I** in the **Data Supplement)**. LUF7244 appeared to be the most potent negative allosteric modulator with 44±2% dofetilide binding left compared to control conditions, while 10μM VU0405601 and ML-T531 reduced dofetilide binding to 63±3% and 77±3%, respectively.

The allosteric effects of VU0405601, ML-T531 and LUF7244 on the K_v11.1 channel were further investigated in traditional radioligand dissociation experiments to determine whether co-administration of these compounds with an excess unlabeled dofetilide would change the dissociation rate of [^{3}H]dofetilide from the K_v11.1 channel. To obtain larger effects, the three compounds were tested at a concentration

of 50μM instead of 10μM as used in the single-point dissociation assays. As shown in **Figure 1D** and **Table I** in the **Data Supplement**, all compounds significantly accelerated the dissociation of dofetilide, in line with the results from the single-point dissociation experiments. The off-rate of [^{3}H]dofetilide was allosterically increased 2.0-fold (from 0.21±0.02 to 0.42±0.04min^{-1}) with 50μM VU0405601. The k_{off} value of [^{3}H]dofetilide rose to 0.33±0.02min^{-1} in the presence of 50μM LUF7244, which was comparable to the effect of ML-T531 ($k_{off,dofetilide}$=0.30±0.03min^{-1}).

Effects of LUF7244 on the Binding of Typical K_v11.1 Blockers to the Channel

Since LUF7244 was the most potent amongst the three allosteric modulators at the lower test concentration of 10μM and may therefore have the best safety profile, its potency to increase the dissociation of [^{3}H]dofetilide from the K_v11.1 channel was investigated. From the corresponding concentration-effect curve (**Figure 2A**), the modulatory potency (*i.e.*, the EC_{50}) of LUF7244 was calculated to be 4.6±0.8μM. Notably, LUF7244 could not completely abrogate [^{3}H]dofetilide binding by accelerating its dissociation from the K_v11.1 channel.

To investigate the effects of LUF7244 on the binding affinities of other compounds besides dofetilide to the K_v11.1 channel, three additional K_v11.1 blockers (*i.e.*, astemizole, sertindole and cisapride) from distinct therapeutic classes were selected (**Figure 2B**). As shown in **Figure 2C-D**, the [^{3}H]dofetilide displacement curves of all four drugs were shifted rightwards in the presence of 10μM LUF7244, implicating that their K_v11.1 affinities were diminished by this negative allosteric modulator. The K_i values of dofetilide, astemizole, sertindole and cisapride in the absence or presence of 10μM LUF7244 are listed in **Table II** of the **Data Supplement**. LUF7244 most strongly modulated cisapride binding to the K_v11.1 channel, increasing its K_i value by 4.0-fold from 21±1 to 85±6nM. Similarly, the K_v11.1 affinities of astemizole, dofetilide and sertindole were reduced by 3.8-, 3.2- and 2.2-fold in the presence of LUF7244. Thus, the negative allosteric effect of LUF7244 on the K_v11.1 channel significantly lowered the channel's affinities for several chemically and therapeutically distinct K_v11.1 blockers.

Analysis of K_v11.1 Protein Expression in NRVMs

Next, the electrophysiological consequences of allosteric modulation of the binding of typical K_v11.1 blockers to the channel by LUF7244 (see **Figure 3A** for experimental setup) were examined in confluent monolayers of NRVMs (**Figure 3B**) as relevant in-vitro model for studying cardiac arrhythmias.[19] Double immunostaining for K_v11.1 and sarcomeric α-actinin showed that all cardiomyocytes in the NRVM cultures expressed the K_v11.1 protein (**Figure 3C**). The K_v11.1 signal had a punctate or linear appearance and was concentrated around nuclei and along the sarcolemma (**Figure 3C**). No significant K_v11.1 protein expression was observed in the low percentage of α-actinin$^-$ cells (mainly NRCFs) present in the NRVM cultures. Consistently, comparison of *Kcnh2* transcript levels between NRVMs and NRCFs by reverse transcription-polymerase chain reaction (RT-PCR) analysis demonstrated ± 40-fold higher Kcnh2 mRNA expression in NRVMs than in NRCFs (**Figure 3D**).

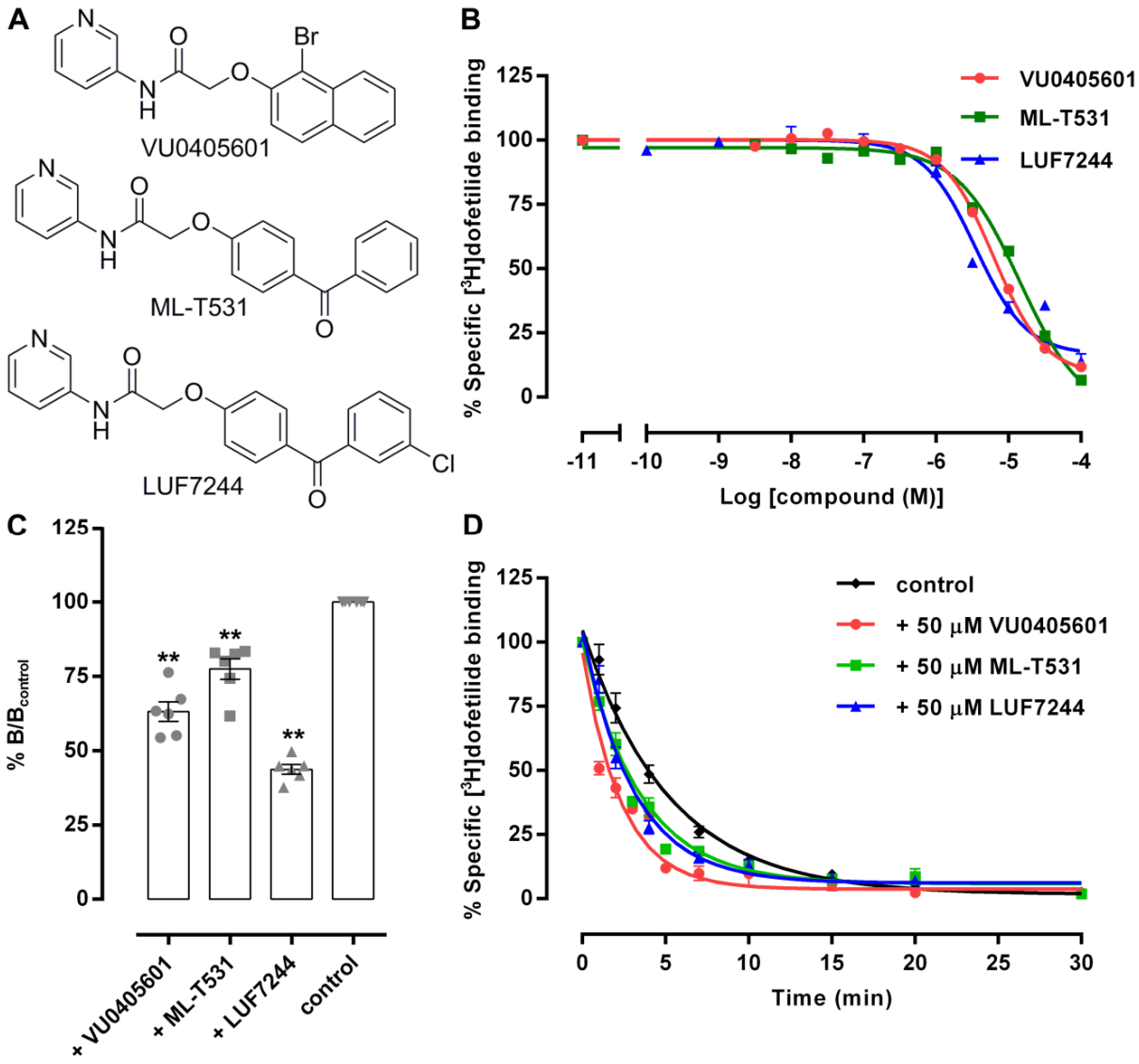

Figure 1. Characterization of allosteric modulators of dofetilide binding to the K_v11.1 channel in a [^{3}H]dofetilide binding assay performed with membranes of HEK293K_v11.1 cells. A: Chemical structures of VU0405601, ML-T531 and LUF7244. B: Displacement curves of VU0405601, ML-T531 and LUF7244. C: Percentage specific binding of [^{3}H]dofetilide to the K_v11.1 channel after 6 minutes of dissociation induced by 10µM dofetilide in the absence (control) or presence of 10µM of VU0405601, ML-T531 or LUF7244. The specific binding of [^{3}H]dofetilide in the absence of the test compounds was set as $B_{control}$, while the specific binding in their presence was set as B. $^{**}P<0.01$. D: Time-dependent dissociation of [^{3}H]dofetilide induced by 10µM dofetilide in the absence (control) or presence of 50µM VU0405601, ML-T531 or LUF7244.

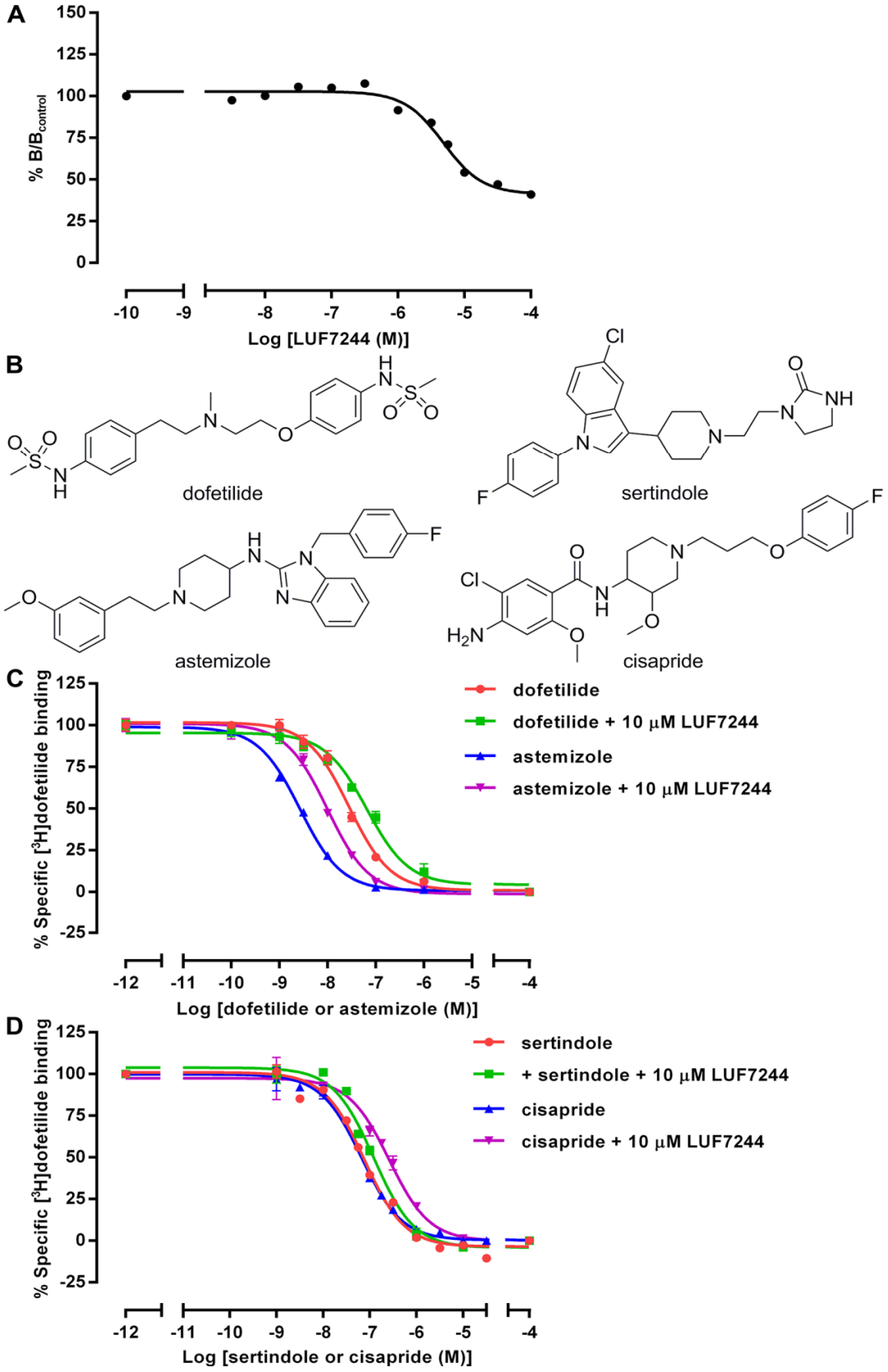

Figure 2. Assessment of the effects of LUF7244 on the binding of K_v11.1 blockers to the channel in a [^{3}H]dofetilide binding assay performed with membranes of HEK293K_v11.1 cells. A: Effect of different concentrations of LUF7244 on the dofetilide-induced dissociation of [^{3}H]dofetilide from the K_v11.1 channel. After preincubating HEK293K_v11.1 cell

membranes with [^{3}H]dofetilide, radioligand dissociation was induced by 10µM dofetilide in the absence or presence of different concentrations of LUF7244 and the incubation was terminated after 6 minutes. Results are expressed as the ratio of the specific binding of [^{3}H]dofetilide in the presence of 10µM dofetilide plus various concentrations of negative allosteric modulators (*B*) over that in the presence of 10µM dofetilide alone ($B_{control}$). B: Chemical structures of dofetilide, astemizole, sertindole and cisapride. C: Displacement curves of dofetilide and astemizole in the absence or presence of 10µM LUF7244. D: Displacement curves of sertindole and cisapride in the absence or presence of 10µM LUF7244.

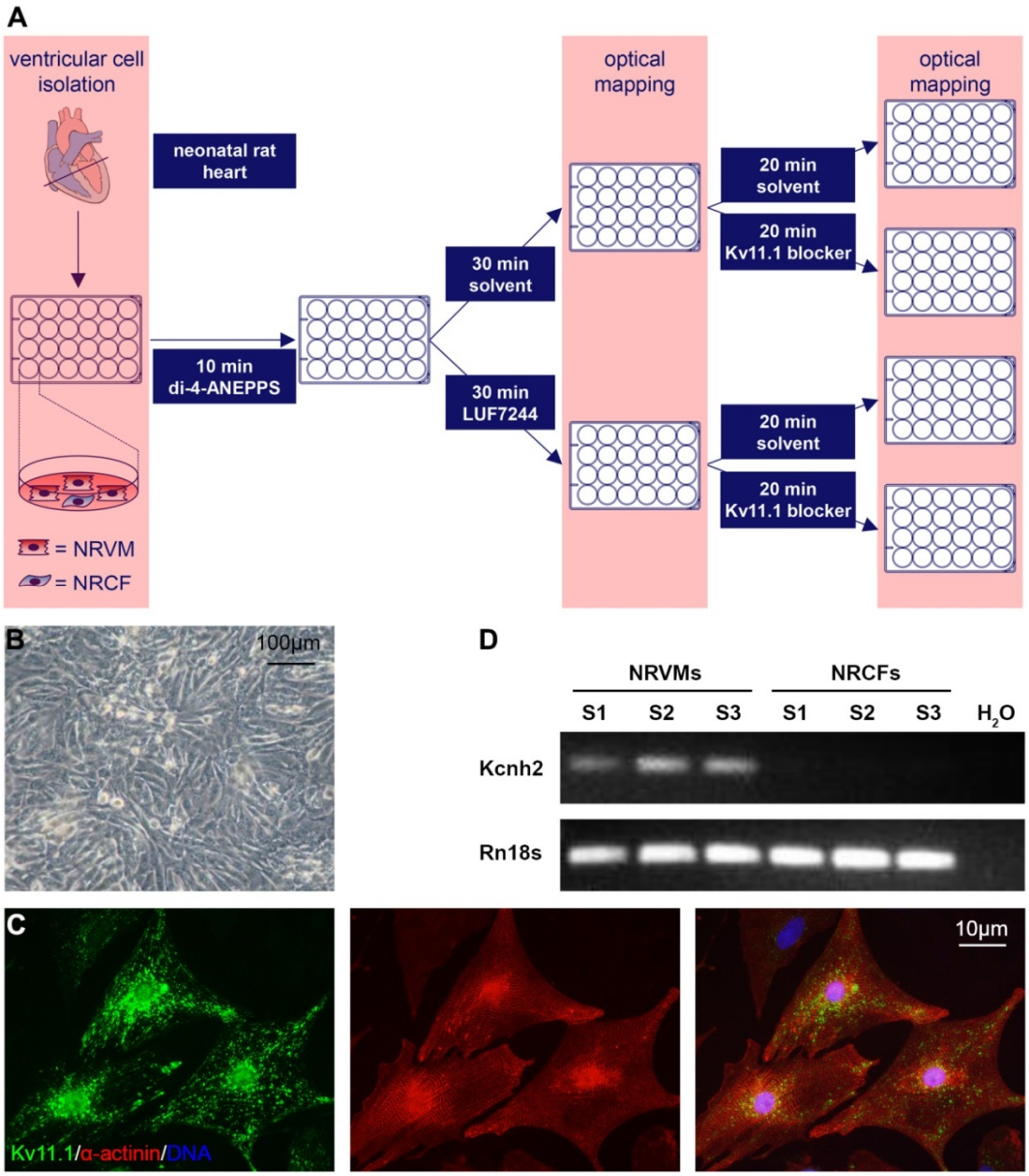

Figure 3. Biochemical characterization of the NRVM model. A: Basic setup of the optical voltage mapping experiments. **B:** Phase-contrast image of a typical confluent NRVM monolayer used for optical voltage mapping. **C:** Immunocytological analysis of K_v11.1 protein expression in NRVM cultures. The K_v11.1 protein (green) is mainly located around the nucleus (blue) and at the sarcolemma of the α-actinin (red)-positive NRVMs and hardly detectable in the α-actinin-negative non-cardiomyocytes. **D:** Analysis of *Kcnh2* mRNA levels in NRVMs and NRCFs by RT-PCR.

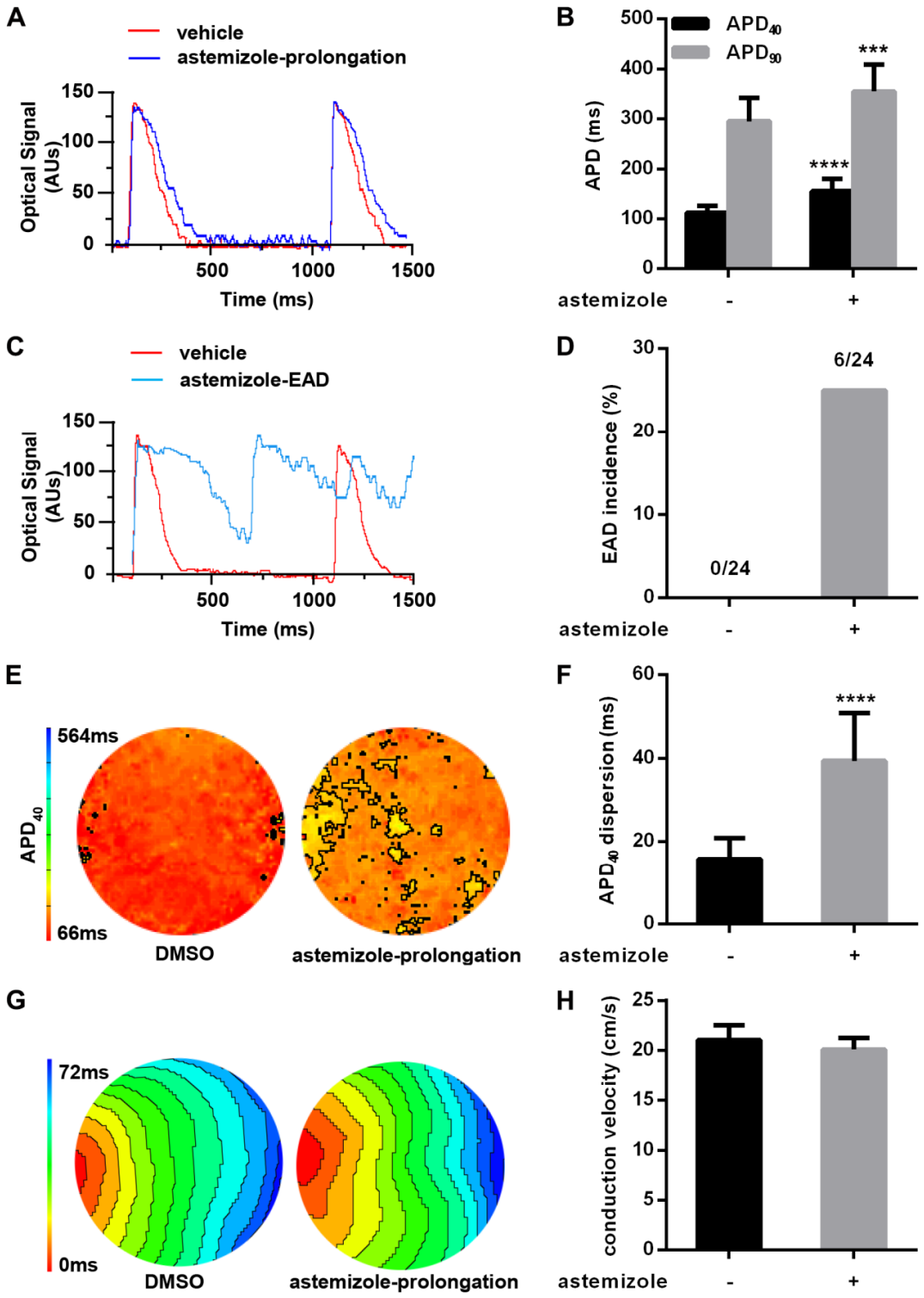

Figure 4. Electrophysiological characterization of the NRVM model by optical voltage mapping following 1-Hz electrical stimulation. Representative filtered optical signal traces (A and C), corresponding APD dispersion and activation maps (E and G, respectively) and quantitative analyses (bar graphs in B, D, F and H) of NRVM cultures exposed for 30 minutes to 100nM astemizole or vehicle (control) and subjected to optical voltage mapping immediately afterwards. Astemizole treatment resulted in APD prolongation (APD_{40} and APD_{90}, A and B), the occurrence of EADs (C and D) and an increase in APD_{40} dispersion (E and F) but did not significantly alter CV (G and H). ***P<0.001 and ****P<0.0001.

Electrophysiological Consequences of K_v11.1 Blockade by Astemizole in NRVMs
Due to its relatively high specificity for the K_v11.1 channel,[20] astemizole was selected to study the electrophysiological consequences of K_v11.1 blockade by optical voltage mapping (**Figure 4**). NRVMs treated with astemizole displayed a concentration-dependent increase in APD and EAD incidence (**Figure I** in the **Data Supplement**). As displayed in **Figure 4A-B**, APD_{40} and APD_{90} values of NRVMs were increased from 112±16 and 295±62ms in vehicle-treated cultures (n=24) to 156±39 and 355±66ms in cultures containing 100nM astemizole (n=24, $P<0.0001$ and $P<0.001$, respectively). Furthermore, exposure to 100nM astemizole resulted in the occurrence of EADs in 25% of the NRVM cultures, whereas no EADs were observed under control conditions (**Figure 4C-D**). As shown in **Figure 4E-F**, the APD_{40} dispersion between NRVMs in the presence of 100nM astemizole was significantly higher than that in its absence (39±11 vs 16±5ms; $P<0.0001$), indicative of aggravated repolarization heterogeneity due to inhibition of I_{Kr} by astemizole. Occasionally, the astemizole-induced APD prolongation resulted in short-lasting, irregular tachyarrhythmias (**Figure II** in the **Data Supplement**) reminiscent of spontaneously terminating TdP episodes. Importantly, as indicated by the activation maps (**Figure 4G**) and corresponding quantitative analysis (**Figure 4H**), the CV in NRVM cultures was not significantly influenced by 100nM astemizole (20±4cm/s vs 21±3cm/s in control cultures; P=0.1254). Collectively, these data validate the utility of NRVM cultures as an in-vitro model for investigating the AP-prolonging and associated proarrhythmic effects of K_v11.1 blockers like astemizole.

Effects of LUF7244 on K_v11.1 Blockade-Associated Proarrhythmic Changes in NRVM Cultures
To investigate the functional consequences of negative allosteric modulation of K_v11.1's interaction with typical K_v11.1 blockers, di-4-ANNEPS-loaded NRVM cultures were incubated for 20 minutes in culture medium containing 10μM LUF7244 before addition of astemizole, sertindole or cisapride. Since the K_i values of sertindole and cisapride for K_v11.1 are more than 10 times higher than that of astemizole (**Table II** in the **Data Supplement**), these drugs were tested at a final concentration of 1μM instead of 100nM as was used for astemizole. After incubation for 30 minutes, the NRVMs were optically mapped. As shown in **Figure 5A**, the APD-prolonging and EAD-promoting effects of astemizole were effectively suppressed by LUF7244. APD_{40} and APD_{90} were significantly shortened from 156±39ms to 118±18ms (n=24, $P<0.0001$) and from 355±66ms to 282±63ms (n=24, $P<0.001$), respectively, *i.e.*, LUF7244 was able to reduce APD_{40} and APD_{90} to control values (**Figure 5B**). Moreover, in the presence of 10μM LUF7244 EADs were no longer observed in NRVM cultures exposed to 100nM astemizole (**Figure 5C**). LUF7244 also prevented the increase in APD_{40} dispersion caused by astemizole (**Figure 5D-E**). Importantly, the CVs in NRVM cultures treated with vehicle, LUF7244, astemizole or LUF7244 plus astemizole did not significantly differ (data not shown). Also, at a final concentration of 10μM LUF7244 per se did not reduce APD or significantly affect APD_{40} dispersion (**Figure 5F-H** and **Figure III** in the **Data Supplement**), suggesting that this negative allosteric modulator poses very little, if any, risk for the development of arrhythmias associated with abnormal APD shortening. Very similar

results of LUF7244 were obtained in NRVM cultures exposed to sertindole or cisapride (**Figure IV** in the **Data Supplement**). LUF7244 can thus suppress the proarrhythmic side effects of drugs from different therapeutic classes by allosteric modulation of the $K_v11.1$ channel without exerting, by itself, any obvious adverse electrophysiological effects on cardiomyocytes.

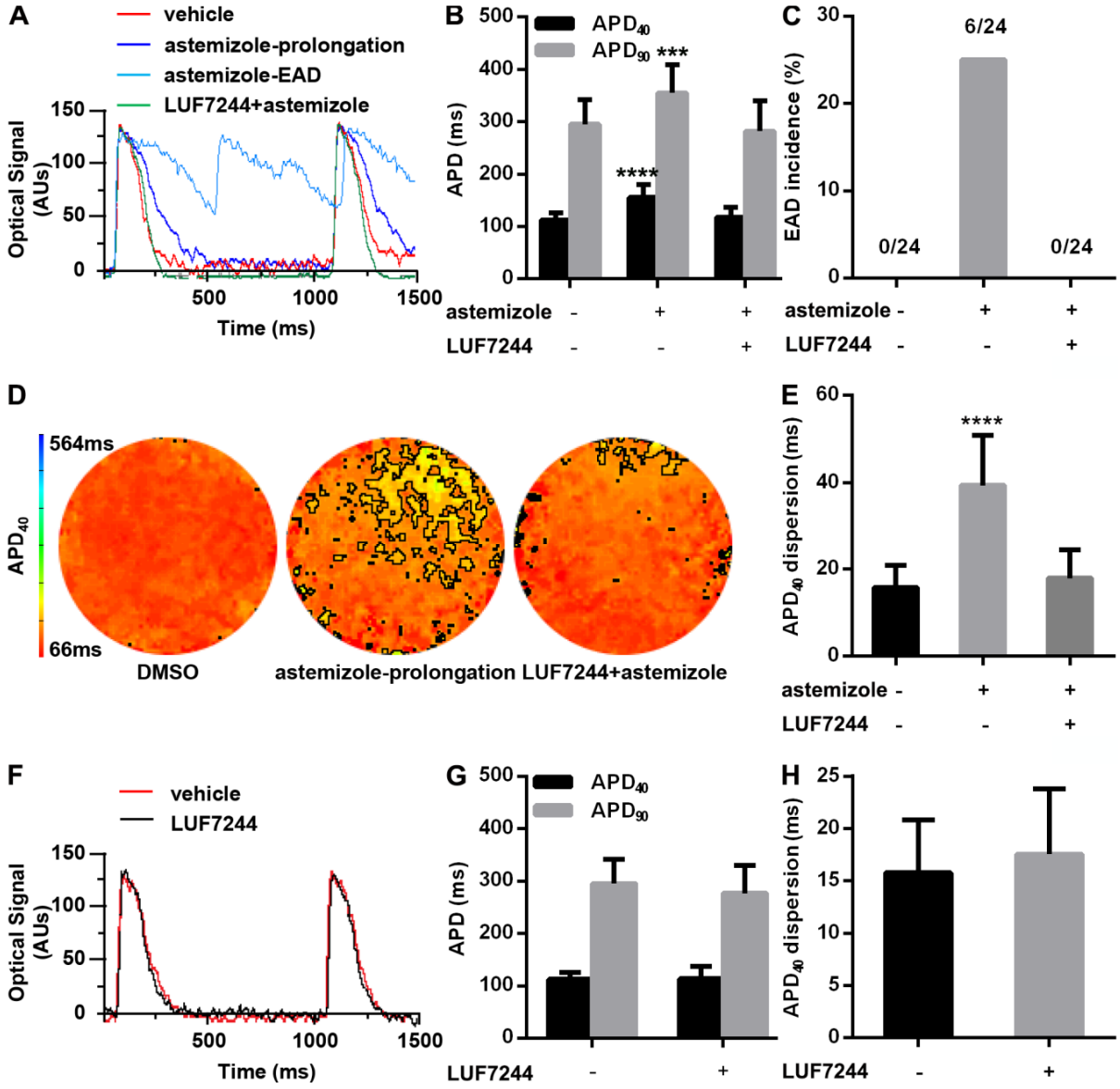

Figure 5. Assessment by optical voltage mapping of the ability of LUF7244 to counteract the proarrhythmic effects of astemizole on NRVMs. Representative filtered optical signal traces (A and F), APD dispersion maps (D) and quantitative analysis (bar graphs in B, C, E, G and H) of control NRVM cultures and of NRVM cultures that had been treated with 100nM astemizole or with 10µM LUF7244 followed by 100nM astemizole immediately before optical voltage mapping. Pretreatment of NRVM cultures with LUF7244 completely prevented the astemizole-induced APD prolongation (APD_{40} and APD_{90}; B), occurrence of EADs (C) and increase in APD_{40} dispersion (D and E). Treatment of NRVM cultures with 10µM LUF7244 only did not change AP morphology (F), APD (G) or APD_{40} dispersion (H). ***P<0.001 and ****P<0.0001.

Discussion

Major Findings

In radioligand binding assays the structurally related compounds VU0405601, ML-T531 and LUF7244 were found to weaken the interaction between the human $K_v11.1$ channel and the class III antiarrhythmic agent dofetilide as well as the unintended $K_v11.1$ blockers astemizole, sertindole and cisapride. VU405601, ML-T531 and LUF7244 exerted their negative effects on the binding of typical $K_v11.1$ blockers to the channel's central cavity by an allosteric mechanism. Importantly, LUF7244 decreased the $K_v11.1$ affinity of astemizole without influencing its affinity at the hH_1R, being astemizole's intentional target (**Figure V** in the **Data Supplement**). Optical voltage mapping showed that incubation of NRVM monolayers with astemizole, sertindole or cisapride led to a significant increase in APD, APD dispersion and, except for cisapride, EAD incidence demonstrating the usefulness of this cellular model system for studying $K_v11.1$ blockade-related proarrhythmic risk. Pretreatment of NRVMs with 10μM LUF7244 effectively prevented the proarrhythmic changes induced by astemizole, sertindole and cisapride without significantly shortening APD by itself and without adversely affecting NRVM viability, excitability and contractility (**Figure VI** in the **Data Supplement**). These findings provide a rationale for further exploring allosteric mo^{du}lation as a strategy to prevent DiVAs.

NRVM Monolayers as Model for Studying Drug-Induced LQTS

Many different methods have been exploited to assess drugs for their $K_v11.1$ blockade-associated arrhythmogenicity.[3,21] The interaction between a drug and the $K_v11.1$ channel is usually first investigated by computational and biochemical assays. Next, the $K_v11.1$ liabilities of suspicious drugs are typically evaluated by electrophysiological measurements on CHO or HEK293 cells expressing the human $K_v11.1$ channel. Despite their practical advantages, these non-excitable cellular models do not recapitulate the complex regulatory circuits governing $K_v11.1$ channel activity in cardiomyocytes and are unsuitable for studying AP generation and propagation. To overcome these shortcomings, human induced pluripotent stem cell-derived cardiomyocytes (hiPSC-CMs) are now often used for cardiotoxicological screenings.[22] However, thus far hiPSC-CMs cannot produce dense monolayers of phenotypically homogeneous ventricular cardiomyocytes for high-resolution optical mapping.[23] We hence employed NRVM monolayers to study the effects of LUF7244 on the proarrhythmic potential of three inadvertent $K_v11.1$ blockers by optical voltage mapping. The reasons to specifically use NRVMs for this purpose are that these cells (i) can be relatively easily isolated and cultured, (ii) are well-characterized and (iii) express functional $K_v11.1$ channels.[24] However, this is the first study using NRVMs to test compounds for their ability to prevent DiVAs resulting from unintended $K_v11.1$ blockade.

Although mechanistic insight into DiVAs is limited, there is broad consensus about spatial dispersion of repolarization and EAD-induced triggered activity providing the substrate and trigger for the genesis of drug-induced TdP, respectively.[2] The EADs typically arise during phase 2 of the cardiac AP due to drug-dependent decreases in I_{Kr} causing increases of APD and QT interval. In support of the validity

of our model, astemizole dose-dependently increased APD and EAD incidence in monolayers of NRVMs (**Figure I** in the **Data Supplement**). Also sertindole and cisapride had APD-prolonging effects (**Figure IVA** and **IVD** in the **Data Supplement**) and each of the three fortuitous $K_v11.1$ blockers increased APD dispersion (**Figure 4F**, **Figure IVC** and **IVF** in the **Data Supplement**). While 100nM astemizole, 1μM sertindole and 1μM cisapride increased APD and APD dispersion to a similar extent, cisapride did not significantly increase EAD incidence in contrast to the other two drugs (**Figure 4D**, **Figure IVB** and **IVE** in the **Data Supplement)**. This finding may be explained by cisapride's inhibitory effect on the $I_{Ca,L}$ in NRVMs.[25]

Initially, EAD-dependent ectopic activity at multiple competing foci was thought to generate the undulating electrocardiographic patterns of TdP. Recently, meandering $I_{Ca,L}$-mediated reentrant circuits initiated by EADs at single foci have been proposed as an alternative explanation for the highly characteristic electrocardiographic signature of TdP.[26,27] Although we did observe several instances of short-lasting, irregular tachyarrhythmias exclusively in NRVM cultures exposed to $K_v11.1$ blockers, they did not allow us to make specific claims about the underlying electrophysiological mechanisms. Pretreatment with LUF7244 rendered NRVM monolayers unsusceptible to the $K_v11.1$-blocking effects of astemizole, sertindole and cisapride. In the presence of LUF7244, these $K_v11.1$ blockers no longer caused heterogeneous APD prolongation and, due to the reduced opportunity for L-type Ca^{2+} channel reactivation, no longer gave rise to EADs. This raises the perspective to use LUF7244 as an antiarrhythmic additive to drugs with unintended I_{Kr}-suppressing effects. Thus, radioligand binding assays in combination with optical voltage mapping experiments of NRVM cultures offer convenient preclinical test systems for evaluating chemical entities that can potentially reduce $K_v11.1$-related cardiotoxicity.

LUF7244's Mode of Action

The chemical structure of LUF7244 resembles those of ML-T531 and VU0405601. In a recent study, 10μM of ML-T531 was shown to reduce the APD of hiPSC-CMs from an LQT1 patient to that of control cells by augmenting I_{Kr}.[11] However, the effects of ML-T531 on the APD of hiPSC-CMs from a healthy individual and ML-T531's ability to inhibit the APD-prolonging effects of unintended $K_v11.1$ blockers were not investigated. Voltage-clamp recordings of $K_v11.1$-expressing CHO cells showed that ML-T531 reduces the deactivation rate of the $K_v11.1$ channel and causes a shift of its inactivation curve towards more positive voltages. Shortly after the discovery of ML-T531, VU0405601 was identified as a compound that, at a final concentration of 5μM, protected Langendorff-perfused rabbit hearts from the proarrhythmic effects of exposure to 100nM dofetilide.[7] Although VU0405601 only partially reversed the dofetilide-dependent increase in APD, its administration prior to dofetilide strongly reduced the pacing-induced arrhythmia incidence from 42% to 4%, which was very close to the 2% of pacing-induced premature ventricular contractions observed in untreated hearts.[7] Exposure of isolated rabbit ventricular myocytes to 5μM of VU0405601 only marginally reduced APD, which is consonant with our finding that 10μM LUF7244 did not noticeably affect the APD of NRVMs. However, at a final concentration of 50μM, VU0405601 decreased the APD_{50} and APD_{90} of rabbit ventricular myocytes by 35±6% and 32±4%, respectively. Patch-clamp analysis of

HEK293K_v11.1 cells linked the APD-shortening effect of 50μM VU0405601 to shifts in the $V_{½}$ of activation and inactivation and to changes in the kinetics of (de)activation and (de)inactivation causing an increase in I_{Kr}.

In this study, we found that VU0405601, ML-T531 and LUF7244 displayed comparatively low K_v11.1 affinities with Hill coefficients significantly different from unity for their [^{3}H]dofetilide displacement curves. This suggests that these ligands bind to the K_v11.1 channel at sites distinct from that of dofetilide, indicative of an allosteric mode of action.[10,28,29] The binding of a drug to a receptor at an allosteric site (*i.e.*, a site topologically distinct from that of the test ligand) triggers a conformational change within the receptor ultimately causing an alteration of the ligand's dissociation rate from its cognate (*i.e.*, orthosteric) binding site.[10,30] Altered ligand dissociation rates have been found representative of allosteric interactions in various drug targets such as muscarinic and adenosine receptors.[10, 31-33] Consistently, VU0405601, ML-T531 and LUF7244 significantly accelerated the dissociation of dofetilide from the K_v11.1 channel, strengthening the conclusion that they are negative allosteric modulators of dofetilide binding to the K_v11.1 channel. Our finding for VU0405601 is in agreement with the results of Potet *et al.*, who presented indirect evidence that VU0405601 binds from outside to the ectodomain of the K_v11.1 channel,[7] while astemizole, cisapride, dofetilide and sertindole all bind to the channel's central cavity from inside.[34-36] In addition, the [^{3}H]dofetilide displacement curves of dofetilide, astemizole, sertindole and cisapride were shifted rightwards by LUF7244 (**Figure 2C-D**) providing further proof for its negative allosteric effect.[10,33] Collectively, the results of the different radioligand binding assays provide strong evidence that VU0405601, ML-T531 and LUF7244 are negative allosteric modulators of dofetilide binding to the K_v11.1 channel. Binding of VU0405601, ML-T531 and LUF7244 likely alters the 3D structure of the K_v11.1 channel, which decreases its affinity for typical K_v11.1 blockers by increasing the dissociation rates of these blockers from the channel. Notably, the vast majority of fortuitous K_v11.1 blockers exert their effects by occupying the central cavity of the K_v11.1 channel and thereby obstructing the transport of K^+ ions through the channel's pore.[37] There are, however, also examples of drugs that reduce I_{Kr} by inhibiting, directly or indirectly, the trafficking of K_v11.1 to the plasma membrane.[38] Given their specific mode of action, it is unlikely that the I_{Kr}-inhibiting effects of these drugs can be abolished by LUF7244 or a related compound.

The ability of LUF7244 to counteract astemizole-, sertindole- and cisapride-related arrythmogenesis may be the combined result of its inhibitory allosteric effect on the binding of these unintended K_v11.1 blockers to the channel and of its direct enhancing effect on the K_v11.1 channel's activity. Indeed, at concentrations ≥25μM, LUF7244 caused APD shortening (**Figure III** in the **Data Supplement**) suggesting that LUF7244 can directly act as (allosteric) K_v11.1 activator like VU0405601 and ML-T531.[7,11] However, the fact that exposure of NRVMs to 10μM LUF7244 alone did not significantly change AP characteristics suggests that LUF7244's K_v11.1-activating activity is not of critical importance for its ability to suppress the proarrhythmic effects of inadvertent K_v11.1 blockers. The absence of a noticeable change in AP shape and duration following exposure of NRVMs to 10μM LUF7244 also argues against a possible effect of this allosteric modulator on cardiac ion channels different from the K_v11.1 channel. In keeping with this notion, Na_v1.5 and

$K_v1.5$ currents and I_{Ks} were not affected or only slightly reduced by 50μM VU0405601.[7] Likewise, ML-T531 at a final concentration of 10μM had a minor suppressive effect on I_{Ks} and did not influence $Na_v1.5$, $Ca_v1.2$, $K_v4.3$ or Kir2.1 activities.[11] Thus, the antiarrhythmic propensity of LUF7244 is dominated by its negative allosteric impact on the binding of typical $K_v11.1$ blockers to the channel.

Since LUF7244 significantly decreased the $K_v11.1$ affinities of drugs with very different chemical structures (**Figure 2B**) in radioligand binding assays and prevented these drugs from causing APD prolongation in NRVMs, LUF7244 may be effective in reducing the cardiotoxicity of a broad range of $K_v11.1$ blockers. Further support for this notion comes from the fact that VU0405601, which was here shown to inhibit dofetilide's interaction with the $K_v11.1$ channel by a similar mechanism to LUF7244, could abolish the blockade of $K_v11.1$ by seven different drugs.[7] The different degree to which LUF7244 increased the K_i values of dofetilide, astemizole, sertindole and cisapride suggests that the sensitivity of different $K_v11.1$ blockers to conformational changes in the $K_v11.1$ proteins differs. Accordingly, different LUF7244 concentrations may be required to abrogate the proarrhythmic effects of distinct $K_v11.1$ blockers.

Although at a final concentration of 50μM LUF7244's ability to weaken the interaction between [^{3}H]dofetilide and the $K_v11.1$ channel was similar to those of VU0405601 and ML-T531 (**Figure 1D**), the new modulator was much more effective than the other two compounds at a final concentration of 10μM (**Figure 1C**). Moreover, even 50μM VU0405601 only modestly inhibited the APD-prolonging effect of 1μM dofetilide (K_i for human $K_v11.1$: 6.0nM) on rabbit ventricular myocytes,[7] while 10μM LUF7244 totally blocked the APD prolongation caused by exposure of NRVMs to 100nM astemizole (K_i for human $K_v11.1$: 1.2nM). These findings together with the substantial decrease in the APD of normal rabbit ventricular myocytes caused by 50μM VU0405601 (see above), suggests that LUF7244 may possess a more favorable safety profile than VU0405601 or ML-T531.

Limitations

Due to the difficulty to obtain and culture adult human ventricular myocytes, NRVMs were used as 2D model system to investigate the effects of LUF7244 on $K_v11.1$ blockade-associated proarrhythmic changes in cardiac electrophysiology. However, ventricular adult human and neonatal rat cardiomyocytes have different AP morphologies because of qualitative and quantitative differences in the molecular components shaping the APs. Also, changes in cardiomyocyte electrophysiological properties may work out differently in a 2D cell layer than in the (3D) heart. Nonetheless, studies on NRVM monolayers have greatly contributed to our current understanding of cardiac electrophysiology. Moreover, in spite of the differences in ventricular ion channel composition between humans and rats, their $K_v11.1$ proteins are very similar showing 95% amino acid identity for the largest isoforms. Consistently, the results of the radioligand binding assays, which were carried out with the human $K_v11.1$ protein, correlated very well with those of the optical mapping studies using NRVMs. Yet, ultimately, the ability of LUF7244 to counteract the proarrhythmic effects of unintended $K_v11.1$ blockers should be investigated in human subjects.

As mentioned above, LUF7244 did not inhibit the binding of astemizole to its intended target in radioligand binding assays (**Figure V** in the **Data Supplement**) and did not compromise the viability, excitability or contractility of NRVMs (**Figure VI** in the **Data Supplement**) at a concentration sufficient to fully abrogate the proarrhythmic consequences of drug-induced $K_v11.1$ blockade in these cells. Despite these encouraging results, certainty about the lack of specific adverse/interfering effects of this negative allosteric modulator of $K_v11.1$ channel in humans can only be obtained through clinical studies. Moreover, now that the ability of LUF7244 to reduce the channel binding affinities of $K_v11.1$ blockers has been established, allosteric modulators with higher safety and/or efficacy than LUF7244 are likely to arise in the near future. The design of such compounds may benefit from identification of the precise binding site of LUF7244 at the $K_v11.1$ channel.

Conclusions

Allosteric modulators of the $K_v11.1$ channel could provide a new pharmacological treatment for drug-induced LQTS by preventing the potentially arrhythmogenic changes in AP characteristics caused by unintended $K_v11.1$ blockers. Through combined administration with a negative allosteric modulator, use of "old" drugs that have been banned because of their "$K_v11.1$ liabilities" may be resumed and new drugs with $K_v11.1$-blocking effects may not have to be excluded from clinical application.

Acknowledgements

We thank Cindy Schutte-Bart (Department of Cardiology, Leiden University Medical Center, Leiden, the Netherlands) for her help with establishing primary NRVM cultures and Prof. Guang-Qian Zhou (Anti-Ageing and Regenerative Medicine Centre, Shenzhen University, Shenzhen, People's Republic of China) for his efforts to establish collaborations between Dutch and Chinese researchers.

Funding Sources

Zhiyi Yu and Jia Liu were supported by the Chinese Scholarship Council. Additional support was provided by ICIN-Netherlands Heart Institute and the Royal Netherlands Academy of Arts and Sciences (Chinese Exchange Programme grant 10CDP007 to Antoine de Vries).

Disclosures

None.

References

1. Stockbridge N, Morganroth J, Shah RR, Garnett C. Dealing with global safety issues. Drug Saf. 2013;36:167-182.
2. Antzelevitch C. Ionic, molecular, and cellular bases of QT-interval prolongation and Torsade de Pointes. Europace. 2007;9:iv4-iv15.
3. Kannankeril P, Roden DM, Darbar D. Drug-induced long QT syndrome. Pharmacol Rev. 2010;62:760-781.
4. Vandenberg JI, Perry MD, Perrin MJ, Mann SA, Ke Y, Hill AP. hERG K^+ channels: Structure, function, and clinical significance. Physiol Rev. 2012;92:1393-1478.
5. Sanguinetti MC. hERG1 channel agonists and cardiac arrhythmia. Curr Opin Pharmacol. 2014;15:22-27.
6. Kang J, Chen X-L, Wang H, Ji J, Cheng H, Incardona J, Reynolds W, Viviani F, Tabart M, Rampe D. Discovery of a small molecule activator of the human ether-a-go-go-related gene (hERG) cardiac K^+ channel. Mol Pharmacol. 2005;67:827-836.
7. Potet F, Lorinc AN, Chaigne S, Hopkins CR, Venkataraman R, Stepanovic SZ, Lewis LM, Days E, Sidorov VY, Engers DW, Zou B, Afshartous D, George AL Jr, Campbell CM, Balser JR, Li M, Baudenbacher FJ, Lindsley CW, Weaver CD, Kupershmidt S. Identification and characterization of a compound that protects cardiac tissue from human ether-a-go-go-related gene (hERG)-related drug-induced arrhythmias. J Biol Chem. 2012;287:39613-39625.
8. May LT, Leach K, Sexton PM, Christopoulos A. Allosteric modulation of G protein-coupled receptors. Annu Rev Pharmacol Toxicol. 2007;47:1-51.
9. Conn PJ, Christopoulos A, Lindsley CW. Allosteric modulators of GPCRs: A novel approach for the treatment of CNS disorders. Nat Rev Drug Discov. 2009;8:41-54.
10. Christopoulos A, Changeux JP, Catterall WA, Fabbro D, Burris TP, Cidlowski JA, Olsen RW, Peters JA, Neubig RR, Pin J-P, Sexton PM, Kenakin TP, Ehlert FJ, Spedding M, Langmead CJ. International union of basic and clinical pharmacology. Xc. Multisite pharmacology: Recommendations for the nomenclature of receptor allosterism and allosteric ligands. Pharmacol Rev. 2014;66:918-947.
11. Zhang H, Zou B, Yu H, Moretti A, Wang X, Yan W, Babcock JJ, Bellin M, McManus OB, Tomaselli G, Nan F, Laugwitz KL, Li M. Modulation of hERG potassium channel gating normalizes action potential duration prolonged by dysfunctional KCNQ1 potassium channel. Proc Natl Acad Sci U S A. 2012;109:11866-11871.
12. Diaz GJ, Daniell K, Leitza ST, Martin RL, Su Z, McDermott JS, Cox BF, Gintant GA. The [^{3}H]dofetilide binding assay is a predictive screening tool for hERG blockade and proarrhythmia: Comparison of intact cell and membrane preparations and effects of altering $[K^+]_o$. J Pharmacol Toxicol Methods. 2004;50:187-199.
13. Ficker E, Jarolimek W, Kiehn J, Baumann A, Brown AM. Molecular determinants of dofetilide block of hERG K^+ channels. Circ Res. 1998;82:386-395.
14. Aronov AM. Predictive in silico modeling for hERG channel blockers. Drug Discov Today. 2005;10:149-155.
15. Yu Z, Klaasse E, Heitman LH, IJzerman AP. Allosteric modulators of the hERG K^+ channel: Radioligand binding assays reveal allosteric characteristics of dofetilide analogs. Toxicol Appl Pharmacol. 2014;274:78-86.

16. Pijnappels DA, Schalij MJ, Ramkisoensing AA, van Tuyn J, de Vries AA, van der Laarse A, Ypey DL, Atsma DE. Forced alignment of mesenchymal stem cells undergoing cardiomyogenic differentiation affects functional integration with cardiomyocyte cultures. Circ Res. 2008;103:167-176.
17. Askar SF, Ramkisoensing AA, Schalij MJ, Bingen BO, Swildens J, van der Laarse A, Atsma DE, de Vries AA, Ypey DL, Pijnappels DA. Antiproliferative treatment of myofibroblasts prevents arrhythmias in-vitro by limiting myofibroblast-induced depolarization. Cardiovasc Res. 2011;90:295-304.
18. Yu Z, IJzerman A, Heitman L. K_v11.1 (hERG)-induced cardiotoxicity: A molecular insight from a binding kinetics study of prototypic K_v11.1 (hERG) inhibitors. Br J Pharmacol. 2015;172:940-945.
19. Himel HD, Bub G, Lakireddy P, El-Sherif N. Optical imaging of arrhythmias in the cardiomyocyte monolayer. Heart Rhythm. 2012;9:2077-2082.
20. Redfern W, Carlsson L, Davis A, Lynch W, MacKenzie I, Palethorpe S, Siegl P, Strang I, Sullivan A, Wallis R, Camm AJ, Hammond TG. Relationships between preclinical cardiac electrophysiology, clinical QT interval prolongation and Torsade de Pointes for a broad range of drugs: Evidence for a provisional safety margin in drug development. Cardiovasc Res. 2003;58:32-45.
21. Heijman J, Voigt N, Carlsson LG, Dobrev D. Cardiac safety assays. Curr Opin Pharmacol. 2014;15:16-21.
22. Khan JM, Lyon AR, Harding SE. The case for induced pluripotent stem cell-derived cardiomyocytes in pharmacological screening. Br J Pharmacol. 2013;169:304-317.
23. Lee P, Klos M, Bollensdorff C, Hou L, Ewart P, Kamp TJ, Zhang J, Bizy A, Guerrero-Serna G, Kohl P, Jalife J, Herron TJ. Simultaneous voltage and calcium mapping of genetically purified human induced pluripotent stem cell-derived cardiac myocyte monolayers. Circ Res. 2012;110:1556-1563.
24. Korhonen T, Hänninen SL, Tavi P. Model of excitation-contraction coupling of rat neonatal ventricular myocytes. Biophys J. 2009;96:1189-1209.
25. Davie C, Pierre-Valentin J, Pollard C, Standen N, Mitcheson J, Alexander P, Thong B. Comparative pharmacology of guinea pig cardiac myocyte and cloned hERG (I_{Kr}) channel. J Cardiovasc Electrophysiol. 2004;15:1302-1309.
26. Murakawa Y. Focal and reentrant mechanisms of Torsades de Pointes: EAD, reentry, or chimera? J Arrhythm. 2011;27:28-37.
27. Chang MG, Sato D, de Lange E, Lee J-H, Karagueuzian HS, Garfinkel A, Weiss JN, Qu Z. Bi-stable wave propagation and early afterdepolarization-mediated cardiac arrhythmias. Heart Rhythm. 2012;9:115-122.
28. Pedigo N, Yamamura H, Nelson DL. Discrimination of multiple [^{3}H]5-hydroxytryptamine binding sites by the neuroleptic spiperone in rat brain. J Neurochem. 1981;36:220-226.
29. van den Nieuwendijk AM, Pietra D, Heitman L, Göblyös A, IJzerman AP. Synthesis and biological evaluation of 2,3,5-substituted [1,2,4] thiadiazoles as allosteric modulators of adenosine receptors. J Med Chem. 2004;47:663-672.
30. Vauquelin G, Van Liefde I. Radioligand dissociation measurements: Potential interference of rebinding and allosteric mechanisms and physiological relevance of the biological model systems. Expert Opin Drug Discov. 2012;7:583-595.

31. Schober DA, Croy CH, Xiao H, Christopoulos A, Felder CC. Development of a radioligand, [^{3}H]ly2119620, to probe the human M_2 and M_4 muscarinic receptor allosteric binding sites. Mol Pharmacol. 2014;86:116-123.
32. Gao Z, Van Muijlwijk-Koezen JE, Chen A, Müller CE, IJzerman AP, Jacobson KA. Allosteric modulation of A_3 adenosine receptors by a series of 3-(2-pyridinyl) isoquinoline derivatives. Mol Pharmacol. 2001;60:1057-1063.
33. Dror RO, Green HF, Valant C, Borhani DW, Valcourt JR, Pan AC, Arlow DH, Canals M, Lane JR, Rahmani R, Baell JB, Sexton PM, Christopoulos A, Shaw DE. Structural basis for modulation of a G-protein-coupled receptor by allosteric drugs. Nature. 2013;503:295-299.
34. Kamiya K, Niwa R, Mitcheson JS, Sanguinetti MC. Molecular determinants of hERG channel block. Mol Pharmacol. 2006;69:1709-1716.
35. Pearlstein RA, Vaz RJ, Kang J, Chen X-L, Preobrazhenskaya M, Shchekotikhin AE, Korolev AM, Lysenkova LN, Miroshnikova OV, Hendrix J, Rampe D. Characterization of hERG potassium channel inhibition using comsia 3D QSAR and homology modeling approaches. Bioorg Med Chem Lett. 2003;13:1829-1835.
36. García-Ferreiro RE, Kerschensteiner D, Major F, Monje F, Stühmer W, Pardo LA. Mechanism of block of hERG1 K^+ channels by imipramine and astemizole. J Gen Physiol. 2004;124:301-317.
37. Perry M, Stansfeld PJ, Leaney J, Wood C, de Groot MJ, Leishman D, Sutcliffe MJ, Mitcheson JS. Drug binding interactions in the inner cavity of hERG channels: Molecular insights from structure-activity relationships of clofilium and ibutilide analogs. Mol Pharmacol. 2006;69:509-519.
38. Nogawa H, Kawai T. hERG trafficking inhibition in drug-induced lethal cardiac arrhythmia. Eur J Pharmacol. 2014;741:336-339.

SUPPLEMENTAL MATERIAL

Materials

Dofetilide was synthesized in-house as previously described.[1] Bovine serum albumin (BSA, fraction V) and the fortuitous K_v11.1 blockers astemizole, sertindole and cisapride were purchased from Sigma-Aldrich (St. Louis, MO). Tritium-labeled dofetilide (specific activity: 82.3 Ci/mmol) and astemizole (specific activity: 78.4 Ci/mmol) were obtained from PerkinElmer (Groningen, the Netherlands). The synthesis and chemical analysis of VU0405601, ML-T531, as well as the design, synthesis and chemical analysis of LUF7244 will be detailed elsewhere. G418 was purchased from Stratagene (Cedar Creek, TX). All other chemicals were of analytical grade and obtained from standard commercial sources. HEK293K_v11.1 cells, *i.e.*, HEK293 cells stably overexpressing the human *KCNH2* gene, were kindly provided by Dr. Eckhard Ficker (Case Western Reserve University, Cleveland, OH).[2] Plasmid pcDNA3.1-hH_1Rwt encoding the human histamine H_1 receptor (hH_1R) was a gift of Prof. Thue W. Schwartz (University of Copenhagen, Copenhagen, Denmark). This plasmid was used to generate HEK293hH_1R cells, *i.e.*, cells transiently overexpressing the human *HRH1* gene (see "*HEK293 Cell Culture and Transfection*").

All animal experiments were approved by the Animal Experiments Committee of Leiden University Medical Center and conformed to the Guide for the Care and Use of Laboratory Animals as stated by the US National Institutes of Health.

Methods

HEK293 Cell Culture and Transfection

HEK293 cells were cultured in a humidified atmosphere at 37°C and 7% CO_2 in Dulbecco's modified Eagle's medium (DMEM; Sigma-Aldrich, catalog number: D6546) supplemented with 10% fetal bovine serum (Sarstedt, Nümbrecht, Germany), 50 IU/mL penicillin (Sarstedt) and 50 µg/mL streptomycin (Sarstedt). When the cells had reached 50-60% confluence, the culture medium was refreshed and 500 µL of 150 mM NaCl containing 15 µg of pcDNA3.1-hH_1Rwt DNA and 45 µg of linear 25-kDa polyethylenimine (Polysciences Europe, Eppelheim, Germany) was added per 100-mm culture dish (Sarstedt). The resulting HEK293hH_1R cells were harvested 48 hours after transfection.

Preparation of Membrane Samples

HEK293K_v11.1 cells were cultured and membranes were prepared and stored as detailed previously.[3] Membranes of HEK293hH_1R cells, were prepared and stored as described for HEK293K_v11.1 cells except that incubation buffer I (50 mM Tris-HCl [pH 7.4]) was used instead of incubation buffer II (10 mM HEPES-NaOH [pH 7.4], 130 mM NaCl, 60 mM KCl, 0.8 mM $MgCl_2$, 1 mM EGTA, 10 mM glucose, 0.1% BSA).

Radioligand Displacement Assays with [^{3}H]dofetilide

[^{3}H]Dofetilide binding assays for the K_v11.1 channel were performed in incubation buffer II as described previously.[3] Briefly, membrane aliquots containing 20 µg

protein were incubated with 5 nM [^{3}H]dofetilide in a total volume of 100 µL at 25°C for 1 hour. Radioligand displacement experiments were carried out with various concentrations of the test compounds. Total binding was determined in the presence of unsupplemented incubation buffer II, whereas non-specific binding was evaluated in incubation buffer II containing 10 µM astemizole. Displacement experiments with different concentrations of dofetilide, astemizole, sertindole and cisapride were conducted in the absence (control) or presence of 10 µM LUF7244. Incubations were terminated by dilution with ice-cold wash buffer (25 mM Tris-HCl [pH 7.4], 130 mM NaCl, 60 mM KCl, 0.8 mM $MgCl_2$, 0.05 mM $CaCl_2$, 0.05% BSA). Free radioligand was separated from bound [^{3}H]dofetilide by rapid filtration through a UniFilter-96 GF/B microplate using a PerkinElmer MicroBeta Filtermate-96 harvester. The filter-bound radioactivity was determined using a Wallac 1450 MicroBeta TriLux liquid scintillation counter (PerkinElmer) after extraction with 25 µL MicroScint 20 (PerkinElmer).

Radioligand Displacement Assays with [^{3}H]astemizole

[^{3}H]Astemizole binding assays for the hH_1R were performed in incubation buffer I. Membrane aliquots containing 15 µg protein were incubated with 3.5 nM [^{3}H]astemizole in a total volume of 100 µL at 25°C for 3 hours. Total binding was determined in the presence of unsupplemented incubation buffer I, whereas non-specific binding was evaluated in incubation buffer I containing 100 µM astemizole. LUF7244 displacement assays were carried out with various concentrations of this compound, while displacement assays with different concentrations of astemizole were conducted in the absence (control) or presence of 10 µM LUF7244. Incubations were terminated by dilution with ice-cold wash buffer (50 mM Tris-HCl [pH 7.4]). Samples were processed further as described under "*Radioligand Displacement Assays with [^{3}H]dofetilide*".

Kinetic Dissociation Assays with [^{3}H]dofetilide

Kinetic dissociation assays of [^{3}H]dofetilide were performed as described previously[3] with the following modifications. Single-point dissociation experiments were conducted by addition of 10 µM dofetilide in the absence (control) or presence of 10 or 50 µM of the selected compounds after preincubating membranes with [^{3}H]dofetilide at 25°C for 2 hours. After 6 minutes of dissociation, incubations were terminated and samples were obtained as described under "*Radioligand Displacement Assays with [^{3}H]dofetilide*". Traditional dissociation experiments were carried out with 10 µM dofetilide in the absence (control) or presence of 50 µM of the test compounds at 25°C for a total period of 2 hours after preincubation with the radioligand. The amounts of [^{3}H]dofetilide still bound to the receptor were measured at various time intervals. The concentration-dependent effect of LUF7244 was determined by addition of 10 µM dofetilide in the absence (control) or presence of different concentrations of LUF7244. After 6 minutes of dissociation, incubations were terminated and samples were obtained as described under "*Radioligand Displacement Assays with [^{3}H]dofetilide*". The non-radiolabeled dofetilide was applied at a concentration 1667-fold higher than the K_i for the interaction of dofetilide

with $K_v11.1$ (**Table II**), to avoid a significant contribution of reassociation of the radioligand with the channel to the results of the kinetic dissociation assays.

Isolation and Culture of Neonatal Rat Ventricular Myocytes (NRVMs)

NRVMs were isolated and cultured as described previously.[4] Briefly, neonatal rats were anaesthetized with 4-5% isoflurane inhalation anesthesia. After adequate anesthesia had been confirmed by the absence of reflexes, the heart was quickly excised. Ventricles were separated from the remainder of the heart, cut into small pieces with a fine scissor and a scalpel and dissociated by collagenase type l (Worthington, Lakewood, NJ) digestion. The resulting cell suspension was applied to Primaria culture dishes (Corning Life Sciences, Amsterdam, the Netherlands) and incubated for 75 minutes at 37°C in a humidified atmosphere of 5% CO_2 to allow preferential attachment of cardiac fibroblasts. The unattached cells (mainly cardiomyocytes) were collected, passed through a cell strainer (70-µm mesh pore size; BD Biosciences, Breda, the Netherlands) and applied at a density of 8×10^5 cells/well of a 24-well cell culture plate (Corning Life Sciences) to fibronectin (Sigma-Aldrich)-coated, round glass coverslips. Proliferation of residual cardiac fibroblasts (10-15%) was inhibited by incubating the cells for 2 hours in culture medium containing 10 µg/mL mitomycin C (Sigma-Aldrich) at 24 hours after seeding (*i.e.*, at day 1 of culture). Cells were subsequently maintained in a 1:1 mixture of DMEM (Life Technologies Europe, Bleiswijk, the Netherlands, catalog number: 22320) and Ham's F10 medium (Life Technologies Europe, catalog number: 11550) supplemented with 5% horse serum (Life Technologies Europe), 2% BSA and sodium ascorbate to a final concentration of 0.4 mM. This so-called NRVM medium was replaced daily.

Immunocytochemical Analyses

NRVMs were plated on fibronectin-coated, 15-mm diameter round glass coverslips at a density of 4×10^4 cells. At day 9 of culture, the cells were washed thrice with ice-cold phosphate-buffered saline (PBS), fixed for 30 minutes in buffered 4% formaldehyde (Added Pharma, Oss, the Netherlands) of 4°C and permeabilized by a 10-minute incubation at room temperature (RT) with 0.1% Triton X-100 in PBS. Next, the cells were double-immunostained for $K_v11.1$ (rabbit polyclonal antibodies raised against the C terminus of human $K_v11.1$, Merck Millipore, Billerica, MA, catalog number: AB5930) and α-actinin (mouse monoclonal antibody, Sigma-Aldrich, clone: EA-53). Incubation with primary antibodies (diluted 1:200 in PBS-0.1% normal donkey serum) and corresponding donkey Alexa Fluor 488/568-conjugated secondary antibodies (1:400 dilution, Life Technologies Europe) lasted for 2 hours. To visualize their nuclei, the cells were incubated for 10 minutes at RT with 10 µg/mL Hoechst 33342 (Life Technologies Europe) in PBS. After each processing step, the cells were washed three times with PBS of RT. To minimize photobleaching, coverslips were mounted in VECTASHIELD mounting medium (Vector Laboratories, Burlingame, CA). Photomicrographs were obtained with the aid of a digital color camera-equipped fluorescence microscope (Nikon Eclipse 80i; Nikon Instruments Europe, Amstelveen, the Netherlands).

Reverse Transcription-Quantitative Polymerase Chain Reaction Analyses

Cultures of NRVMs and of neonatal rat cardiac fibroblasts (NRCFs; maintained in NRVM medium) were washed once with ice-cold PBS after which the cells were lysed in TRIzol reagent (Life Technologies Europe) and total RNA was isolated using the RNeasy Mini kit (QIAGEN Benelux, Venlo, the Netherlands). The RNA was reverse transcribed with the iScript cDNA synthesis kit (Bio-Rad, Hercules, CA) and the resulting cDNA was amplified by PCR using the Bioline SensiFAST SYBR No-ROX kit (GC biotech, Alphen aan den Rijn, the Netherlands). The forward and reverse primers for the amplification of rat *Kcnh2*-specific cDNA were localized in different exons and had the following sequences, respectively: 5′ TAGCCTCCTCAACATCCC 3′ and 5′ CCATGTCTGCACTTAGCC 3′. For normalization purposes, rat 18S rRNA (*Rn18s*)-specific cDNA was amplified in parallel using the following forward and reverse primer, respectively: 5' GTAACCCGTTGAACCCCATT 3' and 5' CCATCCAATCGGTAGTAGCG 3'. PCR amplifications were carried out in a CFX96 Touch Real-Time PCR detection system (Bio-Rad) using a 2-step cycling protocol (20-40 cycles of 95°C 10 sec, 60°C 30 sec) after a 5-minute incubation at 95°C. Quantitative analyses were based on the $2^{-\Delta\Delta CT}$ method using CFX Manager software (Bio-Rad). For these analyses, PCRs were performed *in triplo* on three independent samples.

Optical Voltage Mapping

Action potentials (APs) were investigated on a whole-culture scale by optical voltage mapping using the potentiometric dye di-4-ANEPPS (Life Technologies Europe) as described previously.[5] The measurements were carried out at 37°C on 9-day-old confluent NRVM monolayer cultures (**Figure 3B** in the **Main Manuscript**). Optical signals were captured using a MiCAM ULTIMA-L imaging system (SciMedia, Costa Mesa, CA). To validate the experimental model, cells were incubated for 20 minutes in culture medium containing 0, 10, 30, 100 or 300 nM of the hH_1R antagonist and unintended $K_v11.1$ blocker astemizole and dimethylsulfoxide (DMSO) at a final concentration of 0.03%. In a subsequent experiment, NRVM cultures were first exposed for 30 minutes to 10 μM LUF7244 or its solvent (*i.e.*, culture medium containing 0.1% DMSO). Next, astemizole (final concentration of 100 nM) or vehicle was added to the culture medium raising the DMSO concentration to 0.13%. Following an incubation period of 30 minutes at 37°C, optical recordings were started in the continued presence of the appropriate vehicle/drug combinations (see **Figure 3A** in the **Main Manuscript** for a scheme of the basic experimental setup). Optical traces were analyzed using Brain Vision Analyzer 1208 software (Brainvision, Tokyo, Japan). To minimize noise artifacts, calculations were based on the average of the signals at a selected pixel and its eight nearest neighbors. Conduction velocity (CV), AP duration (APD) at 40 and 90% repolarization (APD_{40} and APD_{90}, respectively), APD dispersion and early afterdepolarizations (EADs) incidence were determined using NRVM cultures showing uniform AP propagation and 1:1 capture after 1-Hz local stimulation. Each of these electrophysiological parameters was the average of values obtained from 6 different positions equally distributed across the cell cultures.

The effects of LUF7244 on the $K_v11.1$-inhibiting antipsychotic drug sertindole and gastroprokinetic agent cisapride were assessed in the same way as for astemizole expect that the final concentration of sertindole and cisapride was 1 μM.

To study the effects of long-term $K_v11.1$ allosteric modulation in the absence and presence of an unintended $K_v11.1$ blocker on cardiac excitability, confluent NRVM cultures were incubated for 3 days in culture medium containing 100 nM astemizole and/or 10 μM LUF7244 prior to potentiometric dye loading, short-term drug treatment (see above) and optical mapping in the continued presence of drug(s) at culture day 9. Confluent NRVM monolayers exposed to culture medium containing vehicle (*i.e.*, DMSO at a final concentration of 0.13%) only, served as negative controls for this experiment. Just prior to optical mapping, movies of the cells were made using a Carl Zeiss Axiovert 40C microscope equipped with a LD A-Plan 20×/0.3 Ph1 objective (Zeiss Nederland, Sliedrecht, the Netherlands) to record their contractions upon electrical field stimulation using two epoxy-coated platinum electrodes with an interelectrode spacing of 13 mm. The electrical stimulus consisted of a 1.5-ms rectangular pulse of 12V produced at a frequency of 1 Hz by a model EV4543 miniature temporary cardiac pacemaker (PACE Medical, Waltham, MA).

Apoptosis Assay

To investigate the effects of long-term $K_v11.1$ allosteric modulation in the absence or presence of simultaneous $K_v11.1$ blockade on cell viability, externalized phosphatidylserine (as early marker of apoptosis) was detected using Alexa Fluor-568-conjugated annexin V (Life Technologies Europe). NRVM cultures in 24-well plates were treated cells for 72 hours with 100 nM astemizole and/or 10 μM LUF7244 as described under *"Optical Voltage Mapping"*. Mock-treated cells and cells incubated for 24 hours in culture medium containing 1 μM doxorubicin (Sigma-Aldrich) served as negative and positive controls, respectively. Next, the cells were washed once with ice-cold PBS and incubated for 15 minutes at RT with annexin V conjugate diluted 40-fold in binding buffer (10 mM HEPES-NaOH [pH 7.4], 140 mM NaCl, 2.5 mM $CaCl_2$) of 4°C containing 10 μg/mL Hoechst 33342. After a single wash with binding buffer of 4°C, photomicrographs were taken using a Leica DMI6000 B inverted microscope equipped with a Leica DFC300 FX digital color camera (both from Leica Microsystems, Rijswijk, the Netherlands).

Data Analysis

Data of the radioligand binding assays were analyzed with GraphPad Prism 5.0 (GraphPad Software, San Diego, CA). Half maximal inhibitory concentrations (*i.e.*, IC_{50} values) in displacement assays were directly obtained from non-linear regression analysis of dose-response curves. Half maximal inhibitory concentrations (*i.e.*, IC50 values) in displacement assays were directly obtained from non-linear regression analysis of dose-response relationships by four-parameter logistic curve fitting. Apparent inhibitory binding constants (K_i values) were derived from the IC_{50} values according to the Cheng-Prusoff relationship[6]: $K_i=IC_{50}/(1+[L^*]/K_D)$, where [L*] is the concentration of radioligand and K_D is its dissociation constant determined by saturation assay[7]. Dissociation rate constants (k_{off}) were obtained by computer analysis of the exponential decay of [^{3}H]dofetilide bound to the $K_v11.1$ channel. Half maximal effective concentrations (*i.e.*, EC_{50} values) from kinetic dissociation assays were calculated by non-linear regression analysis of concentration-effect curves of dissociation in the presence of different concentrations of unlabeled ligands. Values

obtained from the radioligand binding assays are means of three independent experiments performed in duplicate. The number of samples per experimental group in the optical voltage mapping experiments varied from 6 to 24 as indicated. Data are expressed as mean±standard error of the mean (SEM) for the radioligand binding assays or as mean±standard deviation (SD) for the optical voltage mapping experiments. Statistical analysis of all the results were done using non-parametric tests, Mann-Whitney U test for comparison of two groups and Kruskal-Wallis test for comparison of more than two groups. Statistical analysis of the results of radioligand binding assays was done using nonparametric Mann-Whitney U test.

Supplemental Results

Comparison of the Concentration-dependent Effects of LUF7244 and VU0405601 on APD in NRVMs

Given the known APD-shortening effect of VU0405601[8] in rabbit ventricular cardiomyocytes and the similarities in chemical structure between LUF7244 and VU0405601, a side-by-side comparison of the concentration-dependent effects of these 2 compounds on the APD of NRVMs was performed. Consistent with the results shown in **Figure 5F and 5G** of the **Main Manuscript**, at a final concentration of 10 μM, LUF7244 did not significantly affect the APD in NRVMs as assesses by optical voltage mapping (**Figure IIIA**). In contrast, exposure of NRVM monolayers to 25 or 62.5 μM of LUF7244 decreased APD_{40} and significantly decreased APD_{90} to a similar extent. While the APD-shortening effect of LUF7244 was first observed at a final concentration of 25 μM, VU0405601 already caused a decrease of APD_{40} and a significant decrease APD_{90} at a final concentration of 10 μM (**Figure IIIB**). Raising the VU0405601 concentration to 25 or 62.5 μM did not lead to further APD shortening. Moreover, LUF7244 and VU0405601 had very similar maximum effects on the APD. Importantly, neither LUF7244 nor VU0405601 significantly changed the conduction velocity in the NRVM cultures at the 3 concentrations tested. These findings suggest that both LUF7244 and VU0405601 can increase I_{Kr} density but that VU0405601 is a more potent $K_v11.1$ activator than LUF7244.

Effects of LUF7244 on the Binding of [^{3}H]Astemizole to the hH_1R

To be of practical use in preventing drug-induced ventricular arrhythmias, LUF7244 should not interfere with the desired activities of unintended $K_v11.1$ blockers. We therefore tested whether LUF7244 affected binding of the antihistamine drug astemizole to the hH_1R. As displayed in **Figure VA**, LUF7244 did not decrease the binding of [^{3}H]astemizole to the hH_1R. Furthermore, the displacement curve of astemizole binding to the hH_1R was not significantly shifted rightwards by LUF7244 (**Figure VB**). Thus, LUF7244 reduces the affinity of the $K_v11.1$ channel for astemizole without affecting the binding of astemizole to its intended target receptor (*i.e.*, the hH_1R).

Effects of Prolonged Exposure of NRVMs to LUF7244 and/or Astemizole on Cell Viability, Excitability and Contractility

To study the effects of prolonged allosteric modulation and/or blockade of the $K_v11.1$ channel on the viability of cardiomyocytes, 6-day-old NRVM cultures were incubated for 72 hours in culture medium containing 10 μM LUF7244 and/or 100 nM astemizole. Subsequent staining with fluorescently labeled annexin V to detect cell surface-exposed phosphatidylserine yielded only very weak signals for cells exposed to vehicle, LUF7244, astemizole or LUF7244 plus astemizole, while NRVMs incubated for 24 hours with the proapoptotic drug doxorubicin displayed strong annexin V fluorescence (**Figure VIA**). These results indicate that prolonged exposure to 10 μM LUF7244 alone or in combination with 100 nM astemizole does not trigger programmed cell death.

Optical voltage mapping of 9-day-old NRVM cultures that had been mock-treated or treated for 72 hours with 10 μM LUF7244 and/or 100 nM astemizole produced very similar results as were obtained for cells that had only briefly been exposed to these compounds (compare **Figure 4** and **5** of the **Main Manuscript** with **Figure VIB** and **VIC**) and provided no indications for a drug-related reduction in excitability. Moreover, after electrical field stimulation cells in all four treatment groups displayed rhythmic contractions following the pacing frequency of 1 Hz (see **Supplemental Movies 1** through **4**).

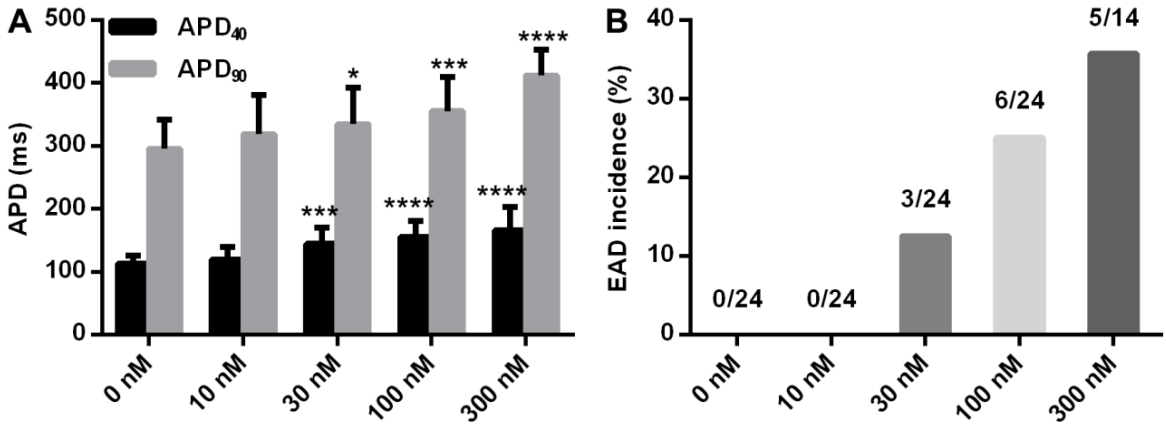

Figure I. Assessment, by optical voltage mapping, of the effect of different concentrations of astemizole on APD_{40} and APD_{90} (**A**) and EAD incidence (**B**) in NRVM monolayers. **P*<0.05, ****P*<0.001 and *****P*<0.0001.

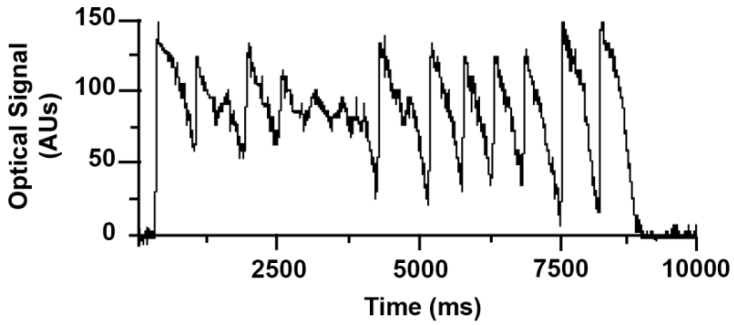

Figure II. Optical voltage trace showing an unstable, self-terminating tachyarrhythmia in an astemizole-treated NRVM culture following 1-Hz electrical point stimulation.

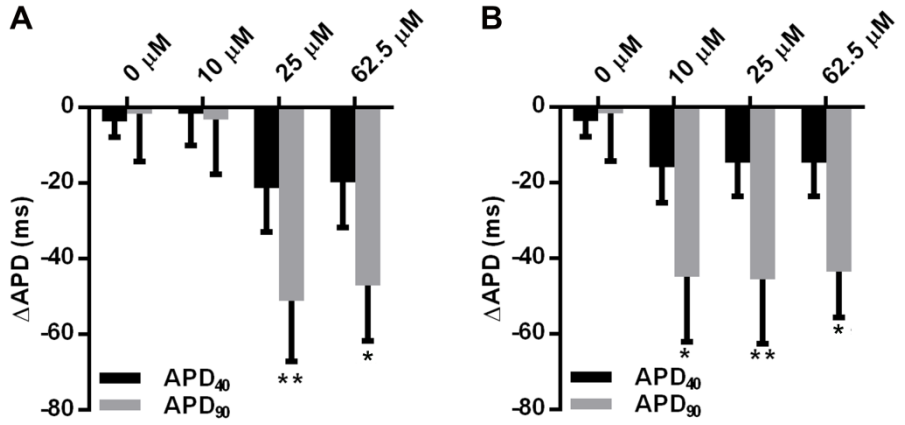

Figure III. Assessment, by optical voltage mapping, of the effect of different concentrations of LUF7244 (**A**) or VU0405601 (**B**) on APD_{40} and APD_{90}. Depicted are the pairwise average changes in APD (ΔAPD) caused by the treatment of NRVM cultures with vehicle or the indicated concentrations of LUF7244 or VU0405601 for 30 min. **P*<0.05 and ***P*<0.01 vs vehicle-treated NRVM cultures. No significant differences in APD_{40} and APD_{90} were observed between the cell cultures exposed to 25 and 62.5 μM LUF7244 and between the NRVM monolayers treated with 10, 25 or 62.5 μM VU0405601. (n=6 per group)

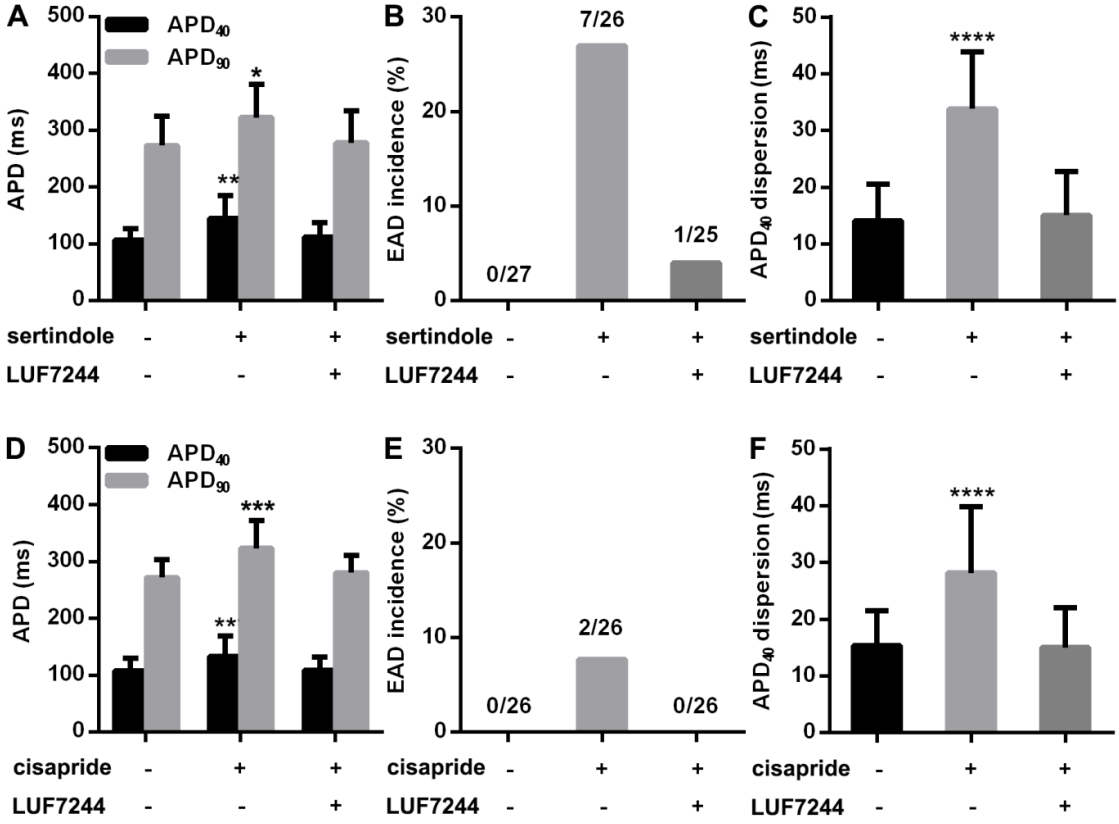

Figure IV. Assessment, by optical voltage mapping, of the ability of LUF7244 to counteract the proarrhythmic effects of sertindole and cisapride on NRVMs. Pretreatment of NRVM cultures with LUF7244 completely prevented the increase in APD_{40} and APD_{90} (**A** and **D**), EAD incidence (**B** and **E**) and APD_{40} dispersion (**C** and **F**) induced by exposure of the cells to 1 μM sertindole (**A**, **B** and **C**) or 1 μM cisapride (**D**, **E** and **F**). **P*<0.05, ***P*<0.01, ****P*<0.001 and *****P*<0.0001.

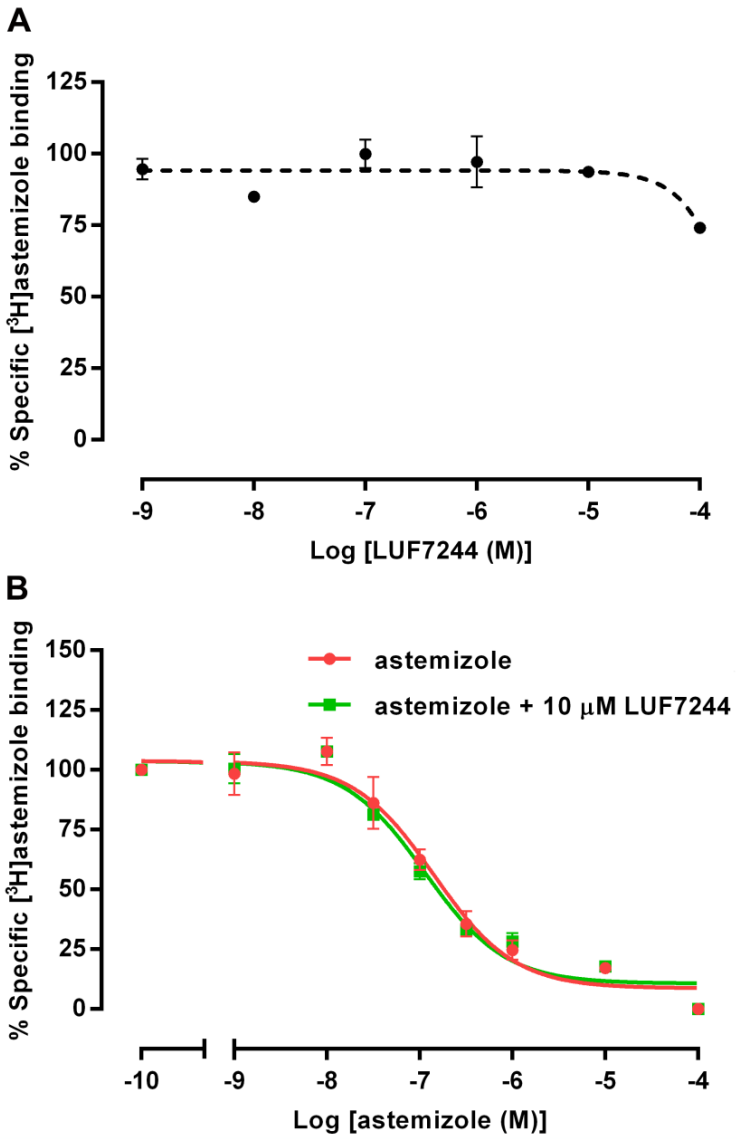

Figure V. Assessment of the effects of LUF7244 on the binding of astemizole to the hH_1R in a [^{3}H]astemizole binding assay performed with membranes of HEK293hH_1R cells. **A:** Displacement curve of LUF7244. **B:** Displacement curve of astemizole in the absence or presence of 10 µM LUF7244.

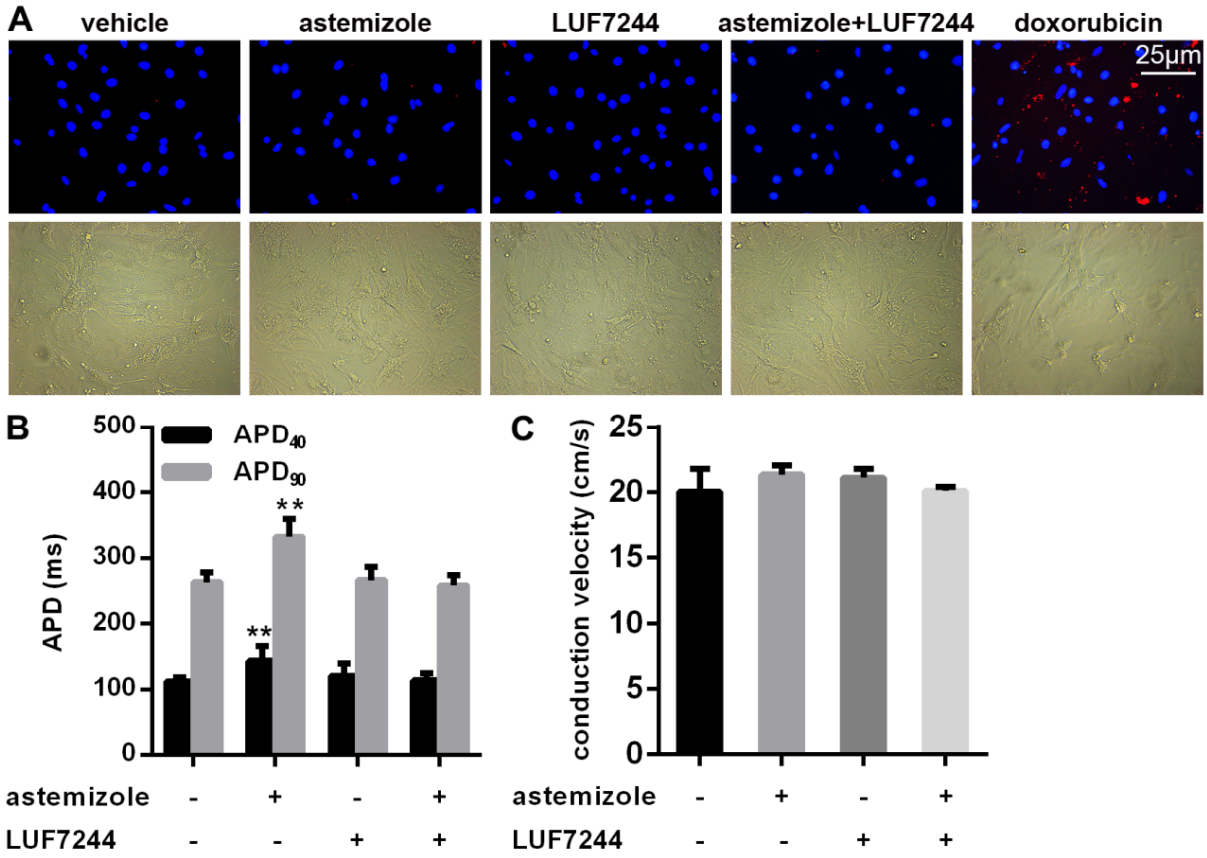

Figure VI. Effects of prolonged exposure of NRVMs to LUF7244 and/or astemizole on cell viability and excitability. **A:** Analysis by Alexa Fluor-568-conjugated annexin V staining of cell surface expression of phosphatidylserine as early marker of apoptosis. NRVM cultures exposed for 72 hours to vehicle, 10 µM LUF7244, 100 nM astemizole or 10 µM LUF7244 plus 100 nM astemizole showed very weak signals, while NRVMs incubated for 24 hours with 1 µM of the proapoptotic drug doxorubicin displayed strong annexin V-associated red fluorescence. The blue fluorescence corresponds to cell nuclei stained with the DNA-binding due Hoechst 33342. **B:** Quantitative comparison of APD_{40} and APD_{90} in NRVM cultures exposed for 72 hours to vehicle, 10 µM LUF7244, 100 nM astemizole or 10 µM LUF7244 plus 100 nM astemizole. $^{**}P<0.01$. **C:** Quantitative comparison of CV in NRVM cultures exposed for 72 hours to vehicle, 10 µM LUF7244, 100 nM astemizole or 10 µM LUF7244 plus 100 nM astemizole. (n=6 per group)

Table I. The half maximal inhibitory concentrations (IC_{50}), percentage specific binding of [^{3}H]dofetilide to the K_v11.1 channel after 6 minutes of dissociation in the absence (control) or presence of 10 μM indicated compounds (%$B/B_{control}$), and dissociation rate (k_{off}) of [^{3}H]dofetilide in the absence (control) or presence of 50 μM indicated compounds.

	IC_{50} (nM)	%$B/B_{control}$	k_{off} (min^{-1})
dofetilide	-	100±0.01	0.21±0.02
+VU0405601	7,757±350	63±3**	0.42±0.04**
+ML-T531	12,000±1,213	77±3**	0.30±0.03*
+LUF7244	3,855±724	44±2**	0.33±0.02**

All values for comparison are means (±SEM) of six samples except that k_{off} values of dofetilide in the absence of indicated compounds or presence of 50 μM ML-T531 are derived from seven samples. Statistical analysis of the results is conducted by Mann-Whitney U test (*P<0.05 vs control; **P<0.01 vs control).

Table II. The K_v11.1 affinities (K_i) of dofetilide, astemizole, sertindole and cisapride in the absence (control) or presence of 10 μM LUF7244.

	K_i (nM)	K_i + 10 μM LUF7244 (nM)	Fold Change
dofetilide	6.2±0.3	20±5*	3.2
astemizole	0.97±0.04	3.7±0.2**	3.8
sertindole	21±2	47±7**	2.2
cisapride	21±1	85±6**	4.0

All values for comparison are means (±SEM) of six samples. Statistical analysis of the results is conducted by Mann-Whitney U test (*P<0.05 vs control; **P<0.01 vs control).

Supplemental Discussion

Clinical Applicability of Allosteric K_v11.1 Modulators

A major concern and obstacle for medicinal chemists involved in the development of drugs to remedy congenital and acquired long QT syndrome is excessive APD shortening resulting in short QT syndrome (SQTS).[9,10] For instance, at a concentration of 10 μM, the potent K_v11.1 activator ICA-105574 shortened the APD in Langendorff-perfused guinea pig hearts by 34% and induced non-"*Torsades de Pointes*"-like ventricular arrhythmias in 2 out of 8 animals.[11] Likewise, in a transgenic rabbit model of LQT1, shortening of the QTc interval by another K_v11.1 activator designated NS1643 was accompanied by an increased incidence of pacing-induced ventricular fibrillation.[12] However, the fact that LUF7244 at a concentration that completely abolished the proarrhythmic effects of astemizole, sertindole and cisapride does not shorten the APD of NRVMs and therefore may not give rise to drug-induced SQTS raises hope for its clinical applicability.

For the experiments in NRVM monolayers, the final astemizole concentration was 100 nM in most cases, while sertindole and cisapride were used at a final concentration of 1 μM. These concentrations are much higher than the therapeutic blood concentrations of these fortuitous K_v11.1 blockers, which are 2-50 μg/L (*i.e.*, 4.4-109 nM) for astimizole, 40-80 μg/L (*i.e.*, 86-172 nM) for cisapride and 50-100 μg/L (*i.e.*, 113-227 nM) for sertindole.[13] The proarrhythmic effects of these drugs on NRVMs were completely prevented by 10 μM (*i.e.*, 3.7 mg/L) LUF7244, a concentration that did not negatively influence the binding of astemizole to the hH_1R and did not noticeably affect the viability, contractility and excitability of the cardiomyocytes (see "*Effects of Prolonged Exposure of NRVMs to LUF7244 and/or Astemizole on Cell Viability, Excitability and Contractility*"). Accordingly, blood LUF7244 concentrations well below 10 μM may suffice to counteract the proarrhythmic effects of unintended K_v11.1 blockers in humans. However, before LUF7244 or other K_V11.1 allosteric modulators can be clinically applied as "*co-drugs*" or otherwise, they should be subjected to rigorous preclinical and clinical testing with appropriate pharmacokinetic and pharmacodynamics assessments to determine their benefit-risk profiles.

Supplemental References

1. Shagufta, Guo D, Klaasse E, de Vries H, Brussee J, Nalos L, Rook MB, Vos MA, van der Heyden MA, IJzerman AP. Exploring chemical substructures essential for hERG K^+ channel blockade by synthesis and biological evaluation of dofetilide analogues. *ChemMedChem.* 2009;4:1722-1732.
2. Ficker E, Dennis AT, Wang L, Brown AM. Role of the cytosolic chaperones hsp70 and hsp90 in maturation of the cardiac potassium channel hERG. *Circ Res.* 2003;92:e87-e100.
3. Yu Z, Klaasse E, Heitman LH, IJzerman AP. Allosteric modulators of the hERG K^+ channel: Radioligand binding assays reveal allosteric characteristics of dofetilide analogs. *Toxicol Appl Pharmacol.* 2014;274:78-86.
4. Pijnappels DA, Schalij MJ, Ramkisoensing AA, van Tuyn J, de Vries AA, van der Laarse A, Ypey DL, Atsma DE. Forced alignment of mesenchymal stem cells undergoing cardiomyogenic differentiation affects functional integration with cardiomyocyte cultures. *Circ Res.* 2008;103:167-176.
5. Askar SF, Ramkisoensing AA, Schalij MJ, Bingen BO, Swildens J, van der Laarse A, Atsma DE, de Vries AA, Ypey DL, Pijnappels DA. Antiproliferative treatment of myofibroblasts prevents arrhythmias in vitro by limiting myofibroblast-induced depolarization. *Cardiovasc Res.* 2011;90:295-304.
6. Cheng Y, Prusoff WH. Relationship between the inhibition constant (K_i) and the concentration of inhibitor which causes 50 percent inhibition (I_{50}) of an enzymatic reaction. *Biochem Pharmacol.* 1973;22:3099-3108.
7. Yu Z, IJzerman A, Heitman L. K_v11.1 (hERG)-induced cardiotoxicity: A molecular insight from a binding kinetics study of prototypic K_v11.1 (hERG) inhibitors. *Br J Pharmacol.* 2015;172:940-945.
8. Potet F, Lorinc AN, Chaigne S, Hopkins CR, Venkataraman R, Stepanovic SZ, Lewis LM, Days E, Sidorov VY, Engers DW, Zou B, Afshartous D, George AL Jr, Campbell CM, Balser JR, Li M, Baudenbacher FJ, Lindsley CW, Weaver CD, Kupershmidt S. Identification and characterization of a compound that protects cardiac tissue from human ether-a-go-go-related gene (hERG)-related drug-induced arrhythmias. *J Biol Chem.* 2012;287:39613-39625.
9. Sanguinetti MC. hERG1 channel agonists and cardiac arrhythmia. *Curr Opin Pharmacol.* 2014;15:22-27.
10. Grunnet M, Hansen RS, Olesen S-P. hERG1 channel activators: A new anti-arrhythmic principle. *Prog Biophys Mol Biol.* 2008;98:347-362.
11. Meng J, Shi C, Li L, Du Y, Xu Y. Compound ICA-105574 prevents arrhythmias induced by cardiac delayed repolarization. *Eur J Pharmacol.* 2013;718:87-97.
12. Bentzen BH, Bahrke S, Wu K, Larsen AP, Odening KE, Franke G, Biermann J, Peng X, Koren G, Zehender M. Pharmacological activation of K_v11.1 in transgenic long QT-1 rabbits. *J Cardiovasc Pharmacol.* 2011;57:223-230.
13. Schulz M, Iwersen-Bergmann S, Andresen H, Schmoldt A. Therapeutic and toxic blood concentrations of nearly 1,000 drugs and other xenobiotics. *Critical Care.* 2012;16:R136.

Chapter 6

Appendix 1

hERG channel (K_v11.1) modulators that enhance dissociation of drugs from their blocking receptor

Saman Rezazadeh, Henry Duff

Adapted from: Circ Arrhythm Electrophysiol. 2016;9:e004003.

Sudden cardiac death secondary to drug-induced long QT syndrome is a major safety concern and has led to withdrawal of several high-profile drugs, such as cisapride and astemizole, from the market. Although these drugs have different chemical structures, they all block the rapid delayed rectifier K^+ current (I_{Kr}) with high potency. The hERG channel (Kv11.1) encoded by the *hERG* gene is responsible for this current. This channel has a high affinity for wide spectrum of compounds compared with other ion channels mainly because of the presence of unique aromatic amino acids in the S6 domain of hERG.[1] This in turn has created a major challenge for development of new drugs.[2] In fact, it is now a routine practice in the pharmaceutical industry to screen compounds for their ability to block hERG early in preclinical safety assessments according to the Food and Drug Administration guidelines. This in turn leads to elimination of a large number of potentially beneficial compounds from chemical libraries.

Interestingly, screening libraries of compounds for their blocking effect on hERG has resulted in discovery of many hERG activators/modulators. These drugs increase current flow through hERG via various mechanisms that include slowing of deactivation, removal of inactivation, and facilitation of activation.[3] In theory, hERG channel activators could have the potential to normalize the QT interval in acquired or congenital long QT syndromes.[4] In fact, the proarrhythmic effects of dofetilide can be reversed, in vitro, by application of hERG channel activators.[5] The draw back in the use of hERG activators clinically has been their inherent ability to shorten the QT interval, possibly to the point of causing arrhythmia.

Given the strain that is placed on drug discovery and also withdrawal of several previously successful drugs because of their QT prolonging properties, it is important to develop reproducible, physiological, and clinically translatable techniques to examine the effect of hERG channel activators and their interaction with long QT inducing drugs. In this issue, Yu *et al*,[6] by using membranes of HEK 293 cells expressing hERG for in vitro radioligand assay, show that a newly synthesized hERG modulator (LUF7244) diminishes the binding affinity of potent hERG blockers, such as dofetilide, astemizole, sertindole, and cisapride. Increased concentrations of this modulator resulted in reduced specific binding of radioactive dofetilide, with Hill coefficient >1, suggesting allosteric interaction rather than direct competition for the same binding site. This notion was fortified by demonstration of altered dissociation rate constant in the presence of LUF7244. This is in agreement with previous findings that openers/modulators may exert their effect by interacting with the channel at sites separate from the pore, where the class III drugs bind.[7] Interestingly, the authors showcase a clever mean to assay the effect of LUF7244 on hERG channel blockers in a physiological setting by using cultured neonatal rate ventricular myocytes. They used high-resolution optical mapping to record action potentials from cells grown to confluence. With this technique, LUF7244 reversed the prolonging effect of astemizole on action potential duration and prevented induction of early after depolarization. Surprisingly, in the absence of hERG blockers, LUF7244 did not shorten action potential duration.

Lack of shortening of action potential duration by LUF7244 was not examined further in their article. This could be because of off-target effect of LUF7244 on other ion channels. For example, NS1643, a known activator of hERG, blocks KCNQ1

current, which is responsible for slow delayed rectifier K^+ current (I_{Ks}).[8] If the ratio of blocking activity at hERG and KCNQ1 balance each other out, then action potential duration will not change significantly, which could be a beneficial feature as it would prevent short QT syndrome. Therefore, it is important to assess the effect of LUF7244 and future hERG activators on a range of ion channels to ensure the absence of unwanted off-target effect.

This article raises 2 interesting questions. First, can hERG modulators/activators be used in combination with drugs that are known to block hERG to mitigate the long QT side effect? This has an immense clinical prospect because it will allow for reintroduction of previously successful drugs and can potentially accelerate drug discovery and development. A significant number of chemicals are eliminated from libraries during drug discovery because of their affinity to hERG. Therefore, by having the ability to counteract this effect, there will be more compounds available to screen for use in variety of diseases. In the future, through mapping the binding site and mechanism of action of various activators, more potent activators will surely be developed.

The second question is can the assays developed by Yu *et al*[6] be used as a high throughput screening strategy? Although patch clamp remains the gold standard in studying the biophysical properties of channels and determining the details by which drugs interact with them, it is technically challenging with low throughput. Here, the authors demonstrate the use of cultured neonatal rat myocytes and optical mapping to assess for action potential duration. The advantage of this technique over existing assays is that it is a physiological screen, capable of determining the effect of a compound on the action potential duration and potential for evoking early after depolarization. Even so, patch-clamp studies of LUF7244 seem essential to clarify its detailed molecular mechanism(s) of action. A detailed understanding of its state-dependent pharmacological affects seems critical. Sitedirected mutagenesis may provide insights as to the topology of its allosteric-binding site on the hERG (KCNH2) channel. Enhanced description of its electrophysiological effects seems an important next step.

A recent article by Yu *et al*[9] proposes interesting potential mechanism(s) for increased dissociation of 3H-dofetilide and 3H-astemizole from the hERG channel by an allosteric modulator (LUF6200). Potassium ions both enhance the allosteric effect of LUF6200 and shift the LUF6200 dose–response curve to the left. Furthermore, their studies suggested a positive cooperativity between LUF6200 and potassium ions. Residence of potassium ions in the selectivity filter of hERG is critical to the C-type inactivation process. Moreover, C-type inactivation state seems to play a pivotal role in stabilizing the dofetilide-associated state of the channel by preventing its dissociation. Alteration of the residence of potassium ions near the C-type inactivation gate (selectivity filter) would shift voltage dependence of inactivation. Modifying C-type inactivation would thus allow dissociation of dofetilide and astemizole from its binding site in the pore. Patch-clamp studies will be necessary to test this hypothesis. Even so, there could be >1 binding site in hERG or binding sites in other ion channels that can indirectly alter dissociation of dofetilide and astemizole from their binding sites. Further studies of this interesting new compound are warranted.

Disclosures

The authors have received funding from the Alberta Heart and Stroke Foundation.

References

1. Sanguinetti MC, Mitcheson JS. Predicting drug-hERG channel interactions that cause acquired long QT syndrome. *Trends Pharmacol Sci*. 2005;26:119–124. doi: 10.1016/j.tips.2005.01.003.
2. Haverkamp W, Breithardt G, Camm AJ, Janse MJ, Rosen MR, Antzelevitch C, Escande D, Franz M, Malik M, Moss A, Shah R. The potential for QT prolongation and proarrhythmia by non-antiarrhythmic drugs: clinical and regulatory implications. Report on a policy conference of the European Society of Cardiology. *Eur Heart J*. 2000;21:1216–1231. doi: 10.1053/
euhj.2000.2249.
3. Zhou J, Augelli-Szafran CE, Bradley JA, Chen X, Koci BJ, Volberg WA, Sun Z, Cordes JS. Novel potent human ether-a-go-go-related gene (hERG) potassium channel enhancers and their *in vitro* antiarrhythmic activity. *Mol Pharmacol*. 2005;68:876–884. doi: 10.1124/mol.105.014035.
4. Seebohm G. Activators of cation channels: potential in treatment of channelopathies. *Mol Pharmacol*. 2005;67:585–588. doi: 10.1124/ mol.104.010173.
5. Kang J, Chen XL, Wang H, Ji J, Cheng H, Incardona J, Reynolds W, Viviani F, Tabart M, Rampe D. Discovery of a small molecule activator of the human ether-a-go-go-related gene (HERG) cardiac K+ channel. *Mol Pharmacol*. 2005;67:827–836. doi: 10.1124/mol.104.006577.
6. Yu Z, Liu J, van Veldhoven JPD, IJzerman AP, Schalij MJ, Pijnappels DA, Heitman LH, de Vries AAF. Allosteric modulation of Kv11.1 (hERG) channels protects against drug-induced ventricular arrhythmias. *Circ Arrhythm Electrophysiol*. 2016;9:e003439. doi: 10.1161/CIRCEP.115.003439.
7. Potet F, Lorinc AN, Chaigne S, Hopkins CR, Venkataraman R, Stepanovic SZ, Lewis LM, Days E, Sidorov VY, Engers DW, Zou B, Afshartous D, George AL Jr, Campbell CM, Balser JR, Li M, Baudenbacher FJ, Lindsley CW, Weaver CD, Kupershmidt S. Identification and characterization of a compound that protects cardiac tissue from human Ether-à-go-gorelated gene (hERG)-related drug-induced arrhythmias. *J Biol Chem*. 2012;287:39613–39625. doi: 10.1074/jbc.M112.380162.
8. Hansen RS, Diness TG, Christ T, Demnitz J, Ravens U, Olesen SP, Grunnet M. Activation of human ether-a-go-go-related gene potassium channels by the diphenylurea 1,3-bis-(2-hydroxy-5-trifluoromethylphenyl)-urea (NS1643). *Mol Pharmacol*. 2006;69:266–277. doi: 10.1124/mol.105.015859.
9. Yu Z, Klaasse E, Heitman LH, Ijzerman AP. Allosteric modulators of the hERG K(+) channel: radioligand binding assays reveal allosteric characteristics of dofetilide analogs. *Toxicol Appl Pharmacol*. 2014;274:78–86. doi: 10.1016/j.taap.2013.10.024.

Chapter 7

Summary and future perspectives

Summary

The general introduction of this thesis, **Chapter 1**, first describes the requirements of proper cell lines that need to be established for research models. Next, p53 and pocket proteins as main regulators in both senescence and quiescence are discussed. Finally, an overview is presented of the capacity of LT to immortalize cells via p53 and RB pathways bypassing senescence or inducing cell cycle reentry of arrested cells.

In **Chapter 2,** the impacts of heterochromatin proteins on premature senescence is investigated. It is shown that the level of heterochromatin protein 1α (HP1α) associated with the nuclear matrix is significantly increased in premature MEFs. Upon DNA damage, HP1α phosphorylation is significantly compromised leading to delayed formation of γ-H2AX foci. Knocking down of HP1α alleviates the delayed DNA damage response and accelerates senescence. Hence, HP1α is identified as a new molecular and mechanistic insight into heterochromatin mis-organization, delayed DNA damage response, and early senescence, providing a promising intervention target for both progeria and normal aging.

Chapter 3 describes a novel bipartite lentivirus vector to quantify cell-to-cell fusion by using the immortalized human myoblasts as a cell fusion model. To this purpose, immortalized human myoblasts are transduced either with a flippase-activatable *Gaussia princeps* luciferase (GpLuc) expression unit (acceptor cells) or with a recombinant gene encoding FLPe, a nuclear-targeted and molecularly evolved version of flippase (donor cells). The key advantage of this system is the replacement of *Photinus pyralis* luciferase (PpLuc) by GpLuc, which is a secretory protein allowing repeated analysis of the same cell culture with a much higher specific luciferase activity than PpLuc. In addition, to investigate whether the speed of FLPe in myotubes is limited due to the presence of the nuclear localization sequence (NLS), the ability of $FLPe^{NLS+}$ and an LV encoding an NLS-less version of FLPe ($FLPe^{NLS-)}$ to activate latent GpLuc genes are compared in myogenic fusion assays. The results show that both $FLPe^{NLS+}$ and $FLPe^{NLS-}$ activate the latent GpLuc gene but when the percentage of FLPe-expressing myoblasts is limiting, $FLPe^{NLS+}$ generally yields slightly higher signals than $FLPe^{NLS-}$. While at low acceptor-to-donor cell ratios, $FLPe^{NLS-}$ is usually superior. However, at high FLPe concentrations the presence of the NLS negatively affects reporter gene expression. This study develops a rapid and simple chemiluminescence assay for quantifying cell-to-cell fusion progression based on GpLuc.

In **Chapter 4**, a conditionally immortalized atrial myocytes (iAMs) line with preserved cardiomyogenic differentiation ability is established. Its proliferative and contractile phenotypes is controlled by a simple change in culture medium composition. Under proliferative conditions, the cells lose most of the properties typical for cardiomyocytes (CMCs) and proliferate with an average doubling time of 38 hour. Under differentiation conditions, the cells stop dividing and gradually reacquire a phenotype resembling that of primary atrial myocytes (pAMs) in gene expression profile, sarcomeric organization, contractile behavior and electrical properties and response to ion channel-modulating compounds. Following high-frequency electrical stimulation reentry is induced in monolayers of these cells resembling atrial fibrillation, which could be terminated by tertiapin treatment, just

like in pAMs monolayers. In addition, iAMs could readily engraft and undergo cardiomyogenic differentiation after injection in atrial tissue. In conclusion, by the controlled expansion and differentiation of iAMs, large numbers of functional CMCs were generated with properties far superior to any of the existing immortalized CMC lines. This cell line provides an attractive cardiac cellular model for disease modelling, drug screening, cell therapy, tissue engineering and fundamental research.

Chapter 5 describes the generation of monoclonal lines of conditionally immortalized brown preadipocytes (iBPAs) using a few mouse brown preadipocytes as starting material. These cells retain long-term proliferation as well as adipogenic capacity. Multilocular lipid droplets are abundantly formed and brown fat markers including uncoupling protein 1 (*Ucp1*) are highly expressed in brown fat cells differentiated from iBPAs. Furthermore, the differentiated cells respond to β3-adrenergic stimulation by increasing glycerol release and *Ucp1* expression. Taken together, iBPA-derived brown fat cells represent a functional easy-to-use model system for fundamental and applied research into BAT.

Chapter 6 shows an *in vitro* model for investigating the action potential (AP)-prolonging and associated proarrhythmic effects of Kv11.1 blockers established by neonatal rat ventricular myocyte cultures. In this study, a newly designed and synthesized compound LUF7244 were proved to fully prevent drug-induced proarrhythmic effects as an allosteric modulator. This is the first study to proof that allosteric modulation of I_{Kr} could protect against drug-induced arrhythmias *in vitro* by preventing potentially arrhythmogenic changes in AP characteristics. This study could therefore provide a rationale to counteract drug-induced ventricular arrhythmias by pharmacological combination therapy relying on allosteric modulation of Kv11.1 channel activity.

Future perspective

Inhibition of premature aging

Except the importance of HP1-mediated heterochromatin formation, heterochromatic gene silencing, chromatin remodelling and DNA damage response, HP1 involved in the repressive function of the retinoblastoma protein (pRB) by binding to the cyclin E promoter[1]. Besides, HP1 was found interacted with a number of other transcriptional repressors[2], indicated that it might have a role in inhibiting many other promoters. Thus, a more general, genome-wide function of HP1 in suppressing gene transcription should be considered in the future study. Rapamycin represses mTOR pathway, which in turn inhibits DNA damage response, and therefore slowing down cellular senescence[3,4]. In the accelerated aging model, mTOR signaling contributes to stem cell dysfunction that occurs in response to endogenous DNA damage, which can be rescued by rapamycin treatment[5]. In this scenario, it would be interesting to examine whether rapamycin could rescue defective DNA repair in *Zmpste24*-null cells and to find the relationship between abnormal prelamin A/ HP1 and mTOR in future study.

Improvement of the cell fusion assay

In **Chapter 3**, an rapid and simple assay to quantify the cell-to-cell fusion progression is developed. However, the use of FLP-FRT system to active the latent Gpluc gene delays the real monitoring time for hours. The sensitivity of the current assay could be improved by changing FLP-FRT system to the bioluminescence resonance energy transfer (BRET) by using two interacted proteins[6]. Besides, the prompter driving monitor genes expression can be optimized by changing a higher activity one.

Improvement of iAM1 differentiation

Various studies have shown that TGFβ critically involved in cardiac differentiation. TGFβ family members have been found to promote cardiomyogenic differentiation in embryonic stem cells (ESCs) and critically involve in the expression of cardiac-specific markers[7-11]. Besides, TGF-β1 significantly increases differentiation efficiency of human CMC progenitor cells into functional CMCs[12]. Apart from TGF-β1, factors such as neuregulin[13], follistatin-like 1[14] and insulin-like growth factor[15,16] have exhibited their cardioprotective effects which may further support the survival of the cells during differentiation. Although iAM1s spontaneously differentiate to functional CMCs in absence of dox with the properties very similar to that of primary AMs, these factors could be candidates to further improve the differentiation and maturation of iAM1s and this will be an interesting topic for future study.

Improvement of the model for drug screening

In **Chapter 6**, the use of neonatal rat ventricular CMC monolayer cultures and optical mapping to investigate compounds is a physiological screening, capable of determining their effects on action potential duration and pro-arrhythmic potential. However, this approach can be further improved by using conditional immortalized human ventricular myocytes. Although mammalian cardiac cell can predict drug responses and cardiotoxicity similar to human cardiac cells, a human system of course has the greater likelihood to mimic the responses in patients. Conditional

immortalized cardiac cells are able to rapidly divide and spontaneously differentiate, therefore they can generate large number of functional CMCs economically. Consequently, combination of these cells and voltage optical mapping can potentially be expanded to high throughput screening for developing drugs including allosteric modulators. In addition, changes in CMC electrophysiological properties upon drug treatment may display differently in a cell layer (2-dimension) than in the heart (3-dimension). The use of Langendorff technique may have greatly contributed to our current understanding of the electrophysiology on the whole heart.

Conditional immortalization in cardiac repair

Heart failure is a growing epidemic caused by the loss of CMCs. Various cell sources have been used for cardiac regeneration and repair, each with its own advantages and challenges.

Human ESCs[17-22] and induced pluripotent stem cells (iPSCs)[23-25] derived CMCs have shown their ability to improve the cardiac function in damaged heart of animal models. However, generation of CMCs from ESCs or iPSCs yields heterogeneous populations of mostly immature CMCs as well as non-CMCs. Their relatively immaturity reduces their efficacy and endogenous integration. Also, the contamination of immature stem cells can induce to teratoma formation after the transplantation[26]. Besides, injection of CMCs derived from human ESCs in damaged myocardium has proarrhythmic risk[22]. Since proper alignment of cardiomyocytes play an important role in the heart function including the electric propagation and the contractile force[27], most likely the injected CMCs cannot align properly with the host CMCs which caused increased electric heterogeneity[28]. Moreover, delivery of high amount of donor cells into the damaged myocardium is very difficult. Cells transplanted in suspensions suffers from low engraftment and cell survival, since the cells may be squeezed out by the contractile force of the heart. Tissue engineering could help the alignment by using graft to guide the alignment of implanted CMCs, however, it is quite challenging to tightly adhere transplanted tissue on the contracting heart as well as subsequent vessel generation and blood supplement into the tissue.

Several groups have directly reprogramed fibroblasts into “induced cardiomyocyte-like cells” (iCMs) using cardiac transcription factors to improve cardiac function[29,30]. These studies provide proof-of-concept that the same cells that cause scar can be reprogramed to replenish the lost CMCs. While much questions remain to be addressed before clinical translation. At present, identification of fibroblast to iCM reprogramming relies on genetic lineage tracing approaches, which may cause false positive by cell fusion and the leakage of Cre activity. Currently, all *in vivo* reprogramming studies have used integrating viruses, which have the potential risk of oncogenesis. Besides, the reprogramming efficiency, maturity and integration of iCMs need to be further improved.

Many factors and pathways showed their functions on stimulation of CMC cell cycle re-entry which bring an attractive strategy to replenish CMCs lost in disease heart by inducing the re-entry of mature CMCs[31-34]. For instance, transgenic expression of Cyclin D2 significantly decreased the infarct size with effective cardiac regeneration[35]. miR-590 and miR-199a stimulated adult CMC proliferation and enhance myocardial recovery after myocardial infarction[36]. However, valid

measurements are required to monitor new CMC expansion as well as their therapeutic outcome. More insights about the molecular mechanisms and stronger pro-mitogenic genes of CMC proliferation need to achieve far more than presently available. Moreover, this strategy is largely limited by the oncogenic potential of pro-proliferative activity.

Another alternative cell source for cardiac repair could be the conditional immortalized cardiac cells. Conditional immortalized CMCs have the ability to amplify sufficiently *in vivo* which avoid the difficulties to delivery large number of cells into the heart. The proliferation of these cells is tightly and reversibly controlled by inducer that provides a protection from oncogenic risk and a repetitive repair upon multiple damage, respectively. Most important, immortalized CMCs could rapidly and synchronously differentiate to pure and mechanically and electrically mature CMCs, in the meantime forming functional couplings with neighbour CMCs from the host. The use of conditional immortalized CMCs in cardiac regeneration would obviate many of the difficulties faced by other cell types, such as immune-compatibility, oncogenic rick, enough cell expansion or delivery of a large number of cells, differentiation, and functional integration.

Future immortalization targets and their applications

Many animals such as rat, mice, dog, and primates are sacrificed to acquire cells from different organs for research purpose which is costly, laborious and not animal-friendly. Immortalization of cell lines from different animal spices and various organs will be an alternative way without sacrificing animals and with advantages.

Disease modeling is important for understanding the mechanisms and finding treatments of the disease. For this reason, models should be able to fully mimic the disease microenvironment. Conditional immortalization of the disease cells caused by the mutations of genes will generate large number of disease cells for development of acquired disease models and identifying new therapeutic treatments. Moreover, immortalization of disease cells from individual patient could be helpful to develop patient specific therapeutics targets.

In cell therapy, the transplanting of patient specific immortalized cells to the damage tissues may eliminate the chances of immune rejection. Similar for the gene therapy, patient specific cells can be genic corrected and amplified by immortalization in the laboratory and then transplanted to one's own body, hence there is no risk of immune rejection. Cell sheet-based tissue engineering is a new generational cell-based regenerative medicine which requires huge amount of functional cells. The conditional immortalization is an attractive cell sources for tissue engineering because it is able to provide pure, abundant, and fully functional cells by using only a few cells as start material.

Cardiac toxicity is a big safety concern for drug development[37]. Immortalized cardiac cell line has shown its globally and efficiently respond to drug induce hazard in **Chapter 4**. Actually, immortalization of human ventricular myocyte would be the ideal cellular model for drug screening upon cardiac safety issue. Moreover, conditional immortalization has the potential to provide a plentiful source of patient-derived cells to screen or test experimental drugs for disease treatment.

Human cell lines have the ability to produce proteins with full human post-translational modifications (PTMs; most notably glycosylation) same to those synthesized naturally in humans, which are a frequently used expression system for biopharmaceutical manufacturing[38]. On one hand, the expression of oncogenes is required for cell lines to grow rapidly to achieve a high cell density and synthesize concentrated protein products. On the other hand, the possibility of transmitting oncogenes from the cell lines to human body raises safety concerns. In this case, conditional immortalization therefore provide an extra layer to protect from this issue.

Moreover, conditional immortalized cell lines provide an attractive new model system for fundamental research. For instance, CMC proliferation and re-differentiation is a potential therapeutic target for myocardial regeneration and repair. However, little is known, on the fundamental mechanisms underlying cell cycle re-entry, proliferation and re-differentiation of CMCs. Given the highly attractive feature of the iAM1s that they spontaneously undergo cardiomyogenic differentiation in the absence of dox and fully differentiated iAM1s resume cell dividing ability in the presence of dox both in a highly synchronized way, this homogenies population provides an useful model to identify the crucial factors involved in cardiac differentiation and de-differentiation (**Figure 1**).

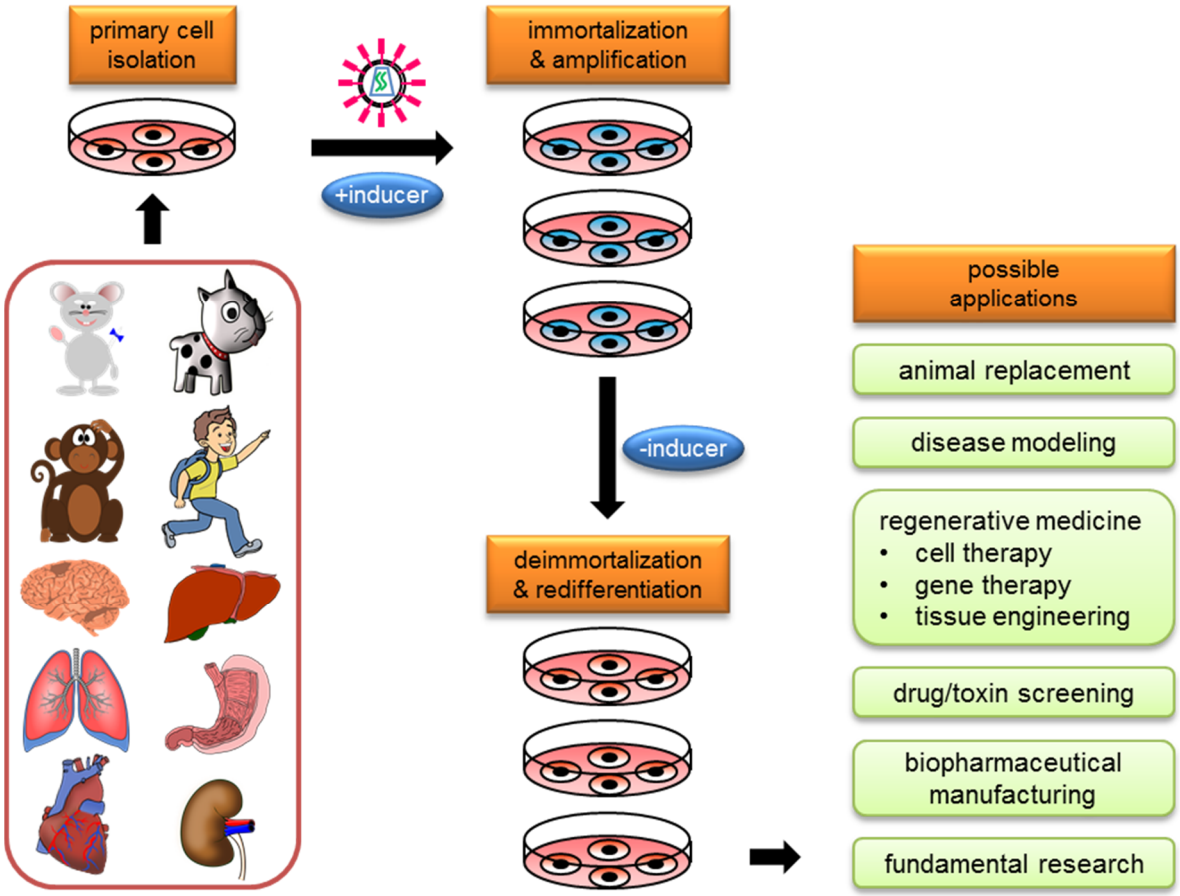

Figure 1. Future immortalization targets and their possible applications. Cell of interesting isolated from different organs of species are used for the reversible immortalization, amplification, re-differentiation and subsequent application.

References

1. Nielsen SJ, Schneider R, Bauer U-M, Bannister AJ, Morrison A, O'carroll D, Firestein R, Cleary M, Jenuwein T, Herrera RE. Rb targets histone H3 methylation and HP1 to promoters. *Nature* 2001;**412**:561.
2. Jones DO, Cowell IG, Singh PB. Mammalian chromodomain proteins: their role in genome organisation and expression. *Bioessays* 2000;**22**:124-137.
3. Pospelova TV, Demidenko ZN, Bukreeva EI, Pospelov VA, Gudkov AV, Blagosklonny MV. Pseudo-DNA damage response in senescent cells. *Cell cycle* 2009;**8**:4112-4118.
4. Demidenko ZN, Zubova SG, Bukreeva EI, Pospelov VA, Pospelova TV, Blagosklonny MV. Rapamycin decelerates cellular senescence. *Cell cycle* 2009;**8**:1888-1895.
5. Takayama K, Kawakami Y, Lavasani M, Mu X, Cummins JH, Yurube T, Kuroda R, Kurosaka M, Fu FH, Robbins PD. mTOR signaling plays a critical role in the defects observed in muscle-derived stem/progenitor cells isolated from a murine model of accelerated aging. *J Orthop Res* 2017;**35**:1375-1382.
6. Pfleger KD, Seeber RM, Eidne KA. Bioluminescence resonance energy transfer (BRET) for the real-time detection of protein-protein interactions. *Nat Protoc* 2006;**1**:337.
7. Sachinidis A, Fleischmann BK, Kolossov E, Wartenberg M, Sauer H, Hescheler J. Cardiac specific differentiation of mouse embryonic stem cells. *Cardiovasc Res* 2003;**58**:278-291.
8. Behfar A, Zingman LV, Hodgson DM, RAUZIER J-M, Kane GC, Terzic A, Pucéat M. Stem cell differentiation requires a paracrine pathway in the heart. *The FASEB Journal* 2002;**16**:1558-1566.
9. Ménard C, Hagège AA, Agbulut O, Barro M, Morichetti MC, Brasselet C, Bel A, Messas E, Bissery A, Bruneval P. Transplantation of cardiac-committed mouse embryonic stem cells to infarcted sheep myocardium: a preclinical study. *The Lancet* 2005;**366**:1005-1012.
10. Slager H, Van Inzen W, Freund E, van den Eijnden-Van Raaij A, Mummery C. Transforming growth factor-β in the early mouse embryo: Implications for the regulation of muscle formation and implantation. *Genesis* 1993;**14**:212-224.
11. Massagué J, Xi Q. TGF-β control of stem cell differentiation genes. *FEBS Lett* 2012;**586**:1953-1958.
12. Goumans M-J, de Boer TP, Smits AM, van Laake LW, van Vliet P, Metz CH, Korfage TH, Kats KP, Hochstenbach R, Pasterkamp G. TGF-β1 induces efficient differentiation of human cardiomyocyte progenitor cells into functional cardiomyocytes in vitro. *Stem cell research* 2008;**1**:138-149.
13. Zhao Y-y, Sawyer DR, Baliga RR, Opel DJ, Han X, Marchionni MA, Kelly RA. Neuregulins promote survival and growth of cardiac myocytes Persistence of ErbB2 and ErbB4 expression in neonatal and adult ventricular myocytes. *Journal of Biological Chemistry* 1998;**273**:10261-10269.
14. Oshima Y, Ouchi N, Sato K, Izumiya Y, Pimentel DR, Walsh K. Follistatin-like 1 is an Akt-regulated cardioprotective factor that is secreted by the heart. *Circulation* 2008;**117**:3099-3108.

15. Hynes B, Kumar AH, O'sullivan J, Klein Buneker C, Leblond A-L, Weiss S, Schmeckpeper J, Martin K, Caplice NM. Potent endothelial progenitor cell-conditioned media-related anti-apoptotic, cardiotrophic, and pro-angiogenic effects post-myocardial infarction are mediated by insulin-like growth factor-1. *Eur Heart J* 2011;**34**:782-789.
16. Mehrhof FB, Müller F-U, Bergmann MW, Li P, Wang Y, Schmitz W, Dietz R, Von Harsdorf R. In cardiomyocyte hypoxia, insulin-like growth factor-I-induced antiapoptotic signaling requires phosphatidylinositol-3-OH-kinase-dependent and mitogen-activated protein kinase-dependent activation of the transcription factor cAMP response element-binding protein. *Circulation* 2001;**104**:2088-2094.
17. Kehat I, Khimovich L, Caspi O, Gepstein A, Shofti R, Arbel G, Huber I, Satin J, Itskovitz-Eldor J, Gepstein L. Electromechanical integration of cardiomyocytes derived from human embryonic stem cells. *Nat Biotechnol* 2004;**22**:1282.
18. Caspi O, Huber I, Kehat I, Habib M, Arbel G, Gepstein A, Yankelson L, Aronson D, Beyar R, Gepstein L. Transplantation of human embryonic stem cell-derived cardiomyocytes improves myocardial performance in infarcted rat hearts. *J Am Coll Cardiol* 2007;**50**:1884-1893.
19. Dai W, Field LJ, Rubart M, Reuter S, Hale SL, Zweigerdt R, Graichen RE, Kay GL, Jyrala AJ, Colman A. Survival and maturation of human embryonic stem cell-derived cardiomyocytes in rat hearts. *J Mol Cell Cardiol* 2007;**43**:504-516.
20. Laflamme MA, Chen KY, Naumova AV, Muskheli V, Fugate JA, Dupras SK, Reinecke H, Xu C, Hassanipour M, Police S. Cardiomyocytes derived from human embryonic stem cells in pro-survival factors enhance function of infarcted rat hearts. *Nat Biotechnol* 2007;**25**:1015.
21. van Laake LW, Passier R, Monshouwer-Kloots J, Verkleij AJ, Lips DJ, Freund C, den Ouden K, Ward-van Oostwaard D, Korving J, Tertoolen LG. Human embryonic stem cell-derived cardiomyocytes survive and mature in the mouse heart and transiently improve function after myocardial infarction. *Stem cell research* 2007;**1**:9-24.
22. Chong JJ, Yang X, Don CW, Minami E, Liu Y-W, Weyers JJ, Mahoney WM, Van Biber B, Cook SM, Palpant NJ. Human embryonic-stem-cell-derived cardiomyocytes regenerate non-human primate hearts. *Nature* 2014;**510**:273.
23. Wu S, Zhu Y, Liu H, Tang L, Du R, Shen Y, Feng J, Zhang K, Xu C, Zhang S. In Vivo Dynamic Metabolic Changes After Transplantation of Induced Pluripotent Stem Cells for Ischemic Injury. *J Nucl Med* 2016;**57**:2012-2015.
24. Funakoshi S, Miki K, Takaki T, Okubo C, Hatani T, Chonabayashi K, Nishikawa M, Takei I, Oishi A, Narita M. Enhanced engraftment, proliferation, and therapeutic potential in heart using optimized human iPSC-derived cardiomyocytes. *Scientific reports* 2016;**6**:19111.
25. Rojas SV, Kensah G, Rotaermel A, Baraki H, Kutschka I, Zweigerdt R, Martin U, Haverich A, Gruh I, Martens A. Transplantation of purified iPSC-derived cardiomyocytes in myocardial infarction. *PloS one* 2017;**12**:e0173222.
26. Yoshida Y, Yamanaka S. iPS cells: a source of cardiac regeneration. *J Mol Cell Cardiol* 2011;**50**:327-332.

27. Pijnappels DA, Gregoire S, Wu SM. The integrative aspects of cardiac physiology and their implications for cell-based therapy. *Ann N Y Acad Sci* 2010;**1188**:7-14.
28. Pijnappels DA, Schalij MJ, Atsma DE, de Vries AA. Cardiac anisotropy, regeneration, and rhythm. *Circ Res* 2014;**115**:e6-e7.
29. Qian L, Huang Y, Spencer CI, Foley A, Vedantham V, Liu L, Conway SJ, Fu J-d, Srivastava D. In vivo reprogramming of murine cardiac fibroblasts into induced cardiomyocytes. *Nature* 2012;**485**:593.
30. Song K, Nam Y-J, Luo X, Qi X, Tan W, Huang GN, Acharya A, Smith CL, Tallquist MD, Neilson EG. Heart repair by reprogramming non-myocytes with cardiac transcription factors. *Nature* 2012;**485**:599.
31. Ahuja P, Sdek P, MacLellan WR. Cardiac myocyte cell cycle control in development, disease, and regeneration. *Physiol Rev* 2007;**87**:521-544.
32. He A, Ma Q, Cao J, Von Gise A, Zhou P, Xie H, Zhang B, Hsing M, Christodoulou DC, Cahan P. Polycomb Repressive Complex 2 Regulates Normal Development of the Mouse HeartNovelty and Significance. *Circ Res* 2012;**110**:406-415.
33. Sdek P, Zhao P, Wang Y, Huang C-j, Ko CY, Butler PC, Weiss JN, MacLellan WR. Rb and p130 control cell cycle gene silencing to maintain the postmitotic phenotype in cardiac myocytes. *The Journal of cell biology* 2011;**194**:407-423.
34. Lin Z, Pu WT. Strategies for cardiac regeneration and repair. *Sci Transl Med* 2014;**6**:239rv231-239rv231.
35. Hassink RJ, Pasumarthi KB, Nakajima H, Rubart M, Soonpaa MH, De La Rivière AB, Doevendans PA, Field LJ. Cardiomyocyte cell cycle activation improves cardiac function after myocardial infarction. *Cardiovasc Res* 2007;**78**:18-25.
36. Eulalio A, Mano M, Dal Ferro M, Zentilin L, Sinagra G, Zacchigna S, Giacca M. Functional screening identifies miRNAs inducing cardiac regeneration. *Nature* 2012;**492**:376.
37. Stockbridge N, Morganroth J, Shah RR, Garnett C. Dealing with global safety issues. *Drug Saf* 2013;**36**:167-182.
38. Ghaderi D, Taylor RE, Padler-Karavani V, Diaz S, Varki A. Implications of the presence of N-glycolylneuraminic acid in recombinant therapeutic glycoproteins. *Nat Biotechnol* 2010;**28**:863.

Samenvatting

In de algemene introductie van dit proefschrift, **Hoofdstuk 1**,worden de voordelen van cellijnen als onderzoeksmodellen beschreven. Vervolgens worden de rollen van p53 en de "pocket proteins" als belangrijke regelaars van zowel "senescence" als "quiescence" bediscussieerd. Tenslotte wordt er een overzicht gegeven over het vermogen van het "simian virus 40" LT eiwit om cellen te immortaliseren via de p53 en pRb signaaltransductieroutes, waardoor "senescence" wordt omzeild en in slapende cellen de celcyclus wordt gereactiveerd.

In **Hoofdstuk 2** wordt het effect van heterochromatine eiwitten op "premature senescence" onderzocht. In dit hoofdstuk wordt aangetoond dat de eiwitexpressie van aan de kernmatrix gebonden heterochromatine eiwit 1α (HP1α) significant verhoogd is in premature MEFs. Wanneer er DNA schade optreedt, leidt dit tot een significante verstoring in de fosforylering van HP1α, wat zorgt voor een vertraging in de formatie van γ-H2AX foci.

Hoofdstuk 3 beschrijft een nieuw tweedelig lentiviraal vectorsysteem om fusie tussen cellen te kwantificeren door gebruik te maken van humane myoblasten als celfusie model. Voor dit doeleinde werden geïmmortaliseerde humane myoblasten getransduceerd met een flippase-activeerbaar *Gaussia princeps* luciferase (GpLuc) expressiemodule (acceptorcellen) of met een recombinant gen coderend voor FLPe, een naar de kern getransporteerde en moleculair geëvolueerde versie van flippase (donor cel). Het belangrijkste voordeel van dit systeem is het gebruik van GpLuc in plaats van *Photinus pyralis* luciferase (PpLuc). GpLuc heeft een veel hogere luciferase activiteit dan PpLuc en wordt bovendien uitgescheiden waardoor dezelfde celkweken meerdere keren geanalyseerd kunnen worden. Daarnaast hebben we onderzocht of de enzymatische activiteit van FLPe in myotubes gelimiteerd is door de aanwezigheid van een kernlokalisatiesignaal (NLS). In een myogene fusie assay werden wild-type $FLPe^{NLS+}$ en een NLS-loze versie van FLPe ($FLPe^{NLS-}$) gebruikt om latent GpLuc te activeren. De resultaten laten zien dat zowel $FLPe^{NLS+}$ als $FLPe^{NLS-}$ het latente GpLuc gen activeren. Maar wanneer het percentage FLPe-expresserende myoblasten gelimiteerd is, wordt er in het algemeen een iets hoger signaal gedetecteerd in $FLPe^{NLS+}$ ten opzichte van $FLPe^{NLS-}$ myoblasten, terwijl bij lage acceptor-donor cel ratio's meestal $FLPe^{NLS-}$ beter functioneert. Echter, bij hoge FLPe concentraties heeft de aanwezigheid van de NLS een negatieve werking op de reporter genexpressie. Deze studie laat een snelle en simpele chemiluminiscentie assay zien voor het kwantificeren van fusie tussen cellen gebaseerd op GpLuc.

In **Hoofdstuk 4** wordt een conditioneel geïmmortaliseerde atriale myocyten (iAM) cellijn met geconserveerd cardiomyogene differentiatie eigenschappen gemaakt waarvan het fenotype (proliferatief of contractiel) kan worden gecontroleerd door een simpele verandering in de compositie van het kweekmedium. Onder proliferatieve condities verliezen de cellen het merendeel van hun eigenschappen die typische zijn voor cardiomyocyten (CMCs) en verdubbelen zich gemiddeld elke 38 uur. Onder differentiatiecondities stoppen de cellen met delen en verkrijgen geleidelijk aan een fenotype dat lijkt op het fenotype van primaire atriale myocyten (pAM) voor wat betreft genexpressieprofiel, sarcomere structuur, contractiel gedrag, elektrische eigenschappen en effecten van ionkanaal-modulerende stoffen. Hoog frequente

elektrische stimulatie induceerde rotors (zogenaamde elektrische stormen) in iAM monolagen lijkend op boezemfibrilleren welke beëindigd konden worden door toediening van tertiapin net zoals in monolagen van pAMs. Daarnaast bleken iAMs zich na injectie in boezemweefsel te kunnen differentiëren in CMCs die niet te onderscheiden waren van de omliggende endogene hartspiercellen. Concluderend kan dus worden gesteld dat met behulp van iAMs, grote hoeveelheden functionele CMCs geproduceerd kunnen worden via gecontroleerde proliferatie en differentiatie. De eigenschappen van deze hartspiercellen zijn superieur aan die van alle bestaande cellijnen van geïmmortaliseerde CMCs. De iAM cellijn is daardoor een aantrekkelijk cellulair modelsysteem voor het nabootsen van hartziekten, drug screening, celtherapie, "tissue engineering", en fundamenteel onderzoek.

Hoofdstuk 5 beschrijft de creatie van monoclonale cellijnen van conditioneel geïmmortaliseerde bruine pre-adipocyten (iBPAs) met enkele bruine pre-adipocyten uit muizen als startmateriaal. De iBPAs behouden langdurig zowel proliferatieve als adipogene eigenschappen. Multiloculaire vetdruppeltjes worden rijkelijk gevormd en markers van bruin vetweefsel, inclusief uncoupling protein 1 (Ucp1), komen sterk tot expressie in gedifferentieerde iBPAs. Daarnaast reageren deze cellen op β3-adrenergische stimulatie door een verhoogde glycerolproductie en een verhoogde expressie van Ucp1. iBPA-afgeleide bruine vetcellen vertegenwoordigen dus een functioneel "easy-to-use model" voor fundamentele en toegepaste wetenschap naar bruin vet.

In **Hoofdstuk 6** wordt een kweekmodel gebaseerd op neonatale ventriculaire myocyten van de rat beschreven om verlenging van de actiepotentiaal (AP) door zogenaamde $K_v11.1$ blokkers en de hiermee geassocieerde pro-aritmische effecten onderzoeken. Deze studie bewijst dat een nieuw ontworpen en gesynthetiseerde stof (LUF7244) pro-aritmische effecten volledig kan voorkomen via allosterische modulatie. Dit is de eerste studie die aantoont dat allosterische regulatie van I_{Kr} *in vitro* bescherming biedt tegen drug-geïnduceerde aritmiën door potentiele aritmogene veranderingen in de AP karakteristieken te voorkomen. Deze studie zou als basis kunnen dienen voor de ontwikkeling van farmacologische combinatietherapieën ter bestrijding van drug-geïnduceerde ventriculaire aritmiën. Effectieve geneesmiddelen die door hun remmende werking op het $K_v11.1$ ionkanaal en het hiermee gepaard gaande risico op plotselinge hartdood momenteel niet kunnen worden toegepast zouden dan alsnog kunnen worden ingezet.

List of publications

List of publications

Full papers

1. **Liu J***, Yin X*, Liu B, Zheng H, Zhou G, Gong L, Li M, Li X, Wang Y, Hu J, Krishnan V, Zhou Z, Wang Z. HP1α mediates defective heterochromatin repair and accelerates senescence in Zmpste24-deficient cells. Cell Cycle 2014;13(8):1237-47.
2. Yu Z*, **Liu J*,** van Veldhoven JP, IJzerman AP, Schalij MJ, Pijnappels DA, Heitman LH, de Vries AA. Allosteric Modulation of Kv11.1 (hERG) Channels Protects Against Drug-Induced Ventricular Arrhythmias. Circ Arrhythm Electrophysiol. 2016 Apr;9(4).
3. Neshati Z, **Liu J**, Zhou G, Schalij MJ, de Vries AA. Development of a lentivirus vector-based assay for non-destructive monitoring of cell fusion activity. PLoS One. 2014;9(7):e102433.
4. Engels MC, Askar SF, Jangsangthong W, Bingen BO, Feola I, **Liu J**, Majumder R, Versteegh MI, Braun J, Klautz RJ, Ypey DL, de Vries AA, Pijnappels DA. Forced fusion of human ventricular scar cells with cardiomyocytes suppresses arrhythmogenicity in a co-culture model. Cardiovasc Res. 2015 Sep 1;107(4):601-12.
5. **Liu J**, Volkers L, Jangsangthong W, Bart CI, Engels MC, Zhou G, Schalij MJ, Ypey DL, Pijnappels DA, de Vries AAF. Generation and primary characterization of iAM-1, a versatile new line of conditionally immortalized atrial myocytes with preserved cardiomyogenic differentiation capacity. Cardiovasc Res. 2018. doi: 10.1093/cvr/cvy134.
   *Equal contribution

Selected abstracts

1. **Liu J**, Yin X, Zhou G *et al*. HP1α-mediated premature aging via interaction with prelamin A in Zmpste24-deficient mouse embryonic fibroblasts. The 20th IAGG World Congress of Gerontology and Geriatrics. 2013, June 23-27, Seoul, Korea.
2. **Liu J**, Yu Z, Van Veldhoven JP *et al*. Full protection from drug-induced torsade de pointes-like arrhythmias by an allosteric Ikr-modulatory mechanism in rat ventricular monolayers. Europace. 2015, June 21-24, Milano, Italy.
3. **Liu J**, Yu Z, Van Veldhoven JP *et al*. Protection from drug-induced arrhythmias by a novel allosteric modulator in a new validated rat ventricular cardiomyocyte model. Rembrandt Symposium. 2016, November, Noordwijk, the Netherlands.
4. **Liu J**, Watanabe M, Jangsangthong W *et al*. Generation and characterization of iAM-1, a versatile new line of conditionally immortalized atrial myocytes with preserved cardiomyogenic differentiation capacity. Rembrandt Symposium. 2017, November, Noordwijk, the Netherlands.
5. **Liu J**, Volkers L, Jangsangthong W *et al*. Conditionally immortalized atrial myocytes as potential cell source for myocardial regeneration. Netherlands Society of Gene and Cell Therapy Spring Symposium. 2018, March 15-16, Lunteren, the Netherlands.

Acknowledgements

Acknowledgements

This thesis was completed due to the guidance, assistance and cooperation of a large group of people. Therefore, I would like to offer my acknowledgements to them who contributed to this dissertation.

First and foremost, I would like to express my most sincere appreciation to my supervisors, Prof. dr. Schalij, Twan and Daniel. I feel extremely privileged and fortunate to have been your student. Prof. dr. Schalij, thank you for continuous support of my PhD training. Twan, thanks for your supervise, patience and encouragement. Daniel, thanks for your guidance, insight and comprehension.

Secondly, a great debt of gratitude should be extended to my lovely colleagues and friends for all the wonderful times that we share inside and outside of the laboratory. I feel very comfortable and relaxed to work in the laboratory of Cardiology. I appreciated all people from this lab: Dick, Margreet, Cindy, Minka, Arti, Linda, Iolanda, Sasha, Magda, Emile, Niels, Pim, Sven, Juan, Annemarie, Rupa, Yoke, Marc, Zeinab, Said, Brian, Masaya and Jan, for your help, kindness and supports. I am deeply grateful to my collaborators, Prof. IJzerman, Laura, Sander, Hetty, Eline, Prof. Christoffels, Antoinette, Prof. Brundel, Deli, Prof. Wang Zimei and in particular, Zhiyi who is also my good friend and Prof. Zhou for introducing me to the world of science.

Thirdly, there are a large group of my close friends, who I wish to thank for your help, supports and joyful gatherings, such as Wenbo, Yingguang, Rui, Puning, Guangsheng, Niu Jing, Wan Yang, Hui, Cui, Xueyu and Depeng, Qingju and Xiao, Zhang Jing and Kong Li, Botao and Juan, Qinggang and Fumei. Jujitsu friends, Hugo, Martin, Lotte, Alex, Joel, Fabian, Bas, Jonathan and many others, thanks for your advice, encouragement and the pleasant times we have spent.

Last but not least, I am deeply indebted to all my family members for your unconditional and constant love, understanding, support and sacrifices during my studies. I warmly appreciate my lovely parents for exhortation and supports throughout my life. Yue, my dear sister, thanks for your encouraging and taking care of our parents when I was away from them. I am deeply grateful to my parents in law, you have provided assistance in numerous ways. My deloved son, Muze, I am so lucky and grateful to have you in my life. Finally, I would like to thank my precious husband, dear Yang, without your support and encouragement I could not have finished this work.

感谢家人一直以来对我无私的爱和付出。爸爸妈妈，感谢你们对我的培养；妹妹，感谢你对家庭责任的承担，让我没有后顾之忧；公公婆婆，感谢你们对我无微不至的关怀；洋，我的学业离不开你的鼓励和付出；沐泽，拥有你是我最大的幸福。

Curriculum Vitae

Curriculum Vitae

Jia Liu was born on July 2nd, 1987 in Shandong, China. She graduated from Weifang No.12 High School in 2005. And afterwards she obtained her bachelor's degree in biology science at Sichuan Normal University in 2009. She started her master study in State Key Laboratory of Biotherapy at Sichuan University in 2009 and she obtained her master's degree in 2012. After her graduation, she joined the Laboratory of Cardiology at Leiden University Medical Centre as a scientific researcher. In 2014, Jia Liu was supported by the China Scholarship Council to conduct a PhD study in the same department under the supervision of Prof. M.J. Schalij, Dr. A.A.F. de Vries and Dr. D.A. Pijnappels. Her doctorate dissertation consisted of two main projects, which were the generation of cell lines by conditional immortalization and the application of cellular models for biomedical research. Jia Liu together with her supervisors developed several valuable collaborations with Leiden Academic Centre for Drug Research and Division of Endocrinology at Leiden University Medical Centre, where she acquired different research skills. Her work is presented in this thesis.